Abstract

Ortiz, Sean C., High Power Spatial Combiners: Tile and Tray Approaches. (Under the direction of Amir Mortazawi.)

Spatial power combining is a method of coherently combining the power of many amplifying devices using free space as the power dividing/combining medium in contrast to traditional circuit based combiners. The spatial combiner is formed from an array of amplifying unit cells, with each cell receiving a signal, amplifying it, and then radiating it into free space. Two methods of spatial power combining, tile and tray, are investigated in this thesis. The tile-based spatial combiner consists of a thick groundplane with receiving microstrip patch antennas on one side and transmitting microstrip patch antennas on the other. In addition, amplifiers are placed on both sides of the thick groundplane, which provides efficient heat removal. This research is focused on the optimal array spacing, biasing, and feeding of tile-based arrays to achieve high output power levels at Ka-band (Lockheed Martin was specifically interested in achieving greater than 25 Watts of radiated power under a DARPA MAFET-3 program). Several arrays were developed, consisting of 13, 45, and 98 elements. Noteworthy results were obtained from the experiments with this design approach.

A tray-based approach is also investigated in this thesis. This approach differs from the tile-based approach by having multiple groundplanes (trays) containing amplifiers stacked to form an array of amplifying unit cells. In addition, microstrip patch antennas are placed at the ends of the trays and radiate in an end-fire pattern with respect to the tray containing the amplifiers. For this purpose, an approach has been developed for the feeding of the microstrip patch antennas. This feeding mechanism allows the amplifiers and radiating elements to be isolated. Thus more room is allowed for the amplifiers, while minimizing coupling that may cause spurious oscillations. An X-band and Ka-band array have been developed, consisting of 25 and 49 elements, respectively. Both arrays provide efficient heat sinking through thick metal groundplanes. In addition, an experimental analysis on the array tolerance to device failure has been performed on both tray-based arrays. This study examines the effect of device failure on the gain, power output, and radiation pattern.

Report Documentation Page

Form Approved
OMB No. 0704-0188

1. REPORT DATE	2. REPORT TYPE	3. DATES COVERED
2001		**00-00-2001 to 00-00-2001**

4. TITLE AND SUBTITLE	5a. CONTRACT NUMBER
High Power Spatial Combiners: Tile and Tray Approaches	5b. GRANT NUMBER
	5c. PROGRAM ELEMENT NUMBER
6. AUTHOR(S)	5d. PROJECT NUMBER
	5e. TASK NUMBER
	5f. WORK UNIT NUMBER
7. PERFORMING ORGANIZATION NAME(S) AND ADDRESS(ES) **North Carolina State University,Department of Electrical Engineering,Raleigh,NC,27695**	8. PERFORMING ORGANIZATION REPORT NUMBER
9. SPONSORING/MONITORING AGENCY NAME(S) AND ADDRESS(ES)	10. SPONSOR/MONITOR'S ACRONYM(S)
	11. SPONSOR/MONITOR'S REPORT NUMBER(S)

12. DISTRIBUTION/AVAILABILITY STATEMENT
Approved for public release; distribution unlimited

13. SUPPLEMENTARY NOTES
The original document contains color images.

14. ABSTRACT

15. SUBJECT TERMS

16. SECURITY CLASSIFICATION OF:			17. LIMITATION OF ABSTRACT	18. NUMBER OF PAGES	19a. NAME OF RESPONSIBLE PERSON
a. REPORT	b. ABSTRACT	c. THIS PAGE			
unclassified	**unclassified**	**unclassified**		**194**	

High Power Spatial Combiners: Tile and Tray Approaches

by

Sean C. Ortiz

A dissertation submitted to the Graduate Faculty of
North Carolina State University
in partial fulfillment of the
requirements for the Degree of
Doctory of Philosophy

ELECTRICAL ENGINEERING

Raleigh, North Carolina

2001

APPROVED BY:

James F. Kauffman	Michael Steer
Angus Kingon	Amir Mortazawi Chair of Advisory Committee

This dissertation is dedicated to my wife, España Ortiz, and to my daughter, Emily Nicole Ortiz, who have sacrificed considerably for the pursuit of my education. Without their understanding and support, my completion of this work would not have been possible. I would also like to dedicate this work to my parents Linda and Rodolfo Ortiz, who have instilled within me the character and resolution to complete this work.

Biography

Sean Christopher Ortiz was born on March 23, 1974 in Charlotte, North Carolina. He graduated from Gateway High School in Kissimmee, Florida in 1992. He then entered the department of Electrical and Computer Engineering at the University of Central Florida in Orlando, FL and received a Bachelor of Science degree in Electrical Engineering in 1996. He continued on at the same university and received a Master of Science degree in Electrical Engineering in 1998. Sean then joined the Department of Electrical and Computer Engineering at North Carolina State University, where he has completed the requirements for a Ph.D. in Electrical Engineering.

Acknowledgments

The author would like to acknowledge Dr. Amir Mortazawi for his guidance and support throughout this effort. Thanks also go to Lee Mirth and John Hubert for their many fruitfull discussions. The author has been partially supported by a National Science Foundation graduate fellowship. This work has been partially funded under a DARPA MAFET-3 program through the Air Force Research Laboratory, Wright-Patterson Air Force Base, contract number N66001-96-C-8628 and an Army Research Office MURI grant under the Spatial and Quasi-Optical Power Combining DAAG-55-97-0132.

Contents

List of Figures

List of Symbols

f	–	Frequency.
dB	–	Decibel.
mm	–	Millimeter.
GHz	–	Giga-cycles per second.
MHz	–	Mega-cycles per second.
W	–	Watt.
K	–	Degrees Kelvin.
$^{\circ}C$	–	Degrees Celsius.
V	–	Volt.
mA	–	Milli-ampere.
V_{DS}	–	Drain to source voltage.
V_{GS}	–	Gate to source voltage.
I_{DS}	–	Drain to source current.
dBm	–	Power in milli-decibels.
mS	–	Milli-Siemens.
μ_e	–	Electron mobility.
v_s	–	Electron velocity.
PAE	–	Power added efficiency.
$EIRP$	–	Effective isotropic radiated power.
f_{max}	–	Maximum operating frequency.
f_t	–	Gain bandwidth product.

Chapter 1

Introduction

1.1 Motivations for Power Combining Amplifiers

The increased demand for smaller, lighter, and more reliable military and commercial communication systems has created a great need for high power solid-state amplifiers operating at microwave and millimeter-wave frequencies. Examples of some military based applications include Ka-band monostatic missile seekers, ground-, air- and ship-based radar, and ground- and space-based transponders. Some of these applications fall into the realm of the commercial marketplace, as with the transponders necessary for communication systems in either satellites or ground-based systems such as Local Multipoint Distribution Systems (LMDS). In order to obtain the high power necessary for these growing number of military and commercial applications, it is either necessary to develop higher power devices meeting the demands of these systems, whether they be semiconductor based or vacuum microelectronics based, or it is necessary to combine the power of many devices to achieve the required power levels.

Vacuum tubes, currently, offer the only commercially viable amplifiers capable of producing high output power levels at microwave and millimeter-wave frequencies. However, much research is currently being focused on wide bandgap semiconductors such as SiC and GaN, since these semiconductors offer the most potential for high output power levels from a single device, although their application at millimeter-wave frequencies has not been established. There is also a growing level of research in the area of field-emission vacuum microelectronics, which is based on the development of vacuum tube type devices using semiconductor fabrication processes. This offers a potential mass production technique for high power device fabrication. In addition, many devices, either traditional or wide bandgap, can be combined in a number of ways to produce high power levels. These methods include circuit-level power combiners, such as the Wilkinson-based power combiners, and spatial power combining methods, which use free space as the power combining medium. However, the utility of the circuit-level power combiner is limited at millimeter-wave frequencies, due to the increased loss of transmission lines at these frequencies. In contrast, trans-

mission line losses are minimized at millimeter-wave frequencies in spatial combiners, since most of the power combining occurs in free space. In addition, losses do not rapidly increase with an increase in the number of devices as with circuit-based combiners but remain at relatively constant levels (i.e. scalable).

Although providing high output power levels, vacuum tube amplifiers are not as attractive as the solid-state amplifier in the mass production marketplace of today. Two important factors for this are cost and reliability. It is expensive and time consuming to produce vacuum tube amplifiers, while semiconductor manufacturing has proven to be very inexpensive in high volume production. In addition, the reliability of a system depending on a single high power vacuum tube (i.e. single point failure) is not nearly as high as a system relying on several power combined solid-state amplifiers, especially when the single solid-state device is more reliable than the vacuum tube. The power level necessary from a vacuum tube amplifier will also be greater due to the increased noise produced by vacuum tubes in comparison to solid-state amplifiers [2]. This places additional burdens on the system design.

In conclusion, it is clear that the development of solid-state amplifiers is necessary for the future of low cost, manufactured military and commercial communication systems. However, their output power tends to be very low, resulting from the small physical size of the active region (i.e. difficulties in heat sinking) and limitations imposed by impedance matching, resulting in the $1/f$ and $1/f^2$ dependency of available power, respectively [1]. This has forced current development efforts to be focused on either high power single devices, using wide bandgap semiconductors (currently at X-band), or spatial power combiners. This thesis is focused on the development of the spatial power combiner as a viable means of producing high power levels at microwave and millimeter-wave frequencies.

1.2 Overview of Power Combining Methods

Two broad categories of power combining are introduced, circuit-level and spatial (also referred to as quasi-optical). These two methods can best be viewed in Fig. 1.1 and Fig. 1.2. The circuit-level combiner divides the power from a single input to several amplifiers combined in parallel through the use of transmission lines. These transmission lines may be microstrip, coplanar waveguide (CPW), rectangular waveguide, strip line, etc. Each of these has its own advantage at various frequencies and for various applications. Clearly the microstrip and CPW transmission lines have the greatest advantage in Monolithic Microwave Integrated Circuits (MMICs), due to their ease of integration into such semiconductor processes. However, losses can be high at millimeter wave frequencies in comparison to other guiding structures such as the rectangular waveguide, which is not easily integrated with MMIC amplifiers or Integrated Circuit (IC) processing techniques. It is evident that, as additional amplifiers are combined, the transmission line lengths and circuit complexity increase. As the line lengths increase to add more devices, the losses accumulate in the circuit, eventually exceeding the gain of the amplifiers being added and negating the benefit of the

additional amplifiers. The spatial power combiner does not use transmission lines to divide an input signal to the amplifiers thus does not suffer from the accumulation of losses in the transmission lines by the addition of more amplifiers. Instead, a signal is radiated from a source and received by an array of parallel amplifying unit cells. Each cell amplifies the signal and then re-radiates it into free space. This, however, creates new design challenges. The overall system size may be large; the design may be complex due to the proximity of amplifying and radiating elements; the dissipation of heat is fundamentally more difficult; and the system may be difficult to model due to its large electrical size. Several basic concepts of spatial and circuit-level power combining will be introduced in the following sections.

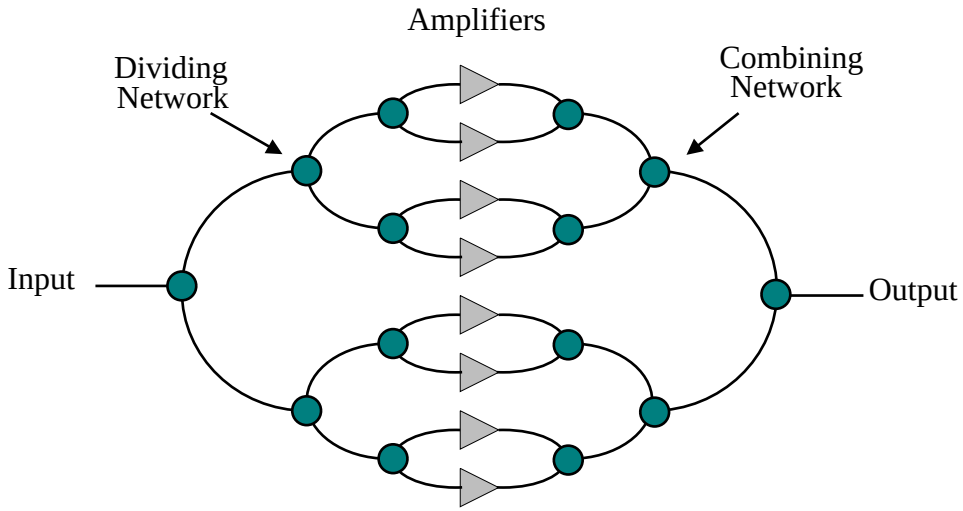

Figure 1.1: A Conventional binary circuit-level combiner.

1.2.1 Circuit-Level Combiners

Traditionally, when the power output from a semiconductor device is insufficient for a particular system application, several devices may be combined using circuit-level power combining techniques. These techniques are applicable to the monolithic as well as hybrid amplifier designs. Several types of circuit-level power combiners are possible [3, 4], but most microwave and millimeter-wave techniques rely on 3-dB directional couplers or power dividers. Essentially, a signal is split between two output ports with the possibility of an isolated port in the case of a directional coupler. This represents the first stage of splitting. A second stage will then divide the two signal paths into four, and a third stage will create eight signal paths. This concepts is illustrated in Fig. 1.1, where each dividing network can be implemented by a Wilkinson power divider, Lange coupler, hybrid network, etc.

As mentioned, there are several possible couplers or dividers that can be used in a circuit-level power divider. One of the most popular is the 3-port Wilkinson power divider [5]. This method

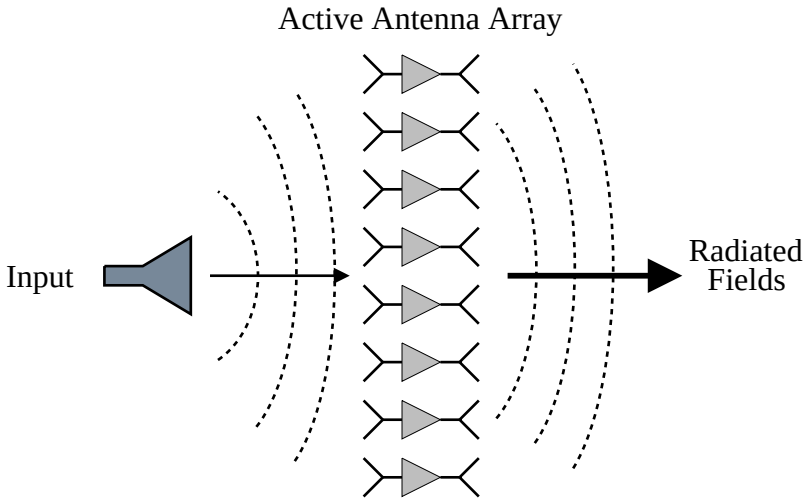

Figure 1.2: An illustration of a spatial power combiner.

involves the equal division of an input signal into two ports, where the input port and output ports are separated by a λ/4 transmission line. Other possibilities include the branchline hybrid in a quadrature configuration, the Lange coupler, and the hybrid ring [6]. Each of these couplers also require lengths of transmission lines between the input and output ports. This length is at least λ/4 and sometimes as large as 3λ/4. In addition, these couplers require that a load be placed at the isolated port to minimize reflection. Since each of these couplers or dividers require a significant space to be implemented, additional transmission lines must be added to connect the stages of the complete corporate divider/combiner. The utility of the circuit-level combiner becomes prohibitive as the number of devices increases. This is best illustrated with the formulation from [1] for the power-combining efficiency of a multistage hybrid type combiner with K stages, given by $\eta = L^K$, where L is the loss per hybrid path. The total output power is $P_{out} = P_0 2^K L^K$, where P_0 is the output power per device.

Combining efficiency versus the number of hybrid combining stages is plotted in Fig. 1.3 for several cases of hybrid loss. The case for 1.35 dB loss per hybrid path was found in [7], which demonstrated a Ka-band Wilkinson power divider on *Rogers TMM3*^{TM} having a dielectric dissipation factor of 0.002. This represents a realistic case in the millimeter-wave regime. As the figure illustrates, the power combining efficiency quickly deteriorates for a large number of devices and is prohibitive for more than 6 stages or 64 devices in the moderate case of 0.5 dB loss per hybrid path. Clearly such power combining methods can not be used alone for the combining of 50 or more devices. However, these methods still form the basis for producing MMIC amplifiers, which may be combined using spatial power combining techniques.

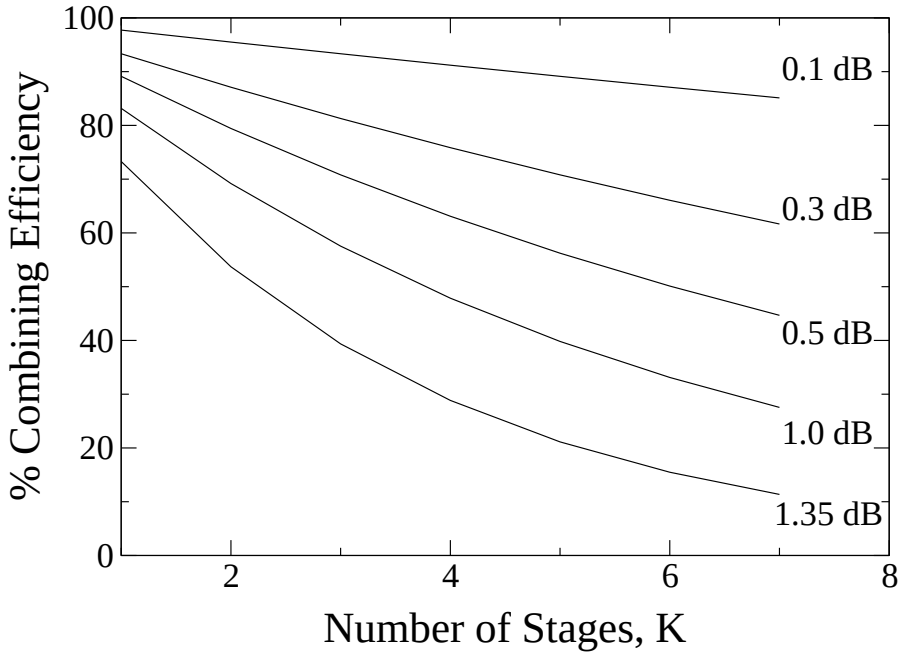

Figure 1.3: Theoretical combining efficiency of a circuit-level combiner for various losses in the combining stages versus the number of stages.

1.2.2 Spatial Combiners

Spatial combining encompasses a broad range of microwave circuits. These include amplifiers, oscillators, beam controllers, and frequency converters [8]. Although, this introduction of spatial combining will be limited to amplifiers. As Fig. 1.2 illustrated, the spatial power combiner, as applied to amplifiers, consists of an array of amplifying unit cells which receive, amplify, and then radiate an impinging signal into free space. Since most of the power division is performed in free space, losses are minimized. This is especially true at millimeter-wave frequencies, where the loss of a copper microstrip line is in excess of 8 dB/m, while free space losses are less than 10^{-4} dB/m [1]. So in principle, spatial power combiners can achieve very high power combining efficiencies. The main limit being the efficiency of the radiating elements and difficulties in uniformly exciting and collecting the output power.

Spatial power combining amplifiers can be categorized according to both array geometry and the mechanism in which they are fed. Most spatial power combiners may be fed in one of two ways, illustrated in Fig. 1.4. The earlier versions of spatial power amplifiers were fed from an input horn located in the far-field of the amplifying array, as seen in Fig. 1.4(a). In addition, a system of lenses is necessary to focus the energy radiated from the source (a Gaussian beam from a horn antenna) onto the array of amplifiers and to focus the radiated signal into a receiving antenna. A second feeding mechanism, shown in Fig. 1.4(b), places the amplifying array in either close proximity or

within a feeding horn antenna.

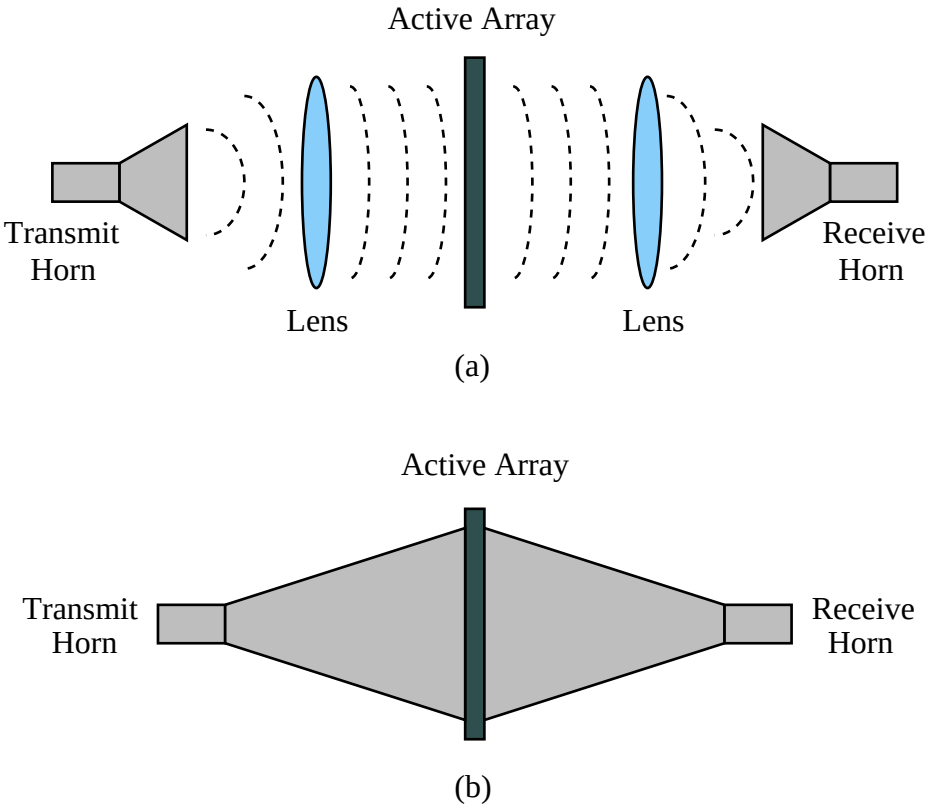

Figure 1.4: Methods of feeding spatial power combiners. (a) An open spatial power combiner using a lens-focused arrangement. (b) A closed combiner using horn antenna feeds in the near-field.

There are several benefits to both methods. The far-field excitation of the amplifying array minimizes the interaction between the radiating elements of the array and the feeding antenna. In addition, the feeding beam may be focused, polarized, or reflected if necessary, much the way beams are manipulated in geometrical optics [9]. However, the system size may be large at microwave and millimeter-wave frequencies, due to the separation between components of the system. Also, spill over losses may be incurred, resulting from incorrect beam focusing. At submillimeter-wave frequencies this may no longer be a disadvantage with the shrinking size of components and wavelength. The near-field excitation offers the main benefit of reduced size and possibly weight. Although, the interaction of the feeding horn and the antenna array must be taken into consideration, but spill over losses are minimized.

Furthermore, several array geometries are possible with two main categories–*tile and tray*. These are illustrated in Fig. 1.5. The tile approach consists of a planar array of amplifying unit cells, where the array of antennas are on the same plane as the radiating elements and radiate broadside with respect to the plane of the amplifiers. Within this category, there are many implementations

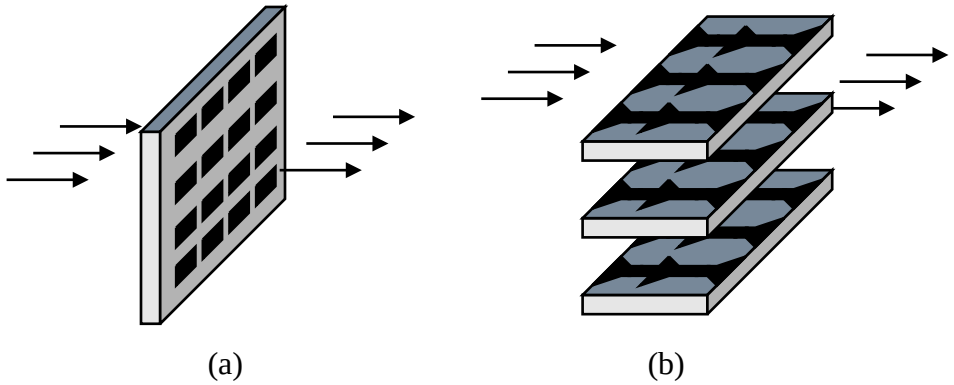

(a) (b)

Figure 1.5: (a) Tile- and (b) tray-based amplifier approaches.

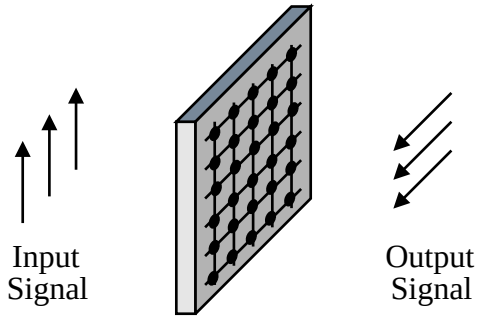

Figure 1.6: A Rutledge grid amplifier.

using various types of radiating elements. The grid amplifier developed by Rutledge is one distinct approach [10]. It consists of a grid of vertically and horizontally polarized wires, where one polarization is connected to the input of amplifying devices located at the intersection of the wires, and the other polarization is connected to the output. This is illustrated in Fig. 1.6. Most other tile approaches use a more conventional active array of amplifiers resembling the illustration in Fig. 1.5(a). The other category, shown in Fig. 1.5(b), is the tray approach. In this amplifier array, the antennas radiate in an end-fire direction with respect to the plane of the amplifying devices. This provides more space to accommodate larger amplifying devices as well as matching and biasing networks that may be present in the circuit. In addition, trays of unit cells are stacked to form an array. Both amplifier topologies may be used in combination with the various feeding methods to produce a wide range of spatial power combining amplifiers. The work performed within this thesis falls into the category of conventional tile arrays and tray-based arrays fed by horns in the near-field.

1.3 Scope and Objectives of Research

The primary objective of this research is to develop a spatial power combining amplifier array capable of producing high output power levels at Ka-band. The spatial power combining method has been chosen for its potential to combine the output power from many amplifiers with high combining efficiencies compared to circuit-level combiners. Two methods of spatial power combining, tile- and tray-based, have been investigated. The tile-based spatial power combiner consists of an array of amplifying unit cells. Each cell consists of a receiving antenna, driver amplifier, power amplifier, and transmitting antenna. The receiving and transmitting layers are separated by a thick groundplane for efficient heat sinking, and the antennas radiate broadside with respect to the plane of the amplifiers. The tray-based spatial power combiner also consists of an array of unit cells. However, the antennas radiate in an end-fire pattern with respect to the plane of the amplifiers. For this purpose, an approach has been developed for the feeding of the microstrip patch antennas. This feeding mechanism allows the amplifiers and radiating elements to be isolated. Thus more room is allowed for the amplifiers, while minimizing coupling that may cause spurious oscillations.

The millimeter-wave, tile-based portion of the research was carried out at Lockheed Martin Corporation, Orlando, Florida. The contribution of this thesis includes the design of the antennas, through-plate transitions, cell spacing studies, and hard-horn feeds, which were carried out in large part by the author. In addition, Lockheed Martin Corp. developed the cell layout, biasing, and thermal management portions of the project. However, the entire project will be outlined in this thesis with emphasis on the original contributions made by the author. Several arrays were developed, consisting of 13, 45, and 98 elements. The experimental results for each array will be reviewed, including gain, power compression, and return loss. Moreover, simulated and experimental results for the horn, antenna, and through-plate transitions will be discussed. In addition, this work has led to the highest output power obtained from a spatial power combiner at these frequencies.

The tray-based approach outlined in this research is an original contribution by the author. Furthermore, the antenna feed and array topology have not been found in literature. Both an X-band and Ka-band array have been developed, consisting of 25 and 49 elements, respectively. Each array provides efficient heat sinking through thick metal groundplanes. In addition to developing an efficient array topology capable of high output power, the ability to analyze these structures in order to gain more insight on fundamental issues involving the design of spatial power amplifiers is of great importance. By isolating the radiating elements and the amplifying circuitry, numerical techniques can be applied to analyze the entire structure. Additionally, experimental verification of the fault tolerance of spatial power combining arrays has been conducted. Such research will examine the effect of device failure on the gain, power output, and radiation pattern through experimental validation.

1.4 Organization of the Dissertation

In Chapter 2, a brief survey of current high power microwave and millimeter-wave amplifier technologies is given. This includes a more detailed discussion of spatial power combining. Chapter 3 discusses the importance of the hard-horn feed and the array spacing for maximum combining efficiency. In addition, experimental results are given, detailing various configurations. In Chapter 4, the tile-based approach is discussed. This includes detailed experimental studies of a 13-, 45-, and 98-element arrays. Much attention is given to the coupling of the amplifier array to the horn feeds. Furthermore, cell uniformity is examined. Chapter 5 discusses the tray-based approach. A detailed explanation of the antenna feed and array topology is given. This is followed by the design, testing, and experimental results for a 25-element X-band array and a 49-element Ka-band array. The experimental results include a study of how device failures affect the gain, power output, and radiation pattern of spatial power combiners. In Chapter 6, conclusions of this research are given as well as recommendations for future work.

1.5 Publications

1.5.1 Journal

1. T. Ivanov, S. Ortiz, and A. Mortazawi, "A passive double-layer microstrip array for the construction of millimeter-wave spatial power-combining amplifiers," *IEEE Microwave Guided Wave Lett.*, vol. 7, pp. 365-367, Nov. 1997.

2. M. A. Ali, S. Ortiz, T. Ivanov, and A. Mortazawi, "Analysis and measurement of hard-horn feeds for the excitation of quasi-optical amplifiers," *IEEE Microwave Theory and Techs.*, vol. 47, pp. 479-487, 1999.

3. S. Ortiz, T. Ivanov, and A. Mortazawi, "A CPW-fed microstrip patch quasi-optical amplifier array," *IEEE Microwave Theory and Techs.*, vol. 48, pp. 276-280, 2000.

4. A. B. Yakovlev, S. Ortiz, M. Ozkar, A. Mortazawi, and M. B. Steer, "A waveguide-based aperture-coupled patch array in the N-port layered waveguide for spatial power combining applications," *IEEE Microwave Theory and Techs.*, vol. 48, pp. 2692-2699, 2000.

5. S. Ortiz, J. Hubert, L. Mirth, E. Schlecht, and A. Mortazawi, "A high power Ka-band quasi-optical amplifier array," *to be published in IEEE Microwave Theory and Techs.*, 2001.

1.5.2 Conference

1. S. Ortiz, T. Ivanov, and A. Mortazawi, "A transmit-receive spatial amplifier array," *IEEE MTT-S Int. Microwave Symp. Dig.*, vol. 2, pp. 679-682, 1997.

2. S. Ortiz, T. Ivanov, and A. Mortazawi, "A CPW fed microstrip patch quasi-optical amplifier array," *IEEE MTT-S Int. Microwave Symp. Dig.*, vol. 3, pp. 1465-1468, 1998.

3. M. A. Ali, S. Ortiz, T. Ivanov, and A. Mortazawi, "Analysis and measurement of hard horn feeds for the excitation of quasi-optical amplifiers," *IEEE MTT-S Int. Microwave Symp. Dig.*, vol. 3, pp. 1469-1472, 1998.

4. M. A. Ali, S. Ortiz, T. Ivanov, and A. Mortazawi, "Hard horn feeds for the excitation of quasi-optical amplifiers," *IEEE AP-S Int. Symp.*, vol. 1, pp. 490-493, 1998.

5. S. Ortiz and A. Mortazawi, "A compact circularly polarized microstrip transmit-receive antenna for LAN applications," *IEEE AP-S Int. Symp.*, vol. 4, pp. 2104-2107, 1998.

6. S. Ortiz and A. Mortazawi, "A perpendicularly-fed patch array for quasi-optical power combining," *IEEE MTT-S Int. Microwave Symp. Dig.*, vol. 2, pp. 667-670, 1999.

7. J. Hubert, L. Mirth, S. Ortiz, and A. Mortazawi, "A 4 Watt Ka-band quasi-optical amplifier," *IEEE MTT-S Int. Microwave Symp. Dig.*, vol. 2, pp. 551-554, 1999.

8. S. Ortiz and A. Mortazawi, "A perpendicular aperture-fed patch antenna for quasi-optical amplifier arrays," *IEEE AP-S Int. Symp.*, vol. 4, pp. 2386-2389, 1999.

9. A. B. Yakovlev, S. Ortiz, M. Ozkar, A. Mortazawi, and M. B. Steer, "Electromagnetic modeling and experimental verification of a complete waveguide-based aperture coupled patch amplifier array," *IEEE MTT-S Int. Microwave Symp. Dig.*, vol. 2, pp. 801-804, 2000.

10. S. Ortiz, J. Hubert, L. Mirth, E. Schlecht, and A. Mortazawi, "A 25 Watt and 50 Watt Ka-band quasi-optical amplifier," *IEEE MTT-S Int. Microwave Symp. Dig.*, vol. 2, pp. 797-800, 2000.

11. A. B. Yakovlev, S. Ortiz, M. Ozkar, A. Mortazawi, and M. B. Steer, "Electromagnetic modeling of an aperture-coupled patch array in the N-port layered waveguide for spatial power combining applications," *IEEE AP-S Int. Symp.*, vol. 2, pp. 518-521, 2000.

12. S. Ortiz, M. Ozkar, A. B. Yakovlev, M. B. Steer, and A. Mortazawi, "Fault tolerance analysis and measurement of a spatial power amplifier," *to be published in IEEE MTT-S Int. Microwave Symp. Dig.*, 2001.

13. Z. Jin, S. Ortiz, and A. Mortazawi, "A novel digital phase shifter design at X-band," *to be published in IEEE MTT-S Int. Microwave Symp. Dig.*, 2001.

14. X. Jiang, S. Ortiz, and A. Mortazawi, "A novel design of a 1 to 8 power divider/combiner," *to be published in IEEE MTT-S Int. Microwave Symp. Dig.*, 2001.

Chapter 2

Literature Review

In this chapter, the literature of several power amplifier technologies is reviewed. Some of these technologies represent competitors to spatial power combining, while others represent possible technologies that can be integrated within the spatial power combiner. The first technology reviewed is the growing field of wide bandgap semiconductors, namely GaN and SiC. This is followed by a review of vacuum tubes, which still dominate the field of high power microwave and millimeter-wave amplifiers. Advances in vacuum microelectronics are then surveyed. Finally, recent advances in spatial power combining are reviewed, including grid amplifiers and the tile- and tray-based approaches.

2.1 Wide Bandgap Semiconductor Power Amplifiers

Semiconductor devices have yet to break into the high power microwave and millimeter-wave amplifier realm. Due to low breakdown voltages, it has not been possible to design and fabricate solid-state transistors that can yield RF output powers on the order of 100s to 1,000s of Watts necessary to compete with vacuum tube amplifiers [11]. This has severely limited the use of solid state microwave devices in power applications, such as transmitters for wireless communication systems, radar, etc. However, recent improvements in the area of wide bandgap semiconductors, such as SiC and GaN, provide promising performance, previously available only from vacuum tubes. In addition, the wide bandgap materials perform particularly well under elevated thermal conditions of up to 500°C. Also under normal room temperature conditions, theoretical models predict RF output powers on the order of 4-6 W/mm and 10-12 W/mm, with power-added efficiencies (PAE) approaching the ideal values for class A and B operation, available from 4H-SiC MESFETs and AlGaN/GaN HFETs, respectively [11]. This is in comparison to the 1 W/mm currently available from GaAs MESFETs. Additionally, the dielectric constant of wide bandgap materials is about 20% lower than conventional semiconductor materials. This permits the device to be larger in area for a given impedance, allowing larger RF currents and higher RF powers to be generated [11].

Both GaN and SiC based amplifiers are reviewed in the following sections.

2.1.1 SiC Amplifiers

The utilization of semiconducting SiC has been of interest to device physicist for many years, and serious work with SiC dates at least to the early 1960's [12]. Devices that can be fabricated on SiC include LED's, thermistors, MESFETs, bipolar and heterojunction transistors, and various types of diodes. The application of MESFETs and bipolar and heterojunction transistors is of particular interest to the design of microwave and millimeter-wave amplifiers. Some of the challenges in developing devices on SiC are problems related to crystal growth and purity and to the development of suitable ohmic rectifying contacts. Although research in this area is rapidly advancing, growth and device fabrication technologies are still primitive compared to Si and GaAs. An excellent review by Trew *et al.* of SiC properties can be found in [12]. Several polytypes (lattice arrangement of a crystal) are discussed of the more than 200 identified polytypes in their review. Also, several polytype lattices are defined, the cubic (C), hexagonal (H), and rhombohedral (R). In particular, the 3C-SiC polytype is denoted by β-SiC, and the H-SiC and R-SiC polytypes are referred to as α-SiC. Though, the only polytypes of interest are the 3C, 4H, and 6H polytypes, where the 3, 4, and 6 refer to the number of layers of Si and C atoms before the atomic arrangement repeats [11].

As early as 1977, researchers were able to develop both field-effect and bipolar transistors grown on SiC [13]. The first β-SiC MESFET was fabricated by Yoshida *et al.* [14]. The device had high channel resistance and a transconductance of 0.09 mS/mm. In addition, the same researchers were able to obtain better transconductances, 1.7 mS/mm and 0.5 mS/mm, at room temperature and 400°C, respectively [15]. More recent work has been reported by Allen *et al.* on a MESFET producing 2 W/mm [16]. It delivers 3.5 W with 45.5% PAE and 6 dB of associated gain. This is nearly three times that obtained with GaAs MESFETs. Also, the maximum available frequency of oscillation, f_{max}, was 25 GHz, and the gain-bandwidth product, f_t, was 10 GHz. Application of the SiC to the static induction transistor (SIT) was performed by Morse *et al.* [17]. They demonstrated a packaged SIT amplifier, providing over 36 W at 3 GHz, with 9.5 dB overall gain and 42% PAE. The amplifier was operated at V_{DS} = 80 V. This work provided nearly four times the power density available from commercial silicon technology without internal package matching components. Another recent work by Trew [18] reports on a 4H-SiC MESFET amplifier. In this work, the amplifier was optimized for X-band RF performance. A maximum channel current of 550 mA and a maximum transconductance of 65 mS/mm was produced. Although the transconductance is low by GaAs MESFET standards, the device produced an f_t of 24 GHz and f_{max} of 56 GHz. In addition, the amplifier was biased at V_{DS} = 40 V and produced a maximum RF output power of 5 W with a maximum power-added efficiency of 50%. The linear gain of the amplifier was 12.8 dB. Also of interest, the experiment was performed at 30 GHz, where the amplifier provided 3 dB of gain and 26% PAE. Recently, Sadler *et al.* [19] produced a SiC MESFET hybrid amplifier that provided 30 W of output power at 10 GHz. This power was produced from a single 12 mm SiC transistor biased at V_{DS} = 50 V. Power densities as high as 5.2 W/mm and 4.5 W/mm were obtained at 3.5 and 10 GHz, respectively. The f_{max} was 40 GHz while the f_t was only 10 GHz,

limiting the PAE to 16-17%.

Much research is still necessary for the development of millimeter-wave power amplifiers using SiC. However, X-band results found in literature are very promising. In addition, considerable power, 36 dBm, is available from single devices at Ka-band [18]. Future work will most likely yield chip-level amplifiers with 10s and possibly 100s of Watts at Ka-band. It may however be necessary to use circuit-level or spatial power combining to achieve 100s of Watts or more.

2.1.2 GaN Amplifiers

As with SiC, GaN and AlGaN/GaN based materials offer opportunities for the production of high power devices. Important factors influencing the use of GaN are its high breakdown electric field ($\sim$2MV/cm), high electron mobility and velocity ($\mu_e \sim 1000\ cm^2\ V^{-1}s^{-1}$ and $v_s \sim 2x10^7$ cm s^{-1} in bulk materials) and heterojunction technology to optimize device design [20]. This has led to the rapid development of AlGaN/GaN HEMTs, grown on either sapphire or SiC substrates. The epitaxial growth of AlGaN/GaN HEMTs on sapphire or SiC substrates is necessary since bulk GaN substrates are currently unavailable [11]. In addition, the AlGaN/GaN heterostructure has been demonstrated to produce a two-dimensional electron gas (2DEG), and this makes possible several novel devices that can operate at frequencies beyond SiC devices and with lower resistances and lower noise performance [11]. In addition, higher power densities are possible with GaN-based devices.

Khan *et al.* first demonstrated the AlGaN/GaN HEMT [21], and Wu *et al.* [22] made the first microwave power measurement of an AlGaN/GaN HEMT with a power density of 1.1 W/mm at 2 GHz on a sapphire substrate. The Wu *et al.* structure was limited by the quality of the buffer layer, leading to reduced charge in the channel, and the high thermal impedance of the sapphire substrate. The thermal impedance may be improved through the use of SiC substrates as was done by Hwang *et al.* [23]. They demonstrated wide-bandwidth wide-temperature-range power amplifier using AlGaN/GaN on SiC. A bandwidth of 6-12 GHz was obtained 6.5 ± 1 dB of gain, 26.5 ± 1 dBm output power, and a PAE of 25 ± 5 % at 300 K. With temperatures ranging from 78-400 K, the gain was 4.5 ± 1 dB with a output power of 26 ± 2 dBm and PAE of 28 ± 6 % at 10 GHz. Also recently, the first broad-band GaN-based amplifier was demonstrated by Xu *et al.* [24]. The amplifier used a modified traveling-wave power amplifier (TWPA) topology, employing four HEMT devices. A small-signal gain of 7 dB was obtained with a bandwidth of 1-8 GHz. The output power at mid-band was 3.6 W when biased at V_{DS} = 18 V and 4.5 W when biased at V_{DS} = 22 V. In addition, a PAE of less than 16% was obtained. Another GaN based amplifier implemented using flip-chip techniques was developed by Wu *et al.* [25]. They were able to achieve a bandwidth of 3-9 GHz with excellent transducer gain up to 11.5 dB at 8 GHz. Saturation power levels of 32 and 35 dBm were obtained for 1- and 2-mm-wide devices, respectively. The PAE obtained was 14-24% for the 2 mm device when biased at V_{DS} = 20 V. Impressive power levels have been recently reported by Wu *et al.* [26] for a 6-10 GHz flip-chip amplifier. The AlGaN/GaN HEMT, active device was bonded to an AlN substrate using the flip-chip method. They were able to obtain 9 dB of linear

gain and 14.1 W of output power, which is the highest power level to date and 4-7 times higher than conventional GaAs HEMT amplifiers of the same size. The amplifier produced 9.5 W with 4 dB of associated gain and a PAE of 32% when biased at 15 V. The output power increased to 14.1 W with 4.5 dB of associated gain and a PAE of 25% when biased at 25 V. The first monolithic GaN distributed amplifier was realized by Green *et al.* [27]. They demonstrated a non-uniform distributed amplifier using AlGaN/GaN HEMT on a sapphire substrate. A PAE of over 20% is obtainable from 1-10 GHz with output powers up to 2.22 W.

Available literature on GaN-based amplifiers shows increased potential over SiC-based amplifiers. However, it will be necessary for the development of bulk GaN substrates for improved results in the future. As with SiC, high power levels are expected in the future, making GaN-based devices ideal candidates for circuit-level and spatial combiners.

2.2 Vacuum Tube Amplifiers

This review of vacuum tube technology will include a discussion of the various types of tubes and their advantages. It is quite evident that vacuum tubes offer by far the highest power levels of any microwave or millimeter-wave device. In addition, the current state of vacuum tube technology compared with semiconductor amplifiers can be seen in Fig. 2.1. A discussion of the advantages and disadvantages of vacuum tubes is also in order. This will clarify the need for high power solid-state amplifiers as replacements for vacuum tube amplifiers.

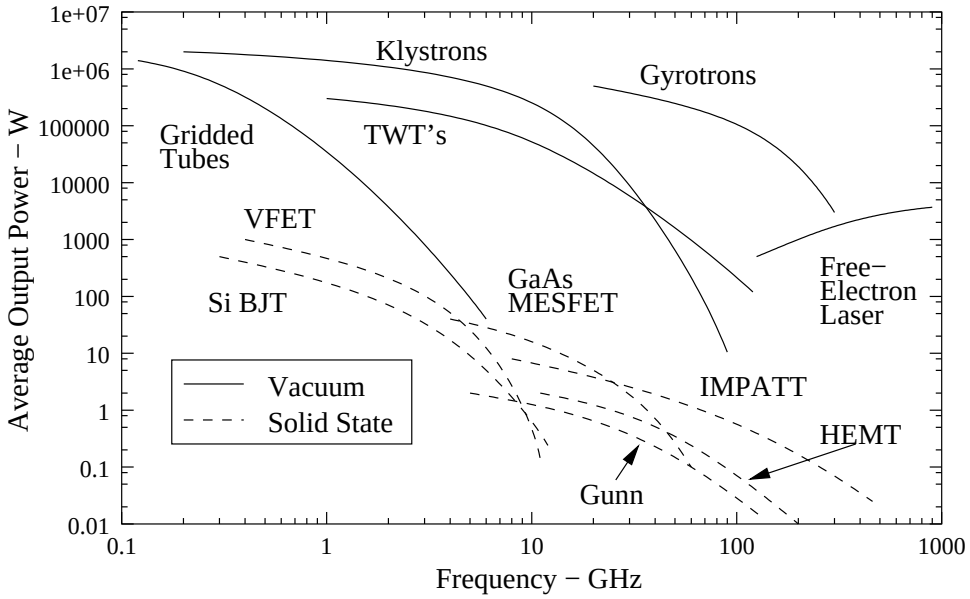

Figure 2.1: Continuous power handling capacity from solid-state and vacuum tube sources. [1]

There are a wide variety of tube geometries, as well as a wide variety of principles on which tube operation is based, but all tubes have several common features. First, all RF/microwave tube's operation is based on the interaction of an electron beam with an electromagnetic field, inside a glass or metal tube. However the RF energy must couple outside the tube through a clear window or coaxial line. Next, a hot cathode is used to generate a stream of electrons through thermionic emission. The electron beam is then focused into a narrow beam by a focusing anode, using a high voltage bias. The beam can be moved or pulsed using this anode. After the electron beam has left the area where it interacts with the RF field, a collector element is used to provide a complete path back to the cathode element. So the electron gun that is created emits an electron beam from a cathode and is focused using an anode onto the collector. Several vacuum tubes can be used as amplifiers, namely the klystron, traveling-wave tube (TWT), cross-field amplifier (CFA), and gyrotron [28]. The klystron behavior is narrow band because of its resonant cavity structure, allowing the electrons in the beam to give up most of their energy to an electric field across a gap [29]. However it has a lower AM and FM noise level in comparison to the other tube amplifiers. In the others (TWT, CFA, and gyrotron) electrons interact with a traveling wave or periodically interact with a time-varying electric field, so there is continual energy exchange between the electrons and the field over an extended time and path. This allows for wider bandwidths and higher output power levels. In addition, the TWT is the most common type of tube amplifier used in millimeter-wave communication systems. It provides bandwidths of 30 to 120% but reduced efficiencies compared with klystrons. The CFA gives very high efficiencies of up to 80% but with a relatively low gain of 10-15 dB. Also, the CFA has a noisier output than either the klystron or the TWT. Finally, the gyrotron is based on the CFA but is capable of much higher output powers and is of primary interest in the millimeter-wave regime.

The first practical microwave source was the magnetron tube, developed in England in the 1930s [28]. This was the impetus behind the radar of World War II. Since then a variety of tubes have been developed as previously mentioned. In more recent years, Ferguson *et al.* [30] have demonstrated a gyrotron-TWT at C-band. This new type of microwave amplifier employs the electron cyclotron maser instability as a basis for the electron-electromagnetic wave interaction. Initial power measurements yielded an output power of 50 kW at 60 kV beam voltage with 16.6% efficiency and 6% bandwidth. After modifying the magnetic field, they were able to obtain 128 kW at 65 kV beam voltage with 24% efficiency. A rippled wall Cerenkov traveling wave tube amplifier is demonstrated by Shiffler *et al.* [31]. The electron beam phase velocity is slowed down using a periodic ripple in the wall of a cylindrical waveguide so that the electromagnetic wave and electron beam can interact. Using this technique, they were able to obtain maximum gains of 33 dB with output powers of 110 MW and efficiency of 11%. However, a narrow bandwidth of only 20-30 MHz was obtained. A new class of multimode high-power vacuum devices named multiple beam TWTs (MBTWTs) are reported by Lopin *et al.* [32]. These are designed for the 3 cm wavelength range with pulsed output powers of 5 kW. The development of both a 3 mm and 8 mm high-power tube amplifier are given by Lopin *et al.* [33]. Their approach to the design of compact millimeter-wave amplifiers with a pulse power of 10s of kW and average power of several kW is the amplifying chain concept. This basically combines a high gain, low current beam TWT amplifier with a high beam current, low gain power TWT amplifier. Smaller sizes are achievable with this method. In

addition, they demonstrated a 50 W CW klystron in the 8 mm regime. At 3 mm wavelength, a pulsed klystron with 1.5 kW power output and 300 MHz bandwidth has been reported. Choi *et al.* [34] have recently investigated a 50 kW, wideband Ka-band slow wave cyclotron amplifier. They predict an efficiency of 15%, gain of 24 dB, saturated output of 50 kW, and an instantaneous bandwidth of 15%. Very recently, Sirigiri *et al.* [35] have developed a theory for a quasi-optical W-band gyro-TWT. This structure promises to give very high output power levels, which is inconceivable for conventional slow-wave microwave tubes. The term quasi-optical refers to the use of confocal mirrors for the selection of specific modes in the apparatus. In addition, their models predict 122 kW of output power at 141 GHz with 38 dB gain, 3% bandwidth, and 27.5% efficiency. Another recent publication by Nguyen *et al.* [36] demonstrates a Ka-band gyro-TWT for radar applications. Instantaneous bandwidths in the range of 2.5 to 3.9 GHz (at 1 dB below saturation) with corresponding peak powers between 92.2 and 57.9 kW are achieved. The corresponding gain gains range from 57 to 36 dB.

Because of the requirement for a high vacuum, and the need to dissipate large amounts of heat, microwave tubes are generally large and bulky [29]. In addition, they require heavy biasing magnets and high voltage power supplies. The excessive size and weight of vacuum tube amplifiers is one of the main reasons solid-state amplifiers are desired for applications where weight and size are of critical importance (i.e. air- and space-borne systems). Vacuum tubes are also generally noisy compared to solid-state amplifiers. Also, they suffer from shot effect, flicker effect, collision ionization, partition noise, induced noise, and miscellaneous noises from microphonics, hum, leakage, charges on insulators, and poor contacts [37]. Increased noise is one of the other key reasons research has been focused on developing solid-state amplifiers that can replace vacuum tubes. Toland and Wong [2] have performed a study discussing the need for solid-state amplifiers in satellite communication systems. In addition to noise related problems, they discuss the extra weight and volume necessary in having redundant TWTAs, since this represents a single point failure in the system. In compromise, the integration of low-noise, solid-state amplifiers and high power vacuum tube amplifiers has recently been investigated by Smith and Dunleavy [38]. The integration of solid-state and vacuum tube amplifiers forms a microwave power module (MPM), which reduces the system noise figure while reducing overall amplifier size. In summary, a review of literature shows that vacuum tubes still dominate in the area of high power radar and communications systems as well as special applications such as particle accelerators.

2.3 Vacuum Microelectronics

Although much research has been focused on solid-state amplifiers for the replacement of vacuum tubes, vacuum tubes still dominate the high power microwave and millimeter-wave marketplace. One of the key advantages vacuum tubes have over solid-state devices is the high current densities that are possible, allowing for the high output power levels. However, they tend to be bulky and expensive to fabricate in comparison to solid-state devices. Also, the use of a hot filament (thermionic emission) as the electron source is inefficient, and the emitters tend to be large. Im-

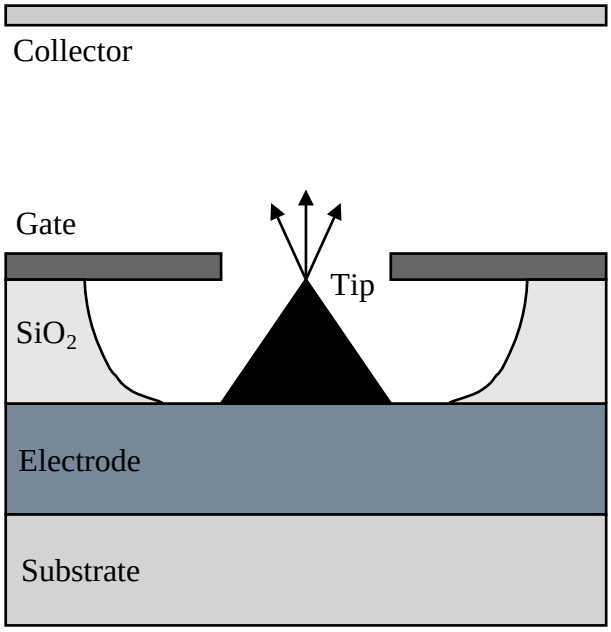

Figure 2.2: A diagram of a conical field-emission cathode.

proved efficiency and miniaturization of vacuum tube device geometries can be achieved if the thermionic source is replaced by a cold cathode electron emission source, based on field-emission. Field-emission vacuum microelectronics has the advantages of fabricating the electron emission devices using electron tunneling and producing electron emission devices with feature sizes in the 10^{-6} to 10^{-7} meter regime [39]. The integration of vacuum electron technology with microelectronic manufacturing has led to the broad class of devices known as vacuum microelectronics. They promise to replace vacuum tubes in such application as flat-panel displays and RF amplifiers, and they have already proven their use in the scanning tunneling microscope. More specifically, the field-emission array (FEA), which is an array of field-emission devices, may be able to replace the thermionic emitters found in vacuum tubes. This would reduce the overall weight and size of such amplifiers. Also with reduced dimensions and at lower operating voltages, a microwave triode is possible. This is the equivalent of a solid-state three-terminal vacuum tube device. These on-chip integrable devices, called micro-triodes, could be combined to form a variety of circuits including distributed amplifiers with enhanced bandwidths.

The principles behind the field-emission device became evident in the early 1950s by Shoulders [40]. He developed the initial concepts of both vertical and lateral field-emission microelectronic devices. These field-emission devices were based on the quantum mechanical tunneling of electrons from a surface under the influence of a strong electric field. Furthermore, the electrons must tunnel across a metal/vacuum barrier, which must be smaller than the uncertainty of the electron position [39]. The electric field is setup between the electrode tip and gate. By minimizing the distance between the tip and the gate, lower voltages can be used. This concept of the

field-emission cathode can be seen in Fig. 2.2. The first field-emission cathode was developed by Spindt in 1968 [41]. In order to achieve higher current densities, arrays of field-emission cathodes or FEAs are necessary. The first FEA was developed by Thomas *et al.* in 1972 [42]. In following years, advances made in semiconductor integrated circuits limited research efforts.

Research efforts have increased in more recent years with hopes of developing field-emission displays (FED) for the flat-panel display market. Moreover, research has continued for the development of RF amplifiers and cathode sources for tube amplifiers. More recently, McKnight *et al.* [43] proposed the use of an FEA for the development of a 10 and 60 GHz amplifier. The FEA would be placed at the end of a resonant patch with a second resonant patch for the collector, located above it. They predicted 8 dB of gain at 10 GHz with 12 W of output power and 6 dB of gain at 60 GHz with 8 W of output power. Another recent proposal is for the use of a coplanar transmission line open-circuited with FEAs in a distributed amplifier [44]. The proposed design may be capable of 10 dB gain up to frequencies of 40 GHz. Although much research has been devoted to the development of FEAs with higher current densities and lower gate voltages, research reveals very few amplifiers based on this technology. Most of the applications seem to be for the replacement of emitters in vacuum tube amplifiers. In addition, Whaley *et al.* [45] have recently presented results on a TWT, using an FEA as the electron source. A C-band amplifier has been fabricated to test their theories. An output power of 55 W at 4.5 GHz was obtained with a saturated gain of 23.4 dB and efficiency of 17%, which is quite close to simulated values. Other recent research reports on the development of micro-triodes but is mostly limited to the modeling of these devices [46]. Some results for recent micro-triodes have been reported in literature [47, 48, 49], but transconductances appear to be limited to 113 μS per device at this time.

The area of field-emission vacuum microelectronics shows promise in the development of electron sources for vacuum tubes and in the area of field-emission displays. The integration with vacuum tubes will definitely have an impact on the development of high power microwave and millimeter-wave amplifiers, especially since they promise to reduce weight and size by replacing the emitter. Also by direct modulation of the gate, they can eliminate the large and bulky magnets of some tubes. However, large voltages are still necessary in order to accelerate the electron beam toward the collector. More promising is the development of the micro-triode, which seems to be far from realization at high frequencies and powers. In summary, the current development of wide bandgap semiconductors seems more mature at this time than the micro-triode and will most likely provide high output power levels at millimeter-wave frequencies first, using low-cost semiconductor manufacturing processes.

2.4 Spatial Power Combining

Spatial power combining (introduced in Section 1.2.2) is a power combining method in which free space is used as the power combining medium. Several types of spatial power combining amplifiers have been introduced, namely the grid amplifier, tile-based amplifier, and tray-based amplifier.

These various methods lend themselves well to the development of solid-state power amplifiers and have been well documented in literature. Furthermore, two methods of feeding the amplifier array have been discussed. Both involve using free space as the dividing and combining medium. However, it is also possible to use circuit-level power dividing to divide the input signal to the various elements of the array, which is similar to phased array antennas. In addition, there are many combinations of spatial and circuit-level combiners in literature. Although at millimeter-wave frequencies, the use of free space for both power division and collection seems most appropriate, and these papers will be the focus of the reviewed material.

Any device may be used to provide amplification in a spatial power combiner. In fact, the earliest known example of spatial power combining actually involved vacuum tubes and was performed previous to World War II by Shintaro Uda [1]. One of his experiments involved the use of nine vacuum tubes and eight dipole antennas alternately spaced along an open-wire transmission line to form a quasi-optical transmitter amplifier. He noted that power increased rapidly as the number of vacuum tubes and antennas increased. Since then, there have been many advances in spatial power combining. The modern era has focused on monolithic grid amplifiers and tile- and tray-based amplifiers incorporating solid-state devices for amplification. This does not necessarily rule out the use of vacuum tubes or field-emission vacuum microelectronics in spatial power combiners, although it unlikely that future research efforts will focus on their use. Though, the use of wide bandgap semiconductors instead of traditional semiconductor devices should see increased activity in the future. Nearly all the literature reviewed in this thesis incorporates the use of traditional semiconductor devices. The main focus of the reviewed material is not the particular device but how it was incorporated into the amplifier array. More important is the characteristics of the array. Some notable aspects that are of concern are the efficiency of the power combiner (i.e. how much loss is in the power combining portion of the circuit), the thermal management, bandwidth, and ease of fabrication. These aspects will be of primary interest in the review of current literature presented in this thesis.

2.4.1 Grid Amplifiers

The first demonstration of a grid amplifier was given by Rutledge *et al.* [10] in 1991. Their group also developed grid oscillators prior to their development of the grid amplifier. The spatial power combining grid amplifier is also commonly referred to as the Rutledge grid for his development of this structure. A more detailed description of the grid amplifier is illustrated in Fig. 2.3. In the figure, a vertically polarized beam is incident from the left, and passes through a polarizer. The grid located in the center amplifies the beam and radiates it with a horizontal polarization, which then passes through a second polarizer to the right. The polarizers provide isolation between the input and output signals. They also allow the input and output stages of the amplifier to be tuned. Fig. 2.4 shows a unit cell of the grid amplifier. Each unit cell contains a differential amplifier pair with both source leads connected together. The gate of the two amplifiers are attached to the vertically polarized strips, and the drains are attached to the horizontally polarized strips. Measurements were performed by placing the amplifier in the far-field of a transmitting and receiving horn antenna.

This method, described in Section 1.2.2, allows the gain of an amplifier array to be measured without using a complicated system of lenses. Additionally, they obtained 11 dB of gain at 3.3 GHz with a 3-dB bandwidth of 90 MHz using 25 cells. These were the first results published for a grid amplifier and are the basis for many spatial power combining amplifiers to follow.

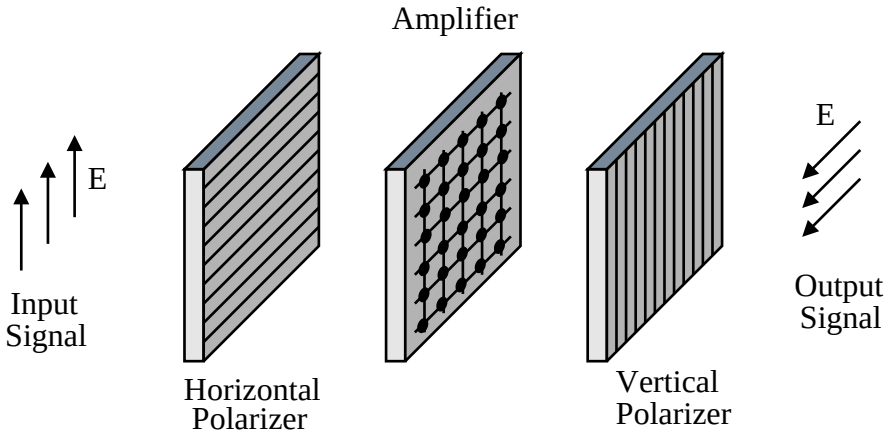

Figure 2.3: The Rutledge grid amplifier with polarizers.

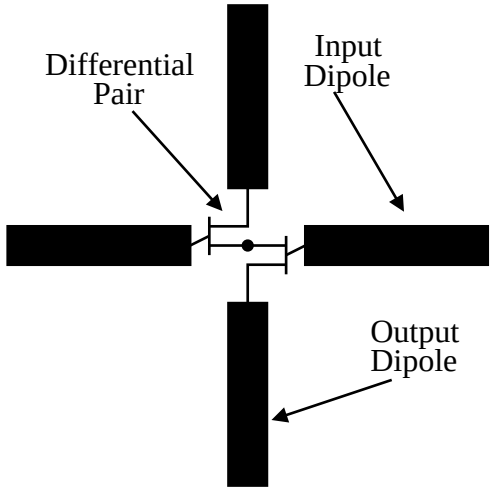

Figure 2.4: Unit cell of the Rutledge grid amplifier.

Since the first grid amplifier, many papers have been published based on the original work. In 1992, Rutledge *et al.* [50] reported results for a 16-element grid amplifier. This design was also fabricated using a hybrid technique with monolithic amplifiers placed on a dielectric substrate containing grids. Furthermore, a planar biasing scheme was developed such that the new array was suitable for monolithic fabrication. The amplifier provided 11 dB of gain at 9.9 GHz with a 3-dB bandwidth of 700 MHz. The gain was provided by a monolithic HBT differential pair. More

significant work followed with the development of a 100 element HBT grid by Kim *et al.* [51]. This grid amplifier provided 10 dB of gain at 10 GHz with a 3-dB bandwidth of 1 GHz. Also, the maximum output power was 450 mW and the minimum noise figure was 7 dB. They also detuned 10% of the amplifiers to determine if the amplifier was tolerant to failures and obtained a 1 dB drop in gain. In addition with 25% of the devices detuned, they obtained a 5 dB drop, and with 50% of the devices detuned, the gain fell all the way to the normal zero-bias gain. The degradation for 10% device failure was near expectations. However, at 25% and 50% device failure, the grid amplifier did not see proportional decreases in gain.

The first monolithic grid amplifier was developed by Liu *et al.* [52]. This 40 GHz monolithic grid amplifier consisted of 36 unit cells containing differential HBT amplifiers. The same grid topology as well as biasing scheme was used as with previous works by Rutledge. In addition to polarizers at the input and output, dielectric tuning slabs were used to tune the impedance seen by the grid amplifier. Using this method, they were able to obtain 5 dB of gain at 40 GHz with a 3-dB bandwidth of 1.8 GHz or 4.5%. The maximum saturated output power was 670 mW at 40 GHz with a peak power-added efficiency of 4%. This work represented a major advancement in spatial power combiners. The main reason being the ability to create a monolithic amplifier that could potentially be produced in mass quantities using semiconductor fabrication processes. However, the output power for this first work was still small in comparison to other alternative power amplifiers. A 44-60 GHz monolithic PHEMT grid amplifier was also published that same year by Rutledge *et al.* [53]. The 36 element array provided a maximum gain of 6.5 dB at 44 GHz. However, maximum gains could be obtained from 44 to 60 GHz by adjusting the positions of the external polarizers and tuning slabs. Furthermore at 60 GHz, the grid amplifier provided 2.5 dB of gain. No information concerning the power output or efficiency of the array were given by the authors. Increased power levels were reported by De Lisio *et al.* [54] with the development of a hybrid grid amplifier containing 100 PHEMT differential pairs. This array provided a maximum saturated output power of 3.7 W at 9 GHz with a power added efficiency of 12%, which was the highest recorded output power of a spatial power combining amplifier at this frequency. The small-signal gain was 12 dB at 9 GHz with a 3 dB bandwidth of 15%.

Currently, the highest power, monolithic grid amplifier operating in the millimeter-wave regime has been reported by Rutledge *et al.* [55]. They have developed a 5 W grid amplifier at 37 GHz, which utilizes 512 transistors. At the 5 W output power, they obtained 5 dB of gain with 15% power-added efficiency. Each unit cell in the grid consists of pHEMT differential pairs and each is capable of producing 11 mW of power. In order to dissipate the nearly 23 Watts of heat, they used a heat spreader consisting of a 2 mm aluminum-nitride substrate. This allowed a better heat flow from the GaAs containing the devices to a water cooled ring at the periphery of the aluminum-nitride substrate. They estimated a gate temperature of 70°C under continuous operation using a thermal imaging camera. This addresses one of the main concerns of monolithic grid amplifiers, which is heat removal. They have successfully demonstrated that heat can be removed using carrier substrates for the monolithic array. Although, the design of such structures becomes more difficult, since the fields must be matched through a second substrate layer to the input and output feeds. A recent grid amplifier which proposes a possible solution to the heat dissipation problem is given by

Lecuyer *et al.* [56]. The basic principle of previous grid amplifiers was based on receiving a signal from one side of the grid and transmitting it toward the other side. This prohibited the use of thick metal carriers beneath the amplifiers for heat dissipation. In the new design by Lecuyer *et al.*, they were able to place the grid on a reflective mirror as shown in Fig. 2.5. In this scheme, the input and output signals are both propagating toward and from the right side of the figure. However, all other aspects of the design are identical to previous grid amplifiers. In fact, the input and output signals are still orthogonally polarized. This initial demonstration of the concept provided 15 dB of gain at 10.2 GHz from a 16-element hybrid grid amplifier using HBT devices. No mention of power or efficiency measurements were given. Although, similar power and efficiencies to other grid amplifiers should be obtainable.

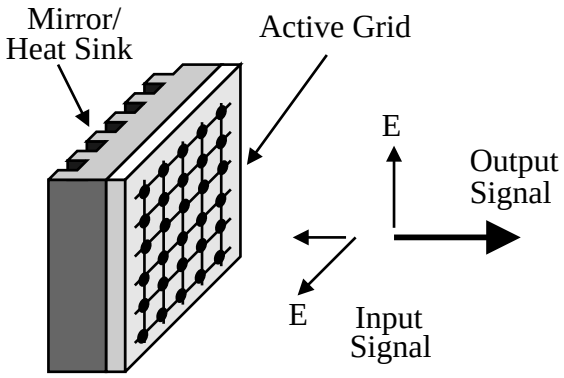

Figure 2.5: Conceptual drawing of a reflective grid amplifier.

Monolithic spatial power combining amplifiers offer a low cost means of producing high power amplifiers, since the amplifiers can be produced in mass quantities with semiconductor processing techniques. However, heat removal is of critical importance to these designs, since solid-state devices are not very efficient at millimeter-wave frequencies. Only recently have monolithic grid amplifiers producing significant power output levels been fabricated. These new designs have begun to address the problem of heat removal through the use of carrier substrates and with the new reflecting grid topology. Designs, using carrier substrates, will most likely be limited to medium power levels by the limited thermal capacity of such substrates. Only the reflector type grid amplifier offers the potential of producing high power levels at millimeter-wave frequencies. Although, it remains to be seen if such designs actually provide these high power levels.

2.4.2 Tile-Based Amplifiers

Tile-based spatial power combining is characterized by the use of broadside radiating antennas with respect to the plane of the amplifying devices as is illustrated in Fig. 2.6. This category of spatial power combiner has typically been applied to arrays composed of separate components (hybrid fabrication), as opposed to a single integrated amplifier (monolithic fabrication). However, the

basic structure of both fabrication methods is the same, whether the amplifier arrays are composed of individual components or are a single monolithic amplifier. In both hybrid and monolithic tile-based amplifier arrays, there are several distinguishable topologies based on the choice of radiating element. Several choices are illustrated in Fig. 2.7, such as the microstrip patch, CPW-fed slot, microstrip-fed slot, and CPW-fed patch. In addition, many variations of each type can be made, such as aperture coupled patch antennas, folded slots, etc. Each choice of antenna offers some advantages and disadvantages. Many of these trade-offs are dependent on the particular application of interest. Some of the trade-offs include bandwidth, radiation efficiency, directivity, ease of circuit integration, and heat dissipation. The review of tile-based approaches in literature will include a discussion of these trade-offs.

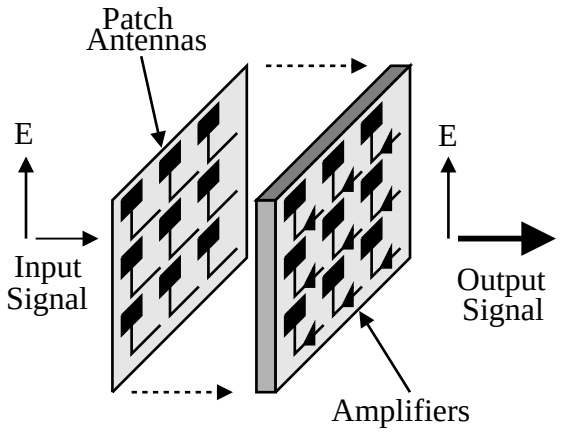

Figure 2.6: A conceptual view of a tile-based spatial combiner with microstrip patch antennas.

Planar spatial power combining was first demonstrated with the Rutledge grid [10] in 1991, discussed previously in Section 2.4.1. This development was followed by many other types of spatial combiners using a planar or tile-based topology. One of the first demonstration of tile-based arrays using broadside antennas was by Mader *et al.* [57]. They demonstrated a microstrip patch array of 24 MESFET devices. The array consisted of a linearly polarized input patch antenna on one side of a substrate and a circularly polarized output patch antenna on the other side. The signal was coupled from the input to the output side of the array using a via wire. Also, the groundplane was placed only beneath the microstrip patch antennas, since a single double sided substrate was used. They were able to obtain a maximum gain of 7.1 dB at 10 GHz, when using a far-field calibration method. This topology isolated the input and output layers, allowing various polarizations to be used. In addition to microstrip patch antennas, early works also experimented with stacked patch antennas and integrated horn antennas. A unit cell incorporating an integrated horn antenna was reported by Chi and Rebeiz [58]. The integrated horn antenna consists of a dipole probe suspended in a micro-machined pyramidal horn formed in silicon. This allows it to be produced through semiconductor fabrication processes. The micro-machined unit cell provided 10.5 dB of gain at 6 GHz with a 3 dB bandwidth of 80 MHz, using the far-field measurement technique. Another early work

demonstrated by Benet *et al.* [59] demonstrated a passive array in a reflection configuration, using stacked patch antennas. Moreover, a signal was received and radiated from/toward the same direction. To isolate the incident and reflected waves, they used the orthogonal modes of a microstrip patch antenna. Thus, the input signal was received horizontally on the patch antenna, then amplified, and radiated with a vertical polarization from the same antenna. The array was also fed using a horn antenna with lens in the near-field. For a passive version of the array, the authors were able to obtain an insertion loss of 2.5 dB at 17.7 GHz with a 3-dB bandwidth of 800 MHz. They predict that such a system may yield nearly 80% combining efficiency based on these initial results.

In 1994, a double layer microstrip patch, power combiner was developed by Sheth *et al.* [60]. This work differed from previous works by having the input and output microstrip antennas share a common groundplane, using two separates substrates joined together. Additionally, the input and output microstrip layers were connected using via wires. The 9 element array provided 5.5 dB of gain at 10.9 GHz with a 3-dB bandwidth of 1 GHz, using a far-field measurement technique. The work of Rebeiz *et al.* [61] was extended with the development of a 75 to 115 GHz quasi-optical amplifier. This was based on the same integrated horn antenna as the first publication. They were able to provide 11 dB of gain from 86 GHz to 113 GHz, using a far-field measurement technique. In addition, a peak gain of 15.5 dB at 94 GHz was found. This was a significant early development from a quasi-optical device, even for a single element array. The development of microstrip patch spatial power combiners was further extended by Ivanov and Mortazawi [62, 63] with the demonstration of multilayer and multi-stage amplifiers. The multilayer amplifier was very similar to their previous double-layer amplifier. However, this new design replaced the via wire with a microstrip-slot-microstrip transition to couple energy from one side of the groundplane to the other. In addition, they placed amplifiers on both sides of the array. Using a far-field measurement setup, they were able to obtain 18 dB of gain at 9.95 GHz from the 9 element array. In their second publication, they measured a single stage array in the near-field using horn antennas. They found 8 dB of gain with 41.5% power combining efficiency, which they noted to be low because of the non-uniform amplitude distribution of a horn antenna. The multi-stage amplifier was constructed using multiple arrays cascaded together in the near-field. They obtained 13.34 dB of gain from the cascading of two amplifiers which provided 7.5 dB of gain individually. Although the separation between stages was small (near-field proximity), the measurement was performed using a far-field setup. Through these experiments, they were able to introduce multi-layered and multistage spatial power combining.

The first demonstration of a quasi-optical millimeter-wave amplifier array was by Hubert *et al.* [64]. They developed a 36 element array consisting of slot antennas, which were fabricated on a monolithic GaAs substrate. The MMIC amplifiers were placed on the substrate to provide the gain. Additionally, the input and output antennas radiated in orthogonal directions to each other and required polarizers to enhance the array performance. For the passive version of the array, they obtained approximately 4.5 dB of loss, including spill-over losses. A 3x3 subsection was used to test the active array, which gave 6 dB of gain at 29 GHz.

An important method of feeding spatial amplifier arrays was given by Ivanov and Mortazawi [65]. They presented a near-field feeding method using a hard-horn antenna, which provides a uniform

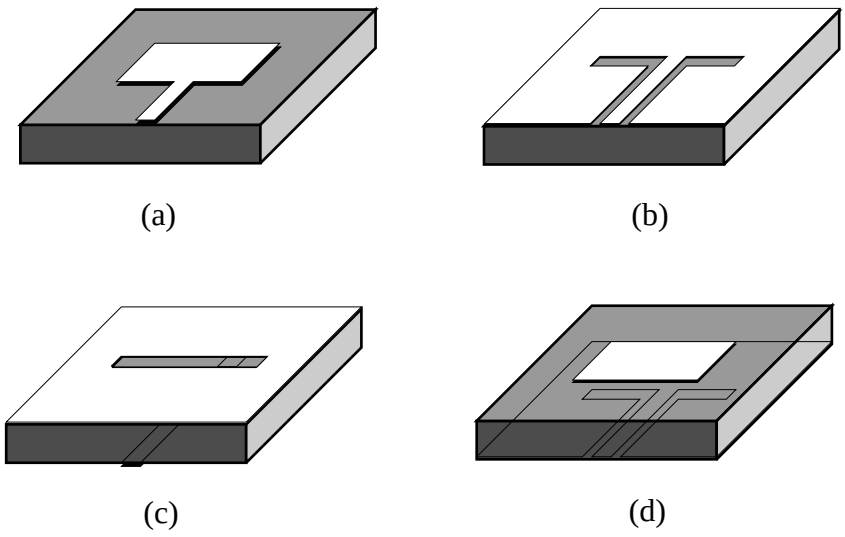

Figure 2.7: Common planar antennas for tile-based arrays: (a) patch antenna; (b) CPW-fed slot; (c) microstrip-fed slot; (d) CPW-fed patch.

amplitude distribution to each cell of the amplifier array, thus allowing the devices to compress uniformly. In their paper, they compare the 2-dB compression points of an amplifier array fed by both a regular horn antenna and a hard-horn antenna, finding nearly 4.8 dB of difference between the two. This increased the utility of near-field feed for spatial power combining amplifiers. Significant advances at millimeter-wave frequencies were reported by Sovero *et al.* [66] with their demonstration of a 42 GHz PHEMT-based monolithic spatial power combiner. The input side consisted of an array of 5x7 slot antennas, and the output consisted of an array of 4x8 patch antennas. The total number of PHEMT amplifiers was 56. They developed an over-sized waveguide fixture to feed the monolithic array in a near-field configuration, so that the measured system was from waveguide flange to waveguide flange. Their amplifier provided 3 dB of gain at 42 GHz with a power output of 0.26 W.

Ivanov *et al.* [67] extended their near-field feeding method using hard-horn antennas to the millimeter-wave regime. In this paper, a passive 138 element double-layer microstrip patch array was presented. It was similar to their previous double-layer microstrip patch designs and provided less that 4 dB of insertion loss at 35 GHz. In addition, this loss included the feeding hard-horn antennas and phase correcting lens that were used. The estimated power combining efficiency of the array was 72%, which represents a significant advance for a power combiner containing 138 elements.

There have been a number of interesting concepts developed recently for the use of spatial combiners as transmit-receive modules. One such design by Ortiz *et al.* [68] describes an amplifier that can amplify either a transmitted or received signal. The two stages are isolated through the use of orthogonal modes of a microstrip patch antenna. This is similar in principal to the previ-

ously reviewed passive array [59]. Furthermore, a horizontal polarization is received by a patch antenna and coupled to the horizontal port of that antenna. It is then amplified and coupled to a second layer, where it is transmitted from a microstrip patch antenna with a vertical polarization. The same configuration is used for a signal received from the other direction (i.e. the patches on each side receive with a horizontal polarization and transmit with a vertical polarization). Using this topology, they were able to obtain 8.2 and 6.9 dB of gain for transmit and receive modes, respectively, at 10 GHz. The measured 3-dB bandwidth was 400 and 350 MHz for the transmit and receive modes, respectively. Another transmit-receive amplifier was developed by Hollung *et al.* [69]. The amplifier was essentially a microstrip-fed slot array with input and output slot antennas orthogonally polarized. In addition, they employed PIN diodes to switch between the receiving and transmitting amplifiers. The array consisted of 24 elements and provided 5.5 dB of gain at 10.1 GHz in receive mode and 2 dB of gain at 10.2 GHz in transmit mode. Recently, Vian and Popovic [70] have developed a transmit-receive active antenna using low-power optical switching. The unit cell of their design uses two microstrip patch antennas on either side of a substrate. Transmit and receive signals are routed through PIN switches controlled by optical power. This is similar in concept to their previous work with a transmit-receive slot array. However, they have now added the functionality of active cell switching, which can be used in beam-forming.

Other antenna topologies that may be used include multi-slot antennas, dipole antennas, and CPW-fed microstrip patch antennas. A multi-slot amplifier array was presented by Tsai and York [71], which used matched 50 Ω multi-slot antennas to form a 4x4 array. This eliminates the need for matching circuits between the antenna and MMIC amplifier. From experiments, they obtained 10 dB of gain with 4% bandwidth at 11 GHz. The use of CPW-fed microstrip patch antennas was demonstrated by Ortiz *et al.* [72] with the development of a 4x4 amplifier array. The focus of the study was to implement an array using CPW circuitry, since it simplifies the integration of monolithic devices by avoiding the need for vias. This is similar to previous CPW-fed slot antenna arrays developed by Popovic. However, microstrip patch antennas were added to increase the directivity of the antennas and to eliminate the need for polarizers. Ortiz *et al.* obtained 5 dB of gain at 9.8 GHz with a 3-dB bandwidth of 400 MHz. The 3-dB compression power was 17.7 dBm with a power combining efficiency of 40%. This included losses due to the input and output hard-horn feeds. Another interesting topology developed by Kolias and Compton [73] is for a monopole-probe-based quasi-optical amplifier array. In order to decrease the array spacing of the unit cells, they implemented monopole antennas with input and output antennas orthogonally polarized. The resulting 3x3 array was tested and gave 5.4 dB of gain with a 3-dB bandwidth of 2.4% at 16.4 GHz, using a focused-Gaussian-beam measurement setup.

Significant power levels have recently been demonstrated from tile-based spatial power combiners at millimeter-wave frequencies. Marshall *et al.* have demonstrated a 6x6 CPW-fed slot array at 31 GHz. They were able to obtain 6.5 dB gain at 31.4 GHz with 145 W EIRP or 0.5 W output power, using a far-field measurement setup. A hybrid topology was used to integrate the MMIC amplifiers onto an aluminum-nitride substrate containing the CPW-fed slot antennas, which provided efficient heat sinking. Nearly one Watt of output power was reported by Sovero *et al.* [74] from a closed monolithic quasi-optical amplifier using microstrip-fed slot antennas. The array con-

tained 112 total amplifiers with a 7x8 array of input slots and a 8x8 array of output slots. They were able to obtain 9 dB of gain at 38.6 GHz with a maximum measured output power of 29 dBm. The array was fed using over-sized waveguides at the input and output, which contained the monolithic amplifiers placed on an aluminum-nitride carrier for improved heat dissipation. The authors note that dielectric loading of the horns (i.e. hard-horns) would have provided increased power output. Several recent developments by Hubert *et al.* [75, 76] have demonstrated the highest output power levels at Ka-band to date. Their first paper reported on a 13-element spatial power combiner which used microstrip patch antennas in a double-layer configuration. Thermal management of the array was provided by the use of 2.54 mm thick steel groundplane. Coupling from the input to the output sides of the array was performed using a microstrip-slot-microstrip transition, where the slots were loaded with dielectric through the 2.54 mm thick groundplane. From this amplifier, they obtained 18 dB of small signal gain at 31 GHz and obtained 4 W of radiated power with 16 dB of gain under compression. In addition, the amplifier array was fed using hard-horn antennas with phase correcting lenses. The same group also developed a 45- and 98-element array at Ka-band using the same array topology. However, the microstrip-slot-microstrip couplers were replaced by coaxial lines drilled through the groundplane, which occupy less space. Thermal management of the 45-element array was provided by the 2.54 mm groundplane and liquid cooling at the periphery of the array. The 98-element array was further enhanced by the addition of liquid cooling through a 12.7 mm groundplane. Both arrays were measured in a near-field setup using hard-horn feeds. The 45-element array provided nearly 25 W of radiated power under compression with 10 dB of gain and 800 MHz of bandwidth at 34 GHz. Also, the radiated power combining efficiency was 56% with a PAE of 7.8%. Preliminary results for the 98-element array show increased output power levels over the 45-element array.

Tray-based spatial power combining has shown significant output power levels at millimeter-wave frequencies. Several topologies have shown efficient heat dissipation methods which are not possible in grid amplifiers. Power levels in excess of 50 W should be possible in the near future using such techniques. Although, manufacturing costs will most likely be higher than monolithic grid amplifiers but will provide higher overall output power levels.

2.4.3 Tray-Based Amplifiers

Although significant power output levels have been demonstrated with tile-based arrays [76], they have been at the expense of lower array feed efficiencies. This does not pose a problem for radiating power combiners, where it is not necessary to recombine the signal. However, high power levels and high efficiencies have been recently demonstrated using tray-based spatial power combining. The conceptual view of one of the first successful tray-based spatial power combiners is shown in Fig. 2.8. This X-band combiner developed by Alexanian and York [77] demonstrated a tray-based approach using tapered slots. Most of the tray-based arrays reviewed are very similar in concept. They offer the advantages of improved heat dissipation through thick metal or substrate carriers and increased cell size for the active devices. The antenna spacing does not increase, although the space between input and output antennas does increase using this topology. Additionally, these

types of structures provide high combining efficiencies using near-field excitation methods.

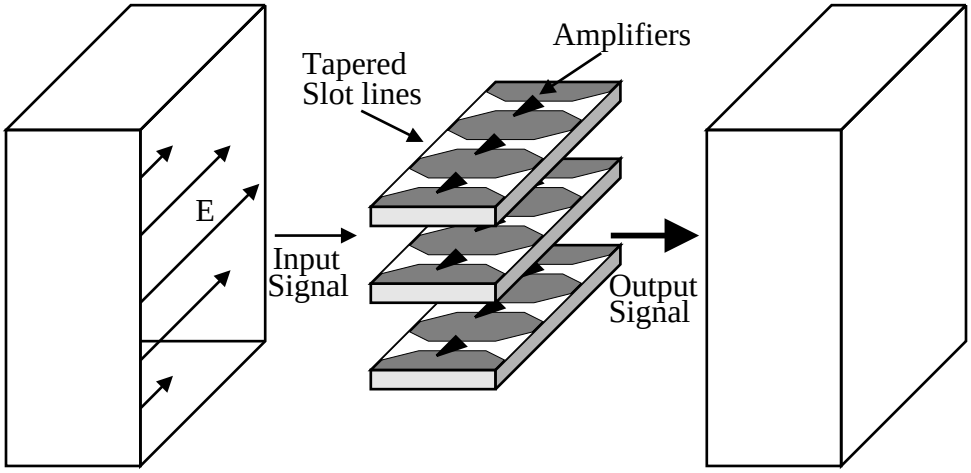

Figure 2.8: Tray-based spatial power combiner using tapered slot antennas.

As mentioned, one of the first spatially combined tray-based arrays was developed by Alexanian and York [77] and can be seen in Fig. 2.8. Several trays containing tapered slot antennas were placed within a waveguide, and each tray contained several tapered slot antennas. Since the distance from the amplifiers to the edge of the tray is small, heat can be removed efficiently. They performed an experiment at X-band with 4 trays containing two amplifiers each. They were able to obtain 2.4 W and 9 dB of power gain at 1-dB compression, with a combining efficiency of 68% and $< \pm 1$ dB of gain variation from 8-12 GHz. The wide bandwidth was provided by the use of the non-resonant tapered slot antennas. Since this initial work, York *et al.* have developed several new power combiners at X-band with increasingly higher output power levels [78, 79, 80]. They have demonstrated a 20 W array in 1998, using the same 2x4 array structure but with more powerful devices. In addition, they obtained 9 dB of gain and 20 W CW with 50% power combining efficiency and 18% PAE. This was followed by a 60 W amplifier using a 4x4 configuration. A maximum power output of 61 W was observed at 8 GHz with a corresponding gain of 12.8 dB and PAE of 31%. Their next publication cites 120 W of power output at X-band. They measured a maximum power output of 126 W at 8.1 GHz with a corresponding gain greater than 13 dB and PAE in excess of 33%. Gain variation was less than ± 1.9 dB covering the frequency range from 8 to 11 GHz. The configuration was the same as previous designs but with 24 amplifiers in a 6x4 configuration. They also measured the performance degradation versus device failure for this array and found that performance degraded gracefully versus device failure. In addition, they lost 57% of their original output power when 50% of the devices failed. This is quite close to expectations and shows one of the strengths of their design. Finally, they were successful in overcoming problems encountered by other designs, i.e. efficient heat removal, high combining efficiency, and ease of fabrication.

Another recent tray-based spatial power combiner has been presented by Saavedra *et al.* [81]. They

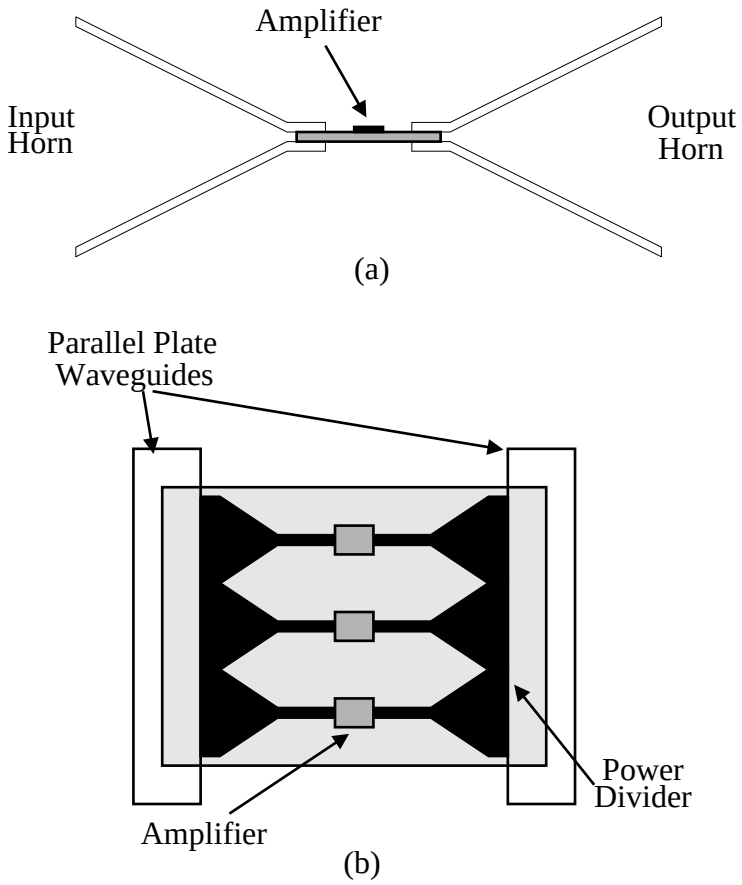

Figure 2.9: Tray-based spatial power combiner using incline-plane horn antennas: (a) side view, (b) top view.

have developed a tray-based array which uses an inclined-plane horn antenna as the radiating element as seen in Fig. 2.9. In this approach, an inclined horn is tapered into a dielectric slab, forming a parallel plate waveguide. The waveguide then feeds several microstrip lines within the array using a power dividing impedance transformation. This topology provides some of the same benefits as the York tray-based array, i.e. efficient heat sinking and a relatively large bandwidth. An experiment was performed, consisting of one inclined-plane horn section with seven amplifiers. They obtained 7.25 dB of gain with a bandwidth in excess of 5.75 GHz at 44 GHz, using far-field measurement procedures. The same group have also recently published work on a 4x4 array using the same principle [82]. They obtained a gain of 6.44 dB at 45.6 GHz with a 3-dB bandwidth of 10%. In addition, 23.7 dBm was obtained under 1-dB compression, including the loss of the feeding horn. The estimated radiated power is 29.7 dBm with a PAE of 10% and a power combining efficiency of 49.7%.

Several recent papers have been published describing the design and analysis of a perpendicular

aperture-fed patch array by Ortiz *et al.* [83, 84, 85, 86, 87]. This topology is illustrated in Fig. 2.10. In the figure, the patch antennas receive a signal from the left, which is then coupled through an aperture in the groundplane to a dielectric filled waveguide. The signal is then coupled from the dielectric filled waveguide to a microstrip line. After amplification, the signal is re-radiated in the same manner. By using the perpendicular aperture-coupled patch antenna, Ortiz *et al.* were able to isolate the amplifying circuitry from the radiating elements. This is similar to the work of Compton but with separate antennas on each tray, allowing individual control of each unit cell within the array. In the perpendicular aperture-fed patch array, efficient heat removal was facilitated by a thick ground plane beneath the amplifying devices. Ortiz *et al.* have demonstrated a 5x5 X-band array, employing MMIC devices, that provided 16 dB of gain with a 3 dB bandwidth of 280 MHz. In addition, under saturation a 50% power combining efficiency was obtained for the amplifier array using hard-horn feeds with phase correcting lenses.

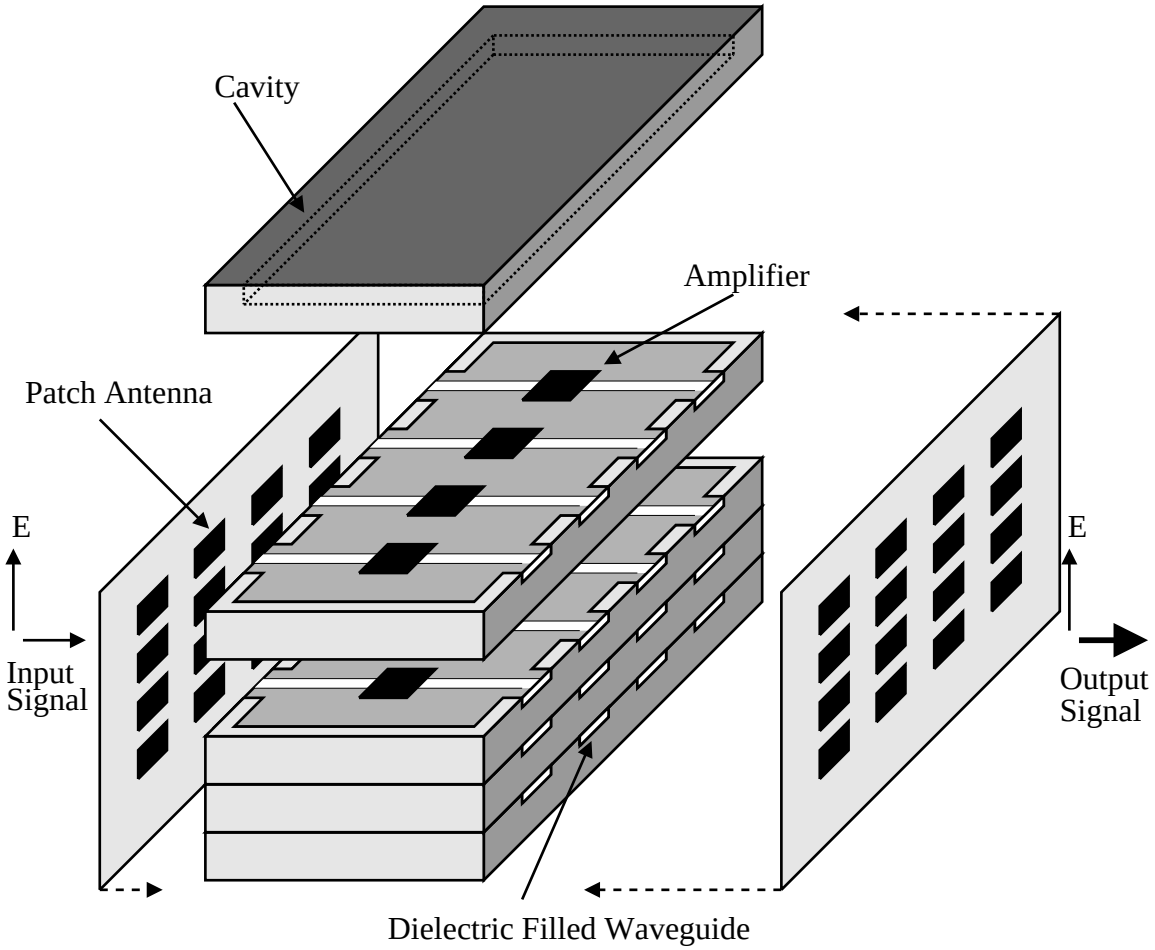

Figure 2.10: Tray-based spatial power combiner using perpendicular aperture-fed patch antennas.

The most significant tray-based amplifier to date is from Sowers *et al.* [88]. They have developed

a 36 W, V-band amplifier using 272 solid state devices. The approach differs from other works previously reviewed in that power division occurs on a tray by tray basis rather than a cell by cell basis. They use a power dividing sectoral horn with lens to divide the power equally among the 17 trays. Power is then divided among 16 amplifiers using circuit-level power dividers. A horn antenna with lens assembly is then used to collect the radiated power after amplification. They collected 36 W at 61 GHz with a combining efficiency of 45 to 50% and a PAE of 5-10%. Furthermore, small-signal gains were in excess of 60 dB. These were the highest output power levels from a V-band solid-state source and the most significant power levels from any spatial power combiner when considering the scaling of device performance with frequency.

Several tray-based spatial power combining topologies have been reviewed. It seems evident from the available literature that tray-based combiners offer superior output power levels. They also offer a modular design, by allowing testing and fabrication to be separated into several trays. This incurs additional time for fabrication but may be worth the increased power levels. Finally, heat removal is simpler in these arrays compared with most tile-based arrays found in literature.

Chapter 3

Amplifier Array Excitation

In order to combine power efficiently, two main criteria must be fulfilled. Firstly, the power dividing and combining system must divide and combine the power equally among the amplifying elements. Secondly, the power must be coherently divided and combined to and from the amplifying elements. The first condition relates to the power distribution of the combined signals. If all the amplifying elements receive the same amount of power, they will produce the same output power and have equal power added efficiencies, resulting in a maximum combining efficiency. The second condition relates to the phase of the combined signals. If for example the combined signals have equal amplitudes but have non-equal phases, they will destructively combine in a non-coherent manner. Therefore, it is necessary for the phase to be uniform in order to coherently combine power.

The process of dividing and combining power equally and coherently to a spatial power amplifier array is discussed in the following sections. The first section describes a method of dividing and combining the power equally among unit cells of the amplifier array using a type of horn antenna known as a “hard-horn”. This is followed by a description of a dielectric lens, which provides the uniform phase necessary for coherent power combining. By using both the hard-horn and dielectric lens to excite the amplifier array, power may be divided with equal amplitude and phase to each of the unit cells of the array.

3.1 Hard-Horn Feed

There are several methods of exciting a spatial power combining amplifier array [65, 79, 10]. In all cases, power must be coupled from a source antenna to an array of amplifying unit cells as shown in Fig. 1.4. This may be done in two basic ways, either using a far-field or a near-field excitation. In the case of the far-field amplifier excitation via a Gaussian beam, a system of lenses must be used in order to focus the signal onto the amplifier array. Without the use of such lenses, the radiated signal from the feeding antenna will diverge, thereby providing a minimal amount of

power to the amplifier array as governed by the *Friis Transmission Equation* [89],

$$P_r = P_t(\frac{\lambda}{4\pi R})^2 G_t G_r \tag{3.1}$$

where P_r is the power received by the array, P_t is the power transmitted by the feeding antenna, λ is the free space wavelength, R is the distance between the antenna and the array, G_t is the gain of the feeding antenna, and G_r is the gain of the array.

In addition, the distance between the various components of the system must be several wavelengths in order to be in the far-field region, which is determined by the following equation [89],

$$R = 2D^2/\lambda \tag{3.2}$$

where R defines the boundary between the far-field region and the near-field region, D is the largest dimension of the antenna, and λ is the free space wavelength.

Such systems are also referred to as quasi-optical power combiners due to their use of optic principles. At microwave frequencies such systems can be rather large. However as the frequency increases, this method of amplifier array excitation becomes more manageable.

The near-field excitation method is characterized by the placement of the amplifier array within the near-field of the feeding antenna within the region from 0 to R defined by Eq. 3.2. One possibility involves the use of either a pyramidal horn antenna or a rectangular waveguide, where the amplifying array is placed at the aperture of the horn or waveguide [63, 74, 79]. This offers the simplest method of feeding the array in the near-field. However, several limitations of this method are apparent. Namely, the field distribution of a homogeneously filled rectangular wave guiding structure is sinusoidal at the aperture for a TE_{10} mode of operation as shown in Fig. 3.1(a). If amplifying elements are placed at the aperture of a waveguide with such a field-pattern, the elements close to the side walls (tangential to E_y) of the waveguide or horn will receive less power than those at the center. This reduces the total power combining efficiency, unless the unit cells are placed non-uniformly, or several cells are combined together. In addition, more cells can be placed at the center to receive the greater concentration of power, resulting in a non-uniform cell spacing. Otherwise, several cells near the sidewalls could be combined to a single amplifier. Alternatively, the use of a hard-horn feed provides a uniform field-pattern across most of the waveguide aperture [65]. This eliminates the need to compensate for the non-uniformity of the electric field. A more detailed description of this technique is given in the following subsections.

3.1.1 Theory

The hard-horn antenna or dielectrically loaded horn has been known for some time to provide a uniform field distribution at the horn aperture [90]. Original investigations focused on the increased directivity provided by a uniform field distribution, which yields an aperture efficiency of

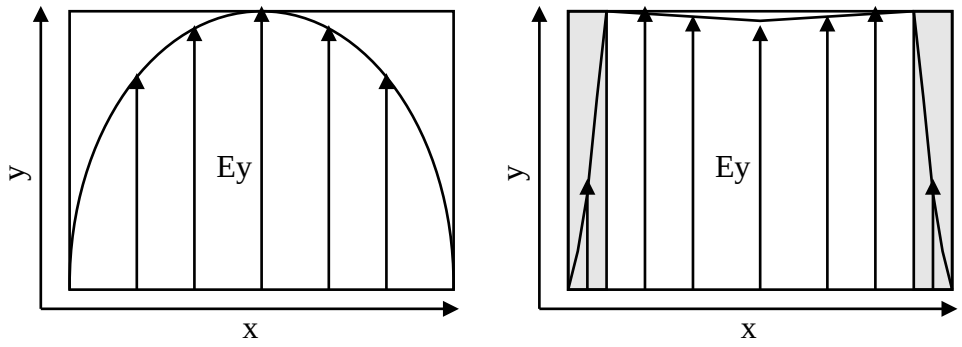

(a) (b)

Figure 3.1: (a) The field distribution of the TE_{10} mode in a waveguide (b) and the LSE_{10} mode in a "hard-horn" antenna.

nearly 100% at a single frequency and thus increased directivity. The dielectric material placed at the sidewalls of the horn antenna, as shown in Fig. 3.1(b), creates the uniform field distribution across the horn aperture. The boundary condition formed by the dielectric sidewall is known as an electromagnetically hard surface, thus the term "hard-horn" [91, 92].

In a standard waveguide, the top and side walls provide a perfect electric conducting (PEC) boundary. These boundary conditions define the TE_{10} mode of operation as well as higher order TE and TM modes. The placement of the dielectric material along the sidewalls tangential to E_y changes the boundary conditions such that an LSE_{10} mode will propagate [93]. This LSE_{10} mode provides a uniform field distribution when the thickness of the dielectric is as follows,

$$d = \frac{\lambda}{4\sqrt{\epsilon_r - 1}} \tag{3.3}$$

where d is the thickness of the dielectric, λ is the free space wavelength, and ϵ_r is the relative permittivity of the dielectric [90].

Therefore at the center frequency of operation (frequency of uniform field distribution), the thickness of the dielectric should be approximately $\lambda_r/4$, where λ_r is the wavelength within the dielectric. This quarter wave length dielectric transforms the PEC boundary to an open boundary condition in much the same way that a quarter wave length transmission line converts a short-circuit impedance to an open-circuit impedance. Thus at this resonance frequency, a TEM mode of operation is formed between the two dielectric side walls [91].

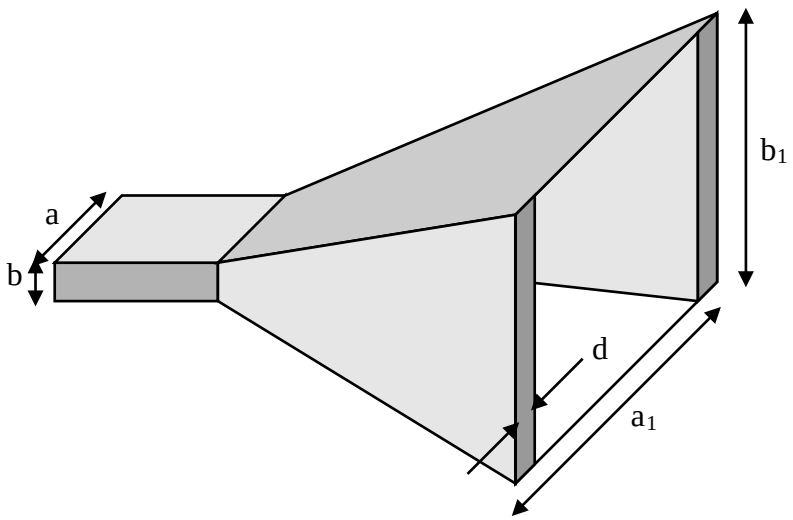

Figure 3.2: A perspective view of a hard-horn antenna.

3.1.2 Design and Construction Methodology

Eq. 3.3 is used as a starting point for the design of the hard-horn feed. However, this assumes that only the LSE_{10} mode propagates. Unfortunately, the excitation of higher order LSE and LSM modes is possible in an oversized dielectric loaded waveguide, which tapers at the angles ϕ_1 and ϕ_2 as shown in Fig. 3.3. It is necessary to simulate the entire hard-horn in order to determine the ratio of power contained in each of the LSE and LSM modes. Such research has been the focus of several papers [94, 95]. However, some practical design and construction guidelines are given.

In the design of a hard-horn antenna, several dimensions must be determined. Firstly, the approximate width of the dielectric, d, must be calculated. This dimension is determined by Eq. 3.3, which depends on both the frequency of operation and the permittivity of the dielectric. The choice in dielectric constant effects the bandwidth of the uniform field as well as the thickness of the dielectric. A detailed discussion of these trade-offs is given in [96, 97]. It has been found that a dielectric constant between 1.2 and 2.2 yields good uniformity across the horn aperture with a ± 1 dB uniformity for 50% of the aperture over a bandwidth of 10% [97]. With a higher dielectric constant, the size of the dielectric decreases as well as the uniformity bandwidth.

The dimensions a and b are determined by the frequency band of operation, while the dimensions a_1 and b_1 are determined by the area of the spatial power combining array. The antennas of the amplifier array should be within the uniform field distribution of the hard-horn. Therefore, $a_1 - 2d$ should equal the width of the amplifier array, and the height should be less than b_1. The length of the hard-horn defines the angles ϕ_1 and ϕ_2 given in Fig. 3.3. As the length of the hard-horn is shortened, these angles increase in size. An increase in the flare angles increases the mode conversion of the LSE_{10} to the higher order LSE and LSM modes. Since the single LSE_{10} mode of operation is desired, the angles should be kept to a minimum (approximately 15° or less). The

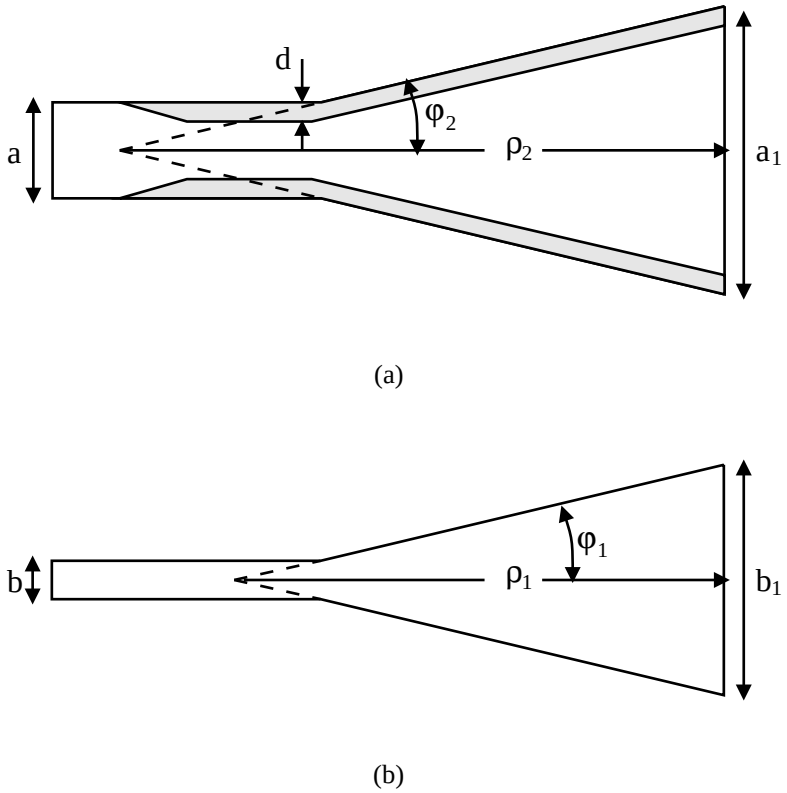

Figure 3.3: (a)The top view and (b) side view of a hard-horn antenna.

same guidelines can be found in the design of standard horn antennas.

Once the dimensions of the hard-horn are determined, it is simulated using a mode-matching code to ensure its proper operation. Then the horn can be fabricated using one of two basic methods. Either the horn may be made from a molded piece of metal as with typical pyramidal horns or can be constructed of two halves of metal fastened together. The latter method is preferable in that the dielectric material can be adhered to the side walls of the horn with greater ease. Also for research and development purposes, it is simpler to have the horn machined from two blocks of metal and then fastened together.

3.2 Dielectric Lens

As was mentioned previously, it is necessary to coherently divide and combine the signal to and from the amplifier array. Unfortunately, the signal output from a hard-horn or even a standard horn antenna, for that matter, is not uniform in phase. This is due to the expanding fields within the horn antenna, which create a near spherical phase front at the aperture of the horn as illustrated in

Fig. 3.4, where the phase front of E_y refers to the curve traced by those points which have equal phase. The non-uniform phase distribution may either be compensated for within the spatial power combining amplifier array or within the hard-horn antennas.

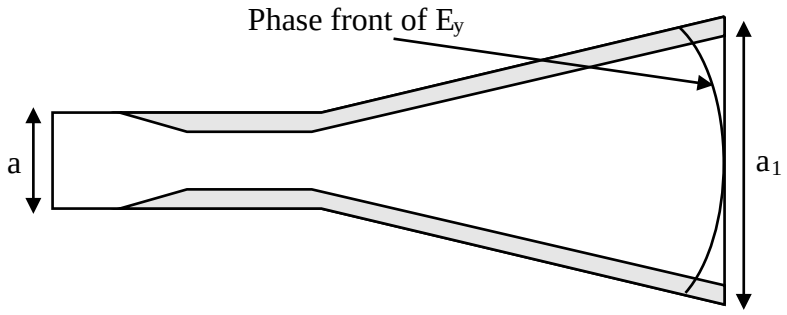

Figure 3.4: Approximate phase distribution from a hard-horn antenna.

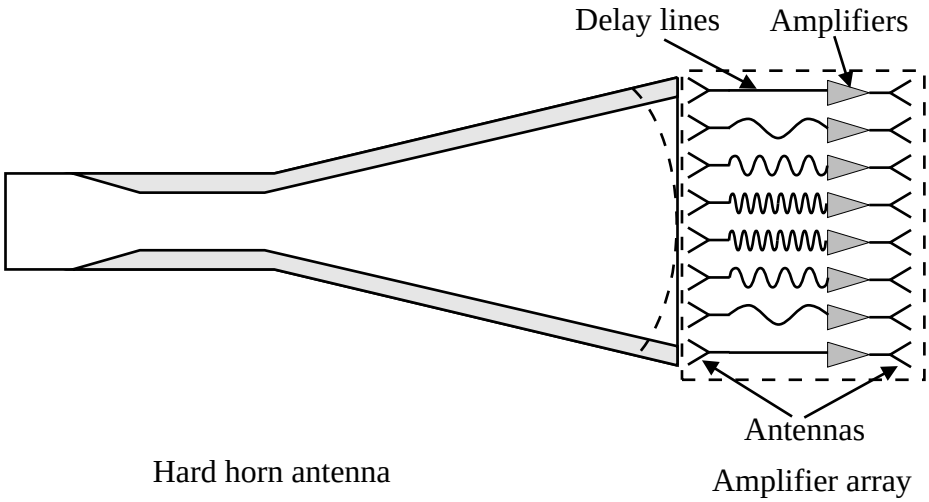

Figure 3.5: Phase compensation of a hard-horn using delay lines within the amplifier array.

If the phase is corrected within the amplifier array, delay lines will be added as shown conceptually in Fig. 3.5. This system delays the signal received by the antennas at the center of the array more than those received at the edge of the array. The total delay path is effectively the same for any antenna of the array. However the addition of extra lengths of transmission lines increases the losses of the spatial power combining system. Also, there may not be sufficient space within the unit cells of the amplifier array to accommodate long lengths of transmission lines.

An alternative method is to use a dielectric lens within the hard-horn antenna as shown in Fig. 3.6. The lens behaves in much the same manner as the delay line approach by delaying the signal output from the horn antenna at the center more than at the edges. The signal output from the horn

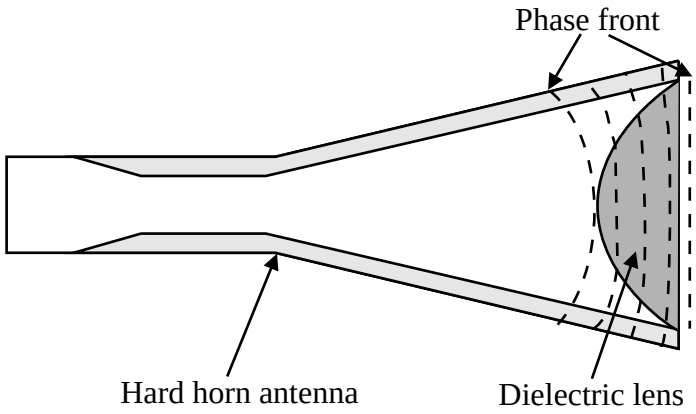

Figure 3.6: Phase compensation of a hard-horn antenna using a dielectric lens.

is therefore uniform in phase. This has the advantage of increasing the aperture efficiency and has been studied extensively in literature for increased directivity horn antennas [98]. A discussion of dielectric lens theory is given in the following sections based upon classical lens design methods for standard horn antennas.

3.2.1 Theory

The dielectric lens produces a constant phase front across the aperture of the lens radiating into free space. The shape of the lens can be determined using the theory of geometrical optics (GO). The use of geometrical optics is actually an approximation, since the lens is placed at or within the aperture of the horn and is therefore in the near-field. However, literature shows that the GO approach yields acceptable results [98]. A basic discussion of GO can be found in [93]. Alternatively, a full wave simulation could be performed on the entire hard-horn and lens structure as shown in Fig. 3.6, using techniques such as the finite element method (FEM) and the finite difference time domain method (FDTD). The time required for such simulations precludes their use as a design tool but may be sufficient for verifying designs created using analytical techniques.

The basic principles of GO is to treat the power radiating from the horn apex as rays shown in Fig. 3.7. This is not necessarily correct, since the lens will be within the near-field of the horn but serves as a good first approximation. Besides, the alternatives for designing the lens are prohibitive. In addition, the radiation from the horn is assumed to be spherical with a symmetric circular radiation pattern about both the E- and H-planes of radiation.

There are several possible lens shapes which can be used to create a uniform phase as illustrated in [98]. An exhaustive description of the various lens types will not be given here. A simple description with advantages and disadvantages will be given instead. The first type is illustrated in Fig. 3.7 and is designated as a single-surface lens, since all the refraction of energy takes place

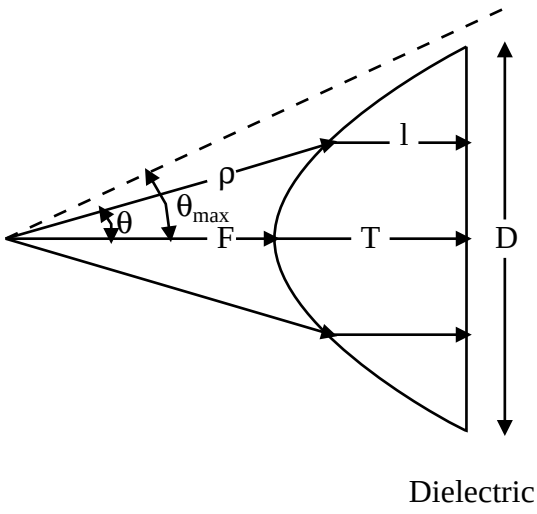

Figure 3.7: A single-surface type lens used for phase correction in a hard-horn.

at a single surface. This type of lens is the one of choice for use in hard-horn antennas due to its placement within the horn aperture. The second type is also a single-surface lens and consists of a concave and convex surface resembling a crescent moon, where the first surface is spherical matching the wave front of the horn and the second creates the refraction necessary for phase correction. The third type is a dual-surface lens since refraction takes place at both surfaces. It resembles the first type, where the flat surface is placed at the aperture of the horn and the convex surface radiates outward. The last type is the classic elliptical lens with convex surfaces on both sides, resulting in its dual-surface designation.

As mentioned, the first type is preferable for use in hard-horn antennas. Traditional horn antennas use the third type because of its simple placement at the horn aperture. The other types may also be used for other circumstances but are not as popular. In addition, zoned lenses may be employed to reduce the lens thickness as with a Fresnel lens [98]. In the following sections, any discussion of the lens will be of the type 1, single-surface lens, since it best fits within the hard-horn.

Two equations are of interest for the design of the lens: an equation describing the profile of the surface; and an equation giving the axial thickness of the dielectric. The equation for the lens surface is derived by equating the optical-path length through an arbitrary point P on the surface to an aperture plane with the optical-path length along the axis [98]. Referring to Fig. 3.7, this becomes

$$\rho + nl = F + nT \tag{3.4}$$

where F is the focal length, n is the refractive index of the dielectric ($\sqrt{\epsilon_r}$), and T is the thickness of the lens. Using the coordinates (ρ,θ), this equation can be written in polar form as

$$\rho = \frac{(n-1)F}{n\cos\theta - 1} \tag{3.5}$$

The ratio of T/D of the axial length to the diameter is

$$\frac{T}{D} = \sqrt{\frac{1}{n^2}\frac{F}{D}^2 + \frac{1}{4n(n+1)}} - \frac{1}{n}\frac{F}{D} \tag{3.6}$$

The previous equations interrelate the parameters of the lens. However these parameters must be applied with the context of the hard-horn antenna. One important relation is between the angle θ_{max} and the horn semi-flare angle ϕ_1 or ϕ_2 – approximately equal since we assumed a spherical radiation. The angle θ_{max} is the angle of the asymptote to the lens. This angle must be greater than the semi-flare angle of the horn, otherwise the lens can never be in contact at its aperture. In other words, the lens cannot compensate for the large curvature of the phase front within the horn unless the lens is placed in front of the horn, which would be an undesirable choice. The angle of θ_{max} is given by [98]

$$\theta_{max} = \cos^{-1}\frac{1}{n} \tag{3.7}$$

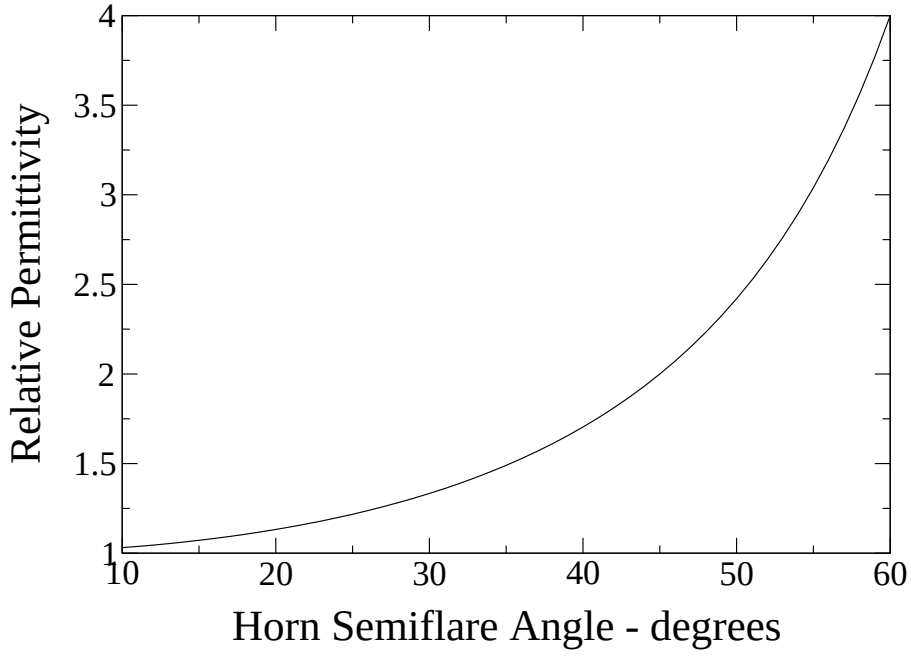

Figure 3.8: Maximum permissible permittivity given a particular semi-flare angle for the horn.

This angle θ_{max} has a lower limit based on a particular horn's dimensions. This lower limit is influenced by the dielectric constant of the material. As the semi-flare angle of the horn increases,

a higher dielectric constant must be used in order to provide the necessary phase correction at the aperture. This is due to the large phase variation between the center and edge of the horn, requiring a larger dielectric constant (thus smaller wavelength within the dielectric) to delay the fields at the center more than at the edges. Therefore if a low dielectric constant material – less than 1.25 – is used, the flare angle must be kept below 25° as shown if Fig. 3.8. Fortunately, this happens to be larger than the 15° semi-flare angle requirement for the hard-horn design.

3.2.2 Design and Construction Methodology

The design of the dielectric lens follows directly from Eqs. 3.5 and 3.6. However, some manipulation of the equations is necessary in order to find the desired dimensions. In addition some knowledge of the phase distribution at the aperture is necessary in order to determine the thickness T and focal length F. If the hard-horn has been designed and fabricated, then the dimensions a and b, defining the width and height of the aperture, should be known. In addition, the semi-flare angles ϕ_1 and ϕ_2, as well as the lengths ρ_1 and ρ_2, should be known as was illustrated in Fig. 3.3. Since the calculation of the lens assumes that the phase front is spherical, we must make some assumptions about the hard-horn. The lens must be designed in two steps based on the E- and H-plane dimensions of the horn. This involves finding the curvature of the lens ρ based on the focal length F for both planes.

For the E-plane, the dimensions ρ_1 and b_1 are known. The lens must be designed such that the focal length plus the lens thickness add up to the length ρ_1

$$F + T = \rho_1 \tag{3.8}$$

In addition, F and T can be related to the aperture dimension b_1 as follows

$$\frac{T}{b_1} = \frac{\rho_1}{b_1} - \frac{F}{b_1} \tag{3.9}$$

and to the semi-flare angle ϕ_1

$$\frac{T}{b_1} = \frac{1}{2}\cot\phi_1 - \frac{F}{b_1} \tag{3.10}$$

Eq. 3.10 allows T/D to be plotted versus F/D for various choices in the semi-flare angle. By using this equation as well as Eq. 3.6, a solution for T/D and F/D based on the intersection of the two curves can be found, where D is the aperture dimension b_1 for the E-plane. This is shown graphically in Fig. 3.9 for several values of n and ϕ_1. If for example the dielectric constant is 1.21 ($n = 1.1$) and ϕ_1 is 15°, then T/D and F/D will be approximately 0.0325 and 1.8, respectively. The curves illustrate the dependence of the dielectric thickness on the semi-flare angle. As the semi-flare angle increases, the dielectric must be increasingly thicker in order to compensate for the larger difference in phase between the center and edges of the horn. It should also be noted that as the dielectric constant increases, the thickness of the lens decreases as expected.

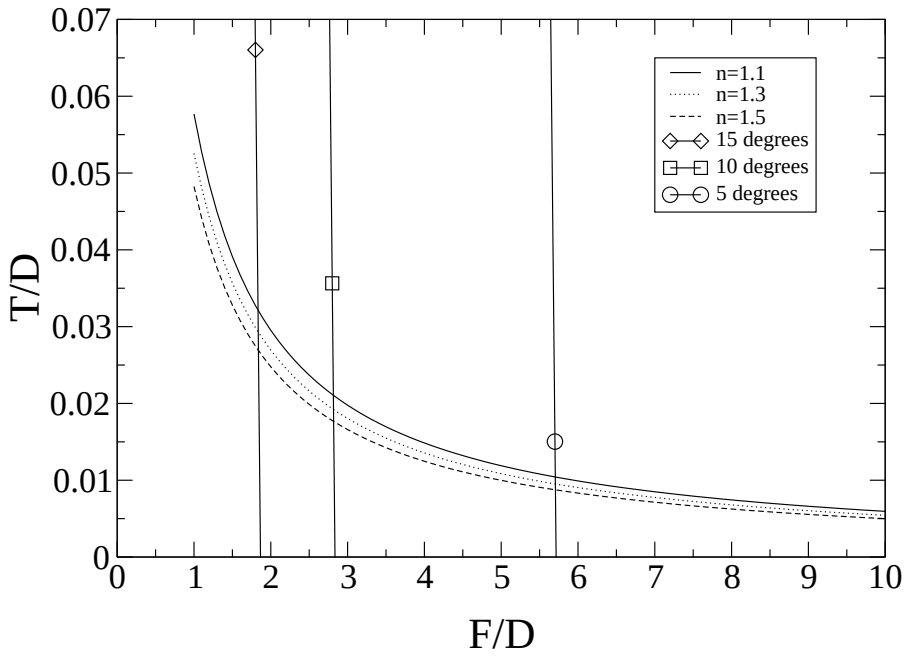

Figure 3.9: The thickness T of the lens plotted against the focal length F, where each are normalized by the horn aperture dimension D. Eq. 3.6 describes the exponential curves, while Eq. 3.10 describes the vertical lines. The intersection of the two curves gives the solution for T and D.

The curvature of the lens in the H-plane may also be calculated in the same manner. Ideally, ρ_1 would equal ρ_2, and a_1 would equal b_1. This would allow the lens shape to be defined by a single curvature. Unfortunately, this is not the case. The two planes must be found separately to create a 3-dimensional curve describing the entire lens. This curvature will only be correct along the two planes. The other planes must be approximated by averaging the points between the planes. Fortunately if ρ_1 and ρ_2 are nearly the same and the semi-flare angle is small, the lens can be approximated by a single curve.

The lens can then be fabricated based upon the previous discussion. All dimensions should readily be found given the dimensions of the horn and the dielectric constant of the lens. A few caveats are in order for the choice in dielectric constant. Namely, it should be low with a small dissipation factor. A lower dielectric constant allows the thickness T to be larger which in turn results in easier machining at millimeter-wave frequencies – less sensitivity to fabrication errors. Another important consideration is the reflection from the air/dielectric and dielectric/air interfaces. This is described by the well known formula $\Gamma = (n-1)/(n+1)$. For a typical solid dielectric with a relative permittivity of about 2.2, the maximum return loss is -14 dB, equivalent to a VSWR

of 1.48. This is substantial. However if a lower dielectric constant is used, the reflection can be ignored. For example if $\epsilon_r = 1.1$, the VSWR is 1.04 and, for $\epsilon_r = 1.4$ the VSWR is 1.18. Finally, the dissipation factor should be low such that the power loss through the lens is small at the center, where it is the greatest.

3.3 Hard-Horn and Dielectric Lens Characterization

The performance of the hard-horn and lens must be verified experimentally. There are two basic methods: a quantitative and qualitative approach. The quantitative method involves measuring the aperture efficiency of the horn. The qualitative approach involves measuring the near-field pattern to determine the uniformity of both the amplitude and phase. Each method has its own merits. The measurement of the aperture efficiency is simple and direct but gives little insight into the field distribution. Conversely, the measurement of the near-field is much more labor intensive but provides good insight into the distribution of the fields at the horn aperture.

An efficiency of 100% is the result of a perfectly uniform amplitude and phase distribution. This is derived from the definition of aperture efficiency ϵ_{ap}, which is defined as the ratio of the directivity of the antenna to that of an aperture with a uniform field distribution of the same size [89]. Therefore if the directivity of the hard-horn antenna with lens is measured, the aperture efficiency may be calculated directly. A good approximation for the directivity can be obtained, if most of the power is contained within the main beam and the sidelobe levels are low. For this, the half-power beamwidths (in radians) of the E- and H-planes must be found. These are defined as the angles at which the power decreases by 3-dB from that at its maximum in both the E- and H-planes. The directivity can then be calculated as follows [89]

$$D_0 \simeq \frac{22.181}{\Theta_{1r}^2 + \Theta_{2r}^2} \tag{3.11}$$

where the D_0 is given in decibels, and Θ_{1r}^2 and Θ_{2r}^2 are the half-power beamwidths of the E- and H-planes, respectively. This directivity can then be applied to the following equation

$$\epsilon_{ap} = \frac{D_0 \lambda^2}{4\pi ab} \tag{3.12}$$

which gives the aperture efficiency for an antenna of dimensions a and b.

Alternatively, the near-field radiation pattern can be measured using various techniques. Many of these techniques involve measuring the E_y and E_x components using waveguide probes [99, 100]. Others have performed such measurements using alternative types of antennas such as dipoles and monopoles [101]. In addition, recent research has focused on the use of electro-optic sampling methods [102]. The most precise method seems to be the electro-optic sampling technique, since the electro-optic probe causes little perturbation of the fields at the aperture of the antenna. However, such systems are extremely expensive to setup and maintain and take more time to perform

the complete measurement. The use of resonant or wave guiding antennas offers a more feasible alternative. The measurement procedure involves scanning the aperture of the hard-horn using the antenna probe as illustrated in Fig. 3.10. The choice of probe depends on the application and distance from the hard-horn. The simplest choice is the rectangular waveguide and is the focus of further discussion.

The use of the rectangular waveguide in near-field measurements has been well documented in literature [99]. Most of these publications have been concerned with the calculation of the far-field radiation pattern from near-field measurements. This eliminates the need for a far-field range or large anechoic chamber. However in this study, we are only interested in the uniformity of the electric-field at the horn aperture. Therefore, the near-field scanning technique used in this research may be simplified. In addition, the measurement of the near-field using a waveguide probe for the calculation of the far-field pattern requires that the probe be outside the reactive near-field of the antenna. Also, the radiation pattern of the probe must be calibrated out of the measurement results to obtain the actual value of the electric-field. There are also techniques to calculate the fields at the aperture of the antenna from the near-field data [103]. This has the advantage of measuring fewer points – at a distance of several wavelengths from the hard-horn – than would be necessary for measurements within the reactive near-field.

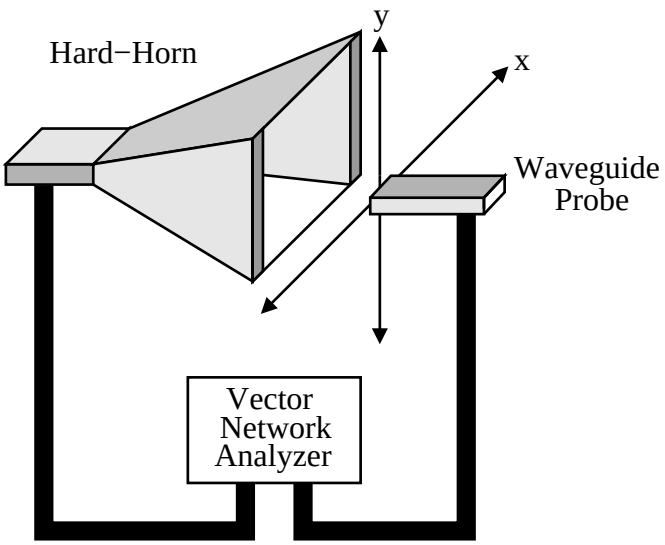

Figure 3.10: A near-field measurement setup using a rectangular waveguide probe and vector network analyzer.

The procedure for measuring the near-field using a waveguide probe is illustrated in Fig. 3.10. For this purpose, several components are necessary: x-y positioner, vector network analyzer, and waveguide probe. It is necessary for the x-y positioner and vector network analyzer (VNA) to

be computer controlled in order to facilitate the collection of data. Since only the amplitude and phase uniformity of the electric-field is of concern, the absolute power of the electric-field is not required. In addition, the relative value of E_y can be measured across the aperture. For this purpose, the amplitude and phase measured by the waveguide probe is calibrated to the center of the horn aperture using a two-port measurement with the VNA. Therefore, all values of E_y, both magnitude and phase, are relative to the center of the horn. The waveguide probe is then scanned across the aperture with the x-y positioner to obtain the entire field distribution.

Several questions regarding this techniques arise. Foremost is the effect of the waveguide probe on the field distribution in which it is being to measured. It seems that the probe has little effect on the horn. This conclusion has been made through observation of the reflection coefficient looking into the horn as the waveguide probe is scanned. However, this is no guarantee that the probe causes little change in the field pattern. The second question that arises is the resolution of the scanned field pattern. There is inherently some averaging between adjacent measurements, if the area of the waveguide probe overlaps between the two measurements. Again since only the uniformity of the field distribution is of concern, some averaging should not impact the qualitative view of the field pattern. This is given that the field pattern has no abrupt discontinuities that may be averaged out.

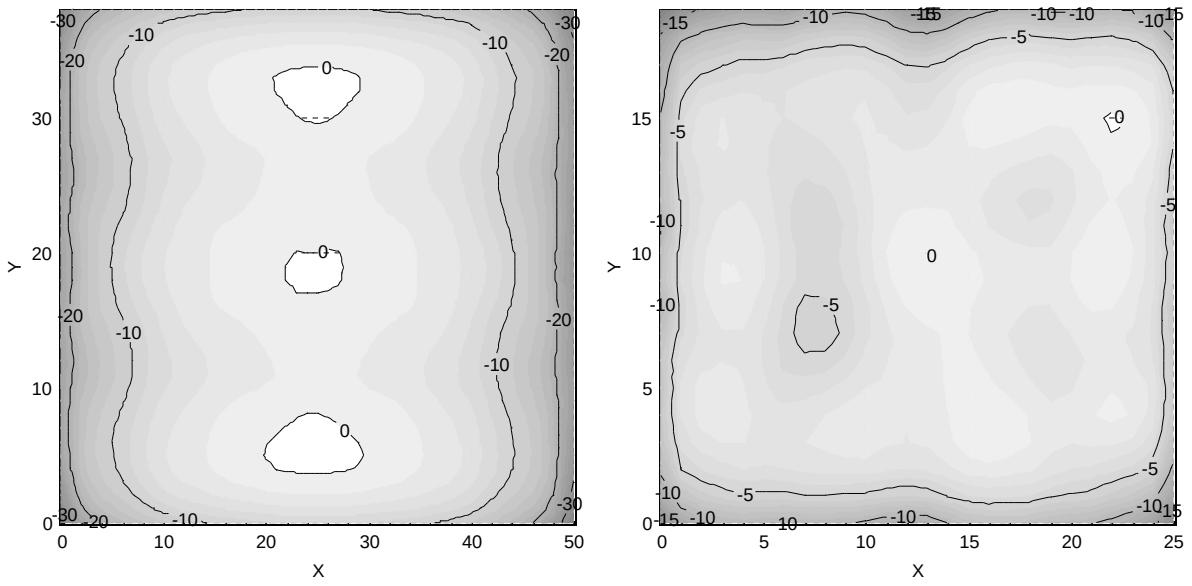

(a) (b)

Figure 3.11: (a)The magnitude of E_y of the standard horn and (b) of the hard-horn at its center frequency.

Several hard-horn feeds with lenses have been designed and fabricated at both X- and Ka-band. The procedure follows the same basic principles outlined in the previous sections with some mod-

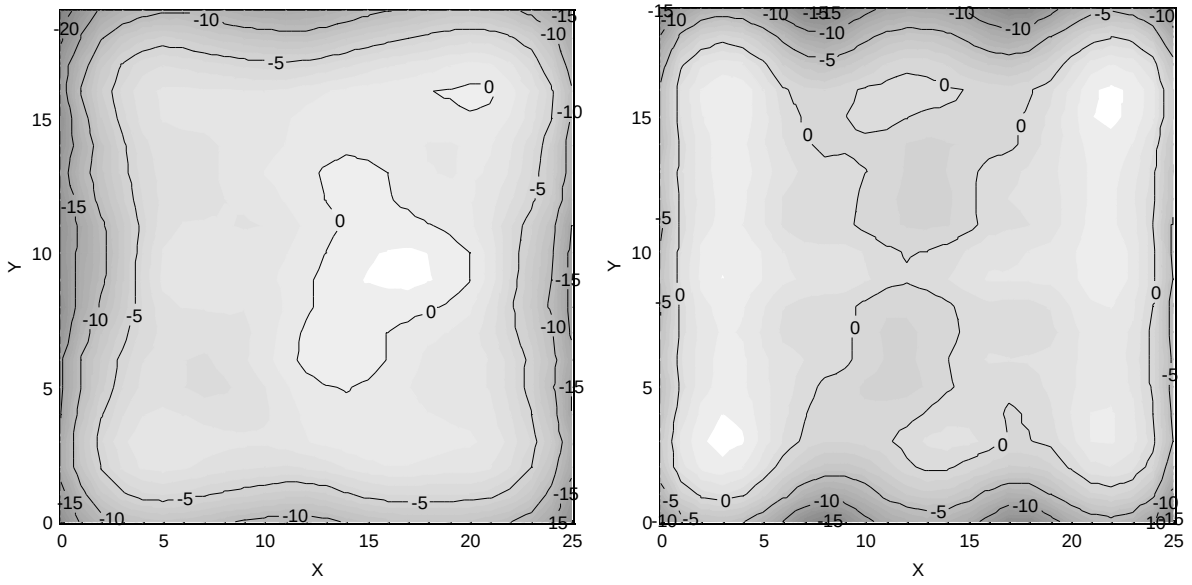

(a) (b)

Figure 3.12: (a)The magnitude of E_y of the hard-horn below and (b) above the center frequency.

ifications. First the horn antenna is built to specifications. This horn is then hardened. The hard-horn field distribution is then measured. This field distribution is shown in Fig. 3.11 compared with the field distribution of the same horn without dielectric. Typically the center frequency (where the fields have the greatest uniformity) is not exactly correct. This is due to the approximate thickness calculated using Eq. 3.3. Furthermore, fabrication errors add to the uncertainty. For either case, the thickness of the dielectric may be increased or decreased in order to lower or raise the center frequency of operation, respectively. The question of whether to increase or decrease the dielectric thickness can be determined by the near-field distribution. In Fig. 3.12, two field distributions are shown illustrating the fields above and below the resonance frequency. As the frequency decreases below the center frequency, the field distribution becomes more sinusoidal; and as the frequency increases above the center frequency, the field distribution dips at the center. Based on these observations the thickness may be tuned.

The lens is then constructed based on the principles given earlier. The field distribution is measured. Typically the phase distribution is quite uniform over most of the aperture but does tend to diverge at the four corners. One possible solution is to make the lens of a dielectric that is slightly thicker than necessary but with the same curvature so that material remains in the corners. Some material can then be removed from the corners to compensate for this phase variation, which is almost always lagging behind the center in phase. Alternatively, a second lens may be machined by calculating the amount of material to removed based on the difference in propagation delay between air and the dielectric. After tuning the lens shape, the phase should be mostly uniform as shown in Fig. 3.13 compared with the phase distribution of an empty horn.

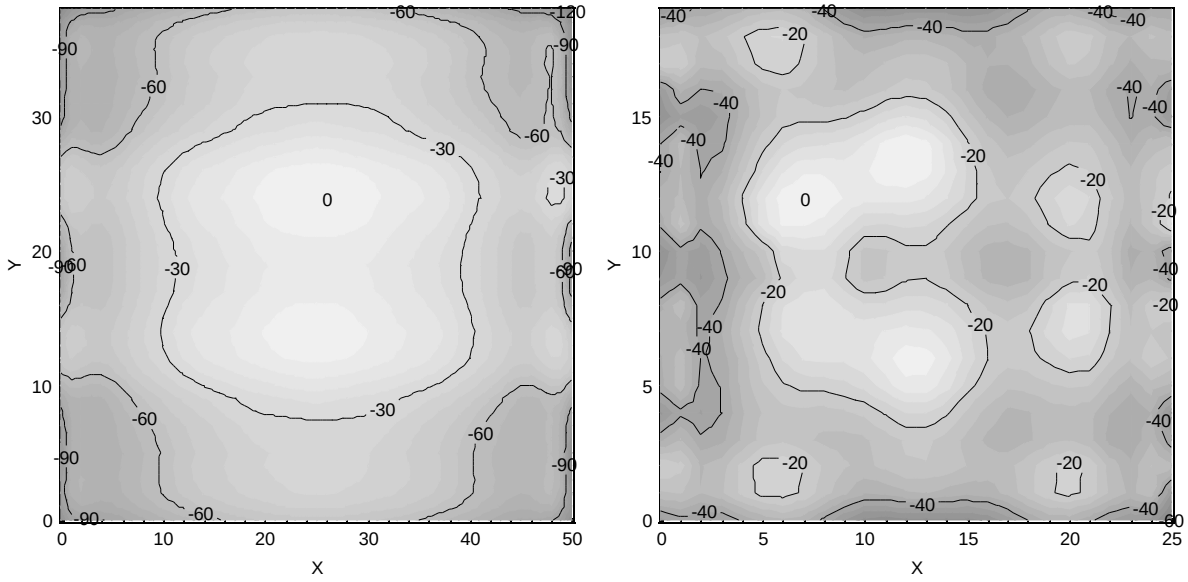

(a) (b)

Figure 3.13: (a)The phase of E_y of the standard horn and (b) of the hard-horn at its center frequency.

Chapter 4

Study of Array Performance

The performance of a spatial power combining amplifier array is affected by many factors. These factors are highly dependent on the type of amplifier array as well as the method of feeding the array. In this work, only arrays fed using hard-horn antennas are considered. In addition, the arrays studied in this work – to be discussed in later chapters – use microstrip patch antennas as the radiating elements. Based on the configuration given above, several factors are present which affect the performance of the array. They are the arrangement of antennas within the array, the influence of the hard-horn feed on the antenna array, and lastly the array itself – amplifying circuits, matching networks, etc. Each of these factors contribute to loss in gain and power combining efficiency. Therefore, each of these factors are of critical importance.

For a particular type of array – microstrip patch antennas based, the amount of energy reflected from the array surface is related to the arrangement of the antennas. This arrangement of antennas is defined by two main constraints in typical antenna arrays: the lattice structure and the unit cell spacing. The lattice structure refers to the relationship between unit cells in an array, where a unit cell is defined as the basic unit radiating element and may include other circuitry. In spatial power combining, the unit cell typically includes a receiving antenna, amplifying circuitry, and radiating antenna. The unit cell spacing is defined as the spacing between cells within the lattice. The actual definition of the unit cell spacing depends on the type of lattice employed, since each lattice type may use multiple dimensions to define the spacing.

The influence of the hard-horn feed has been discussed in the previous chapter. As mentioned, the fields radiated from the hard-horn feed with lens should be uniform in both amplitude and phase. The reasons for these requirements were stated as providing the antenna array with equal excitation so that power could be combined efficiently and coherently. However, the hard-horn may influence the antenna array in other ways. In addition, the close proximity of the hard-horn to the amplifier array may alter the impedance looking into the hard-horn or looking into the antennas of the array. In order to reduce this influence, the fields at the aperture of the hard-horn should closely approximate those fields radiated by the antenna array under uniform excitation. Fortunately, the hard-horn provides a uniform field distribution which closely resembles a plane wave in free space.

This has the advantage of minimizing the influence of the hard-horn on the impedance of the antennas. Unfortunately, the experimental study of the antenna impedances within a hard-horn is beyond the scope of this research. However, numerical studies of these affects are ongoing, using both FDTD and method of moments (MoM) to perform the analysis.

The final factor influencing the gain and power combining efficiency is the array itself. The amplifying array is composed of many elements, including antennas, matching networks, biasing circuitry, and amplifiers. Each of the passive components listed introduces some loss. Some of the losses may be dissipative losses in transmission lines or antennas. Other losses are due to impedance mismatches between components, which cause reflections at their interface. Most of these factors will be discussed in the chapters detailing the design of the amplifier array. However, some discussion of device variations in the amplifiers will be given in the following sections. In particular, differences in gain and phase between amplifiers are of particular interest, since these variations can cause a loss in power.

4.1 Study of the Unit Cell Lattice and Spacing

There are an unlimited number of ways in which antennas may be placed in an array. However, two particular arrangements have traditionally been used in antenna arrays for broadside radiation. The simplest and most obvious is the rectangular lattice as illustrated in Fig. 4.1. In this configuration, the antenna elements are simply placed in a row/column configuration, where each column is separated by R_x and each row by R_y. The other common choice is the triangular lattice as shown in Fig. 4.2. This configuration is characterized by the placement of the antennas along diagonal axis, where the spacing between elements is defined by the diagonal distance between elements R_t.

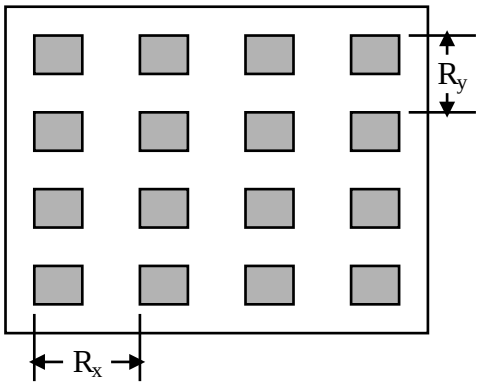

Figure 4.1: An antenna array in a rectangular lattice, where the distances R_x and R_y are the spacing between elements in the x and y directions, respectively.

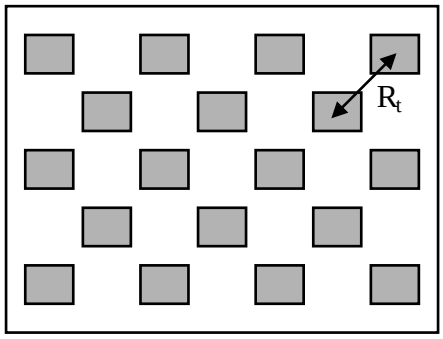

Figure 4.2: An antenna array in a triangular lattice, where the distance R_t is the diagonal spacing between elements.

Given the two common configurations, the question of which to choose arises. The answer depends on the design goals of the system. In general, more elements can be placed in a given space using the rectangular lattice. However, this is not always advantageous. Many times, the unit cell size precludes a close spacing. For these circumstances, the triangular lattice provides the advantage in that the distance between antennas can be larger, while providing the same loss.

In the following sections, the advantages and disadvantages of both lattice types in reference to both tile- and tray-based spatial amplifiers are discussed. This will include experimental data for each type of array versus the spacing between elements.

4.1.1 Rectangular Lattice

An optimum array spacing may be determined either numerically or experimentally. Since the numerical formulation of large arrays on the order of ($4\lambda_0$ x $4\lambda_0$) within close proximity to hard-horn feeds is prohibitively time consuming, some simple experiments were undertaken. The purpose of the experiments was to determine the passive insertion loss of an array of antennas between two hard-horn feeds as shown in Fig. 4.3.

For these experiments, a simple passive spatial combiner was designed and fabricated. The array topology is shown in Fig. 4.4. Each unit cell of the array consists of a receiving microstrip patch antenna, slot in the groundplane, and radiating microstrip patch antenna. This configuration is inherently wide-band since there are no matching networks involved. In addition, the losses should be limited by the antenna efficiency and the hard-horn feed insertion loss. Losses due to transmission lines and matching networks should be nearly eliminated. Based on this assumption, the loss due to the array spacing should be defined by the following

$$IL_{as} = IL_s - (IL_h + 2 * \eta) \tag{4.1}$$

where IL_s is the loss in the system (including hard-horn feeds), IL_h is the loss of the two hard-

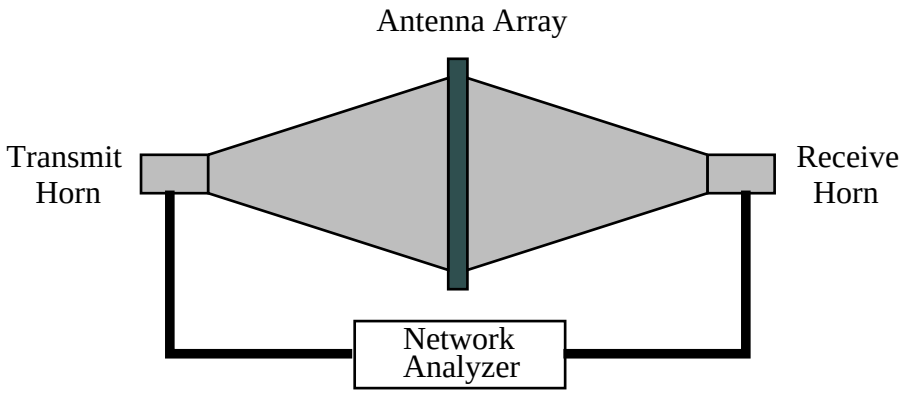

Figure 4.3: The setup for measuring the loss of the spatial power combining array.

horns with lenses (placed back-to-back) in dB and η is the radiation efficiency of the microstrip patch antennas given in dB.

The procedure for designing the patch-slot-patch will not be given, since it does not pertain to this discussion. However, the dimensions of the circuit are given here. A *Rogers TMM3*™ substrate with $\epsilon_r = 3.27$, a dissipation factor of 0.002, and a thickness of 0.381 mm was used. The microstrip patch antenna is 2.083 mm x 2.997 mm, while the slot dimensions are 1.626 mm x 0.254 mm. The efficiency of the patch antenna can then be calculated as described in[89], yielding approximately 94% at 32 GHz. The complete hard-horn dimensions can be found in Section $6.4.4$, where the size of the aperture is given as 45.7 mm x 40.6 mm.

Several experiments were performed as outlined in Fig. 4.3. First the insertion loss of the two hard-horn feeds was measured (Fig. 4.5). This represents the system without the antenna array and gives the loss due to the hard-horns (IL_h). As can be seen in the figure, the loss at 31.6 GHz is approximately 1 dB. The loss of the antenna array, including the hard-horn feeds, was then measured. Each antenna array had a different array spacing and a different number of cells, since a maximum number of cells was placed within the horn aperture (not including the dielectric sidewalls). Several measurements for the insertion loss and return loss of the system are shown in Figs. 4.6 and 4.7 versus frequency, respectively. The loss with a minimum cell spacing of $0.4\lambda_0$ is less than 2 dB at 31.6 GHz. The variation in loss versus unit cell spacing can then be found according to Eq. 4.1 and is illustrated in Fig. 4.8. In addition, the predicted loss of the array is given based on the array's directivity. Using a commercial program, *PCAAD*™, an approximate directivity is calculated. The directivity of an uniform aperture of the same size is then calculated. The ratio of the array directivity to the directivity of an ideal aperture – one having a uniform field distribution across the aperture– is defined as the aperture efficiency. This represents the percentage of energy coupled to the array. The curve designated "effective aperture" in Fig. 4.8 uses this approximation for the calculation of the array loss. In addition, the aperture efficiency has been multiplied by two to represent the loss at the input and output of the array. The curve

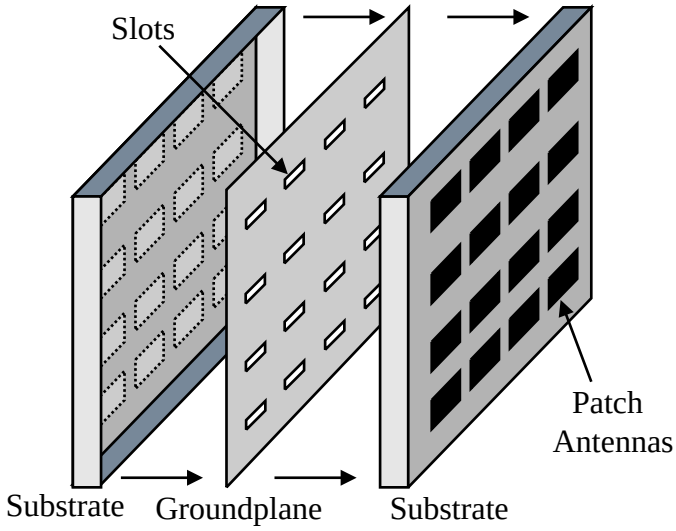

Figure 4.4: Array topology used to characterize the array loss versus unit cell spacing.

seems to predict the loss of the array well up to $0.5\lambda_0$. This may be due to the strong coupling of fields between antennas, which are not accounted for by the program used to calculate the array directivity.

Fig. 4.8 illustrates that the loss due to unit cell spacing decreases to less than 0.5 dB at a cell spacing of $0.4\lambda_0$. In fact, the loss is still less than 1 dB at below $0.5\lambda_0$ spacing. From this point, the losses increase significantly with an increase in unit cell spacing. It is therefore important that a spatial amplifier array have a unit cell spacing below $0.5\lambda_0$, if losses are to be kept to a minimum. This can sometimes be difficult in tiled-based arrays, where the amplifiers, biasing circuitry, and matching networks reside in the same plane as the antenna. However for tray-based arrays, this may not pose a problem, since the amplifying circuitry occupies the space between the input and output antennas – orthogonal to the plane of the microstrip patch antennas. The application of the rectangular lattice in a spatial amplifier array will be the focus of Chapter 5.

4.1.2 Triangular Lattice

The triangular lattice (Fig. 4.2) is of particular interest for spatial power combiners. This is due to the increased distance between antennas in the vertical and horizontal direction, an important requirement for tile-based arrays. This increased space between antennas is illustrated more thoroughly in Fig. 4.9. As can be seen, the amplifier, transmission line, and slot-coupler must reside in the space between adjacent antennas. Therefore, it is also of interest to examine the affect of unit cell spacing on the loss of the array.

The same procedure was again performed as with the rectangular lattice using the experimental

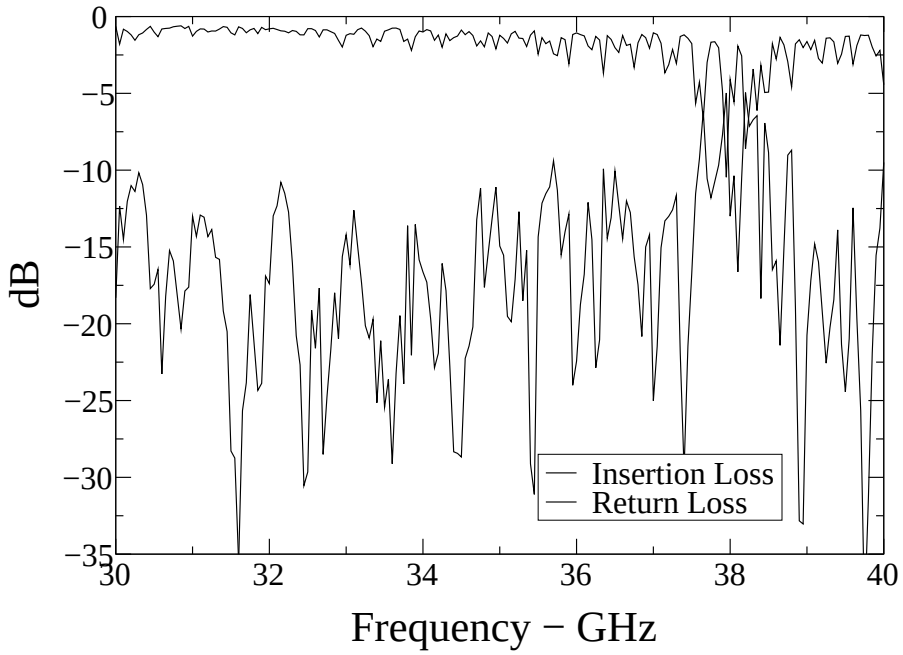

Figure 4.5: The insertion loss and return loss of two hard-horn feeds with lenses placed back-to-back.

setup shown in Fig. 4.3. The results of these measurements are shown in Fig. 4.10. Unfortunately, most of these experiments were performed using various dimensions in antenna size, substrate type, or cell layout. Only the 8.382 x 8.382 mm spacing conforms to the experiments performed with the rectangular lattice. This cell spacing is equivalent to a $0.5\lambda_0$ diagonal spacing. However it allows for approximately 4.5 mm between antennas in the y-direction compared with the approximately 2.54 mm allowed by the rectangular lattice with a $0.5\lambda_0$ spacing. In addition, it has a loss of 2.25 dB, which is slightly higher than the 2 dB of loss found with the $0.5\lambda_0$ rectangular lattice spacing and much less than the 3.1 dB of loss for the $0.6\lambda_0$ rectangular lattice spacing. So for approximately the same loss, the triangular lattice gives a greater distance between cells with a total of 61 unit cells, while the rectangular lattice yields 64 unit cells with little space between antennas.

The other curves illustrated in Fig. 4.10 also use the same hard-horn feed, so the results are comparable. In fact, two of the experiments were performed using the *TMM*™ substrate, so have equivalent antenna efficiencies. However, the final experiment was performed using *Rogers RT6006*™ with an $\epsilon_r = 6.15$, a dissipation factor of 0.0027, and thickness of 0.381 mm. The expected radiation efficiency for this antenna is 83% based on the antenna dimensions of 1.676 mm and 2.54 mm for the resonant length and width, respectively.

Some insight into the loss of the triangular lattice versus unit cell spacing can be derived from Fig. 4.11, where the loss of the antenna array has been calculated using Eq. 4.1. Only a single

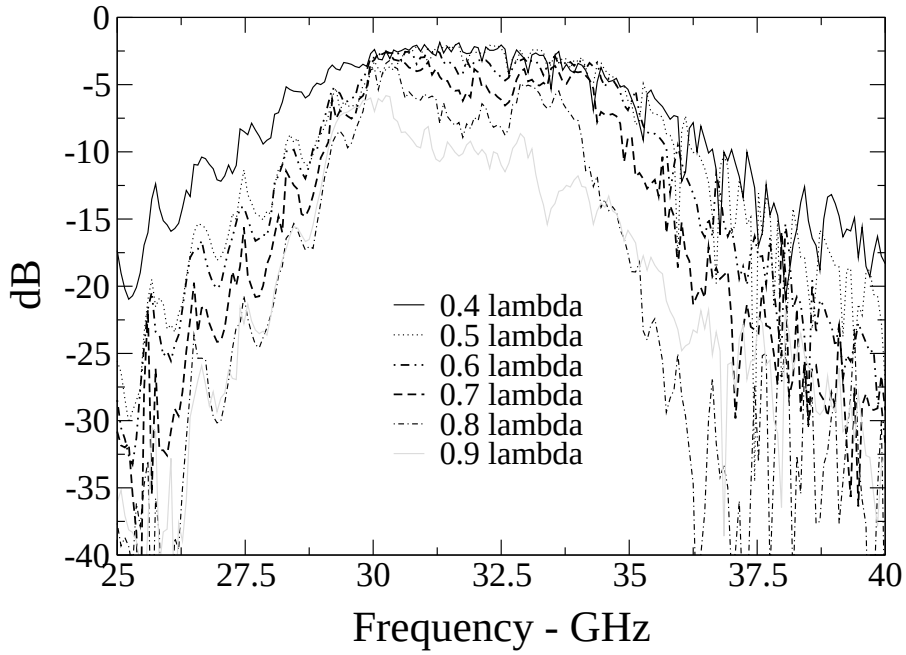

Figure 4.6: The insertion loss of several array spacing values versus frequency for the rectangular lattice.

curve represents the triangular lattice, since the resonant frequencies of the experiments were not the same. Also, each data point represents the loss of the array at its minimum insertion loss. However, the results match well with those of the rectangular lattice, qualitatively speaking. This again illustrates the need for a unit cell spacing on the order of $0.5\lambda_0$ in order to obtain a minimum array loss. This seems to be independent of the substrate height or dielectric constant, since the efficiency of the patch antenna is used in the calculation. However, to obtain a minimum system loss, the antenna efficiency should be high.

The choice of rectangular versus triangular lattice is dependant on the unit cell topology. Either lattice structure will give approximately the same loss for an equivalent unit cell spacing. The rectangular lattice should be used if more unit cells are desired within the same space, given that the circuitry can fit within the unit cell. Alternatively, the triangular lattice should be used in cases where more room is needed for the amplifying circuitry or where fewer unit cells are desired.

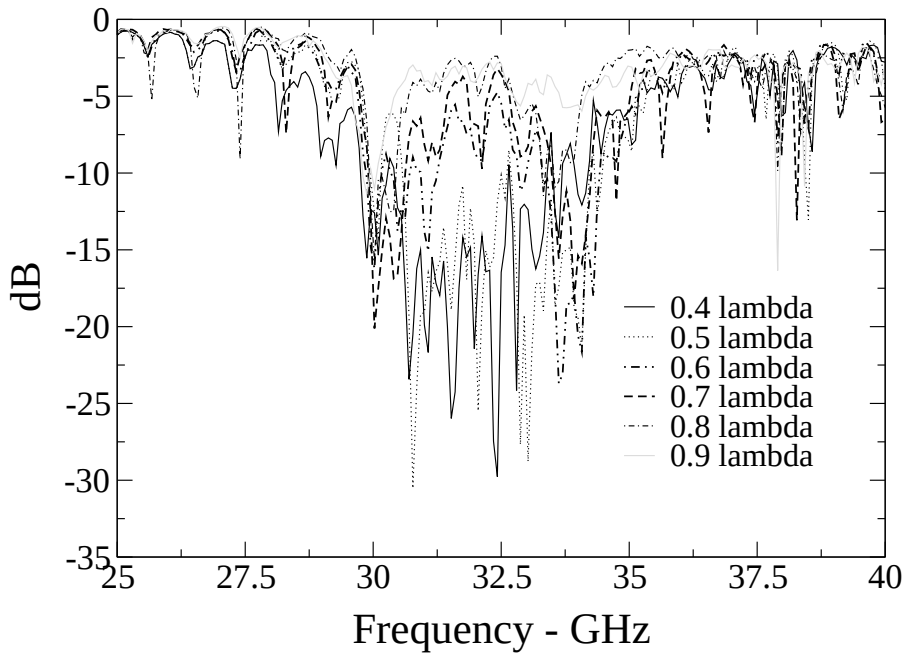

Figure 4.7: The input return loss of several array spacing values versus frequency for the rectangular lattice.

4.2 Effect of Unit Cell Amplitude and Phase Variations

It has been mentioned several times that a uniform field distribution across the aperture of the horn is necessary in order to achieve efficient and coherent power combining. However if device and circuit variations create non-uniformity in either the input or output circuitry, the combining efficiency of the system will suffer. Therefore, it is equally important that each unit cell of the amplifier array have the same gain and phase characteristics. Unfortunately, this is difficult to achieve. There are many factors, which can cause variations in the unit cell performance. These may be variations in transmission line lengths and widths, bondwire lengths and loop heights, and active device performance.

In today's modern fabrication processes, these variations can typically be characterized statistically. Analysis can then be performed to determine the yield of these fabrication processes. For spatial power combiners, it is also advantageous to know the effect of device and circuit variations on the performance of the system. It would, however, be necessary to model the entire structure to obtain the effect of unit cell non-uniformity on the system performance. Such investigations, using both FDTD and MoM analysis techniques, are forthcoming. Until these numerical studies

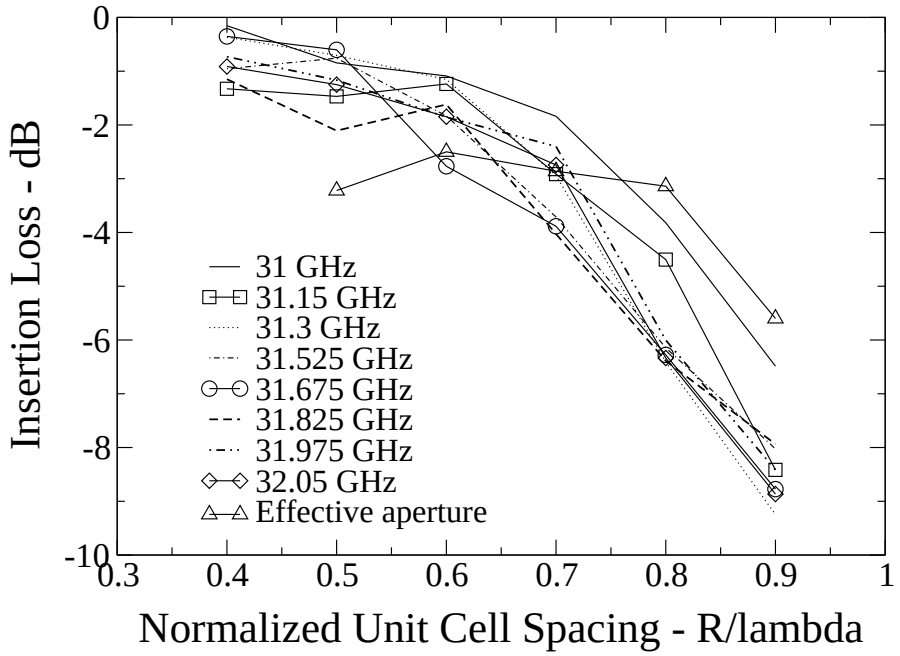

Figure 4.8: The insertion loss of the array versus unit cell spacing for a rectangular lattice.

are available, simpler models of the spatial power combining system may provide some insight into the effect of device variations on system performance.

Once the effect of unit cell variations has been determined, some upper limit must be placed on these variations. This upper limit will be defined by the maximum loss that can be tolerated for the system. The individual components can then be screened in order to meet these criteria. It may however be necessary to screen the unit cell after fabrication, since some of these variations are dependent on the fabrication process itself. For these circumstances, the unit cell gain and phase must be measured individually and independent of the hard-horn feeds. A discussion of this methodology is described in the following sections along with the statistical analysis of a simplified array.

4.2.1 Statistical Analysis

In order to perform a statistical analysis versus unit cell variations, a good model of the system is required. This model would, ideally, represent the system as shown in Fig. 4.12, where each block represents a portion of the system. In addition, the hard-horn to antenna elements would be represented by an $N + 1$ port scattering parameter (S-parameter) matrix; and each unit cell

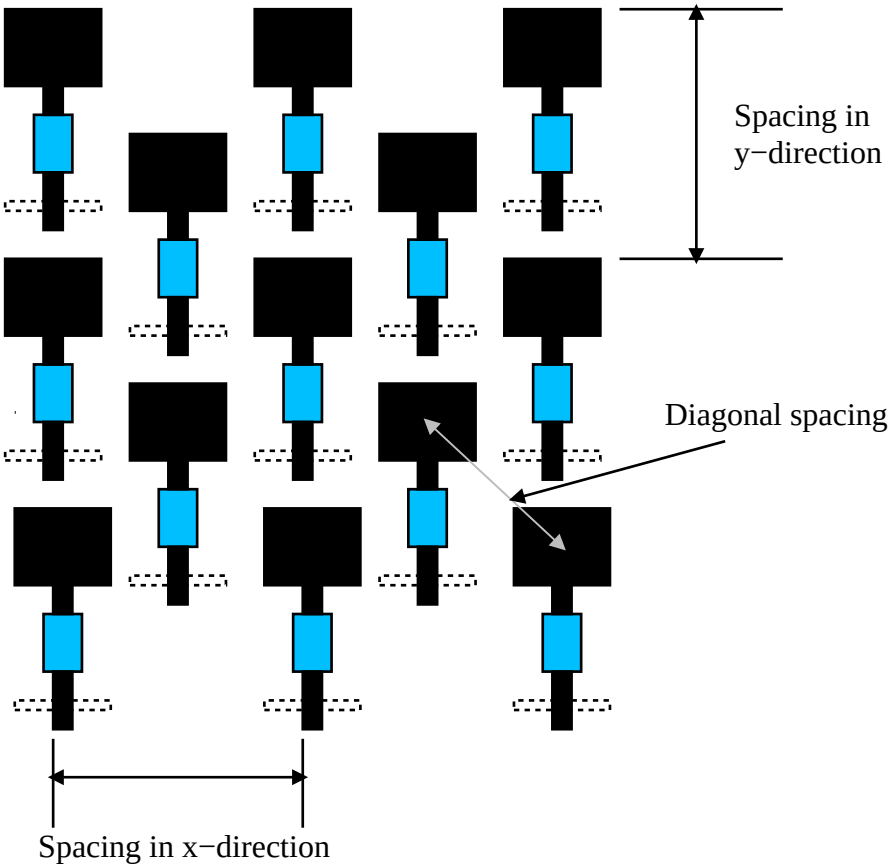

Figure 4.9: The triangular lattice structure used in a tile-based amplifier array.

would be represented by linear and non-linear elements for the passive and active components, respectively. Given such a model of the system, a non-linear circuit simulator could then be used to analyze the effect of unit cell variations.

The most difficult part of analyzing the system, shown in Fig. 4.12, is the modeling of the near-field coupling between the hard-horn and antennas. This is represented by the hard-horn-to-antennas block of the figure. An accurate model would require the full-wave simulation of an array of antennas within close proximity to the hard-horn feed. Such simulations are progressing with methods such as FTDT and MoM. However, a simpler model is required for the fast statistical analysis of the system in lieu of the full-wave techniques. The simplest approach is to create a S-parameter matrix which weights the forward and reverse coupling from the hard-horn input (port one of the S-parameter matrix) to the input of the N antennas (ports 2 to $N+1$ of the S-parameter matrix). This formulation can be represented by the following equations:

$$S_{mn} = \begin{cases} S_{nm} = T_{n-1} & \text{if n=1, m=2..N+1} \\ 0 & \text{otherwise} \end{cases} \tag{4.2}$$

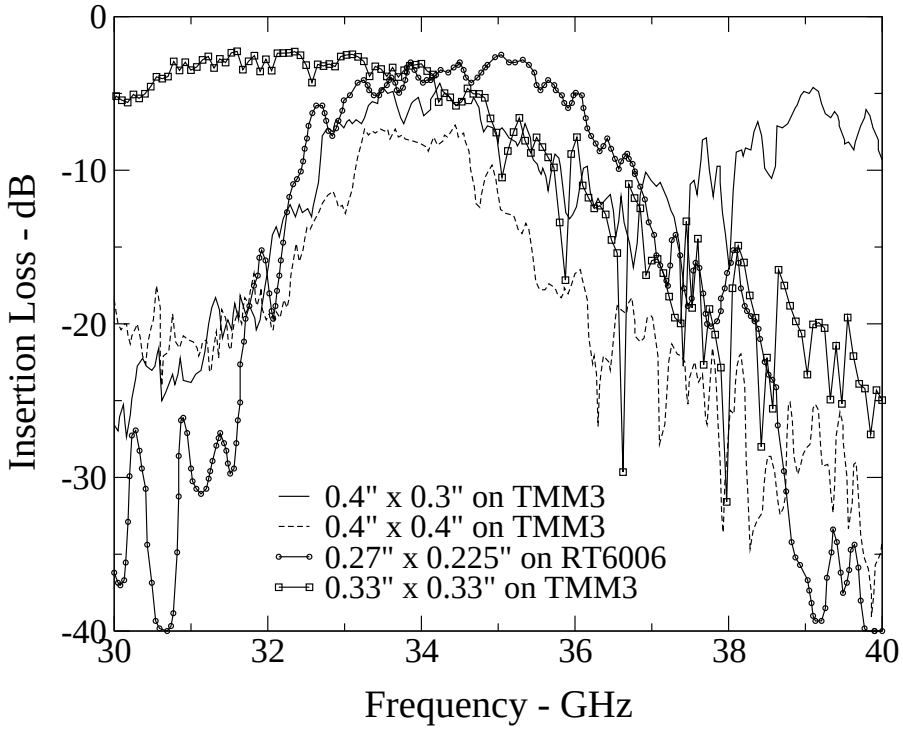

Figure 4.10: The insertion loss of several arrays with different array spacing for the triangular lattice, where the dimensions are for the x and y separation between unit cells, respectively.

where m and n are from 1 to $N + 1$, and T_n represents the N possible transmission coefficients from the horn to the antennas. It is also assumed that all ports are ideally matched and no coupling is present between antennas, thus these terms are zero.

The weights of the transmission terms T_n can be approximated using data obtained from near-field measurements, if we assume that the coupling from the horn to the N antennas is proportional to the magnitude and phase of the near-field distribution at the location of the antennas. This gives a transmission coefficient proportional to the near-field amplitude and phase at the aperture of the horn. Such data can be obtained from actual near-field measurements or from simulated near-field results. Once the un-normalized transmission coefficients t_n are determined, they must be normalized to give a conservation of power as follows:

$$T_n = \frac{t_n}{\sqrt{\sum_{n=1}^{N} |t_n|^2}} \tag{4.3}$$

The S-parameters are then directly obtained using Eq. 4.2, yielding the final matrix representing the division of power from the horn to the input terminals of the antennas. This does not take into account any losses associated with the unit cell spacing, hard-horn, or antenna efficiencies.

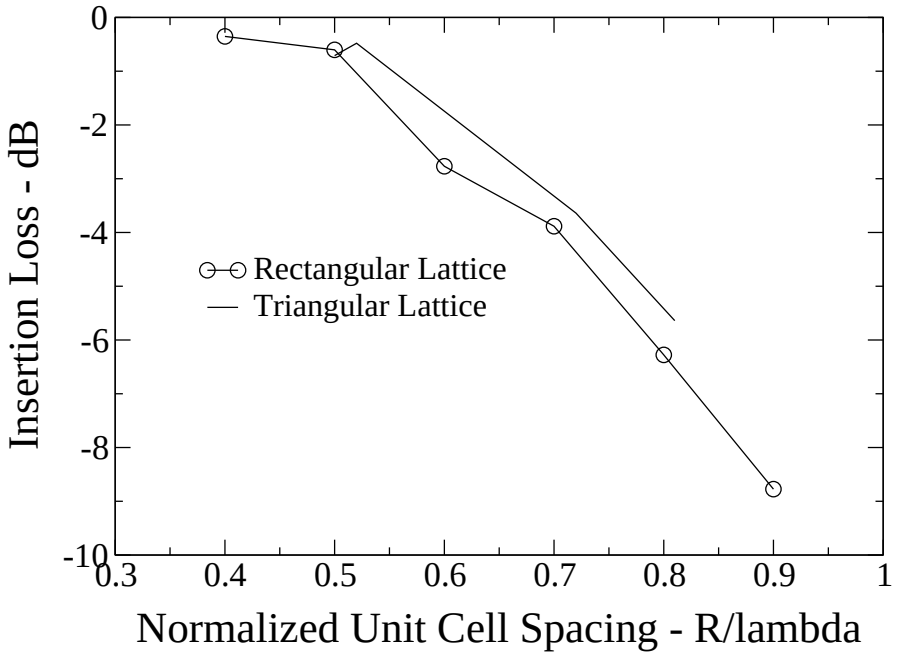

Figure 4.11: The insertion loss of an array versus the unit cell spacing.

Such losses can be added to the model by simply renormalizing the transmission coefficients. Alternatively, the loss could be added to the simulation in the form of attenuators at the input of each antenna, or a combination of the two methods could be used.

The statistical analysis can then be obtained by cascading the various components illustrated in Fig. 4.12 within a non-linear circuit simulator such as *Agilent - Advanced Design System (ADS)*™. The variations within the cell may either be represented by a single element describing the possible changes in gain and phase versus frequency or by the individual components of the unit cell. If the individual components are modeled, a large number of simulations will be necessary in order to analyze the effect of varying each components width, length, thickness, gain, phase, etc. However if a single element is used, only the absolute gain and phase versus frequency need be changed. This element may be a non-linear device model of the amplifier cascaded with an ideal attenuator and phase shifter. The attenuator and phase shifter are then adjusted to represent the change in amplitude and phase from one unit cell to another. By randomly changing this amplitude and phase, the effect of unit cell variations can be found.

The phase and amplitude variations of the unit cell are modeled using a Gaussian distribution with mean m and standard deviation σ as shown in Fig. 4.13. Each unit cell is then chosen randomly using this probability distribution. Several simulations can then be performed with varying σs. It

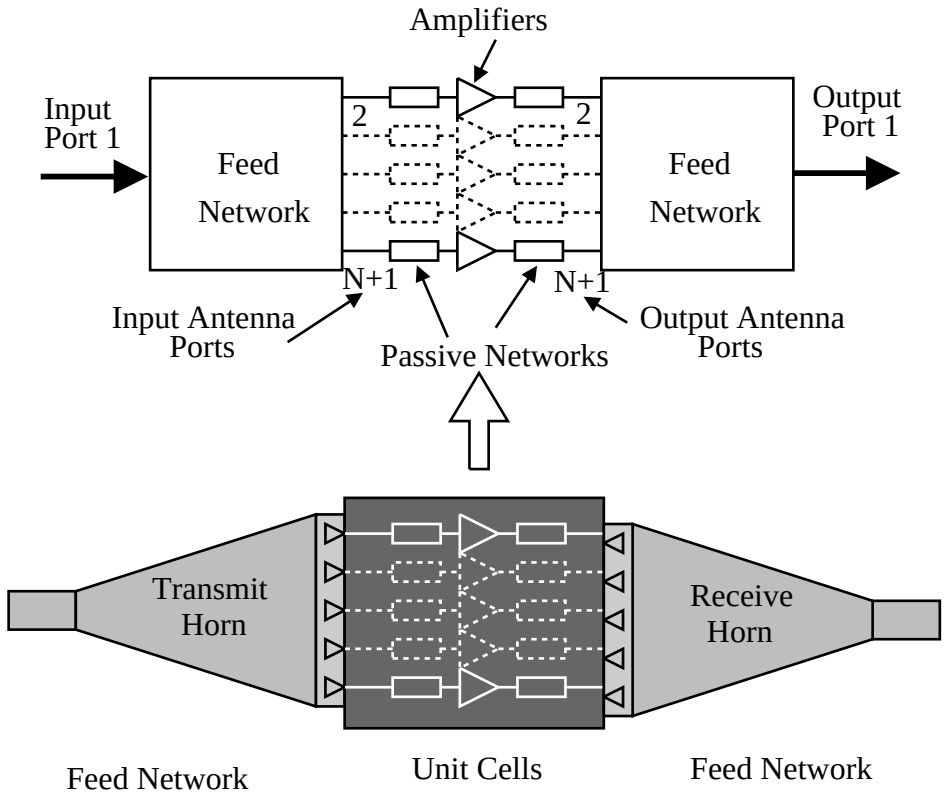

Figure 4.12: A model of a spatial power combiner using blocks to represents the various components of the system.

will be assumed that the average phase and amplitude variations are equal to zero. The results will show the loss of gain and combining efficiency of the system for various values of σ. If a particular maximum loss is defined, a maximum σ may be found. The unit cell variations can then be kept to within this distribution to maintain this maximum loss.

Several cases have been analyzed using this method for an 8x8 array. The unit cell gain is represented by a non-linear amplifier model, which has a randomly varying amplitude and phase. Fig. 4.14 illustrates the insertion loss versus the standard deviation of the phase for two different values of the amplitude's σ. As expected, the loss increases as the probability increases for a larger phase variation in the unit cells. This is also the case for a larger variation in the insertion loss or gain of the unit cell. A second set of simulations were performed to analyze the effect of the field distribution on the power compression of the amplifier. These results are shown in Fig. 4.15. Although the phase and amplitude across the hard-horn meet the tolerances denoted in the previous chapter, they still incur some losses when compared to the ideal uniform distribution. However when compared to a standard horn antenna, the increased power output is readily apparent. In fact under deep compression, the ideal hard-horn and measured hard-horn converge. We suspect that this is due to the flattening in the amplitude distribution, as all the amplifiers are delivering approx-

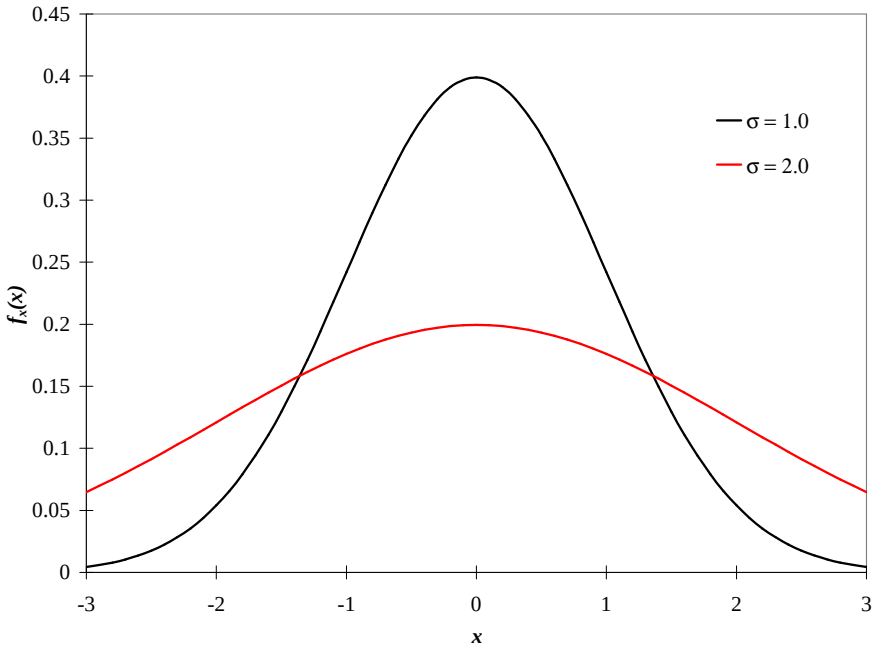

Figure 4.13: A Gaussian distribution with mean m and standard deviation σ.

imately the same amount of power near saturation. The last test case is shown in Fig. 4.16, where the ideal hard-horn is compared with the measured hard-horn data for an amplitude σ of 0.5 dB and a phase σ of 20°. Under these conditions, the loss of the array is significantly larger in the actual hard-horn data than with the ideal field distribution. This is most likely due to an accumulation of phase and amplitude errors as is apparent when observing the accelerated roll-off in the insertion loss of Fig. 4.14. In conclusion, these simulation deliver some insight into the loss in system performance versus the variation in the amplitude and phase of the unit cell. As expected, these simulations verified that the hard-horn provides more power under compression than a standard horn antenna. In addition, more gain is provided under small signal excitation, most likely due to the uniform phase distribution.

4.2.2 Experimental Optimization Techniques

At this point, the statistical distribution of unit cell amplitudes and phases should be known. However if this information is to be applied toward screening the array, the actual unit cell amplitude and phase must be measured, so that cells may be repaired or replaced based on this information. The simplest method to obtain variations in amplitude and phase from cell to cell is through the use of waveguide probes as illustrated in Fig. 4.17. This method provides the transmission coefficient (loss or gain) through a unit cell relative to its neighbors. Using an x-y positioner, the probes can scan across the array to measure the transmission characteristics of every unit cell in the array, thus automating the process.

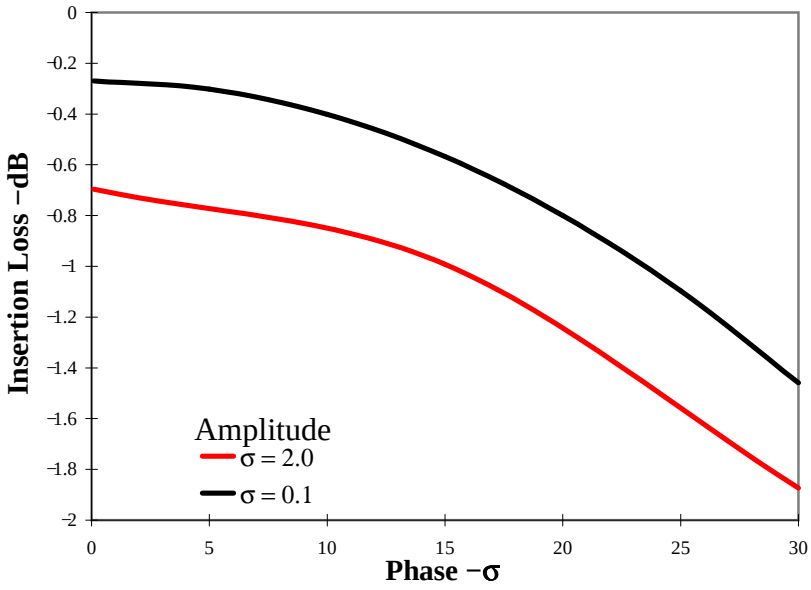

Figure 4.14: The simulated insertion loss of an 8x8 array fed by an ideal hard-horn versus the standard deviation of the phase in degrees.

Although the waveguide probe method is extremely simple. It does come with some caveats. Firstly, the probes must be very close to the antennas (less than a wavelength) in order to measure the transmission characteristics of a single cell without receiving any energy from the neighboring elements. This can incur some coupling between the probe and the antenna, causing changes in the input impedance of the antenna. The second problem involves the non-linear change in field intensity with a change in distance from the antenna within the reactive near-field zone [89]. This means that the measured amplitude and phase characteristics of the unit cell can vary rapidly as the probe moves closer or further from the antenna. However if the probe distance can be well maintained, the relative amplitude and phase intensity should be the same between cells.

The first problem given above is the most important one to address. The input impedance of the antenna must not change from its designed value if the unit cell is to operate properly. Therefore, the variation in input impedance should be measured versus the probe distance from the antenna. This can be done in a number of ways. One example is shown in Fig. 4.18, where the antenna is attached to a network analyzer via a probe station. The input impedance can then be measured versus the probe distance from the antenna. An example of one such measurement is illustrated in Fig. 4.19 for a Ka-band antenna to be used in a 45-element tile-based array. The desired input impedance is 50Ω, which occurs at distances greater than 12.7 mm. Also at a distance of approximately 2.54 mm, the input impedance is again 50Ω. Therefore if the probe is kept at 2.54 mm, the near-field measurements can be made without affecting the unit cell performance.

Based on the above discussion, a process can be developed for the automated characterization of all the unit cells. This information can then be used to locate cells which fall outside the predetermined

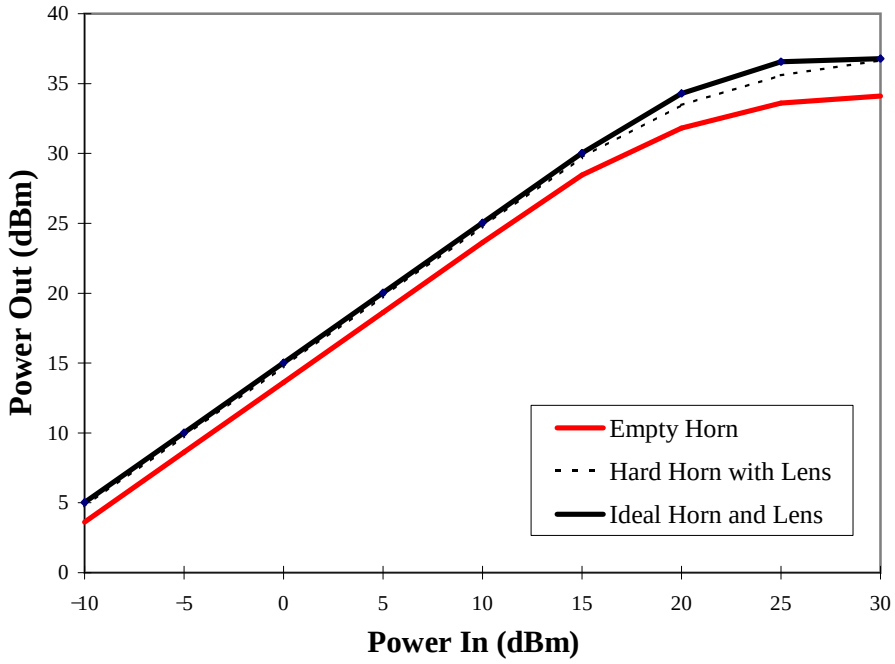

Figure 4.15: The simulated power compression of an 8x8 array for various near-field excitations.

limits. These cells may then be corrected by investigating the cells for faulty devices, bondwires, or transmission lines, which can either be replaced or repaired.

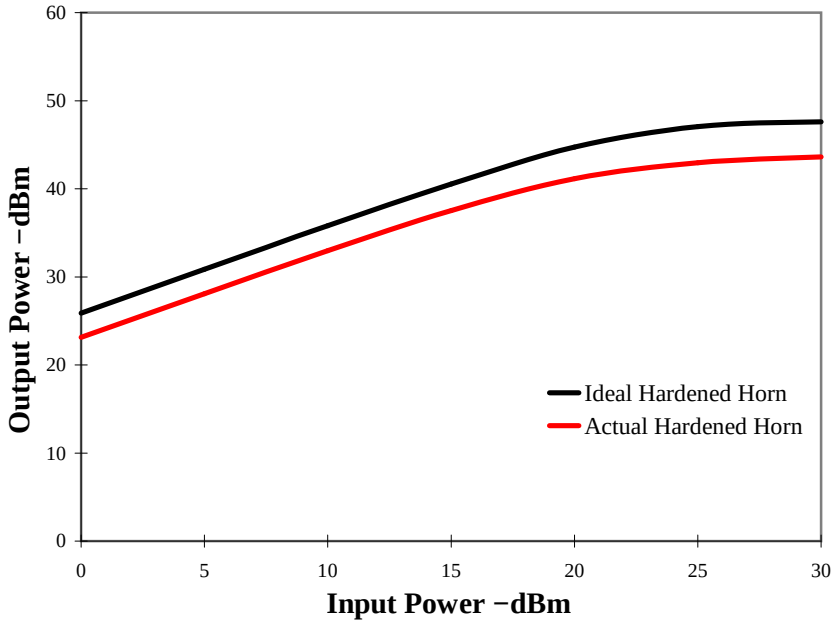

Figure 4.16: The simulated power compression of an 8x8 array for a standard deviation in phase of 20° and 0.5 dB in gain.

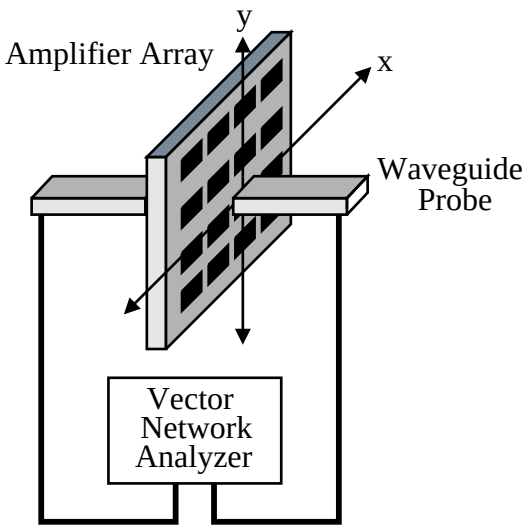

Figure 4.17: Near-field unit cell characterization using waveguide probes.

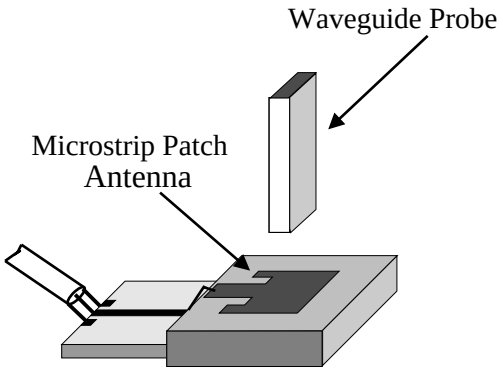

Figure 4.18: A waveguide probe measurement setup to test the effect of the waveguide probe on the antenna input impedance.

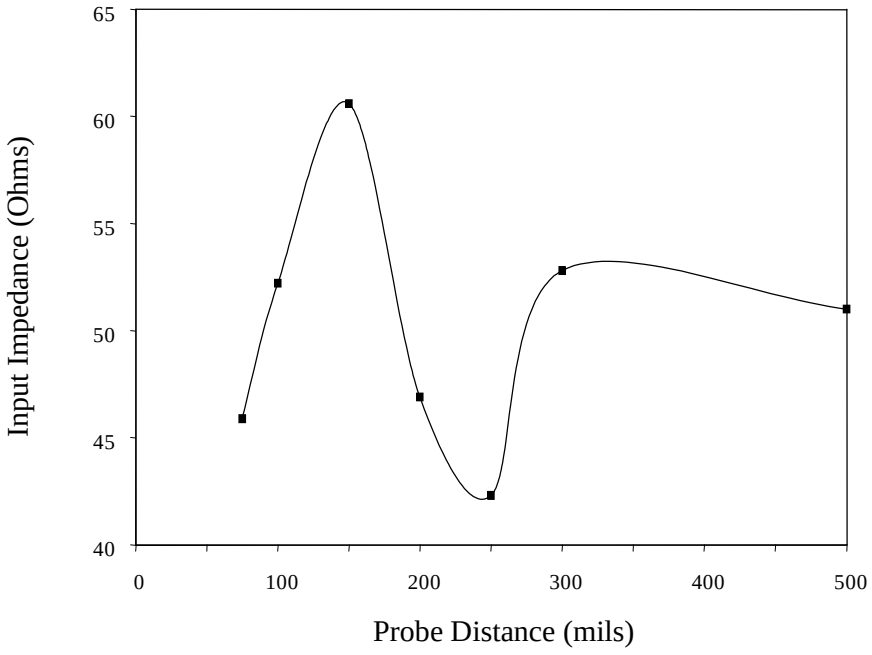

Figure 4.19: The measured real impedance of an antenna versus waveguide probe distance.

Chapter 5

Tile Approach

In Chapter 1, two basic types of spatial power combiners were introduced (tile- and tray-based). In this chapter, the tile-based approach has been applied to the design of several arrays consisting of 13-, 45-, and 98-elements, all of which operate at Ka-band. The basic configuration of these designs is shown in Fig. 5.1. They consist of an array of input microstrip patch antennas, driver amplifiers, through-plate transitions, power amplifiers, and output microstrip patch antennas. In addition, the amplifier arrays are fed using hard-horn antennas with dielectric lenses.

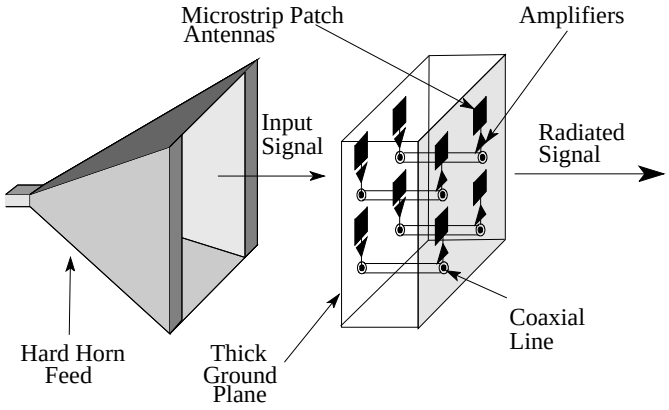

Figure 5.1: An illustration of the tile-based approach used in a 13-, 45-, and 98-element arrays.

In this configuration, the hard-horn feeds provide a field with uniform amplitude and phase at the aperture of the horn. This signal is coupled to the microstrip patch antennas located on the first layer of the array to the left of Fig. 5.1. The signal is then amplified by a driver amplifier and coupled to the second layer via a through-plate transition. Finally the signal is amplified through a power amplifier and radiated either into free space or into a receiving hard-horn feed at the output.

The tile-based amplifier arrays discussed here have been developed under a DARPA MAFET-3

program through the Air Force Research Laboratory, Wright-Patterson Air Force Base (contract number N66001-96-C-8628) with Lockheed Martin Corp. as the primary investigator. The primary focus of this program was the development of a spatial power amplifier, which provided at least 25 Watts of radiated power with 10 dB of gain at Ka-band. A secondary goal of 50 Watts of radiated power was also established.

In either case, several fundamental problems were to be answered in the development of this high power spatial amplifier. One such problem is the ability to remove excess heat produced by the MMIC amplifiers. This issue has been addressed in several ways [75, 79, 88]. Possible approaches for the removal of the excess heat include the utilization of exotic substrates, thick metal carriers as the heat sinks, and liquid cooling. Exotic substrates such as diamond can be used to remove heat but are typically expensive and difficult to process. Substrates such as Al-N and SiC provide alternatives for smaller arrays in which the amplifiers are not far from the metal carrier. Removing heat through the use of a thick metal carrier is more attractive due to the lower cost involved in both materials and the processing of such materials. In some circumstances, thick groundplanes may not be sufficient for heat removal. Such circumstances arise when the heat generated by an increased array size exceeds the thermal capacity of the groundplane, limited in thickness by the constraints of the QO system. This limitation in groundplane thickness may be due to size constraints or coupling limitations from one side of the array to the other. In such cases, a liquid coolant, flowing through or around a thick groundplane, can provide enough heat sinking.

A second question that must be answered is the choice of radiating element and lattice type. In order for the spatial amplifier to operate efficiently, the radiating element must also be efficient. In Chapter 3, the literature was surveyed, citing many examples of amplifier arrays with varying types of radiating elements. For the tile-based array, the most common choice of radiating element was the CPW-fed slot and the microstrip patch antenna. At millimeter-wave frequencies, the use of CPW transmission lines is preferable for MMIC implementations. However since the slot antennas radiate equally in the front and back directions, polarizers are typically used to regain the energy radiated in the undesirable direction. This is done by providing constructive interference between the forward radiated fields and the reflected back radiated fields. Alternatively microstrip patch antennas could be used, eliminating the need for polarizers. In addition, microstrip patch antennas radiate relatively efficiently at about 70 - 80% at Ka-band [67]. The choice of lattice type was discussed in Chapter 4. As was mentioned, a triangular lattice is preferable in tile-based arrays, due to the increased inter-antenna spacing in the x- and y-directions. This allows more room for the amplifiers, matching circuits, and biasing networks.

The answers given above defined the topology of the tile-based arrays developed in this research. Each amplifier array utilizes microstrip patch antennas as the radiating elements along with a thick groundplane for heat removal. Several variations have been implemented. Specifically, several variations in groundplane thickness, as well as the through-plate transition, were made. The reasons for these choices will be outlined in their respective sections. In addition, the design, fabrication, and experimental results will be presented for the 13-, 45-, and 98-element tile-based arrays. Since each of these arrays were developed to meet the goals outlined above, they all share some characteristics in common. Therefore, the common characteristics of the unit cell structure will be

described first to eliminate the need for repeated discussion. In particular, the antenna implementation and amplifier layouts are shared by all three designs. Particular care will be given to delineate between those contributions of the author, which were outlined in the first chapter, from those of the other team members.

5.1 Unit Cell Structure

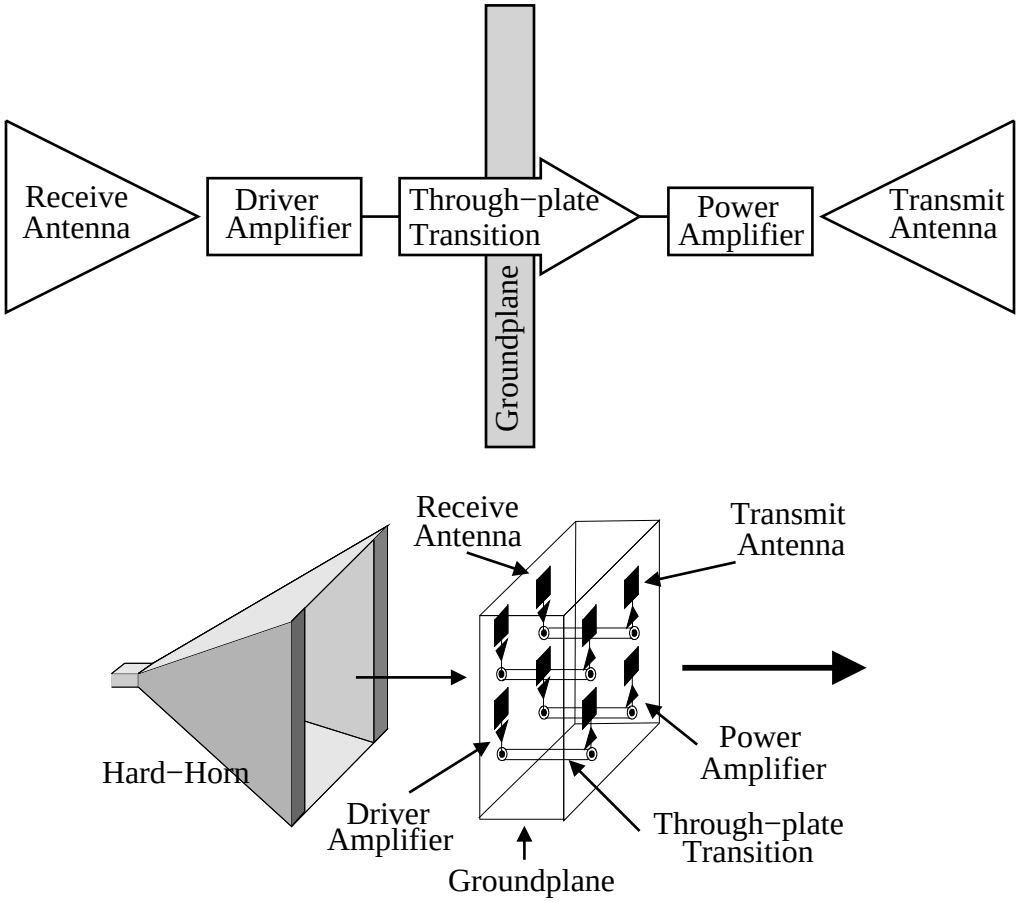

Figure 5.2: The unit cell layout used in the 13-, 45-, and 98-element arrays.

The basic unit cell structure was the product of collaboration between the University of Central Florida (Amir Mortazawi, Toni Ivanov, and Sean Ortiz), the University of Maryland (Eric Schlecht), and Lockheed Martin Corporation (Lee Mirth and John Hubert). This structure is outlined in Fig. 5.2, where the unit cell consists of a receiving microstrip patch antenna, driver amplifier, through-plate transition, power amplifier, and transmitting microstrip patch antenna. In addition, a thick ground was chosen for the efficient removal of heat. Based upon these preliminary

guidelines, several arrays were built at Lockheed Martin Corp. in Orlando, FL. The University of Central Florida was responsible for the design of the hard-horn feeds, as well as the array topology. Eric Schlecht provided initial designs for the microstrip patch antenna and for a coaxial through-plate coupler. Subsequent antenna, hard-horn, and through-plate coupler designs were performed by Sean Ortiz. In addition, Lockheed Martin provided expertise in the design and layout of the amplifier and biasing networks, thermal analysis, and the mechanical designs associated with the hardware.

Several initial constraints were placed on the array design. First the choice of amplifiers was decided. *Northrop Grumman*™ driver and power amplifiers, providing 0.5 and 1 Watt power outputs under 2 and 1 dB compression, respectively, were to be used. This defined the maximum power output from a single unit cell of the array and also the minimum distance between antennas of the array (10.16 mm). An initial study on system insertion loss versus array spacing was also performed as outlined in Chapter 4. The conclusions of this study defined the array topology to be used – triangular lattice.

The initial experiments were then followed by the fabrication of a small, 13-element, sub-array. The experiments on the 13-element array provided crucial data for the development of the subsequent arrays – 45- and 98-element. Furthermore, the number of elements necessary to produce 25 and 50 Watts of radiated power was determined from these initial experiments. Work then progressed to fabricate each of these arrays in turn. Therefore, the design of each array is inherently related. Little change was made between the basic structure of the arrays in order to have a scalable design for higher output power levels. The same basic cell layout was used, including cell spacing, amplifiers, biasing networks, and antenna designs. The development of the microstrip patch antenna for the three designs will be described in the first section, followed by the amplifier layout, and finally the various through-plate transitions to be implemented in the three arrays.

5.1.1 Antenna Implementation

A microstrip patch antenna was chosen for its ease of integration within a planar array topology and for its relatively high radiation efficiency. In addition, the design of microstrip patch antennas is well documented in literature. It was therefore a simple matter in determining such parameters as the optimum antenna width to length ratio and the expected radiation efficiency. Other parameters such as substrate type and thickness, as well as matching networks, could then be designed.

The antenna must fit within the unit cell topology shown in Fig. 5.2. It must be small in order to leave room for the amplifier, yet have a high radiation efficiency. A *Rogers TMM3*™ substrate with an $\epsilon_r = 3.27$, dissipation factor of 0.002, and height of 0.381 mm was chosen to meet these requirements. This gives an approximate radiation efficiency of nearly 94% for an antenna operating at 34 GHz, as calculated in Chapter 4. Higher efficiencies can be obtained with lower dielectric constants or thicker substrates. However, this will either increase the antenna size or will increase the bondwire distance between the antenna and the MMIC device (height of 0.1 mm).

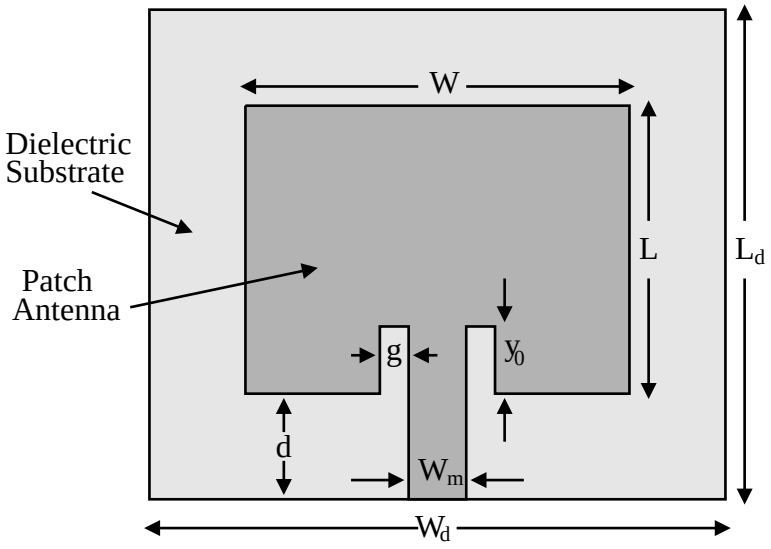

Figure 5.3: The microstrip patch antenna used in the 13-, 45-, and 98-element arrays.

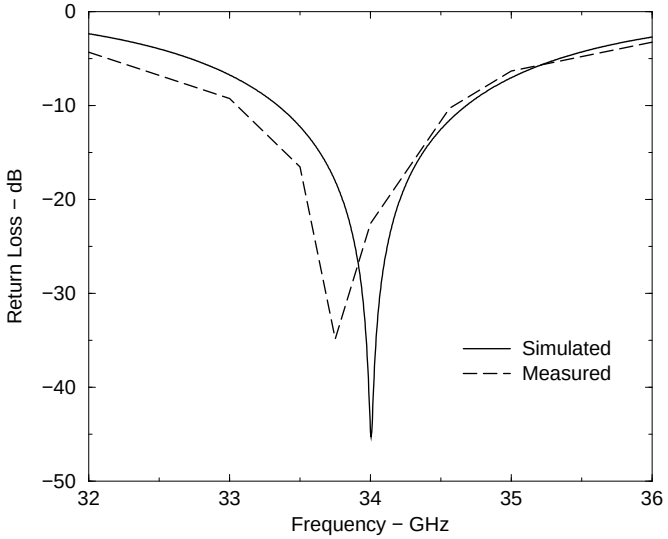

Figure 5.4: The simulated and measured return loss for the microstrip patch antenna used in the 13-, 45-, and 98-element arrays.

Fig. 5.3 illustrates the microstrip patch antenna layout. Several features are apparent in this figure. First, the microstrip patch antenna is located on a finite size substrate in order to accommodate the MMIC chips epoxied to the groundplane. Most microstrip patch antenna models assume that the antenna substrate is infinite. Therefore, a full-wave simulation package is necessary to model

this antenna. Furthermore to decrease the size of the matching network, a recessed microstrip line feed is used. Since this changes the geometry of the antenna, it also requires the use of a full-wave simulation package.

Several software packages were used to design the antenna in addition to basic closed form design equations. First, the dimensions of the microstrip patch antenna were calculated using the method described in [89], also verified using a program (*PCAAD*™). These parameters were then used as the basis for simulations in *Agilent - High Frequency Structure Simulator (HFSS)*™ to determine the exact values of the input impedance versus frequency. The input impedance found was for the patch antenna on a finite size dielectric substrate, fed at the edge of the antenna by a microstrip line. The length of the recessed microstrip line feed could then be found according to the following equation [89]:

$$R_{in}(y_0) = R_{in}(y=0)\cos\frac{\pi}{L}y_0^{\,2} \tag{5.1}$$

where y_0 is the length of the recess, L is the resonant length of the antenna, and $R_{in}(y=0)$ is the input impedance at the edge of the patch antenna.

In addition, the gap width between the recessed microstrip line and the patch antenna must be determined. Unfortunately, the effect of this gap width was not well documented, so simulations were necessary to optimize its effect. It was also found that a larger bandwidth could be obtained, if the recessed microstrip line feed was not matched directly to 50 Ω, but to some higher impedance. This impedance could then be transformed to 50 Ω, using an impedance transformer. However, the gap adds some reactance to the impedance. Therefore a slightly shorter length transformer is needed to match the complex impedance to 50 Ω. This combination allowed for a larger bandwidth, while maintaining the reduced size of the recessed microstrip line feed. All of the above optimizations were performed using HFSS. The final dimensions found through simulations are as follows:

$$\begin{aligned} L &= 2.1844 \text{ mm} \\ W &= 3.0 \text{ mm} \\ g &= 0.1016 \text{ mm} \\ y_0 &= 0.5334 \text{ mm} \\ d &= 0.7112 \text{ mm} \\ W_m &= 0.508 \text{ mm} \end{aligned}$$

where all of the dimensions are in reference to Fig. 5.3. In addition, the width and length of the dielectric were 4.369 mm and 3.556 mm, respectively. The simulation and measurement results are given in Fig. 5.4 Both measured and simulated results include the effect of a bondwire from the edge of the microstrip patch antenna to a 50 Ω transmission line on a 0.127 mm alumina substrate. The error between the measured and simulated antenna return loss is less than 1% in frequency. In addition to return loss, the simulations gave a radiation efficiency of approximately 73%, which is lower than the previously calculated value of 94%. It is suspected that these discrepancies are

due to the finite size substrate and the bondwire length. This antenna was used in both the 45- and 98-element arrays. A slightly lower frequency antenna was used in the 13-element array.

5.1.2 Amplifier Layout

The amplifier layout was performed by John Hubert at Lockheed Martin. A brief description of the layout is given here for completeness. Two Northrop Grumman amplifiers were chosen for the driver and power amplifiers. The two-stage driver amplifier is able to deliver 0.5 Watts under 2 dB compression with a small signal gain of 12 dB. The driver is biased at $V_{GS} = -0.2$ V and $V_{DS} = 5$ V, yielding $I_{DS} = 210$ mA. The power amplifiers have 8 dB of large signal gain when biased at $V_{GS} = -0.2$ V and $V_{DS} = 5$ V, giving $I_{DS} = 1.2$ A. Stability was carefully considered and enhanced by adding 1000 pF and 27 pF capacitors to each amplifiers' bias lines. In addition, 0.1 μF capacitors were added to the perimeter of the array to ensure stability.

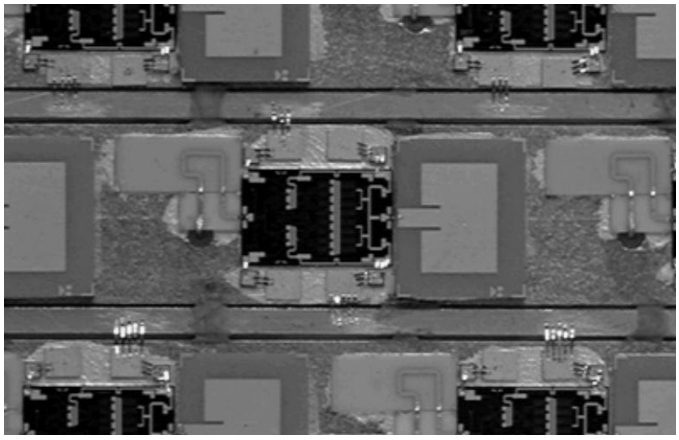

Figure 5.5: A photograph of a unit cell in the 45-element array, illustrating the placement of the amplifier.

A photograph of the unit cell in the 45-element array illustrates the layout of the amplifiers described above, Fig. 5.5. The only difference between the driver and power amplifier layouts are the amplifiers themselves. The same capacitors are used in both cases. The simulated performance of the driver and power amplifiers based on data taken from Northop Grumman is shown in Fig. 5.6. As can be seen in the figure, the driver and power amplifier, when cascaded, should provide a total of 21.5 dB of gain under small signal excitation at 34 GHz.

5.1.3 Through-Plate Transition

Each of the amplifier arrays utilize a slightly different through-plate transition. Although, each has the same purpose – to couple power from one side of the thick groundplane to the other. The

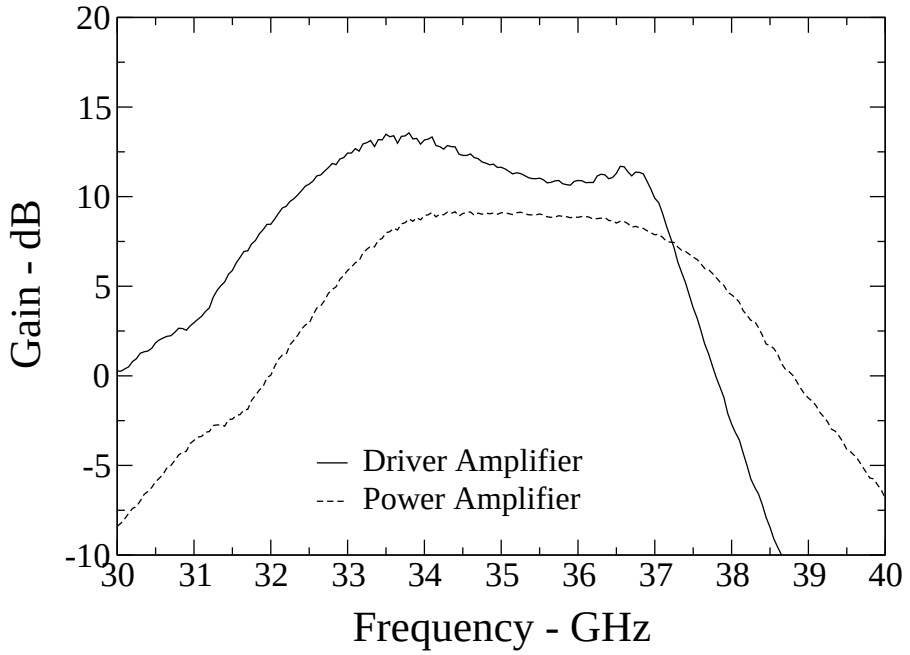

Figure 5.6: The gain of a *Northrop Grumman*™ driver and power amplifier.

differences between the designs is due to varying groundplane thickness and also a change in approach.

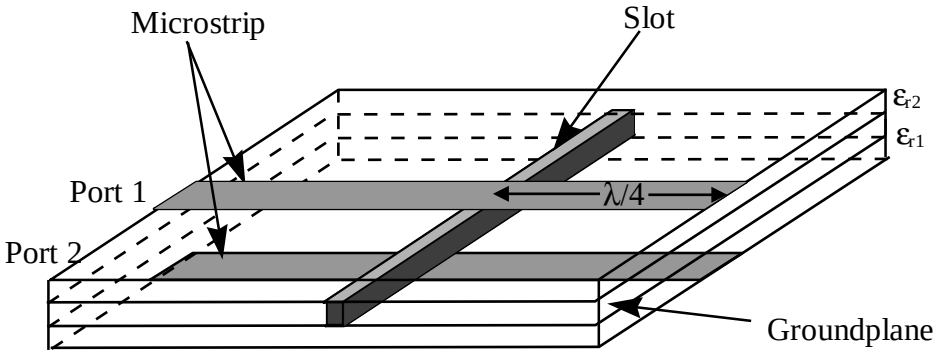

Figure 5.7: The microstrip-slot-microstrip through-plate transition with a thick groundplane.

The 13-element array used a carbon steel groundplane with a thickness of 2.54 mm. For this array, a microstrip-slot-microstrip transition was used as shown in Fig. 5.7 to couple energy from

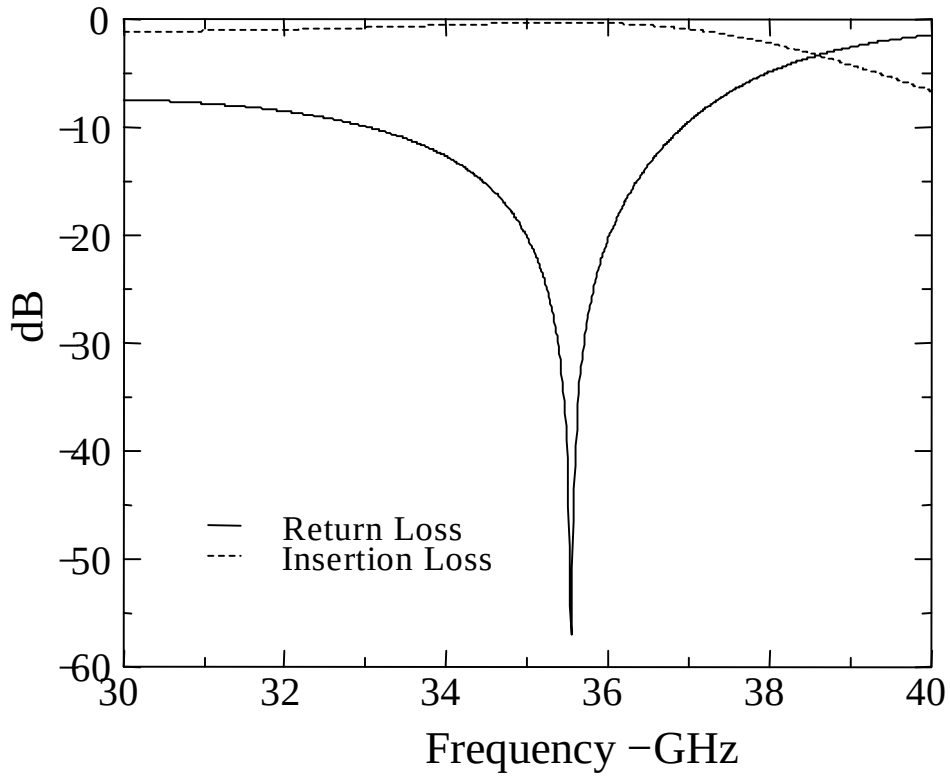

Figure 5.8: Simulated results for the microstrip-slot-microstrip through-plate transition.

one side of the array to the other. The basic principles of this transition can be found in several papers [63, 65]. The open circuited $\lambda/4$ microstrip lines serve to short the impedance across the slot, resulting in power transmission through this aperture. However for thin groundplanes, the coupling takes place through evanescent modes in the short waveguide. Therefore, its width is less than a $\lambda/2$. However as the waveguide (slot thickness) increases, the waveguide width approaches $\lambda/2$. Due to size constraints, this approach could not be used for the arrays incorporating thick groundplanes. One possible solution is to fill the waveguide with low loss dielectric material in order to reduce its size.

Full-wave simulations were performed with HFSS. The design was optimized to give a minimum insertion loss. The simulated results are shown in Fig. 5.8, where the transition provided 1 dB of insertion loss at 34 GHz. The resulting slot length and width were 2.794 mm and 0.254 mm, respectively, using a dielectric constant of 6.15 and dissipation factor of 0.0009 within the short waveguide (thick slot).

For the 45-element array, a different type of through-plate transition was developed. The idea was given by Erich Schlecht for a coaxial through plate transition (Fig. 5.9). This was a simple solution but rather difficult to implement. The placement of the coaxial line through the groundplane and the bonding to the microstrip lines proved a difficult task. However, preliminary experiments verified

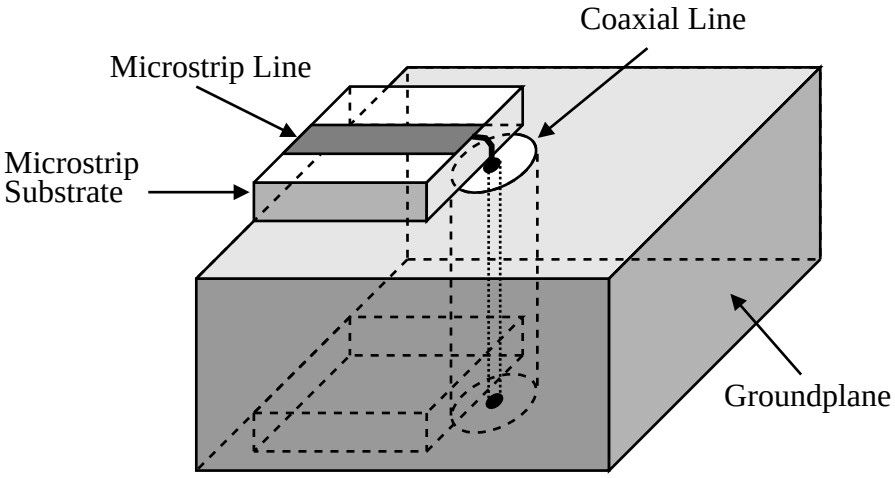

Figure 5.9: The coaxial through-plate transition.

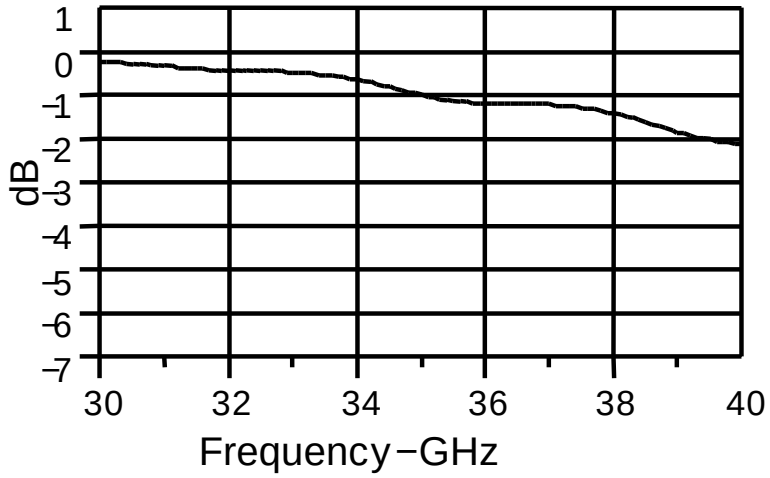

Figure 5.10: The simulated insertion loss of the 2.54 mm long coaxial through-plate transition.

its utility, having an insertion loss of less than 1 dB.

A 50 Ω micro coaxial line was used for this purpose. The 50 Ω transmission line was simply placed within a hole drilled through the groundplane. In addition, the outer conductor was removed, and the center conductor was replaced. The dimensions of the new inner and outer conductor were 0.1524 mm and 0.6604 mm, respectively, with a dielectric constant of 2.0. Measurements, as well as simulations, were performed for this transition. The simulation was performed in *HFSS*™ for the coaxial line and input and output microstrip lines. Furthermore, the results were de-embedded to the coaxial line input. Of particular concern was the interface between the coaxial line inner conductor and the microstrip line. The simulated results are shown in Fig. 5.10. Measured results

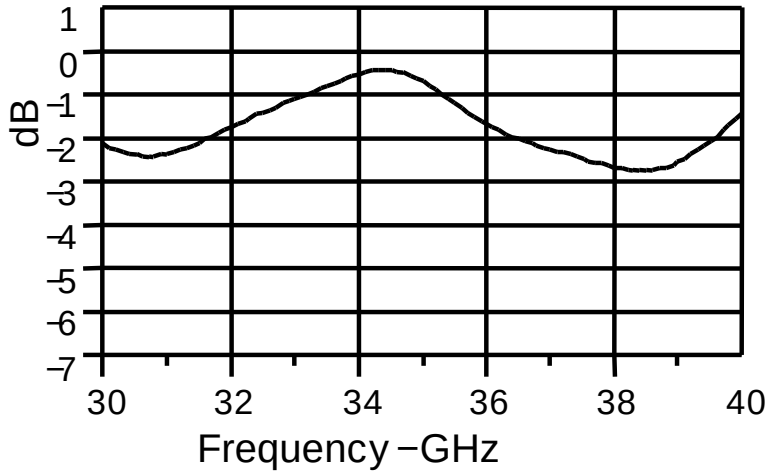

Figure 5.11: The simulated insertion loss of the 12.7 mm long coaxial through-plate transition.

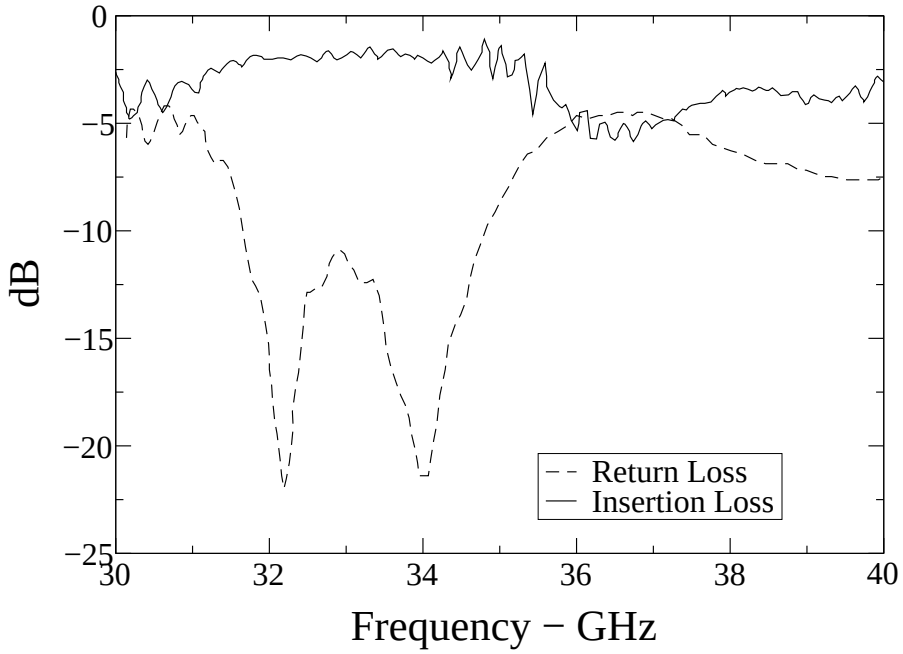

Figure 5.12: The measured insertion loss of the 12.7 mm long coaxial through-plate transition.

of the same structure de-embedded to the microstrip-to-coaxial line interface yield similar values with less than 1 dB of loss at 34 GHz.

The coaxial line was identical for the 98-element array as with the 45-element array, only differing in length. However, preliminary simulations showed a resonance due to the length of the coaxial

line terminated by the two non-ideal loads (the coax-to-microstrip line transition). A thickness of 12.7 mm was found to give a good insertion loss centered at 34 GHz, as illustrated in Fig. 5.11. The measured results are shown in Fig. 5.12. The simulation predicted the center frequency of resonance. However, differences are seen in the level of the insertion loss. Some of these differences may be attributed to the extra lengths of transmission lines and coax-to-microstrip adapters used in the test fixture, which contribute approximately 1 dB of loss at 34 GHz.

5.2 A 13-Element Array

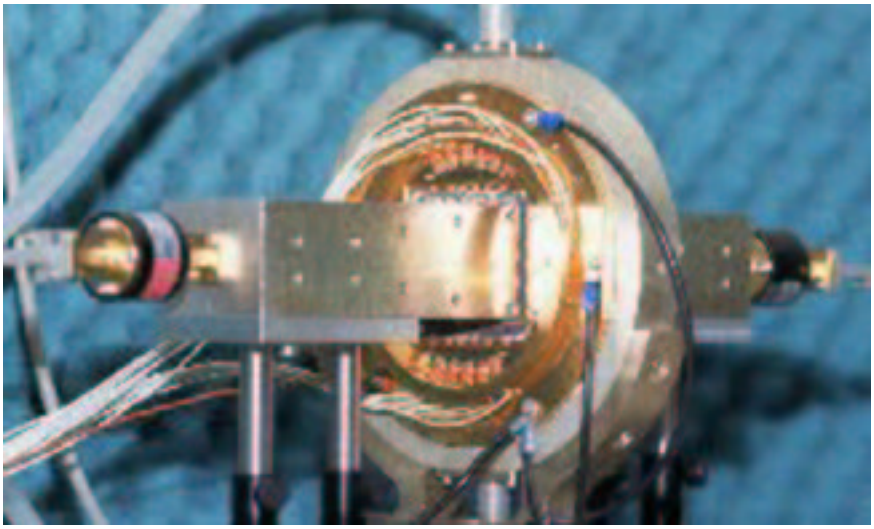

Figure 5.13: A photograph of the 13-element array fed by a hard-horn antenna.

Section 5.1 described the basic configuration of the tile-based arrays using microstrip patch antennas for the radiating elements. This was followed by a discussion of the common unit cell components. In the following subsections, these components will be brought together to complete the unit cell design. In addition, measurements of the unit cell will be given, based on near-field probe measurement techniques as outlined in Chapter 4.

The 13-element array represents a proof of concept design. It was intended to verify the chosen array topology and serve as a basis for future designs. Furthermore, experimental data on the array loss, gain, and unit cell performance could be used to estimate the expected performance of larger arrays. This would give a basis for estimating the number of unit cells necessary to achieve the desired goals of 25 and 50 Watts of radiated power.

Shown in Fig. 5.13 is a photograph of the 13-element tile-based array. This photograph illustrates the array fed by a custom designed hard-horn feed as was illustrated by the measurement setup given in Fig. 4.3 (isolators have been added to the input and output in lieu of directional couplers

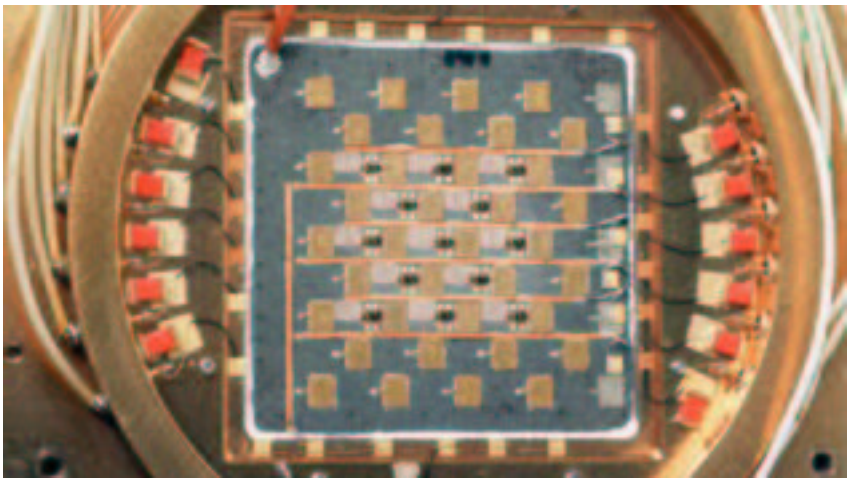

Figure 5.14: A photograph of the input side of the 13-element array.

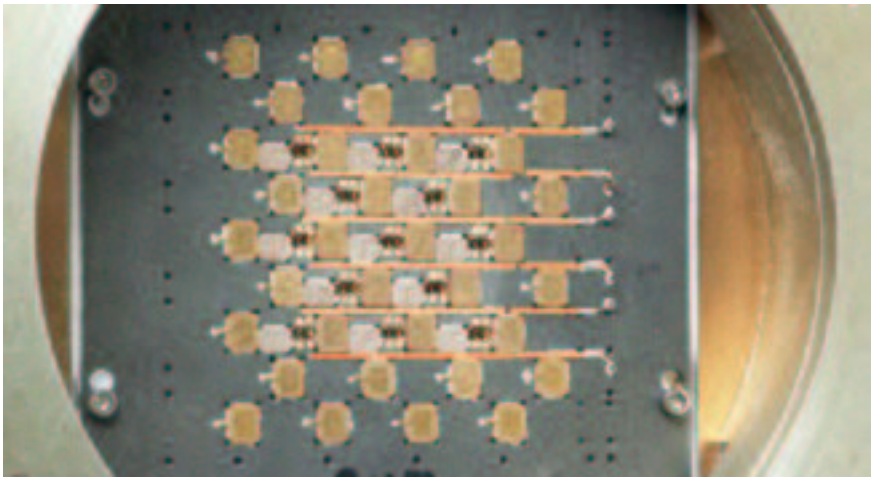

Figure 5.15: A photograph of the output side of the 13-element array.

as shown in Fig. 5.34). In addition, the array is mounted to a heat sink at its periphery. The heat sink consists of a ring carrying a liquid coolant, which enters the top of the ring and flows around to the lower half. The liquid is then pumped through a cooler and recirculate through the ring. The input side and output side of the array is shown in Figs. 5.14 and 5.15, respectively. This liquid cooling of the array allows for sufficient heat removal of the nearly 26 Watts produced by the 26 driver amplifiers (13 on each side).

5.2.1 Unit Cell Design

The 13-element array unit cell is illustrated in Fig. 5.16. This is a photograph of the input side. However, the input and output sides are identical. The unit cell consists of a microstrip patch antenna, which is wire bonded to a Northrop Grumman driver amplifier. The output of the driver is then wire bonded to a 50 Ω microstrip line on *Rogers RT6006*™ substrate (the same material within the thick slot). A microstrip-slot-microstrip transition then couples the energy to the output layer of the array. Finally the signal is amplified by a second driver amplifier and radiated back into free space.

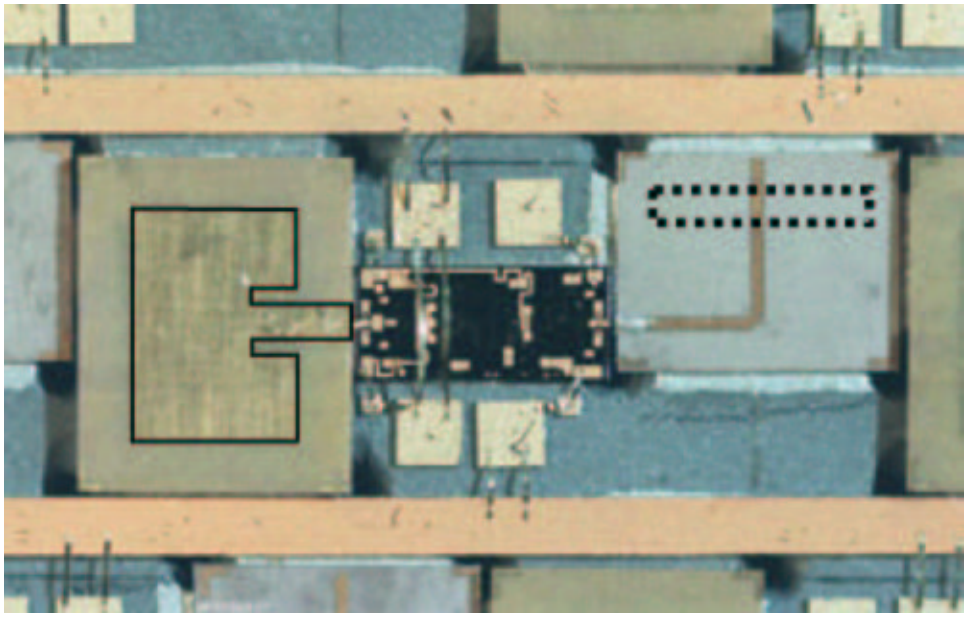

Figure 5.16: A photograph of the 13-element array unit cell.

The unit cell design follows directly from the discussion given in the previous sections. However, there are some differences. Namely, the microstrip patch antenna was slightly larger in resonance length. The parameters for this antenna are given below:

$$\begin{aligned} L &= 2.19 \text{ mm} \\ W &= 3.0 \text{ mm} \\ g &= 0.1 \text{ mm} \\ y_0 &= 0.535 \text{ mm} \\ d &= 0.765 \text{ mm} \\ W_m &= 0.5 \text{ mm} \\ L_d &= 4.53 \text{ mm} \\ W_d &= 3.72 \text{ mm} \end{aligned}$$

This antenna was designed by Eric Schlecht and verified by Sean Ortiz using *HP - Momentum*™ (a planar method of moments program). In addition, a microstrip-slot-microstrip transition was used for the through-plate coupler. The dimensions and design process can be found in Section 5.1.3.

Some notable features of the unit cell layout are illustrated in Fig. 5.16. In particular, the dotted line over the microstrip $\lambda/4$ stub represents the slot through the groundplane. Also, the bars crossing from left to right, above and below the amplifier are the bias lines. These are made of an alumina substrate plated with gold and epoxied to the carbon steel groundplane. All other components are also epoxied to the groundplane using a silver epoxy that compensates for the TCE mismatch between the MMICs and the steel carrier. The 27 and 1000 pF single layer capacitors are also shown, where the larger of the two is 1000 pF.

It should be noted that the microstrip-slot-microstrip transition is perpendicular to the polarization of the electric field incident on the array. This was done for two reasons. First it increased the isolation between the slot aperture and the microstrip patch antenna to ensure amplifier stability. The second reason is to decrease the unit cell size. If the $\lambda/4$ microstrip line remained straight, it would increase the unit cell size.

5.2.2 Unit Cell Measurement Results

The measurement setup can be seen in Fig. 4.17, where waveguide probes are used to measure the gain (amplitude and phase) of each unit cell in the array. The results of this measurement are then used to determine if any amplifiers should be replaced. The probes were place at a distance of approximately 2.54 mm from the groundplane and centered with respect to the microstrip patch antenna.

A typical gain measurement for one of the unit cells is shown in Fig. 5.17. It should be noted that this is a relative measurement and is for the comparison of unit cell performance only. The other unit cells were also measured. Any defective cells were replaced. The resulting array provided a variation in gain of ± 2 dB and a variation in phase of $\pm 30^{\circ}$. The unit cell can provide approximately 26 dB under small signal conditions at this frequency. However, there is some loss between the waveguide probe to microstrip patch interface. This loss is approximately 2 dB from the input of the antenna to the input of the waveguide probe. Two such transitions give approximately 4 dB of loss. The additional loss can be attributed to the microstrip-slot-microstrip transition. This component was difficult to fabricate, and variations in this fabrication process greatly effect the performance of the transition. This is the main reason that a coaxial interconnect was later chosen.

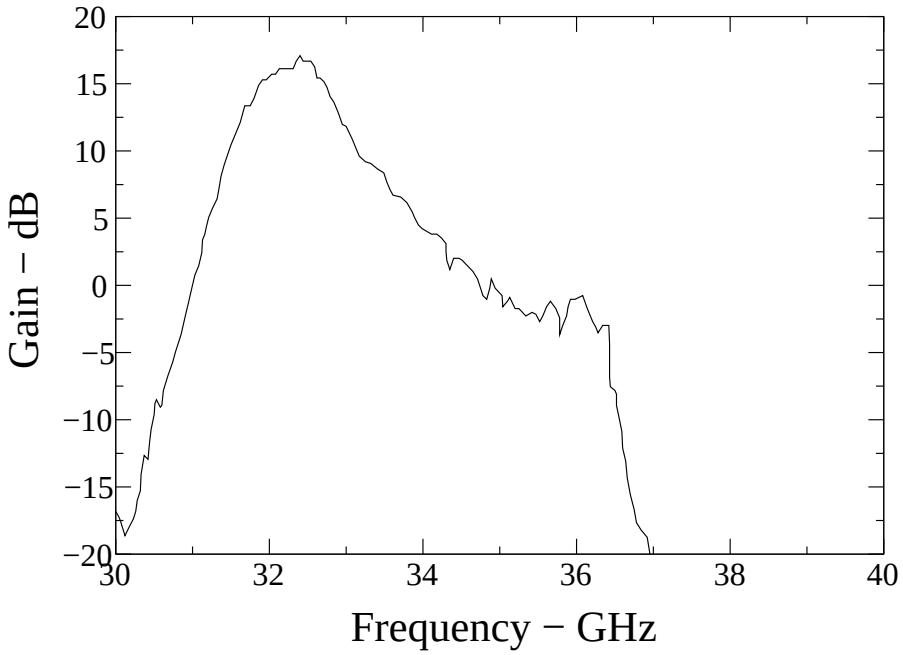

Figure 5.17: The gain of unit cell in the 13-element array measured with waveguide probes.

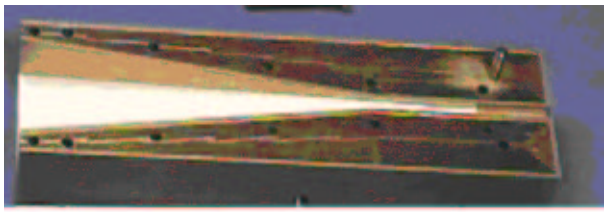

Figure 5.18: A photograph of half of the hard-horn used in the 13-element array.

5.2.3 Hard-Horn Feed

The hard-horn feed with lens was designed and fabricated for the 13-element array with an aperture size of 39.37 x 29.972 mm. The resulting horn is shown in Fig. 5.18, where half of the horn is displayed. The dimensions of this horn are as follows:

$$\begin{aligned} a_1 &= 39.37 \text{ mm} \\ b_1 &= 29.972 \text{ mm} \\ \rho_1 &= 92.92 \text{ mm} \\ \phi_1 &= 8.09^\circ \\ \rho_2 &= 139.91 \text{ mm} \end{aligned}$$

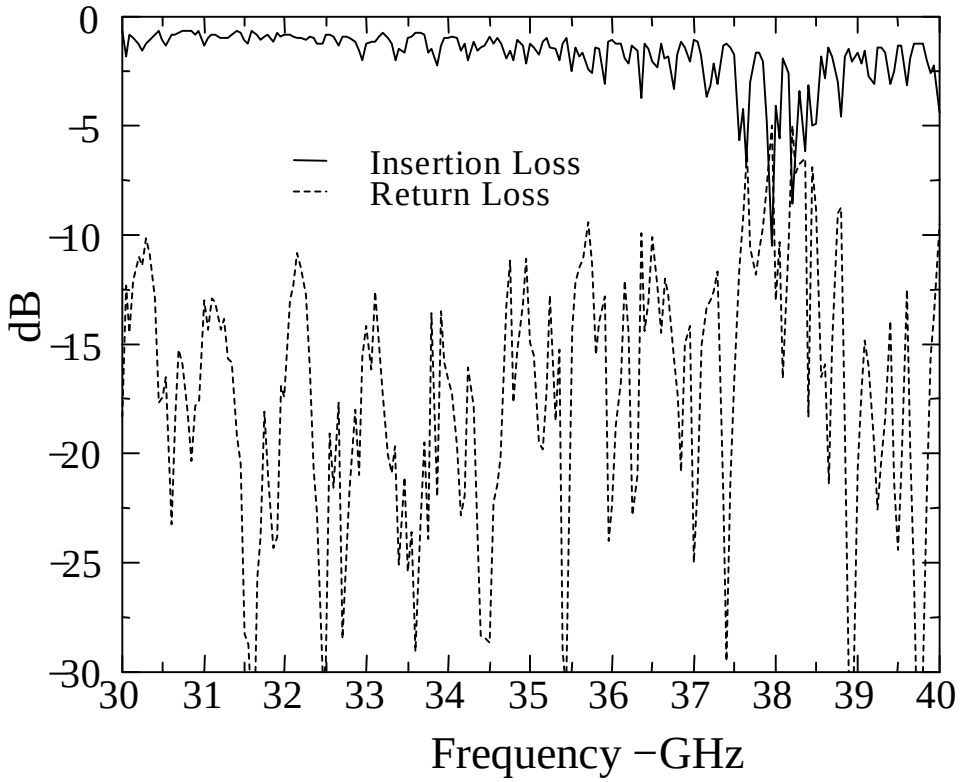

Figure 5.19: The insertion loss and return loss of the hard-horn for the 13-element array in a back-to-back configuration.

$$\phi_2 \;=\; 8.01^\circ$$

where a definition of these dimensions is given in Figs. 3.3(a) and 3.3(b). In addition, a dielectric material with an $\epsilon_r = 1.4$ and thickness of 4.572 mm was used along the sidewalls. The lens was fabricated from a foam dielectric with an $\epsilon_r = 1.14$. The resulting hard-horn with lens was measured in a back-to-back configuration, and the results are shown in Fig. 5.19. An insertion loss of less than 1.25 dB was obtained from 30.5 to 33 GHz. In addition, the return loss was below 10 dB over the entire band of interest.

5.2.4 Array Measurement Results

The 13-element spatial power amplifier was measured in a test setup capable of testing QO amplifiers, unit-cells and hard-horns, illustrated by Fig. 5.13. The amplifier array was tested with the addition of a collecting hard-horn to facilitate measurements. The measured small signal gain of the amplifier with the extra hard-horn is 18 dB and is shown in Fig. 5.20. This gives approxi-

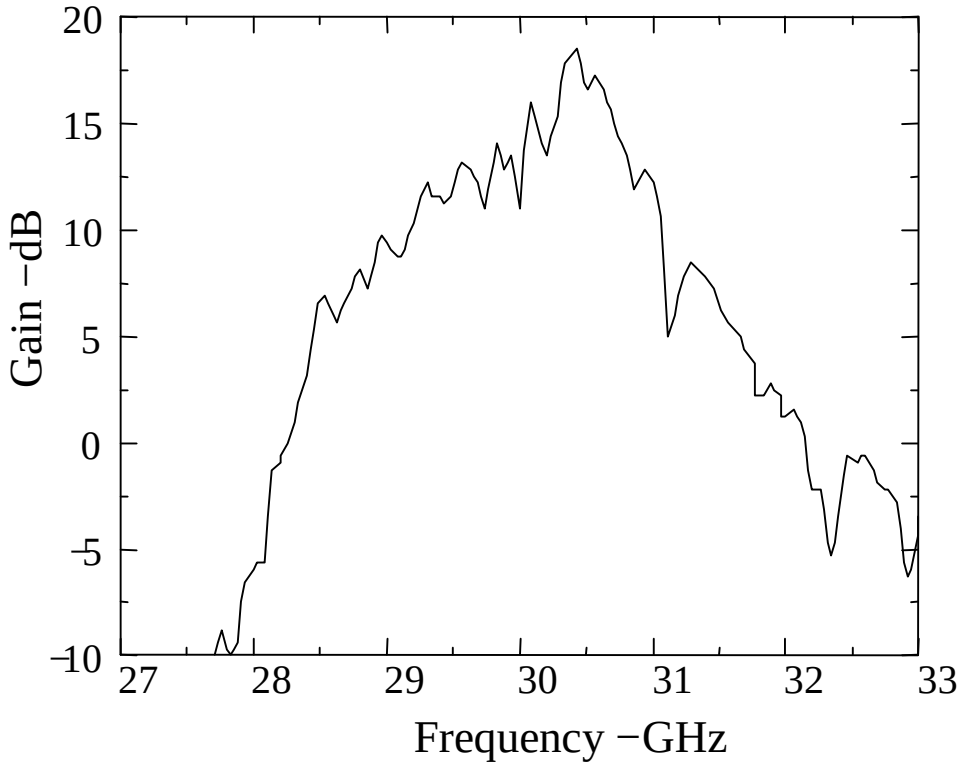

Figure 5.20: The small signal gain of the 13-element array.

mately 8 dB less gain than expected, since the two driver amplifiers provide a total of 26 dB. However, the hard-horns in a back-to-back configuration provide approximately 1 dB of loss, while the microstrip-slot-microstrip transition simulation yield nearly 1 dB of loss. The remaining 6 dB of unaccounted loss is due to the array spacing and antenna efficiency losses discussed is Chapter 4.

In addition to the small signal gain measurements, a large signal power compression measurement was taken. The large signal gain under 2-dB compression was 16 dB with a total output power of approximately 4 Watts.

5.3 A 45-Element Array

The 13-element array provided a framework in which to build a larger and more powerful 25 Watt array. The 25 Watts of radiated power was one of the main objectives of this work. In addition, the array was required to provide a minimum of 20 Watts, CW, of radiated power at Ka-band (10 dB gain and 1 GHz, 3-dB bandwidth). A spatial power combining approach was chosen for its capability to produce high output power levels. As has been mentioned, the power combining efficiency is limited by the array's element spacing, the efficiency of the radiating elements, and any

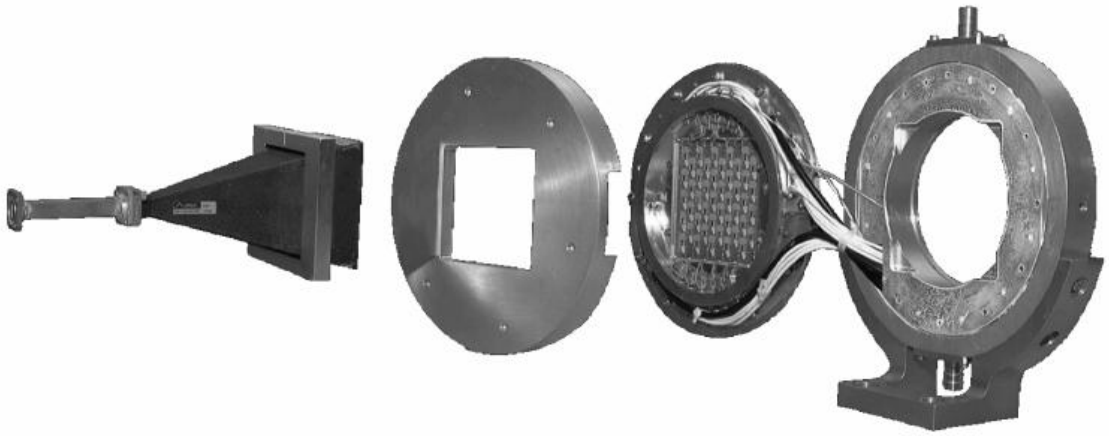

Figure 5.21: A photograph of the 45-element array fed by a hard-horn antenna.

matching networks between the amplifiers and the antennas, assuming that each of the radiators are excited at the same power level and the same phase. In order to develop a system meeting these requirements, some fundamental decisions had to be made concerning the choice of array topology and method of heat removal.

Again, several spatial amplifier topologies were considered in the development of the amplifier array. These included CPW-fed slot arrays and microstrip patch arrays on both thin and thick metal carriers. A microstrip patch array was chosen for its simplicity and unidirectional radiation. Also, a microstrip patch array can use a thicker groundplane, which serves as the heat sink for the MMIC amplifiers. The choice of the array feed was also an integral part of the system topology and was greatly influenced by the size requirements. In addition, the array feed, consisting of the hard-horn and lens, must provide a uniform amplitude and phase distribution to each element of the array.

In order to provide the 25 Watts of radiated power, an appropriate array size must be chosen based upon expected and measured unit cell performance, which is limited at best by the antenna's radiation efficiency. Based on [89, 104], the best expected efficiency for a microstrip patch antenna is 94% at Ka-band using a 0.381 mm thick *Rogers TMM3*™ substrate, which corresponds to very little loss (less than 0.5 dB). However, antenna simulations, using *Agilent* - *HFSS*™, and measurements give an efficiency of 73%, which corresponds to 1.4 dB of loss at 34 GHz. The antenna efficiency was mentioned previously in the section 5.1.1. The reduced efficiency is most likely due to the finite size substrate and the wire bond between the antenna and the amplifier. Assuming a minimum loss of 1.4 dB, an array containing 45, 1 Watt unit cells should provide in excess of 30 Watts of radiated power. As previously mentioned, a triangular lattice layout was chosen to accommodate the amplifier circuitry, while minimizing losses due to non-ideal radiator spacing in the array. This configuration is illustrated in Fig. 5.21, which details a perspective view of the amplifier array fed by a hard-horn. In most ways, this configuration is the same as that of the

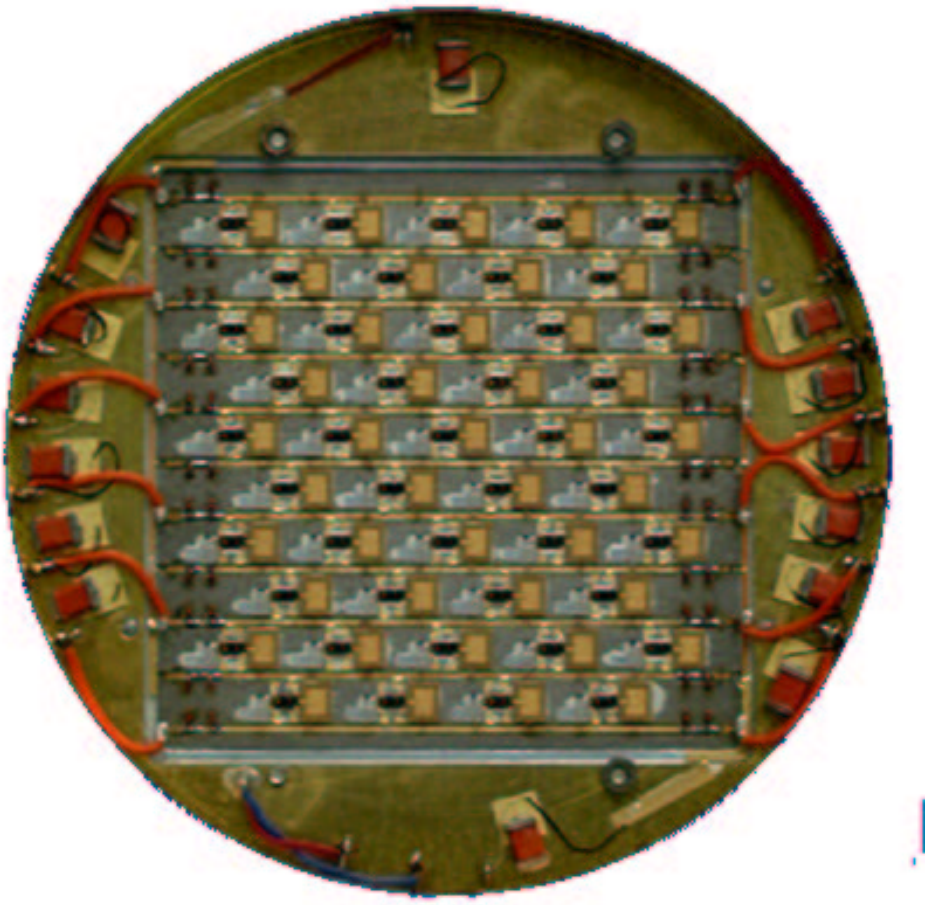

Figure 5.22: A photograph of the input side of the 45-element array.

13-element array. This includes the use of the same cooling ring around the periphery of the array. However, different hard-horns were fabricated to feed the 25-element array, since the array occupied a larger area. Also power amplifiers were placed on the output layer to provide higher output power levels. These modifications are better illustrated by the photographs of the input and output sides of the arrays, Figs. 5.22 and 5.23, respectively.

A thermal analysis for the 45-element array was also performed to determine the plate thickness to achieve a temperature gradient across the array of less than 25°C, which was found to be 0.254 cm (carbon-steel). The thermal simulation was performed using *SINDA* from *C&R Technologies* and *MSC PATRAN* for the pre- and post-processing. As with the 13-element array, liquid cooling was utilized around the periphery of the array to further dissipate heat.

In the following sections, the unit cell design of the 45-element array will be discussed. This is similar to the 13-element array. However, there are some noticeable differences. The measurement

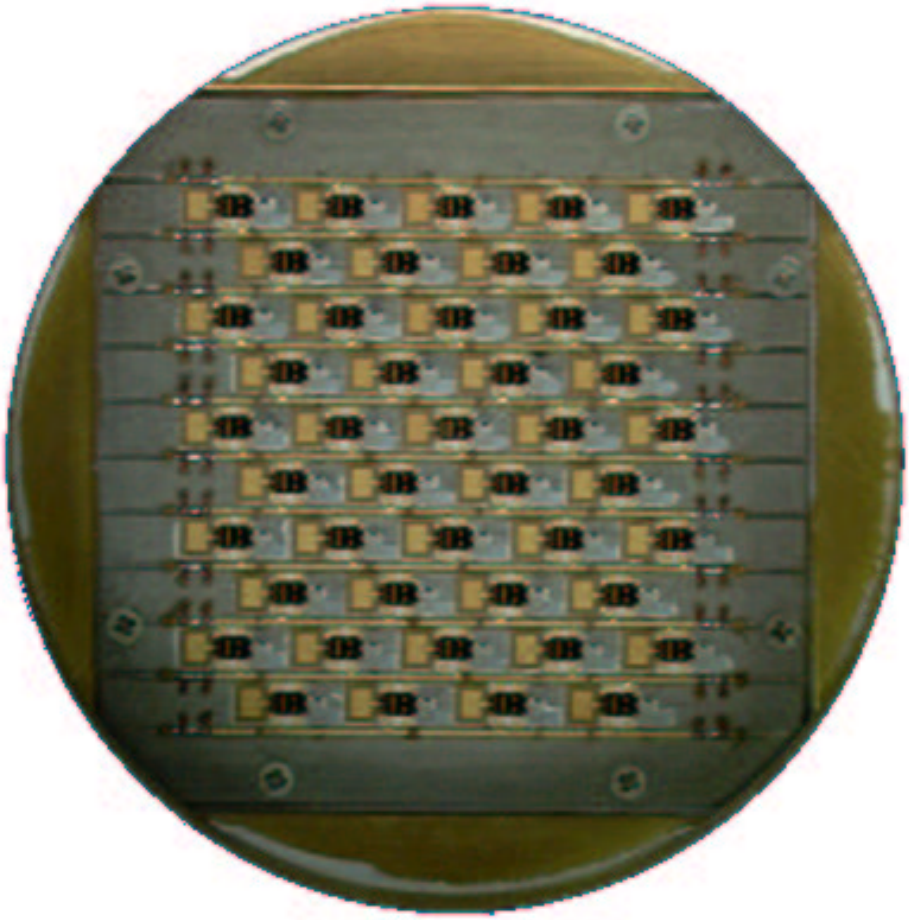

Figure 5.23: A photograph of the output side of the 45-element array.

results will then be given for the unit cell as well as for the active and passive arrays.

5.3.1 Unit Cell Design

The 45-element array unit cell consists of a receiving microstrip patch antenna, driver amplifier, coaxial through-plate transition, power amplifier, and transmitting microstrip patch antenna. In addition, a microstrip delay line has been added to the unit cell layout for unit cell phase adjustment. These components are illustrated in the figures of the input and output unit cells, Figs. 5.24 and 5.25, respectively.

Most of the components are placed in the same manner as with the 13-element array. However, some basic modifications were made. The same basic unit cell was simply improved. First, the

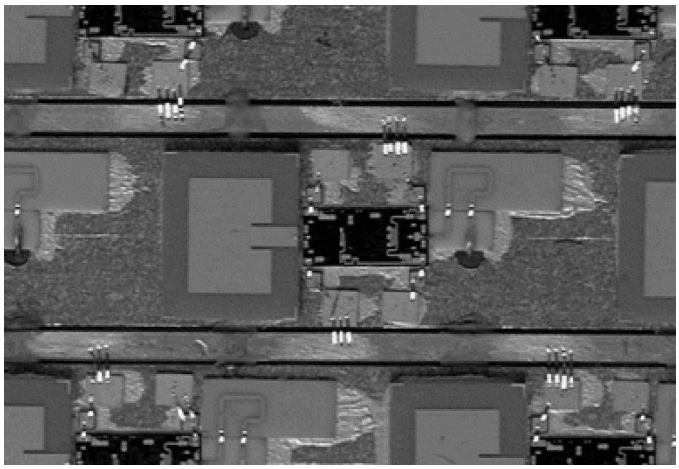

Figure 5.24: A photograph of the input unit cell of the 45-element array.

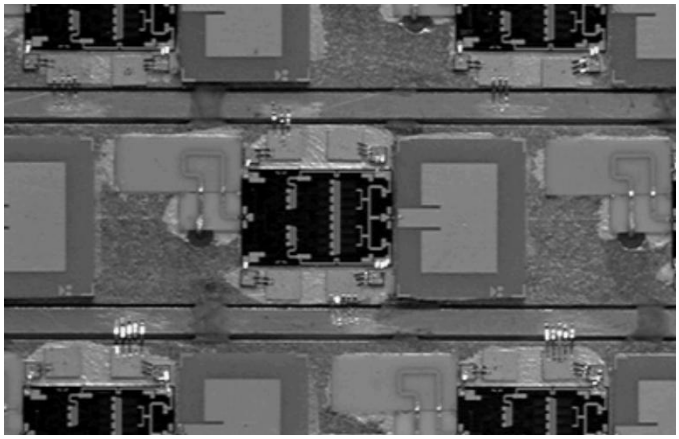

Figure 5.25: A photograph of the output unit cell of the 45-element array.

microstrip patch antenna was redesigned to have a higher resonant frequency. This is the same design that was discussed in Section 5.1.1 and involved the use of better models. Secondly, the microstrip-slot-microstrip transition was replaced by the coaxial through-plate transition, given in Section 5.1.3. By replacing the microstrip-slot-microstrip transition, more space was made available between the amplifier and the microstrip patch antenna. It was decided that the additional space would be best utilized by a delay line. This is simply a microstrip transmission line that can be replaced in order to adjust the phase of the unit cell after characterization. This is illustrated in the photograph of the unit cell by a "U" shaped section of microstrip line between the amplifier and the coaxial through-plate transition.

On the output side of the array, the driver amplifier was replaced by the power amplifier, in order to obtain more power. The biasing scheme remained the same. All of the previously mentioned

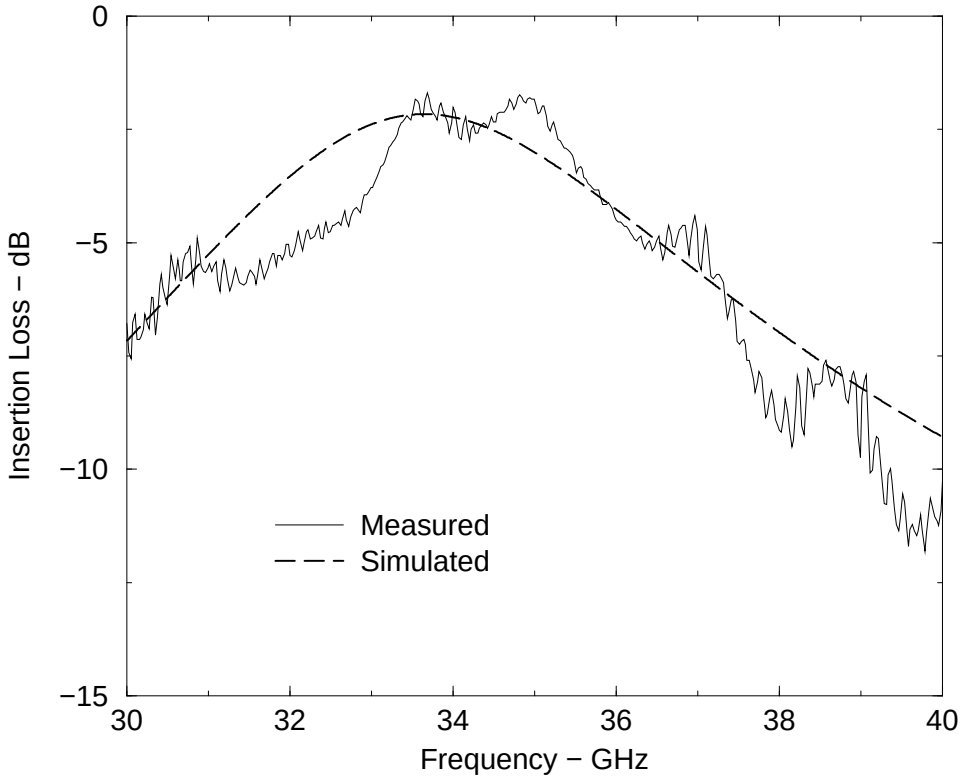

Figure 5.26: The insertion loss from the waveguide probe to the microstrip patch antenna with a separation of 2.54 mm.

capacitor values were again used. The only change made to the biasing circuitry was the use of channels to place the bias lines within. Each bias line was placed in a groove cut into the groundplane, such that the top of the bias line was flush with the groundplane of the antennas. This change was made to further reduce coupling between the bias lines and the microstrip patch antennas.

5.3.2 Unit Cell Measurement Results

Several experiments were performed to evaluate the performance of the 45-element amplifier array, including measurements to determine the individual performance of the unit cells. The unit cell performance was verified through measurements of the individual microstrip patch antennas and measurements of the passive and active unit cells using WR28 waveguide probes as shown in Fig. 4.17. Following these, experiments, a passive and active version of the 45-element array was fabricated and measured, including the small and large signal gain and power compression.

The resonant frequency of the microstrip patch antenna was measured first and was shown in

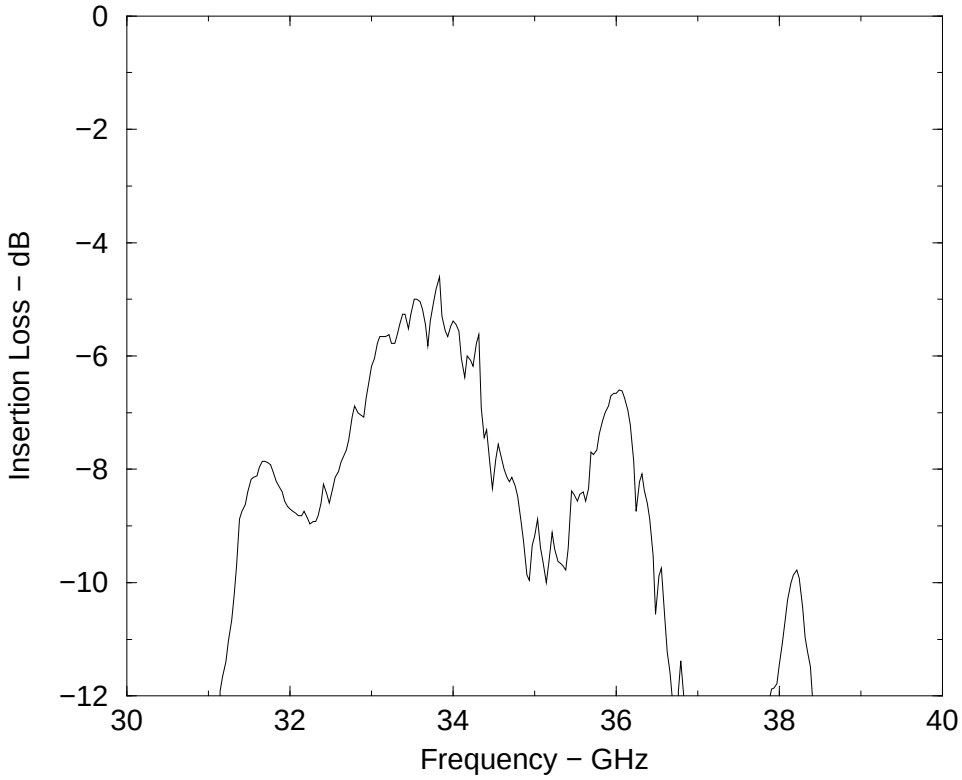

Figure 5.27: The insertion loss of the passive unit cell measured with waveguide probes at a separation of 2.54 mm.

Fig. 5.4, where it is compared with the simulated results from *Agilent - HFSS*™. In order to characterize the performance (amplitude and phase variations) of each unit cell in both the active and passive arrays, an automatic measurement system was developed. The details were given in Section 4.2.2 for the array characterization, where two waveguide probes were placed in the near-field of the input and output antennas of each individual unit cell. By measuring the loss and phase of each cell, bad cells could be replaced or repaired. In addition, the phase of the active unit cells could be adjusted to compensate for amplifier variations. However, the effect of these probes on the antenna's return loss was investigated before performing any unit cell measurements. For this procedure, the input impedance of the microstrip patch antenna was measured with a waveguide probe (WR28) placed at a distance of 2.54 mm above the groundplane and centered with respect to the microstrip patch antenna as shown previously in Fig. 4.19. The coupling from the microstrip patch antenna to the waveguide probe was also measured and is shown in Fig. 5.26 along with the same structure simulated with *Agilent - HFSS*™. Good agreement can be seen between the simulated and measured insertion loss. Since the return loss of the unit cell was not adversely affected, this method was used to determine the relative phase and amplitude variations between individual unit cells.

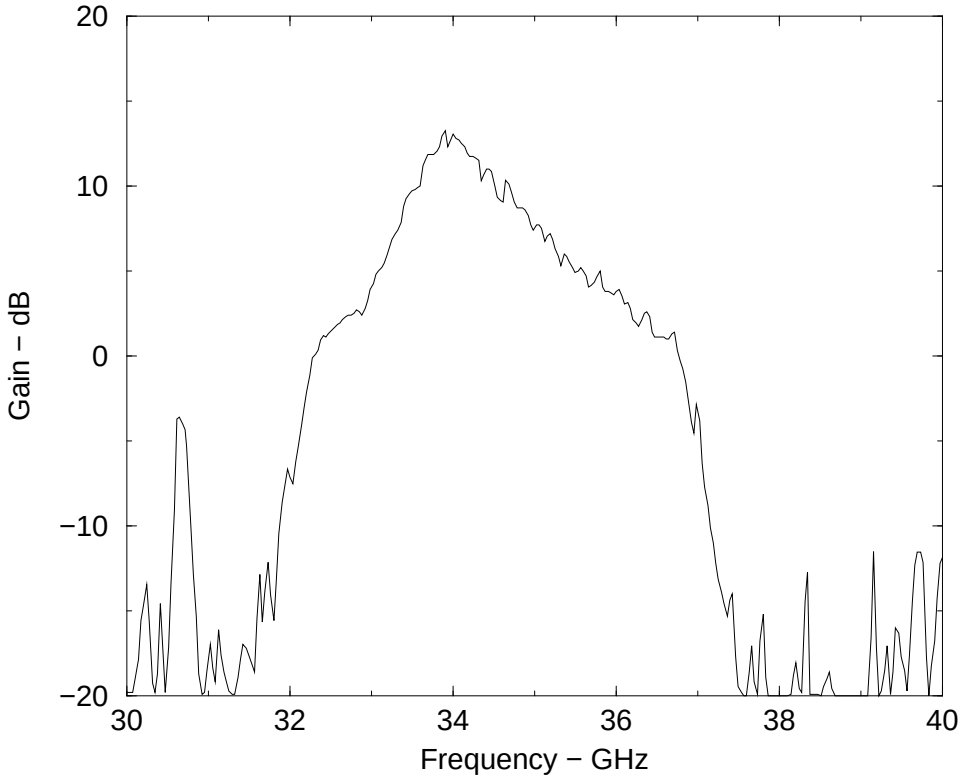

Figure 5.28: The gain of the active unit cell measured with waveguide probes at a separation of 2.54 mm from the patch antennas.

The passive unit cell, consisting of the antennas, delay lines, through-plate coaxial line, and through lines for the amplifiers, was measured using waveguide probes as shown in Fig. 4.17. Each waveguide was placed at a distance of 2.54 mm from the antenna's groundplane and centered with respect to the antennas. The active unit cell was measured in the same manner as the passive unit cell. Results for both the passive and active unit cells are shown in Figs. 5.27 and 5.28, respectively. The passive unit cell insertion loss is 5 dB, which is consistent with the losses expected from two waveguide to microstrip patch antenna transitions (4 dB) and the through-plate coaxial line with the microstrip circuitry (less than 1 dB). The active unit cell provided 13 dB of small signal gain at 33.9 GHz, which is lower than the 15 dB of gain expected from two amplifiers, including the losses of the passive unit cell. The additional losses are due to device variations, which vary by ± 1.5 dB from the nominal gain, and from amplifier/circuit mismatches.

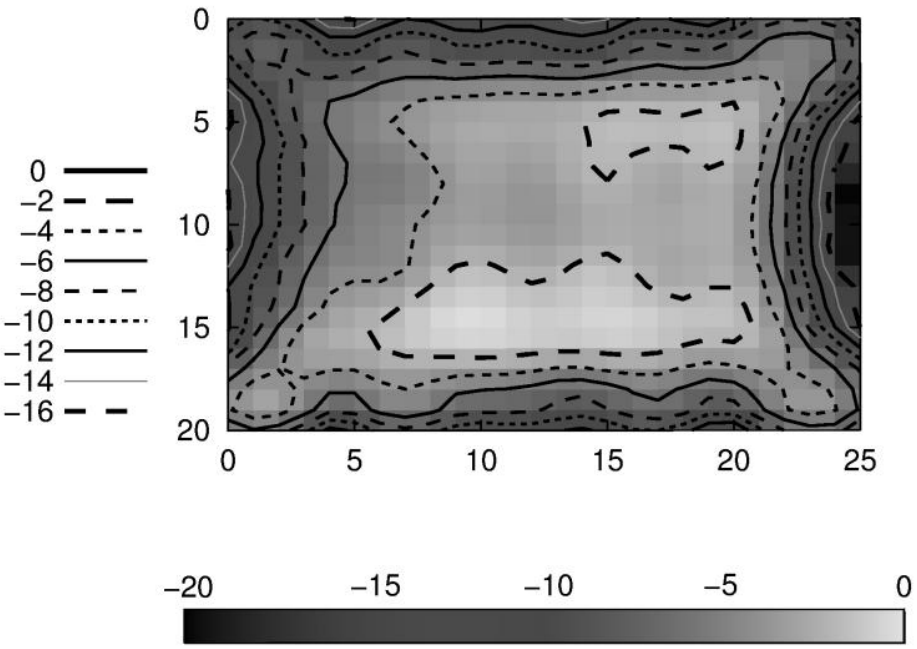

Figure 5.29: The amplitude distribution of the hard-horn for the 45-element array at 34 GHz.

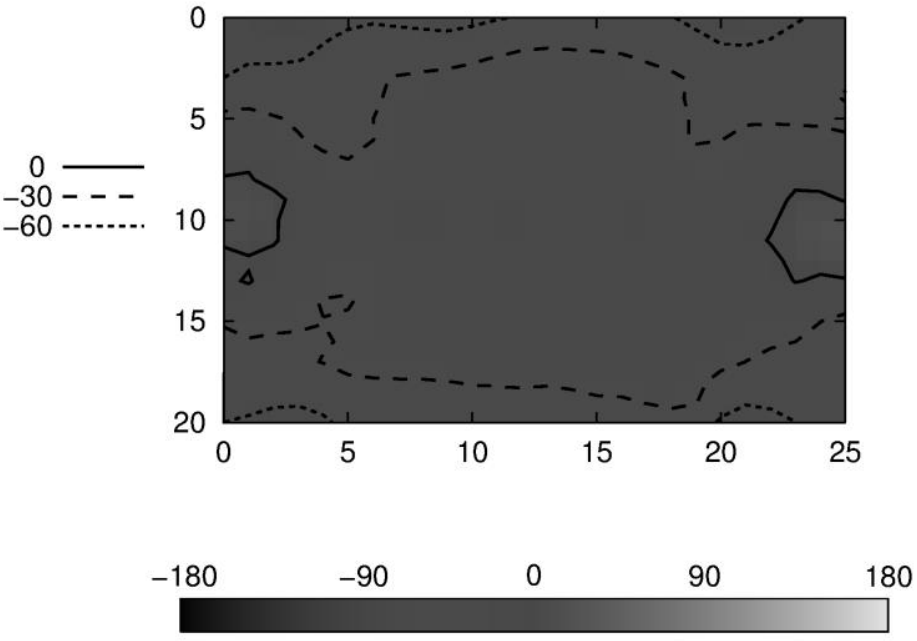

Figure 5.30: The phase distribution of the hard-horn for the 45-element array at 34 GHz.

5.3.3 Hard-Horn Feed

The hard-horn feed used with the 45-element array was shown on the left side of Fig. 5.21. This feed was actually a standard gain horn from *Millitech*™, which was dielectrically loaded on the sidewalls. The dimensions of this horn are as follows:

$$\begin{aligned} a_1 &= 39.37 \text{ mm} \\ b_1 &= 29.972 \text{ mm} \\ \rho_1 &= 92.92 \text{ mm} \\ \phi_1 &= 8.09^\circ \\ \rho_2 &= 139.91 \text{ mm} \\ \phi_2 &= 8.01^\circ \end{aligned}$$

where a definition of these dimensions is given in Figs. 3.3(a) and 3.3(b). The associated normalized near-field power and phase distributions for this horn at 34 GHz are shown in Figs. 5.29 and 5.30, respectively. Figs. 5.31 and 5.32 show the normalized near-field amplitude and phase distributions for the horns without the lens or dielectrically loaded sidewalls at 34 GHz. The horns were modeled using a mode-matching program as outlined in [94]. In addition, a dielectric material with an $\epsilon_r = 2.2$ and thickness of 2.032 mm was used along the sidewalls. The lens was fabricated from a foam dielectric with an $\epsilon_r = 1.2$. The resulting hard-horn with lens was measured in a back-to-back configuration, and the results are shown in Fig. 5.33. An insertion loss of less than 3 dB was obtained from 30 to 35 GHz. In addition, the return loss was below 10 dB over this entire band.

5.3.4 Array Measurement Results

Several measurements were performed on both a passive and active version of the 45-element array, both having a unit cell size of 7.8 mm in the diagonal direction. In both cases, each unit cell was measured as outlined previously and modified if necessary. In addition, unit cells giving little or no gain were checked for loose bondwires. If the bondwires were good, the amplifiers were replaced. A deviation in phase from one unit cell to another was corrected by changing the delay lines in the unit cells. Once all the unit cells gave a phase variation of less than $\pm 15^\circ$ and gain variation of less than ± 2 dB, the performance of the array could be measured.

The active and passive arrays were placed between two hard-horn feeds located approximately 2.54 mm from the antenna's groundplane to characterize their performance as was illustrated in Fig. 4.3. The insertion loss of the passive array including the feeding and collecting horns was found to be approximately 10 dB at 35 GHz, while the active array provided 10 dB of small signal gain at 34 GHz and almost 7 dB of gain under 3-dB compression at 34 GHz with a 3-dB bandwidth of over 800 MHz in both cases. As mentioned, both measurements were calibrated from the hard-horn feed waveguide inputs, and thus include the losses of the two horns.

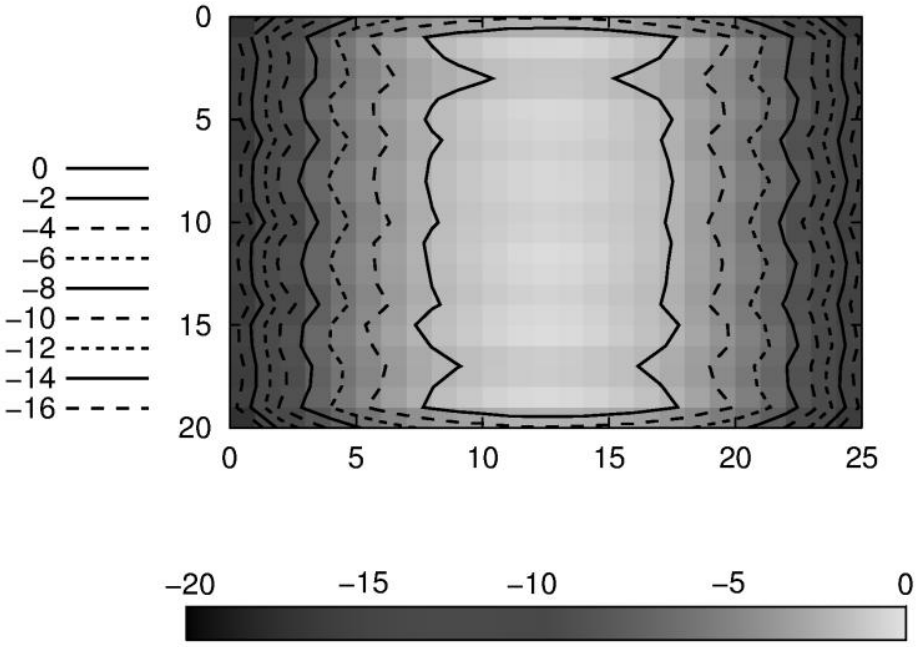

Figure 5.31: The amplitude distribution of a non-hardened horn at 34 GHz.

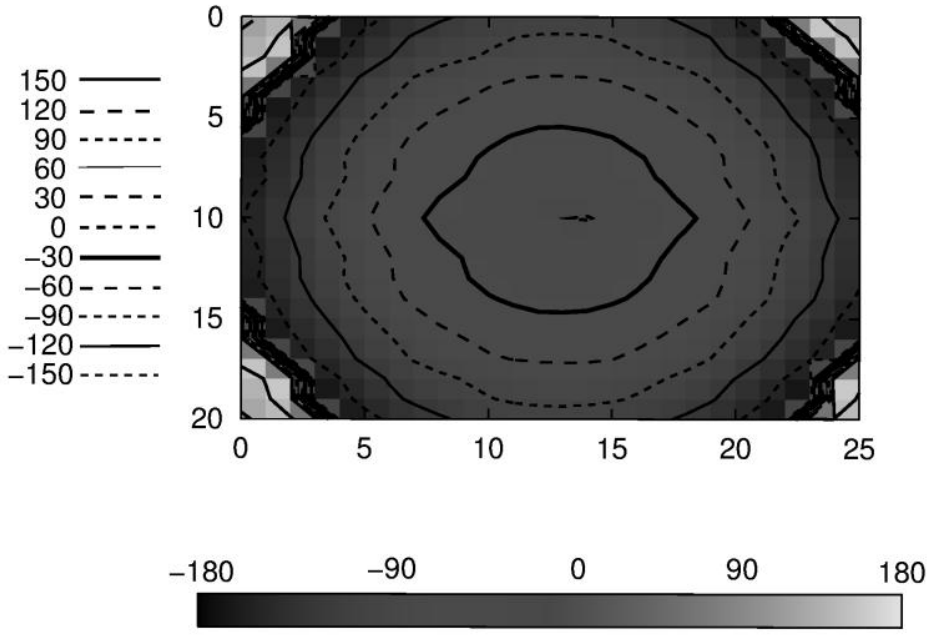

Figure 5.32: The phase distribution of a non-hardened horn at 34 GHz.

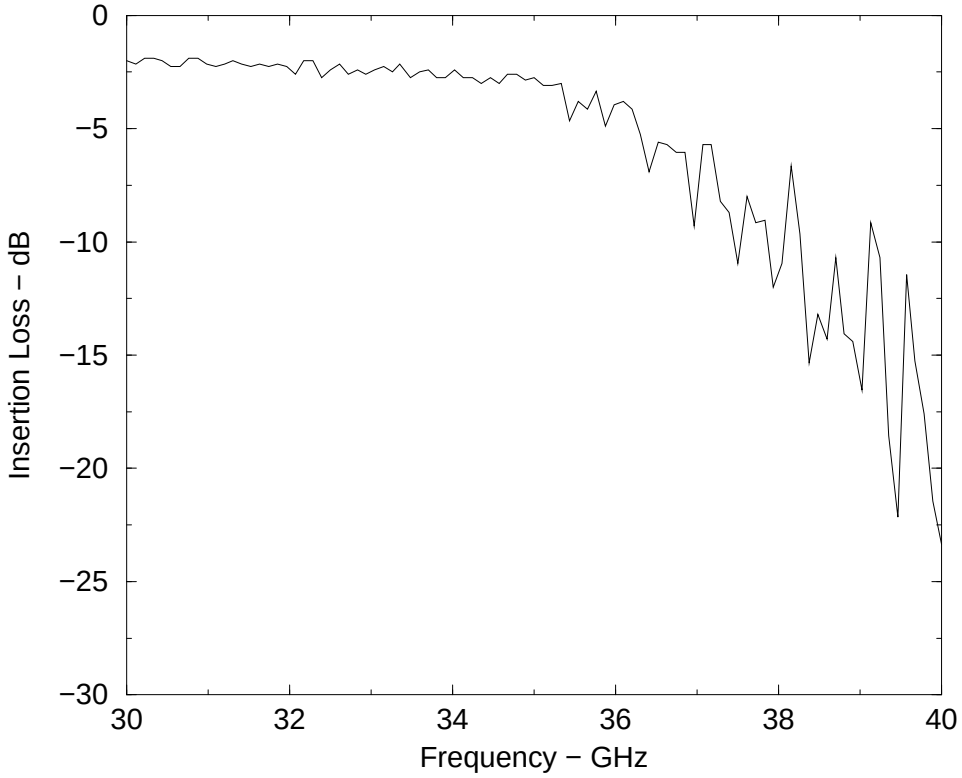

Figure 5.33: The insertion loss of the two hard-horns placed back-to-back.

An estimate of the radiated power was necessary, not having the availability of a far-field measurement system. The radiated power was calculated by subtracting the loss associated with the power combining portion of the system from the collected output power. The loss associated with the power combining portion of the system is the insertion loss of the passive array (10 dB) minus the losses associated with the unit cell (3.8 dB), including losses associated with the antenna efficiency, microstrip lines, and through-plate coaxial transition, divided by two. This gives approximately 3 dB of loss associated with the power combining portion of the system at 34 GHz. The losses of the antennas are considered as part of the amplifier and are not taken into account as part of the collecting losses. Using this calculation, the radiated 3-dB compression power was 44 dBm or nearly 25 Watts at 34 GHz as shown in Fig. 5.36. This provides an estimated PAE of 7.5% under 3-dB compression with a power combining efficiency of 56%. Fig. 5.35 shows the radiated power of the 45-element array under 3-dB compression (34 dBm input power) versus frequency.

The near-field pattern of the active amplifier array was also measured. From these measurements, the far-field radiation pattern of the arrays was calculated using *PCAAD*™ as shown in Figs. 5.37 and 5.38. This calculation was performed by weighting the magnitude and phase of each patch antenna excitation within the simulation by the normalized magnitude and phase of the measured near-field distribution at the location of each antenna. Both the E-plane and H-plane radiation

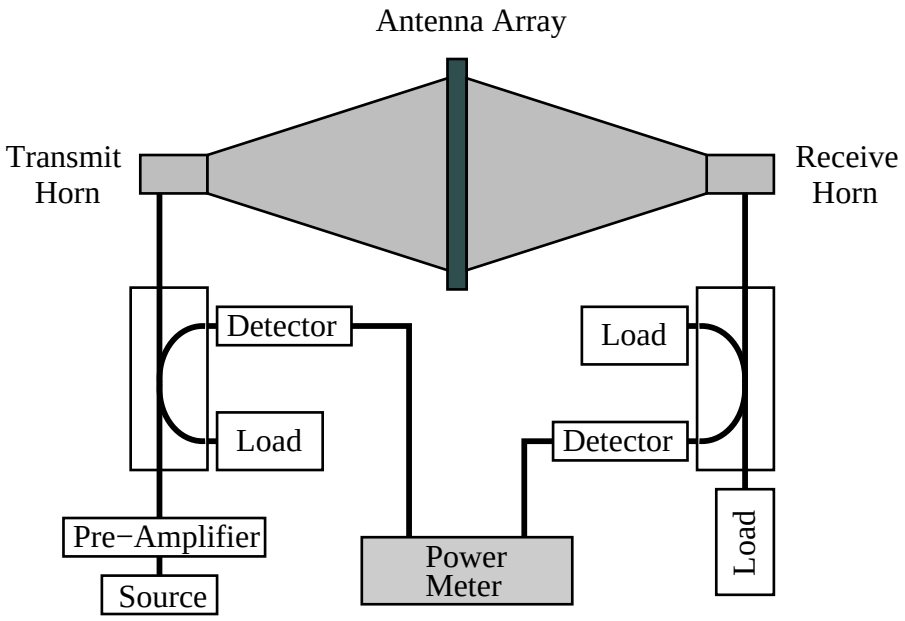

Figure 5.34: The power compression measurement setup for a spatial amplifier array.

patterns agree well with simulated radiation patterns of an array of the same dimensions but with equal magnitude and phase excitation of the elements.

5.4 A 98-Element Array

The 98-element array was designed to provide in excess of 50 Watts of radiated power at Ka-band. To achieve this goal, the same architecture that successfully achieved the 25 Watts of radiated power was further scaled to 98-elements. Only two major changes were made between the two designs. First, the groundplane thickness was increased to 12.7 mm. Secondly, the unit cell spacing was changed slightly to allow more space for thicker bias lines (this is expected to increase the array loss). The other components (antennas, amplifiers, capacitors, coaxial lines, and phase adjusters) remained the same. Two photographs of the new array are shown in Figs. 5.39 and 5.40.

The groundplane thickness was increased to 12.7 mm due to thermal problems with the previous design. In addition, the cooling methodology was completely revised by placing tubes within the center of the groundplane. Each was formed by drilling a hole through the solid copper groundplane. Two tubes pass between adjacent rows of coaxial through-plate couplers as illustrated in Fig. 5.41. In addition, a manifold is connected on either edge of the groundplane to disperse and collect the liquid coolant to the 30 tubes, each with a diameter of 3.9624 mm and spacing of 5.969 mm. As with the 45-element array, the coolant was circulated through a refrigerator to

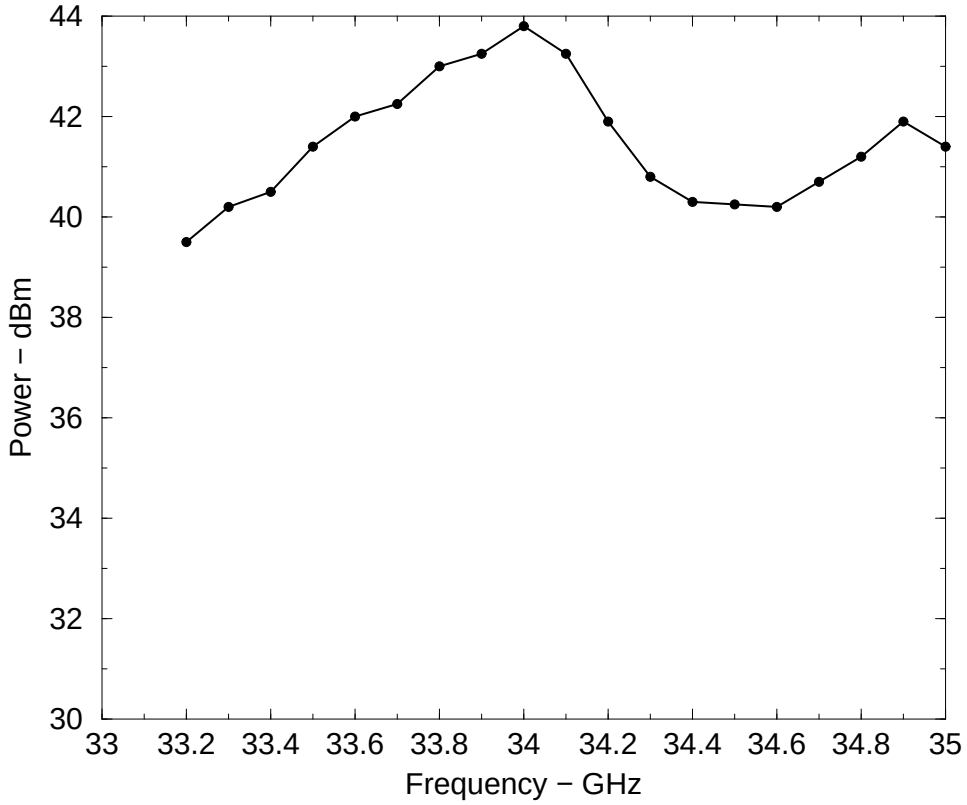

Figure 5.35: The radiated output power of the 45-element array under 3 dB compression.

remove the heat. This refrigerator is capable of dissipating nearly 1 kW of energy.

The array spacing was increased to a total of 8.44 mm. This will effectively increase the insertion loss of the array as compared to the previous 45-element design. However, the small increase should not impact the loss significantly. The increased groundplane thickness also changed the length of the coaxial line connecting the input and output layers. The details were discussed in Section 5.1.3. It will increase the loss of the transition by nearly 1 dB when compared to the 45-element array.

In the following sections, the unit cell design, hard-horn design, and array performance will be discussed. The discussion of the unit cell will be brief, since it is basically the same design as in the 45-element array. The resulting design of the hard-horn will include measurement results of both the near-field pattern and back-to-back insertion loss. Finally, the measurement results will be given for the 98-element array. These results will not be extensive, since this project was not fully completed at the time of this writing.

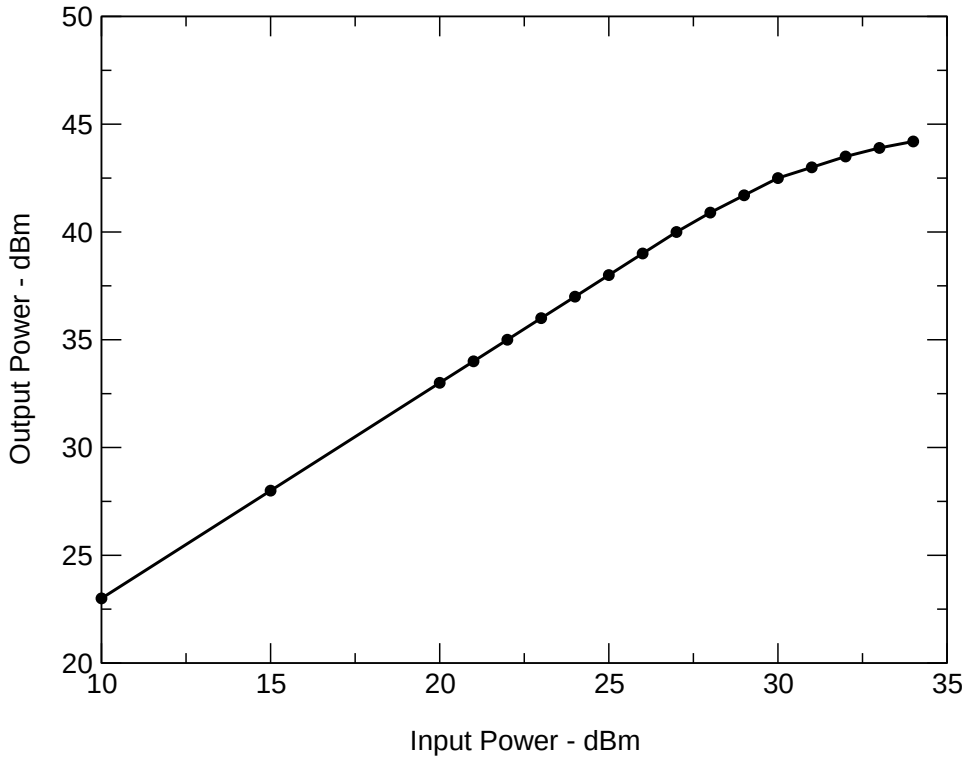

Figure 5.36: The output power versus input power for the 45-element array at 34 GHz.

5.4.1 Unit Cell Design

As with the other unit cell designs, the 98-element array unit cell contains a receiving microstrip patch antenna, a driver amplifier, through-plate coaxial transition, a power amplifier, and a radiating microstrip patch antenna. In addition, a microstrip delay line has also been added to correct the phase of the unit cell after constructing the array. A photograph of the 98-element array unit cell is shown in Fig.5.42.

It should be noted that no oscillations were observed any of the three arrays, using this unit cell layout. In addition to the well placed biasing capacitors, much of this stability is due to the large separation distance between the radiating elements and the amplifiers. Also, the use of the finite size substrates improves the isolation between the antennas and bias lines. One last feature, which has aided in stability, is the recessed bias lines located between the microstrip patch antennas (running orthogonal to the polarization of the electric field radiated by the antennas). By recessing the bias lines, coupling is minimized. However, a smaller array spacing would have been possible if these bias lines were formed with a thicker metal plating, allowing the width of the bias line to be decreased.

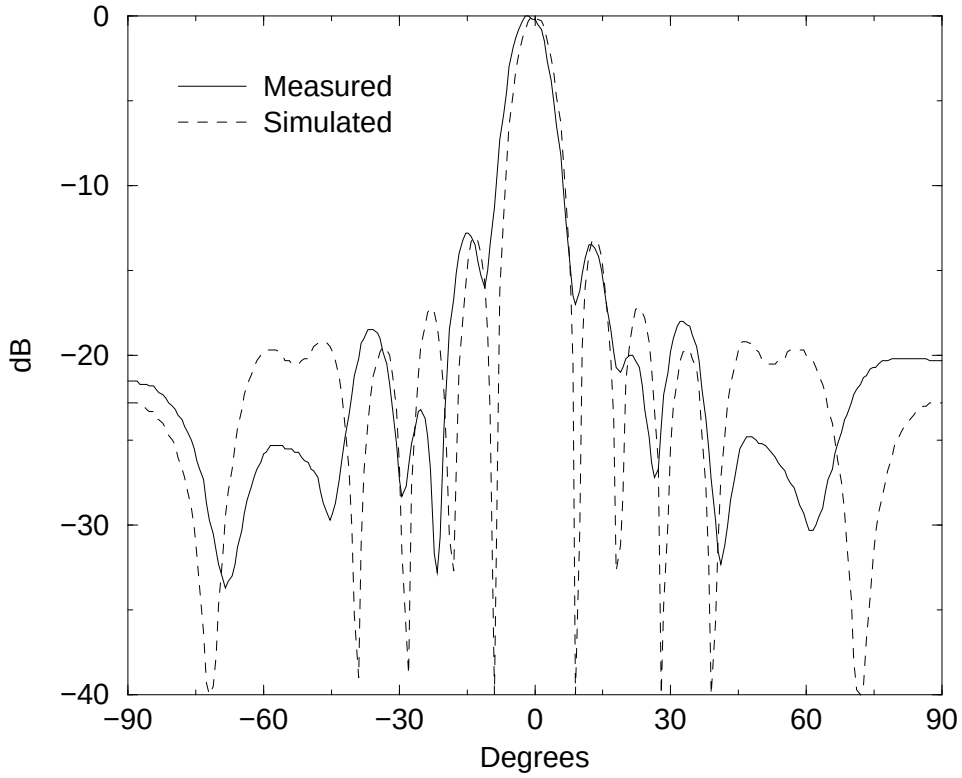

Figure 5.37: The E-plane radiation pattern of the 45-element amplifier array.

5.4.2 Hard-Horn Feed

The 98-element array required rather large hard-horn feeds to provide the uniform magnitude and phase distribution necessary for coherent and efficient power combining. These hard-horns were designed in the same manner as was outlined in Section 3.1. A photograph of the hard-horns exciting the 98-element array was shown in Fig. 5.39. Each horn was formed from two pieces with the division occurring along the center y-axis (axis of maximum E_y field intensity), and each halve was formed by welding smaller pieces of aluminum together to form the completed part. This method of fabrication creates larger variations in the horn dimensions and is therefore not recommended. However, it is a more economical to implement and creates a lighter horn (compared to a horn machined from two pieces of solid metal). The final dimensions of the horn are as follows:

$$\begin{aligned} a_1 &= 105.41 \text{ mm} \\ b_1 &= 86.868 \text{ mm} \\ \rho_1 &= 332.6 \text{ mm} \\ \phi_1 &= 7.44^\circ \end{aligned}$$

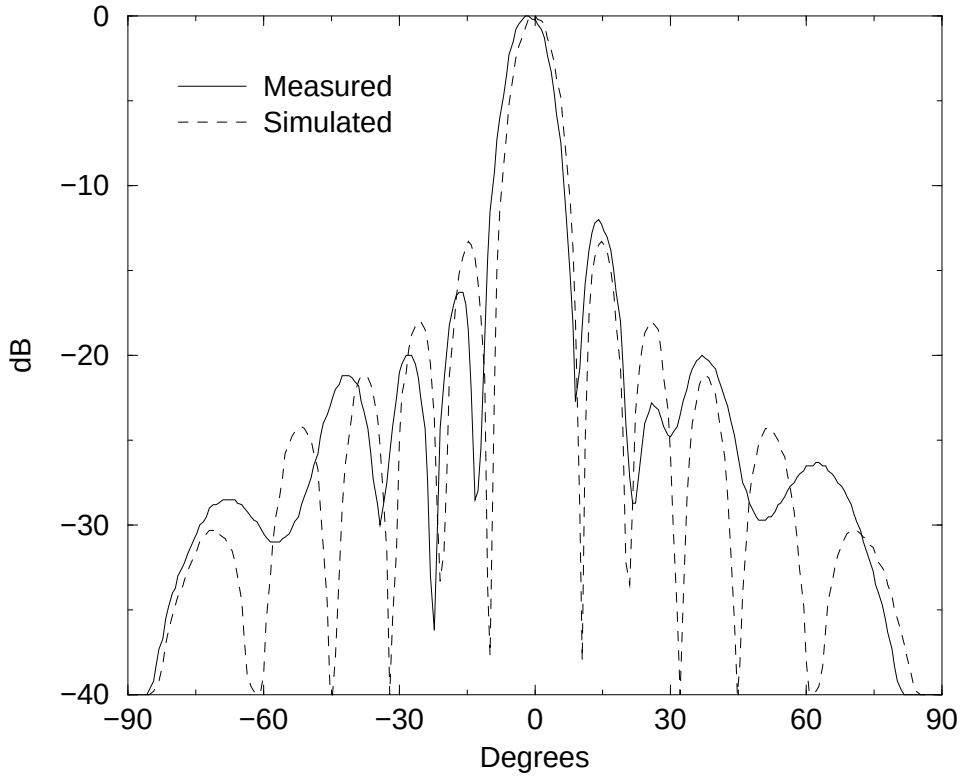

Figure 5.38: The H-plane radiation pattern of the 45-element amplifier array.

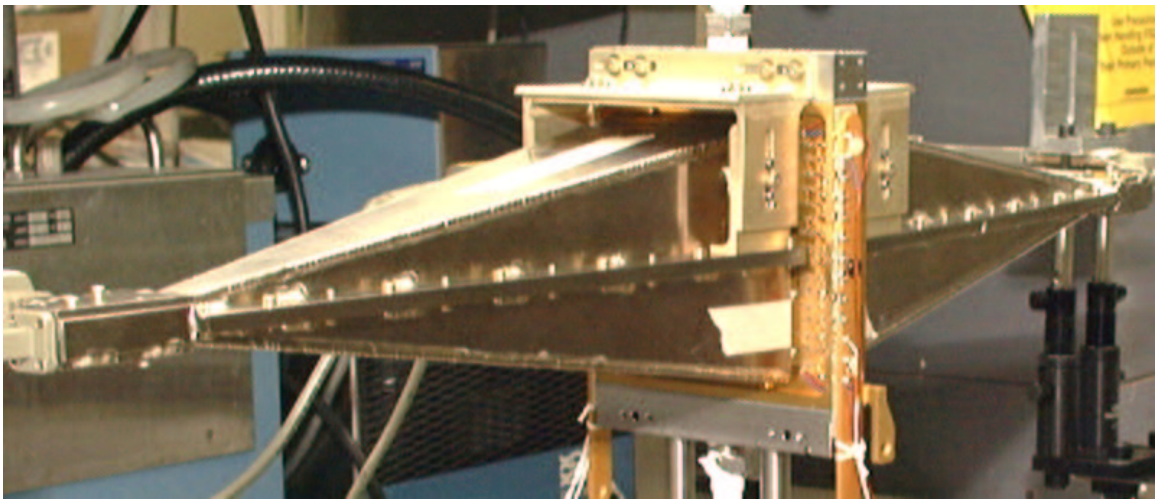

Figure 5.39: A photograph of the 98-element amplifier array with hard-horn feeds.

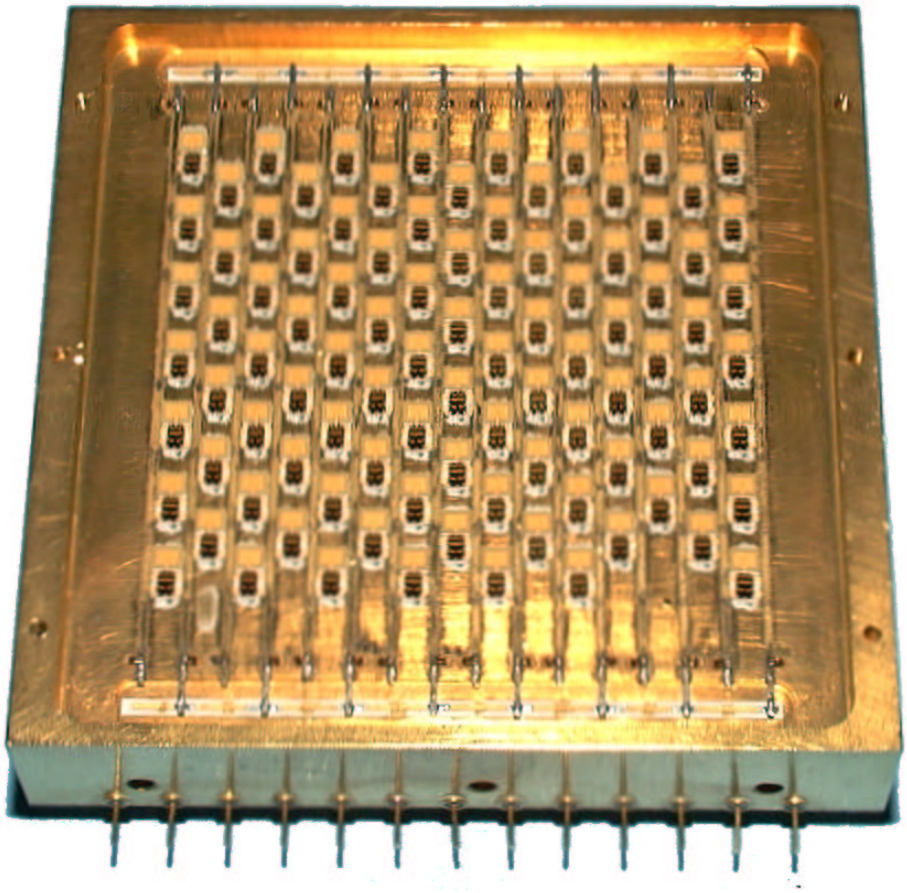

Figure 5.40: A photograph of the output side of the 98-element amplifier array.

$$\begin{aligned} \rho_2 &= 330.2 \text{ mm} \\ \phi_2 &= 9.44^\circ \end{aligned}$$

where a definition of these dimensions is given in Figs. 3.3(a) and 3.3(b). The dielectric sidewalls are formed from a dielectric material with an $\epsilon_r = 2.2$ and thickness of 2.032 mm was used along the sidewalls. The lens was fabricated from rexolite with an $\epsilon_r = 2.53$.

The associated normalized near-field power and phase distributions for this horn at 34 GHz are shown Figs. 5.43 and 5.44, respectively. The near-field amplitude and phase distribution of the same horns without being hardened are shown in Figs. 5.45 and 5.46, respectively. The near-field distribution shows a slight over-moding of the horns about the y-axis. This is caused by variations in the horn dimensions and discontinuities within the horn due to machining errors. In addition, both the hardened and un-hardened horns exhibit the same behavior. The hard-horn with lens was measured in a back-to-back configuration, and the results are shown in Fig. 5.47. An average

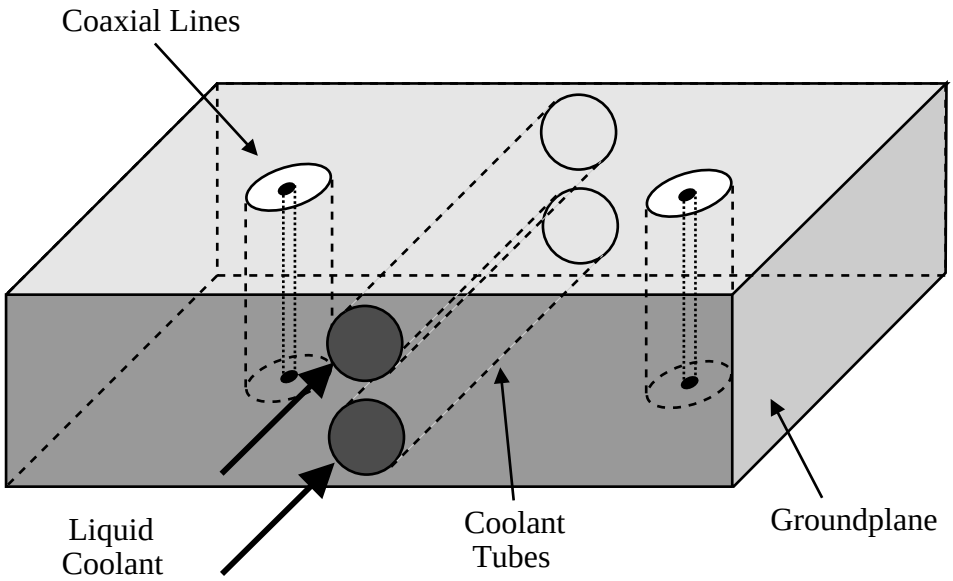

Figure 5.41: The liquid cooling tubes placed within the groundplane of the 98-element array.

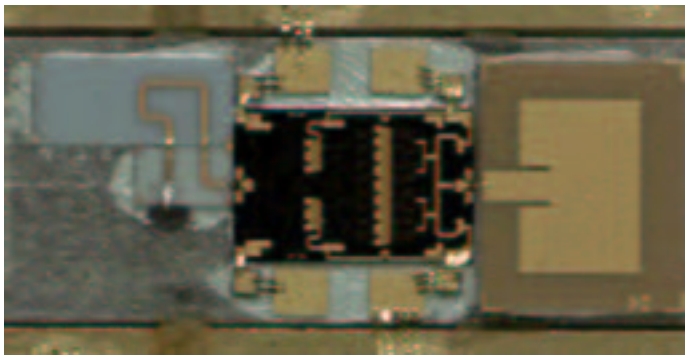

Figure 5.42: A photograph of the output unitcell of the 98-element array.

insertion loss of less than 4 dB was obtained from 32 to 34.5 GHz. In addition, the return loss was below 10 dB over this entire band.

5.4.3 Array Measurement Results

Two measurements have been performed on the active 98-element array, thus far. This includes the small signal gain and the output power versus input power. Both measurements were performed using the measurement setup shown in Fig. 5.39. In the case of the small signal gain measurement, the amplifier array gain, including hard-horn feeds, was measured using a scalar network analyzer

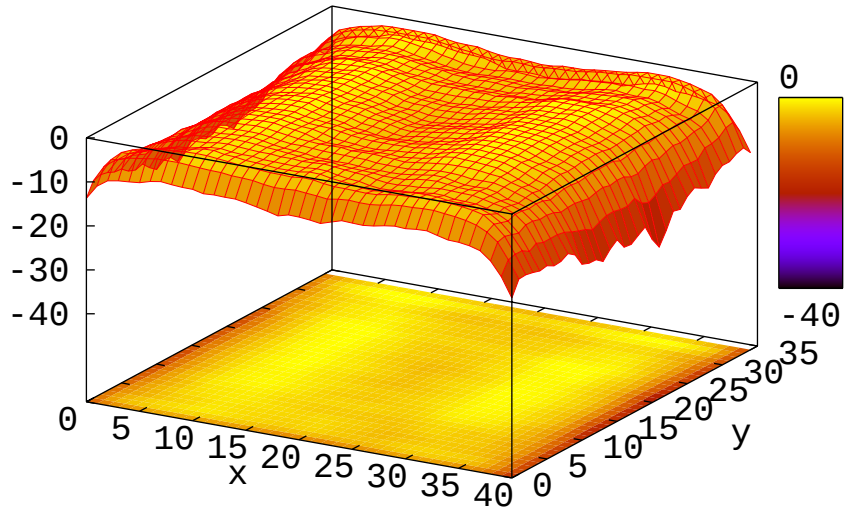

Figure 5.43: The amplitude distribution of the 98-elment array hard-horn at 34 GHz.

and is shown in Fig. 5.48. Only the transmission gain was measured, since directional couplers were used at the output to protect the equipment from damage (the possibility of oscillations, although unlikely, may cause in excess of 50 Watts to be radiated). The measurement results gave nearly 5.3 dB of gain at 33.5 GHz with a 3-dB bandwidth of 700 MHz. This is less than the 10 dB of gain measured with the 45-element array. However, the hard-horn feeds contributed an additional 1.5 dB of loss, and the array spacing and through-plate coupler were changed from the previous array. Also, it should be noticed that the resonant frequency of the array has shifted 0.5 GHz down in frequency from the 45-element design. This is believed to be caused by a combination of the change in array spacing and the increased through-plate coupler length.

The power compression measurement was performed with an input and output hard-horn feed as illustrated in Fig. 5.34. An additional pre-amplifier was used to provide the 36.5 dBm input power necessary to compress the 98-element array. In addition, a directional coupler was used at the input and output to sample the input and output power, respectively. Both the input and output power were measured using a power meter, simultaneously. Also, a spectrum analyzer was used to observe the integrity of the signal (i.e. verify that oscillations were not occurring). The resulting power compression curve is shown in Fig. 5.49. A collected power of 40.5 dBm or 11.2 Watts was obtained under 1-dB compression. We were unable to fully compress the amplifier by 3 dB, because of the pre-amplifiers limited power output. The total DC power consumption of the 98-element array was 800 Watts under compression (a significant amount of heat to be dissipated). We were very happy to observe good dissipation of the heat by the cooling system. Finally, the

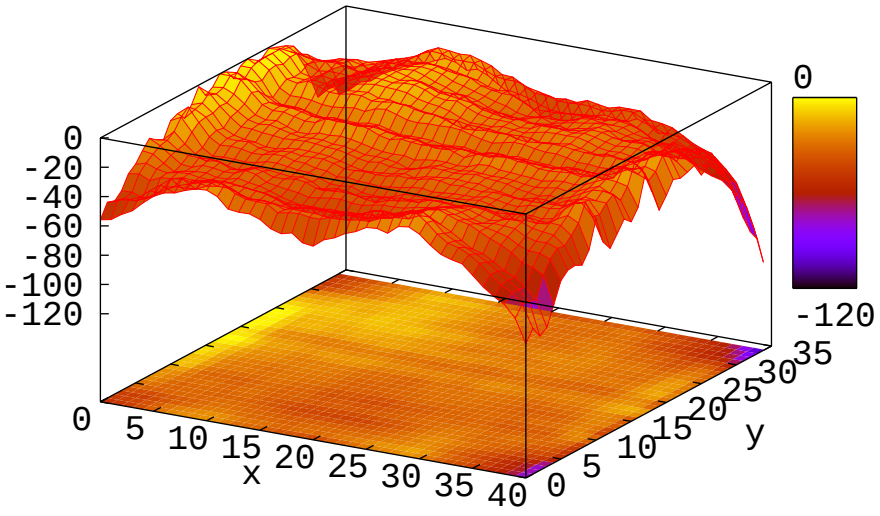

Figure 5.44: The phase distribution of the 98-element array hard-horn at 34 GHz.

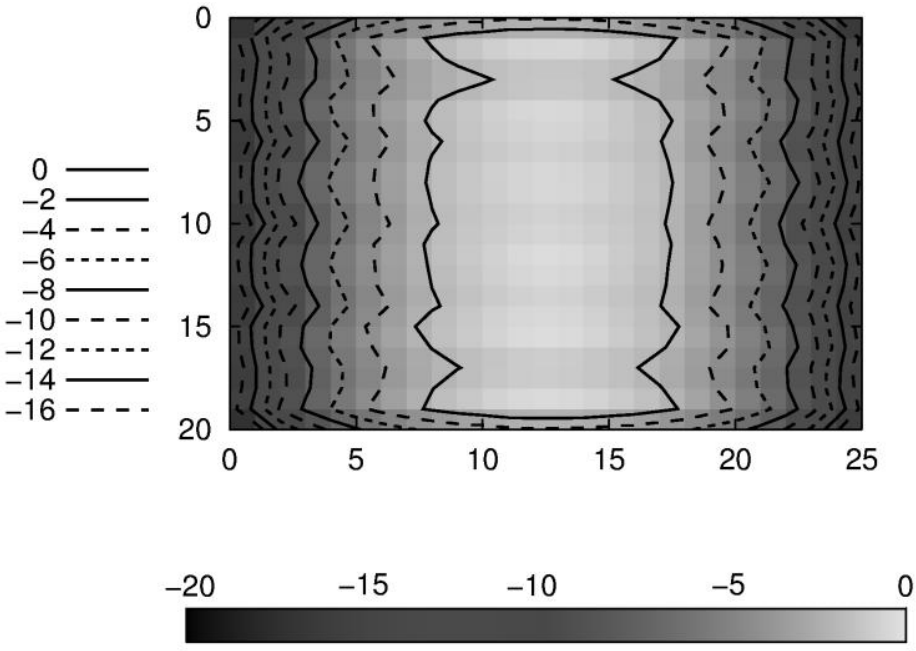

Figure 5.45: The amplitude distribution of a non-hardened horn at 34 GHz.

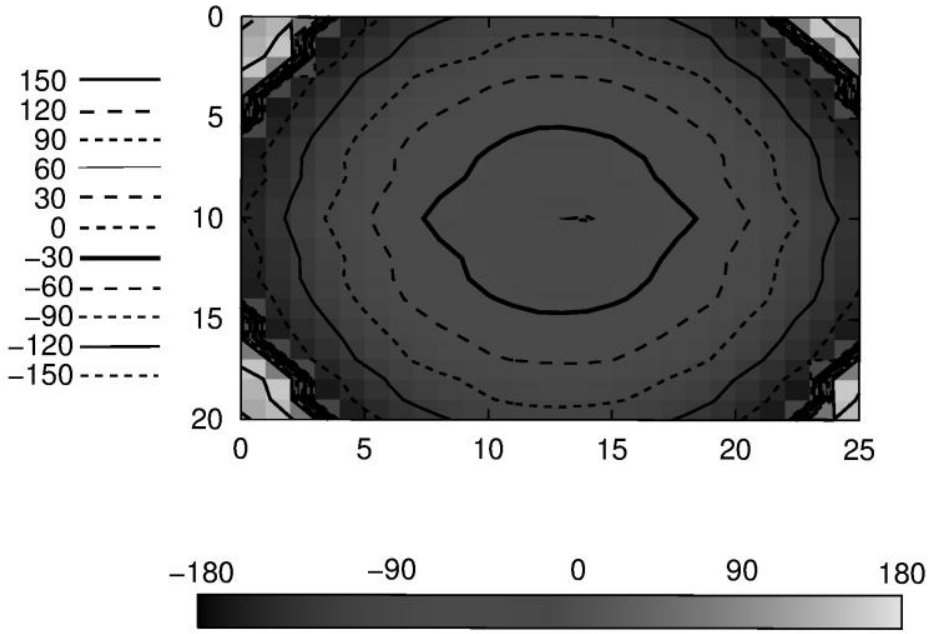

Figure 5.46: The phase distribution of a non-hardened horn at 34 GHz.

power added efficiency of the array was 8.4% under 1-dB compression.

Further measurements have not been performed, due to the time constraints on the project. This includes the measurement of each unit cell throughout the array for the purpose of detecting improper unit cell performance, as was done in the 45-element array. In addition, the radiation pattern of the 98-element array is desired. This would allow for the calculation of the directivity. Furthermore, the radiated power may be calculated by using this directivity in conjunction with measurements of the radiated power received by some known antenna in the far-field.

Future work should also attempt to shift the center frequency of operation from 33.5 GHz to 34 GHz. This is of critical importance, since the power amplifier gain begins to roll-off at the lower frequencies, most likely affecting both the small signal gain as well as power output. The frequency shift may be accomplished by either replacing the microstrip patch antennas or possibly by modifying the antennas in place.

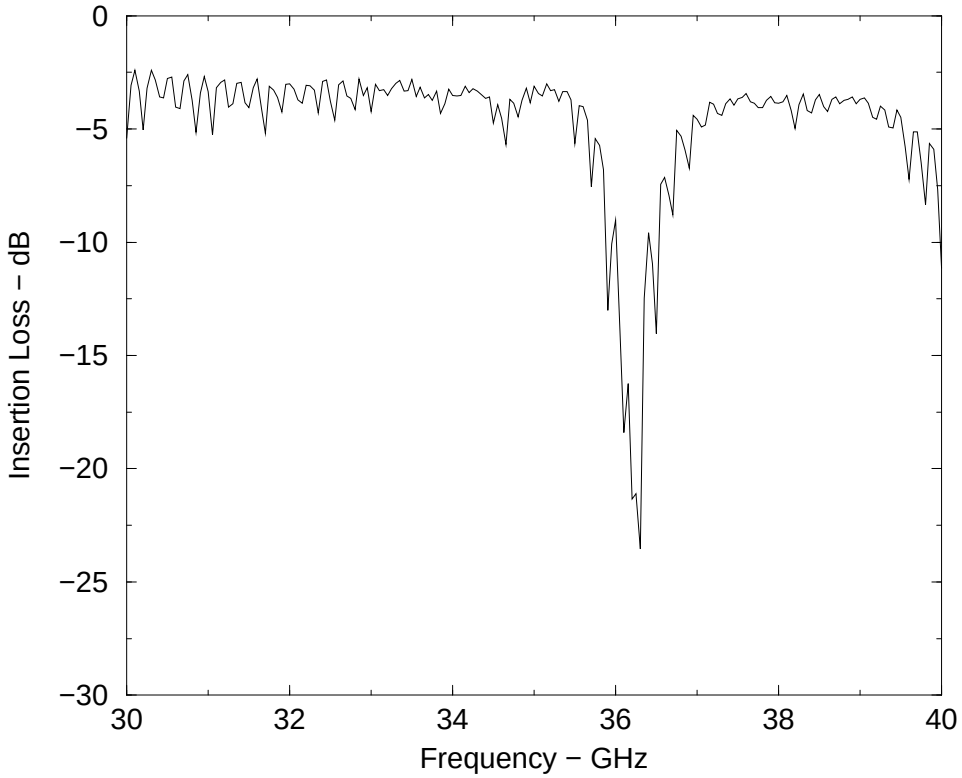

Figure 5.47: The insertion loss of the 98-element array hard-horn feeds placed back-to-back.

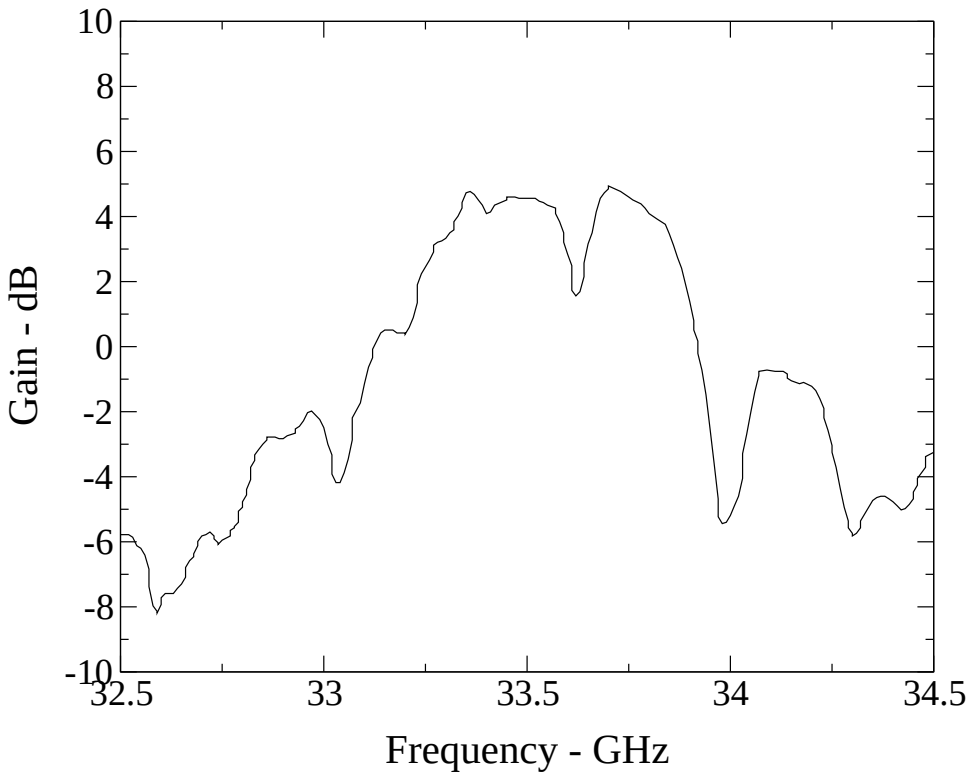

Figure 5.48: The small signal gain of the 98-element array, including the hard-horn feeds.

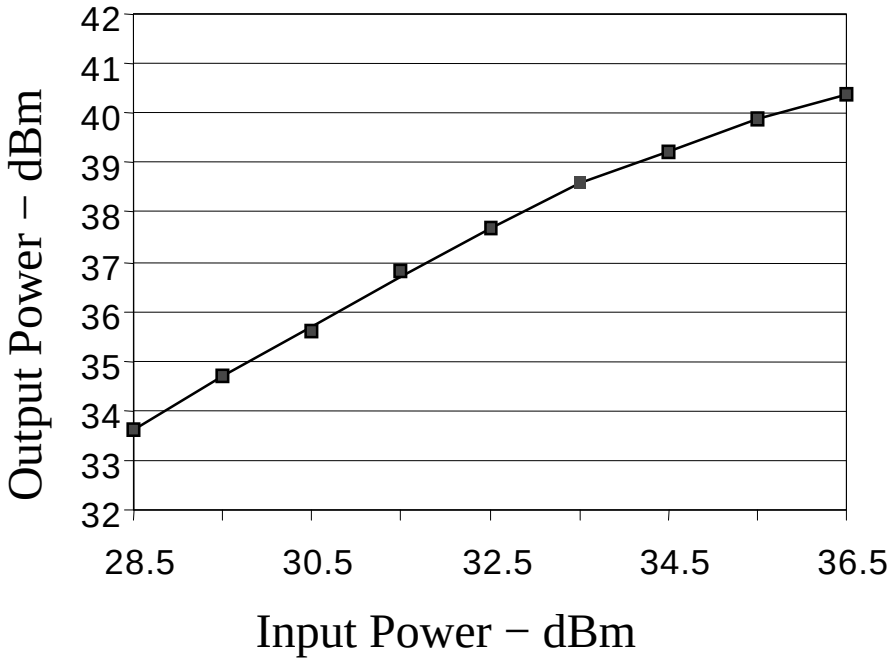

Figure 5.49: The output power versus input power for the 98-element array, including the hard-horn feeds, at 33.5 GHz.

Chapter 6

Tray Approach

Several methods of spatial power combining have been introduced in Chapter 1. These methods were separated into two main categories (tile- and tray-based). In this chapter, a new type of tray-based array will be presented. The general concept for this array configuration is shown in Fig. 6.1, where the patch antennas on the left of the diagram receive an incident signal radiated from the feeding hard-horn antenna. The signal is then coupled through apertures in the groundplane to the microstrip transmission lines located perpendicularly to the antenna groundplane. After amplification, it is then radiated through the aperture coupled patch antennas on the last layer and is collected by the receiving horn. This implementation utilizes the perpendicularly-fed patch antenna as the radiating element and the application of a novel microstrip-to-waveguide transition for coupling energy from a microstrip line within the array to the dielectric filled waveguides, which are terminated by the aperture coupled patch antennas.

This array topology has several advantages over tile-based arrays and also other tray-based arrays. The most notable advantage is the reduced unit cell size, which is common among tray-based arrays. As can be seen in Fig. 6.1, the amplifiers and biasing networks are located on trays, which are stacked to form the array. In addition, the amplifying portion of the unit cell occupies the space between the input and output microstrip patch antennas. By placing the amplifying circuitry between the input and output antennas, the unit cell size has been reduced to its smallest possible dimensions, since a 3-dimensional approach has been taken. Furthermore, the amplifying elements have been isolated from the radiating elements, through the microstrip patch antenna groundplane (only slot apertures are present in this groundplane as seen on the right side of the figure). The groundplane with the slot apertures, shown in Fig. 6.1, has been formed by stacking the individual trays on top of each other. Stacking the trays also forms the dielectric filled waveguide on either side of the array. This dielectric filled waveguide is the conduit between the microstrip transmission lines in the center of the tray and the microstrip patch antennas on the left and right sides of the array. The isolation formed between the amplifying circuitry and the radiating elements simplifies the system design. In addition, the radiation characteristics of the antenna array are no longer influenced by finite size substrates, bias lines, bondwires, etc. More importantly, the isolation reduces

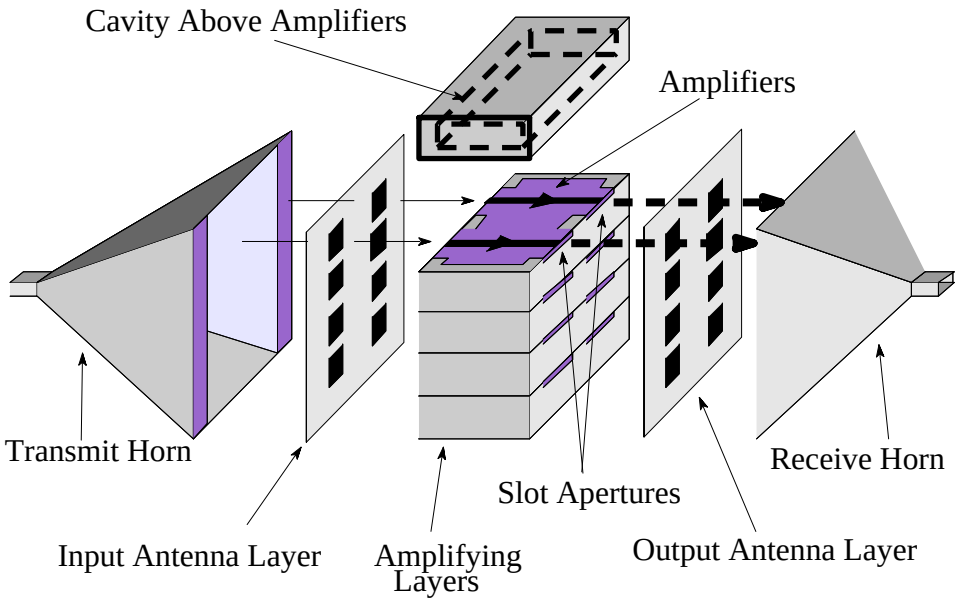

Figure 6.1: A conceptual drawing of the perpendicularly-fed tray-based amplifier array.

the possibility of potential oscillations. Finally, the stacked trays provide thick groundplanes for the removal of heat. Each groundplane may be half or more of the unit cell size. At Ka-band, this is on the order of 2.54 mm for a $0.5\lambda_0$ spacing. Furthermore, the groundplane need not remove the heat from as many unit cells, since each tray carries only a fraction of the total number of unit cells.

There were two main reasons for developing this array architecture. First and foremost was the development of a spatial power combining amplifier array that could provide high output power levels. This array is believed to have more potential for high output power levels than the tile-based arrays. In addition, the minimum distance between unit cells of the previous chapter's designs were quite large, much larger than the optimum $0.5\lambda_0$ spacing. This large spacing was necessary for the placement of the amplifiers, biasing circuits, and microstrip patch antennas within the unit cell. However in tray-based arrays, the amplifiers and biasing networks are placed in the space between the input and output radiating elements, as was mentioned above. This can effectively reduce the unit cell size to dimensions comparable to either the radiating element size or the width of the amplifiers. Thus, unit cell spacing values of $0.5\lambda_0$ are more readily be achieved. Therefore, the tray-based array should provide lower loss and higher combining efficiencies than the tile-based arrays, if the radiating elements are as efficient.

The second goal was to provide a robust spatial amplifier array for test and measurement purposes. In addition, an array which could be both modeled and efficiently measured was desired. Many previous attempts have been made to model an entire spatial amplifier array. This is inherently a difficult task, since the amplifiers, biasing and matching networks, and radiating elements occupy

the same layer and must therefore be modeled as a whole. However in this architecture, the amplifiers and biasing networks are isolated from the microstrip patch antennas through an aperture in the groundplane. This isolation was by design, since an isolation between the microstrip patch antennas and the amplifying circuitry will reduce the possibilities of oscillations and also allow the system to be modeled in blocks (radiating antenna array and amplifying unit cells). Fortunately, this particular geometry was conducive to simulations by a method of moments program being developed [85]. The method of moments program was able to simulate an array of microstrip patch antennas fed by a dielectric waveguide and radiating into an oversized horn antenna. This was the same basic geometry except for the use of a hard-horn feed, which has already been modeled in previous research efforts [105]. However, the integration of the hard-horn (mode-matching) and microstrip patch array (method of moments) simulations was no easy task. A detailed discussion of this modeling approach will not be given here but can be found in several papers [85, 86, 87].

In addition to providing an array which could be modeled, several sets of experimental data were desired from the spatial amplifier array. The desired data included the failure analysis of a spatial amplifier array. More specifically, the degradation in output power versus the number of devices failed was important. This data would help verify the fault tolerant nature of spatial power combiners using near-field excitation. This graceful degradation in output power is one of the key features of spatial power combining, when compared with the single point failure characteristics of amplifiers based on vacuum-tube technology. Furthermore if a single device fails in a spatial power combiner, the amplifier array's output power will decrease (but not significantly when the number of devices is large). In contrast, the vacuum tube amplifiers are prone to single point failures, since they rely on a single amplifying element. Therefore, redundant vacuum tube amplifiers are necessary in mission critical applications.

The perpendicularly-fed amplifier topology was also desired for the support of other projects, specifically a near-field optical scanning system. The results of that research will not be discussed here but can be found in literature [102]. The near-field optical scanning system allows the measurement of the electric field within the reactive near-field of an electromagnetic source (antenna, transmission lines, amplifiers, etc.) with little perturbation of these fields. In addition, they are able to perform thermal measurements using the same basic technology.

In the following sections, several tray-based spatial amplifier arrays are presented at both X- and Ka-band. This discussion will begin with a description of the novel perpendicular antenna feed developed in this research. Then the design, fabrication, and measurement results of two X-band systems will be given. These will be followed by the design, fabrication, and measurement results of a 49-element array at Ka-band. For both the X- and Ka-band amplifiers, a fault tolerance analysis will be performed to verify the fault tolerant nature of these designs.

6.1 Antenna Implementation

The general concept of the perpendicularly-fed patch array was outlined in the previous section. An illustration describing the system was shown in Fig. 6.1. In this section, a more detailed description of the perpendicularly-fed patch antenna and microstrip-to-waveguide transition is given. Both elements are of critical importance to this amplifier array topology. The microstrip-to-waveguide transition is particularly interesting, since it allows for an elegant method of coupling energy from a microstrip transmission line into a dielectric filled waveguide and is easily extended to PCB manufacturing techniques.

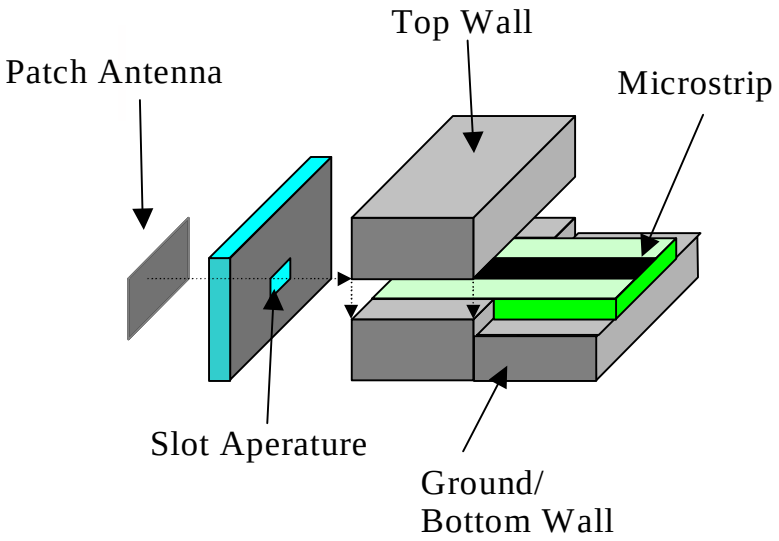

Figure 6.2: A conceptual drawing of the perpendicularly-fed patch antenna.

A conceptual view of the entire antenna implementation is shown in Fig. 6.2. In this figure, a signal input into the microstrip line is coupled to the dielectric filled waveguide through the microstrip-to-waveguide transition. Then the signal is radiated by the aperture coupled patch antenna, terminating the dielectric filled waveguide. Since the dielectric filled waveguide separates the aperture coupled patch antenna from the microstrip-to-waveguide transition, the two components can be modeled separately. Both components can also be modeled as a whole, but such simulations are not necessary unless the length of the dielectric waveguide is not long enough to ensure the presence of only the dominant TE_{10} mode of operation (i.e. all of the evanescent modes must have decayed).

In the following sections, the perpendicularly-fed patch antenna and the microstrip-to-waveguide transition will be discussed. The perpendicularly-fed patch antenna is not in itself a new concept. However, the integration of this antenna with the microstrip-to-waveguide transition is a new concept. Furthermore, the use of either structure within a spatial amplifier array is both new and exciting.

6.1.1 Perpendicularly-Fed Patch Antenna

In planar active arrays, where the devices are placed in the same layer as the radiating elements, coupling between elements may cause unwanted oscillations. The unit cells used to construct the array can limit the size of the devices and/or the complexity of the matching circuit used. This is because both amplifiers and matching circuits, as well as the antenna, must be contained within the area determined by the array spacing. This is especially true of spatial amplifier arrays, which must receive a signal, amplify it, and re-radiate it into free space. Therefore, they either contain both radiating elements in the same unit cell, as with slot antenna arrays, or they have two or more layers to separate the radiating elements. One design, which addresses this issue in spatial power combining, is found in [80], where the amplifiers are placed between input and output tapered slot antennas.

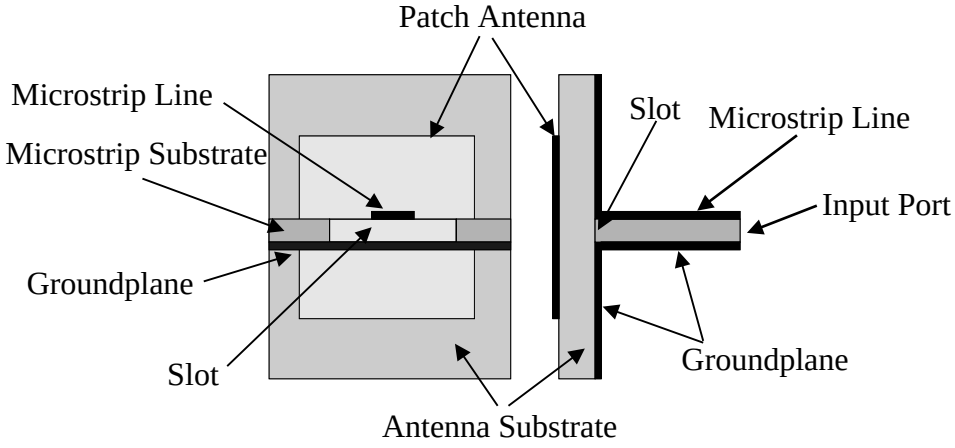

Figure 6.3: A conceptual drawing of a perpendicularly-fed patch antenna developed by Pozar[106].

A convenient method devised in [106] provides a good means for separating the radiating elements and active components, through the use of a perpendicular feed to an aperture coupled patch antenna as illustrated by Fig. 6.3. However, this may not be practical in an array configuration, due to the higher fabrication costs in creating a good connection between the microstrip and groundplane at the aperture. A modified version, which alleviates this problem is illustrated in Fig. 6.2 in a spatial amplifier array configuration [84]. This structure separates the antenna from any active components. In addition to isolating the antennas from the amplifiers, this topology allows for a reduced unit cell size by placing the amplifier circuit between the input and output antennas.

The development of aperture-coupled patch antennas, perpendicularly-fed patch antennas, and waveguide-fed patch antennas has been documented in literature [106, 107, 108]. These configurations are limited to having thin groundplanes, otherwise adverse effects such as back radiation [107] may occur. By using a thick groundplane for the aperture, the microstrip line may be extended into the aperture, creating a waveguide. A connection will then be formed between the microstrip line and the top wall of the waveguide. The waveguide is then terminated by a slot,

which couples to a microstrip patch antenna. The resulting structure is a dielectric filled waveguide, terminated by an aperture coupled patch antenna [84].

The design of the perpendicularly-fed patch antenna, using a dielectric filled waveguide feed, is a multi-step process. First, the dimensions of the dielectric filled waveguide are determined. These dimensions will be defined by the type of substrate and frequency of operation. A detailed discussion of this design will be given in the following section. It should suffice to say that the height of the dielectric filled waveguide should be small (i.e. the same height as the microstrip line substrate). The initial dimensions of the microstrip patch antenna are then determined using *PCAAD*™. They may also be determined from papers found in literature [107]. In either case, the dimensions of the patch (length and width) and the dimensions of the slot (length and width) must be determined from aperture coupled patch antenna models. These initial values may be based on aperture coupled patch antennas fed from a $\lambda/4$ microstrip line as in [107]. Then the entire structure is simulated (not including the microstrip-to-waveguide transition) in *HFSS*™. The dimensions of the slot will typically need to be varied in order to compensate for the waveguide feed.

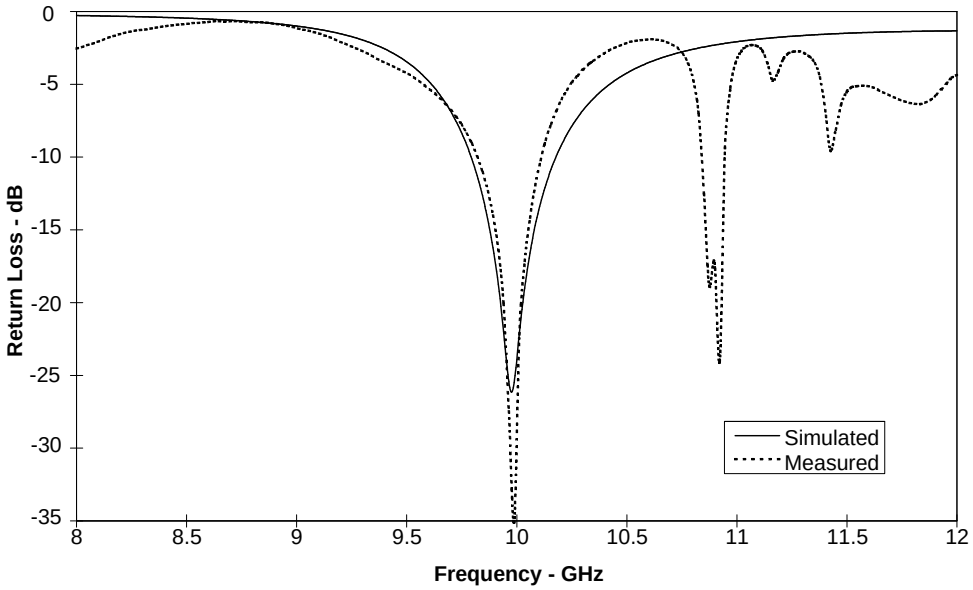

Figure 6.4: Simulated and measured results for a perpendicular-fed patch antenna at X-band.

To verify the concept, a perpendicularly-fed patch antenna was designed and fabricated at X-band, also including the effect of the microstrip-to-waveguide transition. The bottom tray, top tray, microstrip line, and the patch antenna forming this transition are shown in Fig. 6.2. The bottom tray forms both the groundplane of the microstrip line and the bottom and sidewalls of the dielectric filled waveguide. The top tray forms the top wall of the dielectric filled waveguide, which also forms a pressure contact between the top wall and the microstrip line. A dielectric substrate is used for both the microstrip line and the dielectric filling for the waveguide (i.e. the microstrip

line actually extends into the waveguide and serves as the dielectric filling). Finally, the microstrip patch antenna with slot aperture in the groundplane is glued to the dielectric filled waveguide groundplane using a low loss adhesive.

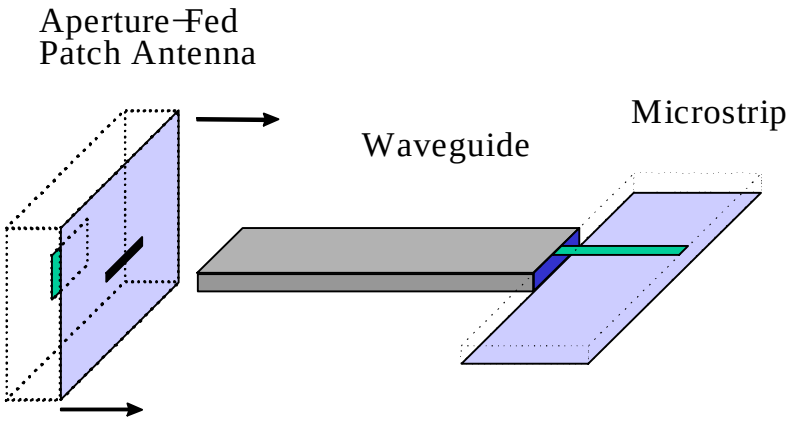

Figure 6.5: A conceptual drawing of the perpendicularly-fed patch antenna modeled in *HFSS*™.

Simulated and measured results are shown in Fig. 6.4. These results are for the structure shown in Fig. 6.5, where the dimensions of the antenna are as follows:

$$\begin{aligned} L_p &= 8.636 \text{ mm} \\ W_p &= 10.16 \text{ mm} \\ L_s &= 6.35 \text{ mm} \\ H_s &= 0.381 \text{ mm} \\ H_w &= 0.381 \text{ mm} \\ W_w &= 11.43 \text{ mm} \\ L_w &= 2.54 \text{ mm} \end{aligned}$$

where L_p and W_p are the resonant length and width of the patch antenna, L_s and H_s are the length and height of the slot aperture, and H_w, W_w, and L_w are the height, width, and length of the dielectric filled waveguide, respectively. In addition, a *Rogers RT5880*™ dielectric with an $\epsilon_r = 2.2$ and dissipation factor of 0.0009 was used for both the antenna and dielectric filled waveguide substrate. The simulated results compare well with the measured results. In fact, the resonant frequency is almost identical in both cases. Some variation is observed at higher frequencies with the measured results. This may be due to differences between the measured and simulated antenna. Additionally, the fabricated antenna substrate was finite in size, while the simulated antenna substrate was much larger in extent. The 10-dB return loss bandwidth was nearly 400 MHz for the simulated case and approximately 300 MHz for the measured case.

The perpendicularly-fed patch antenna with dielectric filled waveguide feed was relatively simple to design and fabricate, although it was necessary to have the trays made at a machine shop. However, this should not serve as a deterrent, since CNC machining is common place among manufacturing facilities. Finally, the agreement between the measured and simulated return loss was extremely good and encouraging for future work.

6.1.2 Microstrip-to-Waveguide Transition

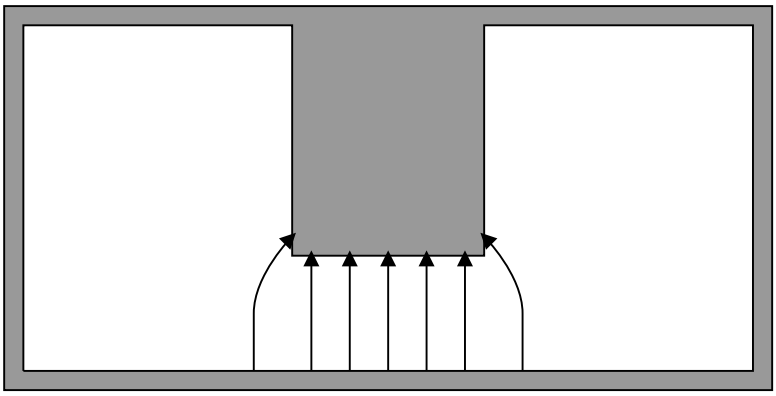

Ridged Waveguide

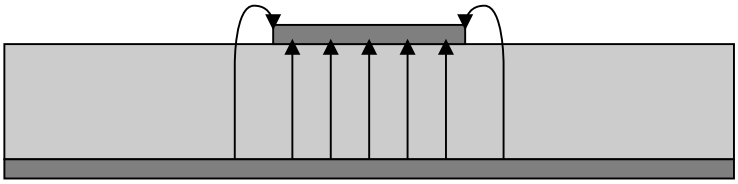

Microstrip Line

Figure 6.6: The electric field distribution of a microstrip line and a ridged waveguide.

The transition from a microstrip line to a waveguide has traditionally been made using a ridged waveguide [109]. This is done to both match the fields and impedance of the waveguide to the microstrip line as shown in Fig. 6.6. However, a ridge is not necessary for matching the fields of the microstrip line to those of the waveguide. The microstrip line can be directly matched to a dielectric filled waveguide as illustrated by the fields of Fig. 6.7. This has most likely not been investigated in literature, since such transitions between waveguides and microstrip lines

would require a non-standard waveguide size and one filled with dielectric material. To the authors knowledge, publications derived from this research [83, 84] represent the first published results for a direct transition between a dielectric filled waveguide to a microstrip line as represented by Fig. 6.8.

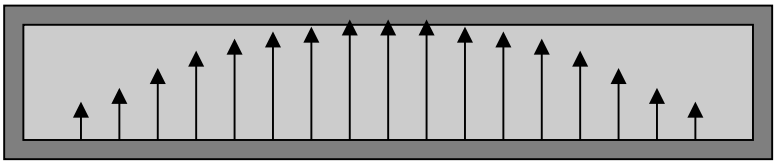

Dielectric Filled Waveguide

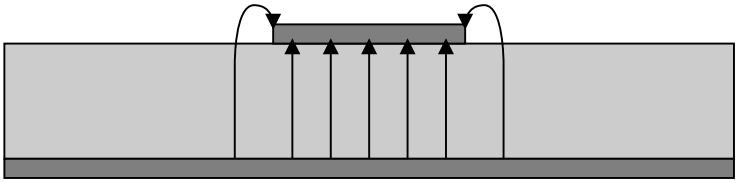

Microstrip Line

Figure 6.7: The electric field distribution of a microstrip line and a waveguide.

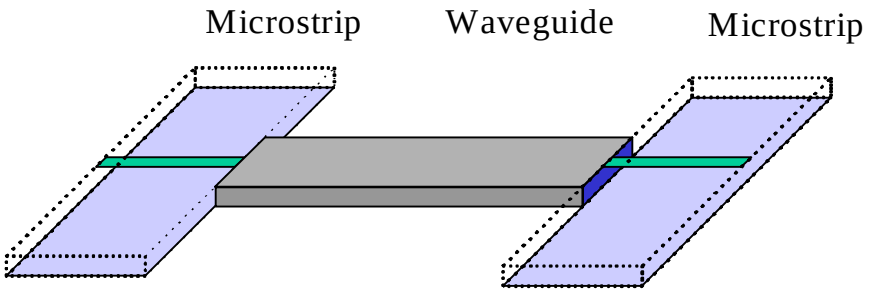

Figure 6.8: A conceptual drawing of two microstrip-to-waveguide transitions back-to-back.

The impedance of the dielectric filled waveguide may be matched to that of the microstrip line if the

height of the waveguide is properly chosen. This impedance is given by the following equation [6]:

$$Z_0 = \frac{377\frac{b}{a}\sqrt{\frac{\mu_r}{\epsilon_r}}}{\sqrt{1-\left(\frac{f_c}{f}\right)^2}} \tag{6.1}$$

where a and b are the height and width of the waveguide, respectively, f_c is the cutoff frequency, μ_r and ϵ_r are the relative permeability and permittivity, respectively. The length of a is chosen based on the minimum cutoff frequency required. For a design frequency of 34 GHz, a is chose to be 2.286 mm giving a cutoff frequency of 26 GHz based on $\lambda_c = 2a$. The height b of the waveguide is chosen to give an impedance of $50\ \Omega$ but must also meet available substrate restrictions. A height of 0.381 mm yields an impedance of approximately $40\ \Omega$ at 34 GHz. Simulated results, using *HFSS*™, are shown in Figs. 6.9 and 6.10, where there are two transitions present in the model. The insertion loss and return loss for a 10.16 mm long waveguide versus frequency is quite good. Less than 10-dB return loss is obtained over the entire band from 30 to 40 GHz. In addition, a change in the length of the dielectric waveguide does not affect performance. This simulation was performed to ensure that no evanescent mode propagation was contributing to the low loss coupling found in the microstrip-to-waveguide transition. If this were the case, the simulations would have shown increased loss as the dielectric waveguide was lengthened.

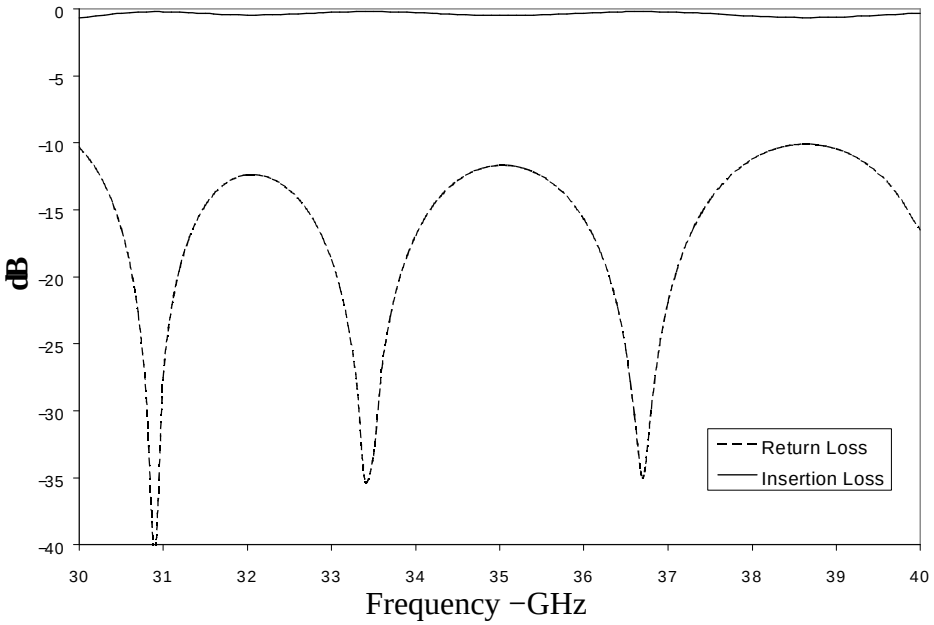

Figure 6.9: The simulated insertion loss and return loss of two microstrip-to-waveguide transitions back-to-back versus frequency.

Experimental verification was not performed for the microstrip-to-waveguide transition alone. However, experiments were performed for the combination of the microstrip-to-waveguide transition and the aperture coupled patch antenna. Results for these experiments were given in the

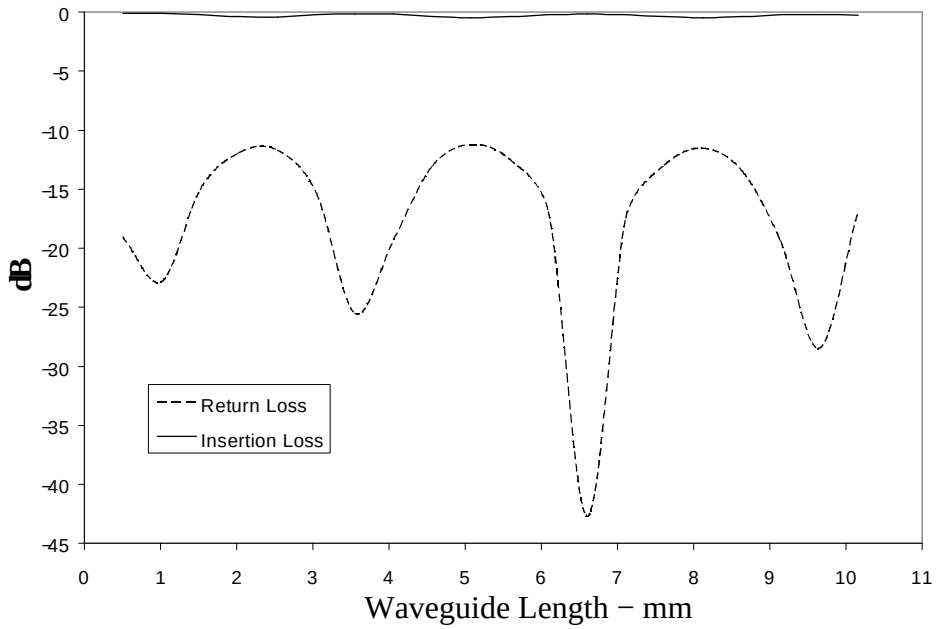

Figure 6.10: The simulated insertion loss and return loss of two microstrip-to-waveguide transitions back-to-back versus waveguide length.

previous section for an X-band antenna. Since good agreement was found between the simulated and measured results, the microstrip-to-waveguide transition is also assumed to exhibit good performance.

6.2 A 25-Element Array: First Implementation

This section will describe the design, fabrication, and experimental results for a 5x5 perpendicularly-fed patch array at X-band. A general description of this amplifier array configuration was given in the previous sections and was illustrated by Fig. 6.1. In addition, a detailed description of the antenna feed was also given in the previous sections. Particular attention was given to the design of the aperture coupled patch antenna and to the microstrip-to-waveguide transition.

A more detailed illustration of the 5x5 amplifier array is shown in Fig. 6.11, while Figs. 6.12 and 6.13 illustrate the top and bottom views of an individual tray. Each of these trays are machined on both the top and bottom sides. The top of the tray is recessed to accommodate the dielectric for both the microstrip lines and the dielectric filled waveguide. In addition, the dielectric filled waveguide (without the top wall) is visible on the front edge of the tray in the top view. Additionally in the bottom view, a cavity can be seen on the bottom side of the tray, which provides space above the microstrip transmission lines as well as for the active devices.

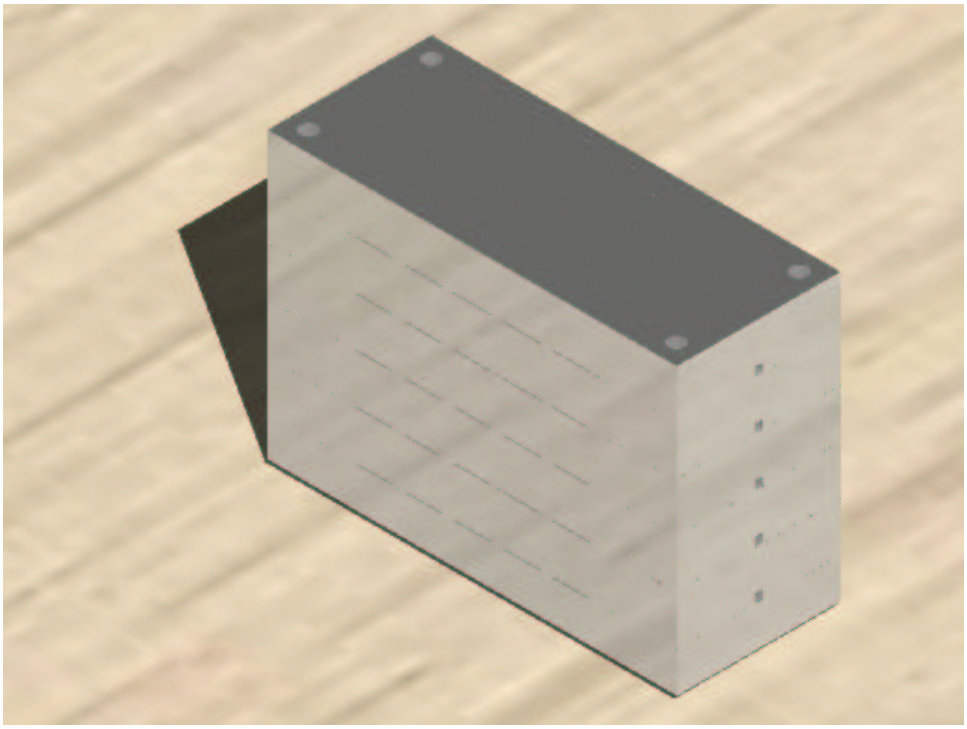

Figure 6.11: An illustration of the 5x5 amplifier array without the microstrip patch substrate.

A more detailed description of the 5x5 array design will be given in the following subsections. The first section will discuss the unit cell design, including antenna, microstrip-to-waveguide transition, and amplifier biasing. This will be followed by a discussion of the hardware design, giving detailed illustrations of the fabricated trays. Finally, the performance of both a passive and active version of the 5x5 array will be given.

6.2.1 Unit Cell Design

The unit cell consists of the input and output aperture coupled patch antennas, the microstrip-to-waveguide transitions, and the amplifying circuitry. The unit cell design must thus encompass all of these elements. By far the most difficult portion of the design is that of the radiating elements, which will be discussed first. This will be followed by the layout of the amplifiers and bias lines, which is much simplified in comparison to the tile-based arrays (coupling between antennas and both bias lines and amplifiers is eliminated).

The transition from the microstrip patch antenna to the perpendicular microstrip transmission line through the slot aperture is an essential part of this design. One possible approach was introduced in [106], Fig. 6.3, where the microstrip line, feeding an aperture coupled patch antenna, has been rotated by 90° to achieve a perpendicular feed structure. This feed structure was found to be

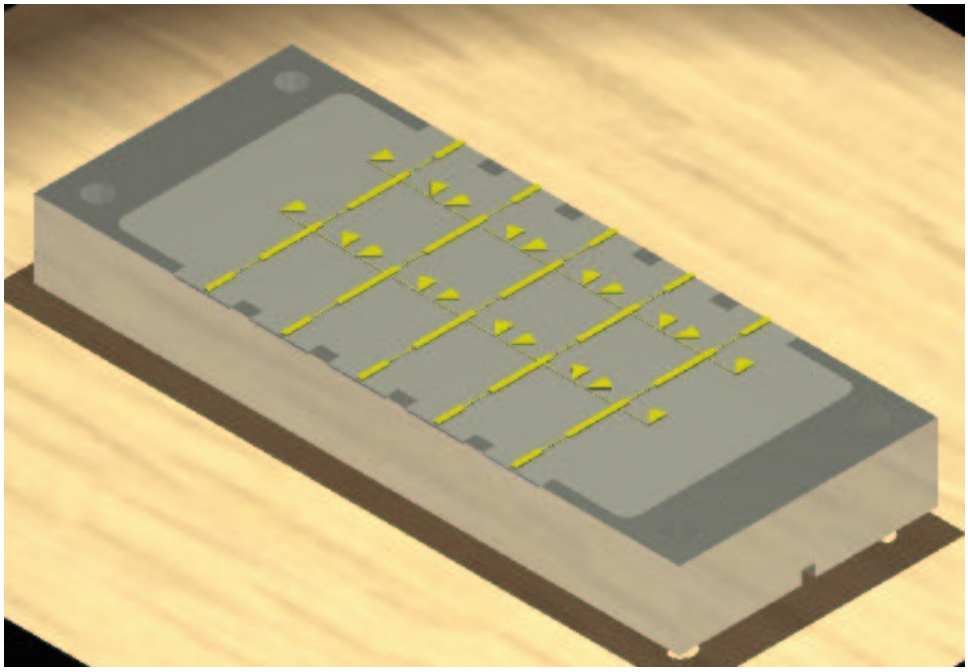

Figure 6.12: A single tray of the 5x5 amplifier array (Top View).

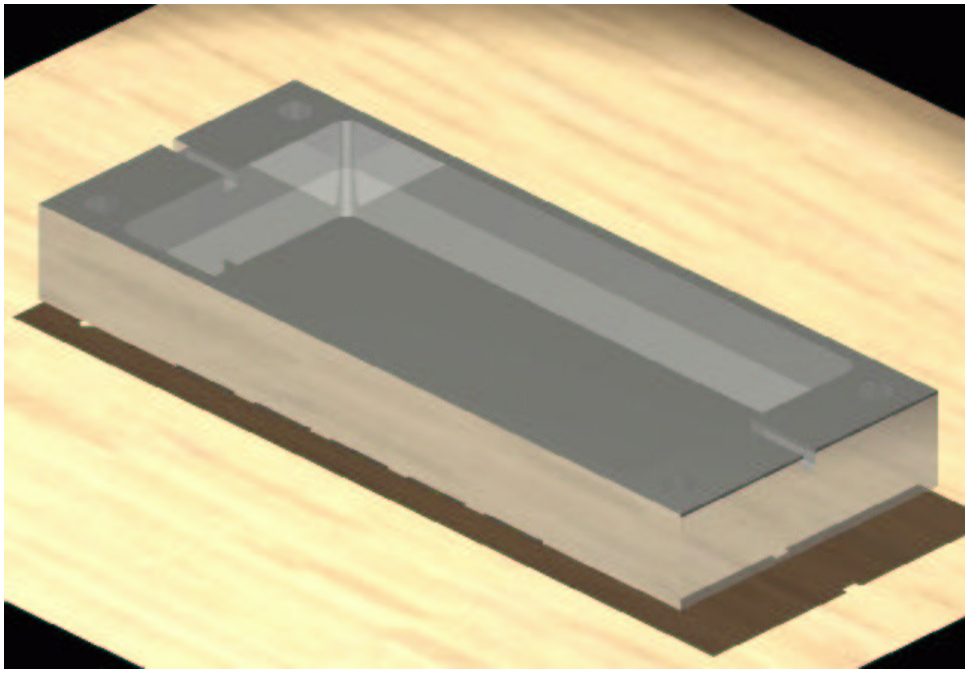

Figure 6.13: A single tray of the 5x5 amplifier array (Bottom View).

inconvenient, since it would be difficult and impractical to solder the microstrip line to a slot located in the center of the array shown in Fig. 6.1. In order to make a connection from the microstrip line to the slot without any soldering, the microstrip line was placed inside a waveguide as illustrated previously in Fig. 6.2. The bottom wall of the waveguide is the groundplane of the microstrip line, and the top wall is pressed against the microstrip line to form a connection. This can now be viewed as a waveguide excited patch antenna.

The design of the antenna feed was performed using *Agilent - HFSS*™ as was described in Section 6.1.1 . The height of the waveguide was chosen to be the same as the height of the slot, while its width was chosen such that the cutoff frequency would be 9 GHz. The antenna design was refined as outlined in Section 6.1.2 until a center frequency of 10 GHz and a 10-dB return loss of over 400 MHz was achieved, Fig. 6.4. The final dimensions of this patch and dielectric filled waveguide were given in Section 6.1.1.

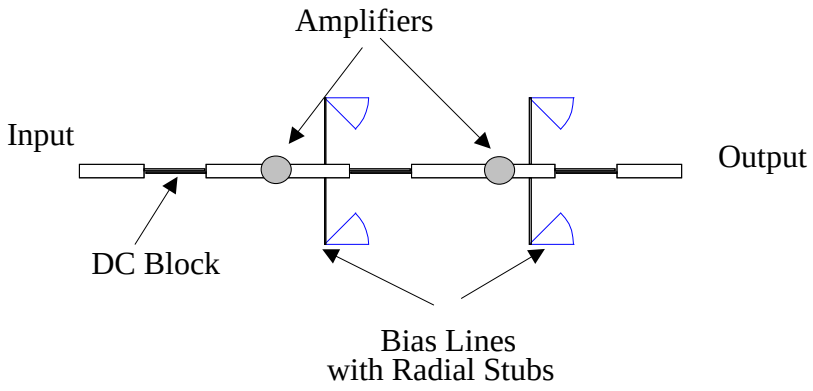

Figure 6.14: The unit cell layout of the amplifier circuit using matched monolithic amplifier and interdigitated capacitors.

Only the amplifier circuit remains to be designed in the unit cell, as illustrated at the center of the tray in Fig. 6.12. This layout is better illustrated in Fig. 6.14, where two *Mini-Circuits ERA1*™ matched monolithic amplifiers are cascaded to provide the active gain. No matching circuits were necessary, but three DC blocking circuits were needed to isolate the two amplifiers and the input and output of the network [110], since otherwise the top wall of the dielectric filled waveguide would short circuit the microstrip line to ground. In addition to the DC blocks, radial stubs were added along the bias lines to suppress any coupling from one unit cell to the next. The insertion loss of the network without the amplifiers was simulated to be 0.6 dB at 10 GHz using *Agilent - Momentum*™.

Several measurements were performed on the unit cell without antennas. First, the insertion loss of the unit cell was measured without the amplifiers. The resulting insertion loss was 0.8 dB from 9.5 to 10.5 GHz. This gives good agreement between the simulated and measured loss of the passive unit cell. Subsequently, the two amplifiers were added to the unit cell. The gain for the active unit cell (without antennas) is shown in Fig. 6.15, where a gain of 18 dB at 10 GHz was

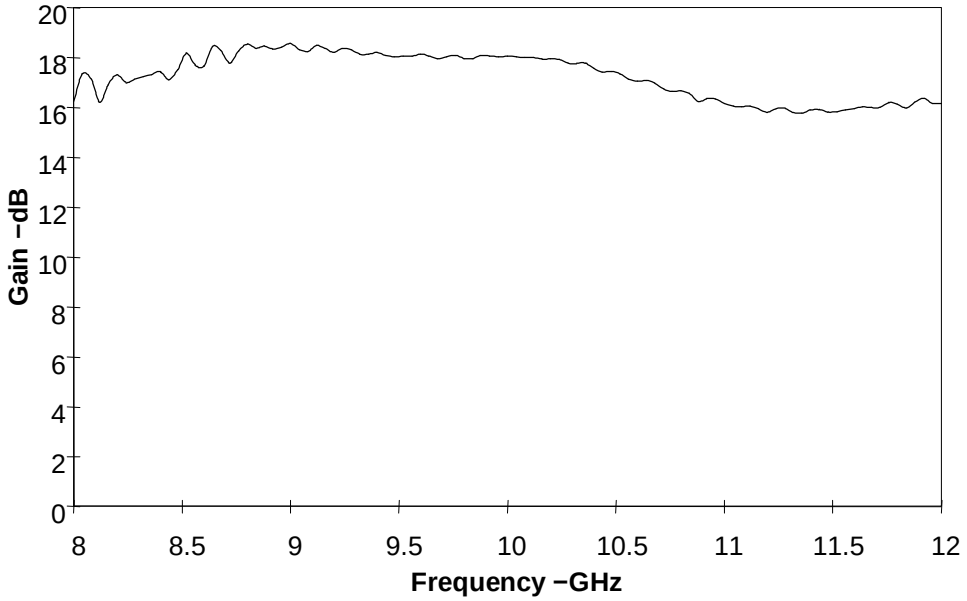

Figure 6.15: The gain of 5x5 amplifier array unit cell without input and output antennas.

obtained. Finally, the return loss of the patch antenna was measured and is shown in Fig. 6.4 along with the simulated results. Both the simulated and measured results give a center frequency of 10 GHz, although the measured 10 dB return loss bandwidth is only 300 MHz as compared with the 400 MHz of the simulated antenna.

6.2.2 Design of Array Hardware

The 5x5 amplifier array was constructed using 5 populated layers plus a single cover layer. Each layer (Figs. 6.12 and 6.13) contains 5 unit cells with two amplifiers per unit cell. The layers were then stacked to form the array of slots shown in Fig. 6.11. The input and output microstrip patch antennas, spaced 15.24 mm or $0.51\lambda_0$ apart, were added to complete the array. In addition, the microstrip patch substrates were glued to the trays using a low loss adhesive.

Each tray was machined from a block of aluminum, according to the dimensions given in Figs. 6.16,6.17, 6.18, and 6.19. The resulting trays were then populated by the amplifiers and microstrip circuitry as illustrated by Fig. 6.14. First, the microstrip and dielectric waveguide substrate was bonded to the aluminum trays. Then the amplifiers were soldered in place. In addition, grounding pads were screwed into the tray to allow the amplifier sources to be soldered to ground.

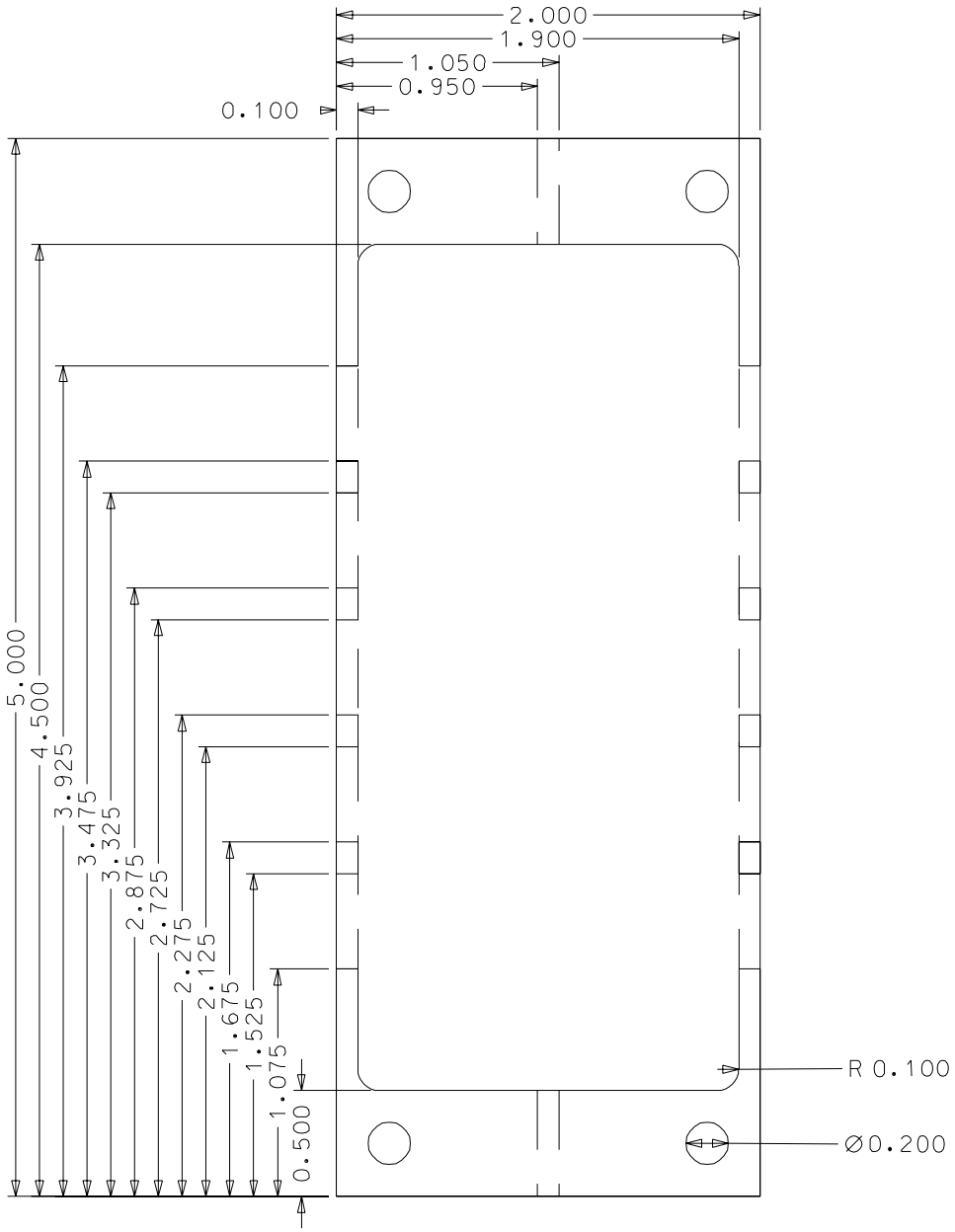

Figure 6.16: A detailed illustration of a tray from the 5x5 array (Top View).

6.2.3 Array Measurement Results

Three experiments were performed on the passive and active arrays. All of these experiments were performed in a test setup illustrated by Fig. 4.3, where an input and output hard-horn feed are used to distribute and collect energy to and from the amplifier array. In addition, the back-to-back insertion loss of the two hard-horn feeds was measured first. They gave an insertion loss of less

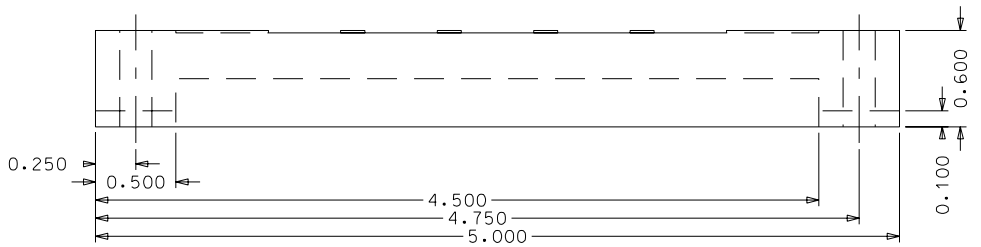

Figure 6.17: A detailed illustration of a tray from the 5x5 array (Side View).

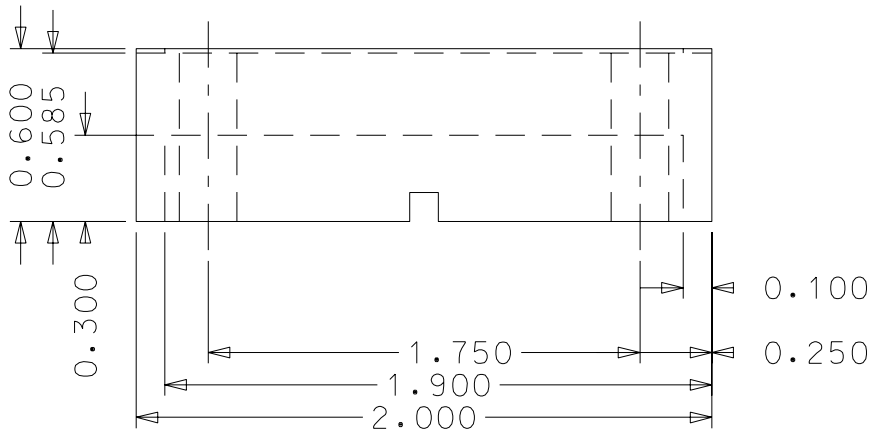

Figure 6.18: A detailed illustration of a tray from the 5x5 array (Front View).

than 1.2 dB at 10 GHz. The active and passive gains of the array were then measured as well as the power compression of the active array.

The passive array, without amplifiers, was placed between the two hard-horn feeds and measured. The results of this measurement are shown in Fig. 6.20. The insertion loss was 3.9 dB at 10 GHz with a 3-dB bandwidth of 300 MHz. Therefore, the insertion loss due to the addition of the array is 2.7 dB. The active array was then placed in the horn-to-horn setup and measured. The overall gain for the 5x5 amplifier array with hard-horn feeds was measured to be 12.4 dB at 10 GHz with a 3-dB bandwidth of 310 MHz as shown in Fig. 6.21. Considering 3.9 dB of loss associated with the passive array measurement, the device gain is 16.3 dB, which is lower than expected from the active unit cell (18 dB). This additional 1.7 dB of loss may be due to the packaging of the amplifiers within the array cavity.

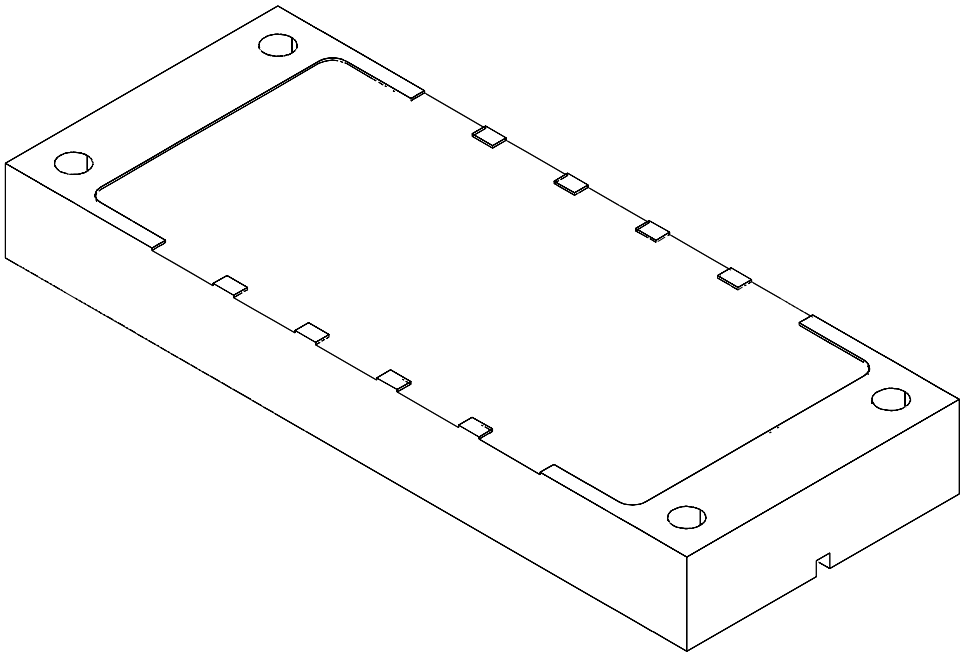

Figure 6.19: A detailed illustration of a tray from the 5x5 array (Isometric View).

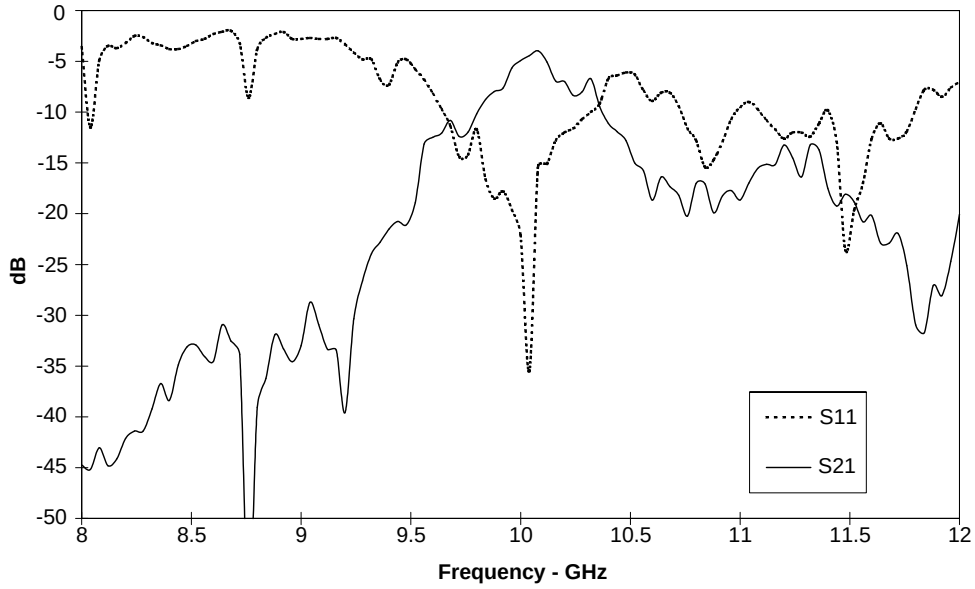

Figure 6.20: The insertion loss and return loss of the passive 5x5 amplifier array with hard-horn feeds at X-band.

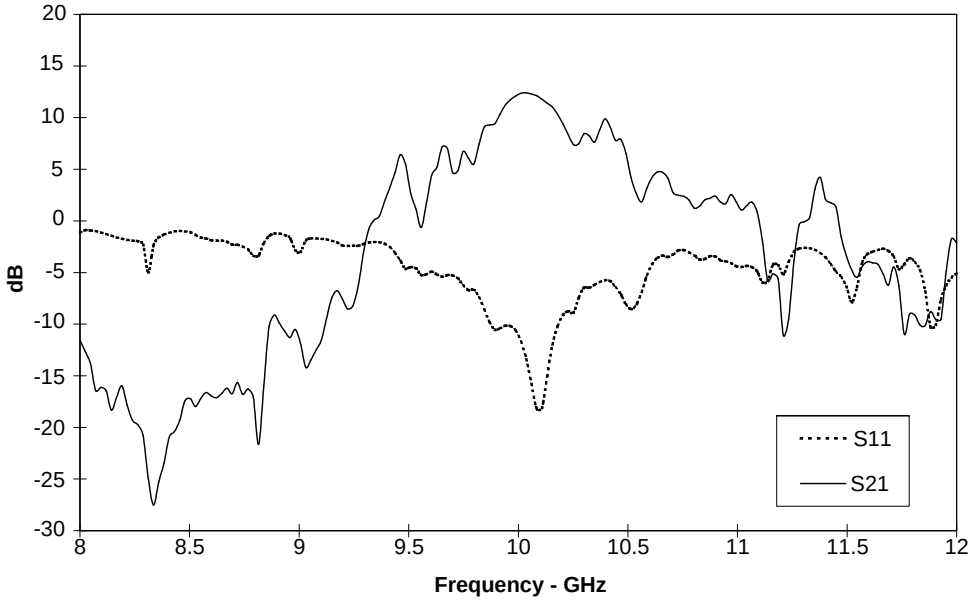

Figure 6.21: The gain and return loss of the active 5x5 amplifier array with hard-horn feeds at X-band.

In addition to the amplifier gain, the power compression curve was measured. The setup for this measurement was similar to that in Fig. 4.3 but with a signal source and power meter replacing the network analyzer. The 3-dB compression power was measured to be 20.65 dBm at 10 GHz. The two device unit cell under 3-dB compression in a $50\ \Omega$ system provided 13.6 dBm of power. Therefore, the maximum power obtainable from the 25 device array under 3-dB compression after taking into account the output array losses is 22.6 dBm. The power combining efficiency, the array power divided by the power output of the amplifiers times the number of amplifiers, is calculated as 20%. The power combining efficiency expected from this array is 52% when taking into account half the passive losses (1.95 dB) as well as half the unexpected losses in the active array (0.85 dB). The additional reduction in power combining efficiency is due to the non-uniform excitation of the amplifiers caused by placing the outer two columns in close proximity to the edge of the hard-horns (i.e. the power density drops rapidly at the edges of the horns).

6.3 A 25-Element Array: Second Implementation

Several advantages of spatial power combining were discussed in previous chapters. Most of these advantages revolve around the high power output potential of the spatial amplifier array. In addition, free space is used as the power dividing/combining medium. By doing so, losses are reduced by eliminating the need for transmission line based power dividers (Wilkinson, Lange, etc.). Also they are expected to be more fault tolerant when compared to traveling wave tube

amplifiers, due to the large number of devices used in parallel. Verifying this is the focus of the second implementation to the 5x5 element array.

In order to study the degradation in amplifier performance versus device failure, a suitable array is necessary. For this purpose, an existing perpendicularly-fed patch array (Section 6.2) was modified to allow for the complete control of the individual amplifiers (turning on or off individual devices). A conceptual drawing of this array was shown in Fig. 6.1. In this figure, an array of microstrip patch antennas receive a signal of uniform amplitude and phase from a hard-horn feed on the left. The signal is then coupled to microstrip lines within the array, where it is amplified. Finally, it is coupled to the microstrip patch antennas on the right and radiated into free space. With planar arrays of grids, microstrip patch antennas, or CPW-fed slot antennas, it would be difficult to bias individual amplifiers, since the bias line would have to pass between the radiating elements. However with the perpendicular-fed patch design, the amplifying and biasing circuitry are located in the space behind the antennas, making it much simpler to bias the individual amplifiers. Using such a structure, the power collected either in the far-field with a standard gain horn or in the near-field with a hard-horn feed could be measured versus the number of active amplifiers. In addition, this system has also been modeled using a combination of numerical methods [87]; thereby allowing a comparison between simulated and measured data to be made.

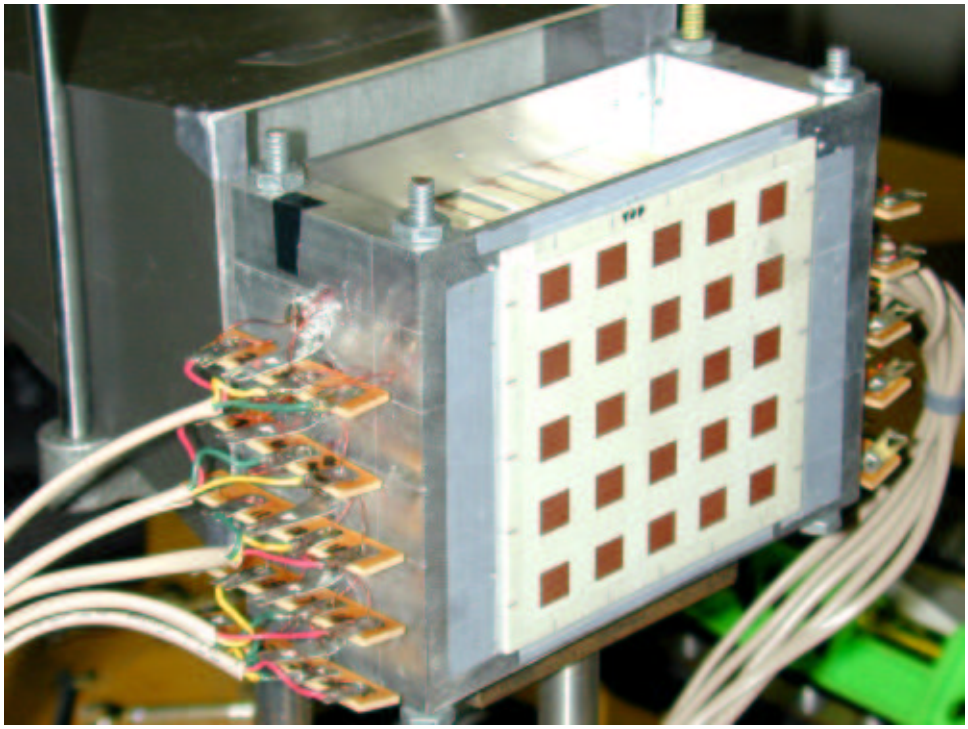

Figure 6.22: A photograph of the second implementation of the 5x5, X-band amplifier array.

In the following subsections, the design, fabrication, and measurement results for this second implementation of the 5x5 perpendicularly-fed patch array will be given. An illustration of the new

array with hard-horn feeds is shown in Fig. 6.22. The design of the 5x5 array will be given first. This follows directly from the previous design of the 5x5 array. In fact, the same aluminum trays were again used. Following this, the design and measurement results of the hard-horn feed will be given. Then experimental measurements of the unit cell and active and passive arrays will be shown. Finally, the device failure analysis will be discussed.

6.3.1 Array Design

The development of the 5x5 perpendicularly-fed patch array was detailed in Section 6.2. A brief description of this structure will be given with an emphasis on the changes made to facilitate the individual biasing of the devices. Each unit cell consists of a receiving antenna coupled to a microstrip line, an amplifier, and a transmitting antenna. In addition, the new 5x5 amplifier array utilizes a single MMIC amplifier to provide the gain.

The microstrip patch antenna feed was designed as described in Section $6.1.1$ and simulated using *Agilent - HFSS*™. A *Rogers TMM3*™ substrate with $\epsilon_r = 3.27$ and thickness of 0.381 mm was chosen for both the microstrip lines and the microstrip patch antennas. The antenna dimensions were then optimized and found to be as follows:

$$\begin{aligned} W_p &= 8.1 \text{ mm} \\ L_p &= 7.4 \text{ mm} \\ W_s &= 0.381 \text{ mm} \\ L_s &= 4.8 \text{ mm} \end{aligned}$$

where W_p and L_p are the width and length of the patch, respectively, while W_s and L_s are the width and length of the slot, respectively.

The dielectric filled waveguide dimensions remained the same. However, the dielectric material was changed. This change resulted in a different wave impedance for the dielectric filled waveguide. Therefore, an impedance transformer was necessary to match the waveguide to the $50\ \Omega$ microstrip line. The dimensions of this impedance transformer are as follows:

$$\begin{aligned} W_1 &= 4.572 \text{ mm} \\ W_2 &= 2.134 \text{ mm} \\ L_2 &= 4.496 \text{ mm} \\ W_3 &= 0.889 \text{ mm} \end{aligned}$$

where W_1 is the width of the microstrip line in the waveguide, W_3 is the width of the $50\ \Omega$ microstrip line, and W_2 and L_2 are the width and length of the impedance transformer.

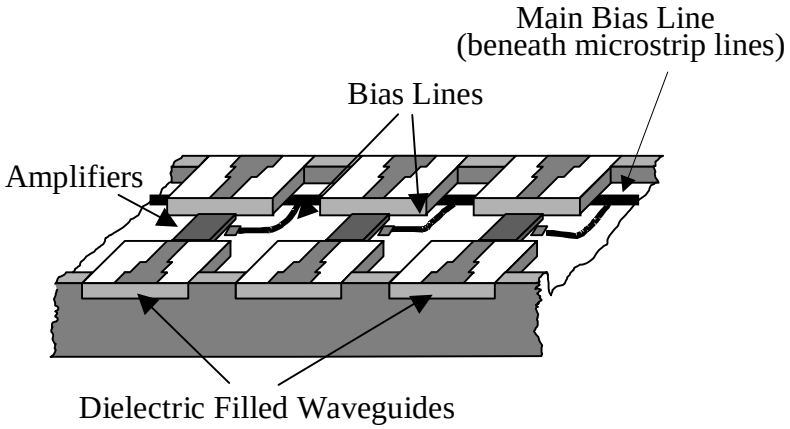

Figure 6.23: A conceptual drawing of the unit cell layout for the 5x5 array.

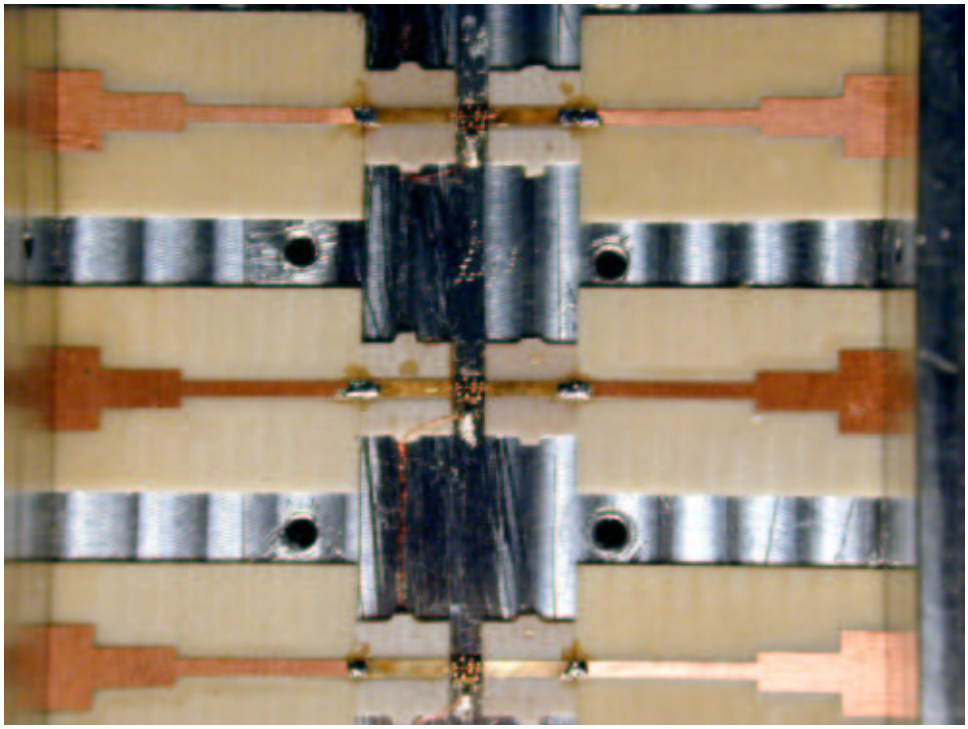

Figure 6.24: A photograph of the unit cell in the 5x5 array.

For amplification, a self-biasing, PHEMT, GaAs MMIC amplifier (*Filtronic LMA411*™) with 18 dB of gain and 17 dBm of output power at 1-dB compression was employed. The biasing arrangement can be seen in the unit cell layout illustrated in Figs. 6.23 and 6.24. Each bias line (magnet wire) passes beneath the groundplane of the microstrip lines feeding the amplifiers. In

this way, each amplifier has a separate bias line and can be individually controlled. Also, the microstrip lines and MMIC amplifiers are epoxied to the aluminum groundplane using a two-part silver epoxy, cured at 120° C for 15 minutes. Finally, two gold bondwires (0.0254 mm diameter) are used to connect the input and output of the MMIC amplifier to the microstrip lines.

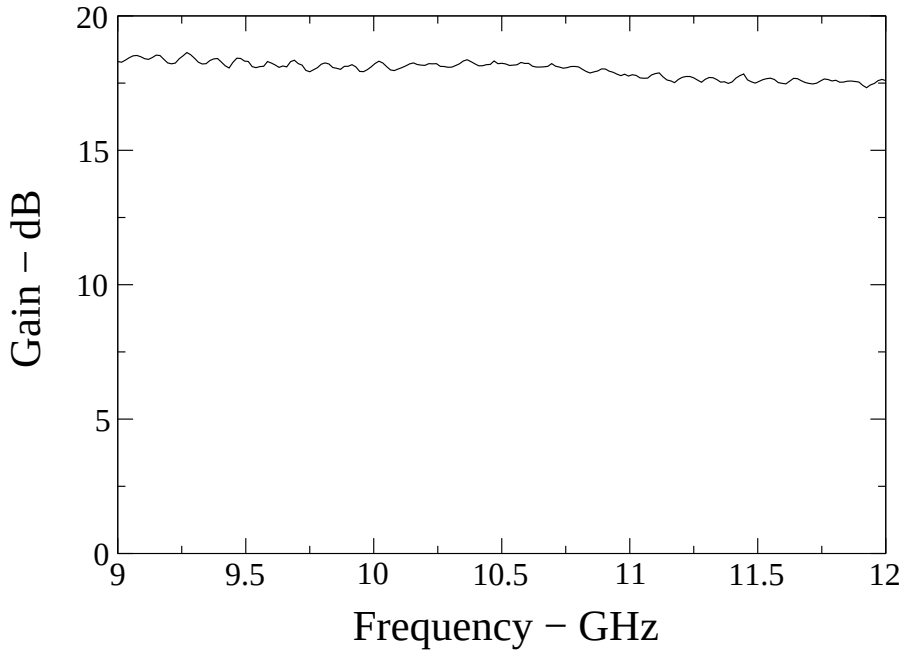

Figure 6.25: The measured gain of a *Filtronic LMA411*™ MMIC amplifier.

The gain and power compression for a single MMIC device were measured to verify their performance before fabrication of the array. Results for gain and power compression measurements are shown in Figs. 6.25 and 6.26, respectively. Both figures compare well with the expected performance of the amplifier (based on published data).

6.3.2 Hard-Horn Feed

Two hard-horn feeds with lenses were developed for the new 5x5 array. These horns were designed to accurately fit the size of the array. In addition, all of the microstrip patch antennas were within the dielectrics on the side walls of the horn. The new hard-horn antenna can be seen in Fig. 6.22, where it feeds the 5x5 amplifier array.

The same design procedures from Section $3.1.2$ were again implemented. Although, a standard gain horn was purchased, instead of being custom manufactured. This was mostly due to the time restraints, otherwise a custom horn would have been designed and fabricated. However, the design of the dielectric side walls and lens was necessary. The resulting dimensions of the optimized

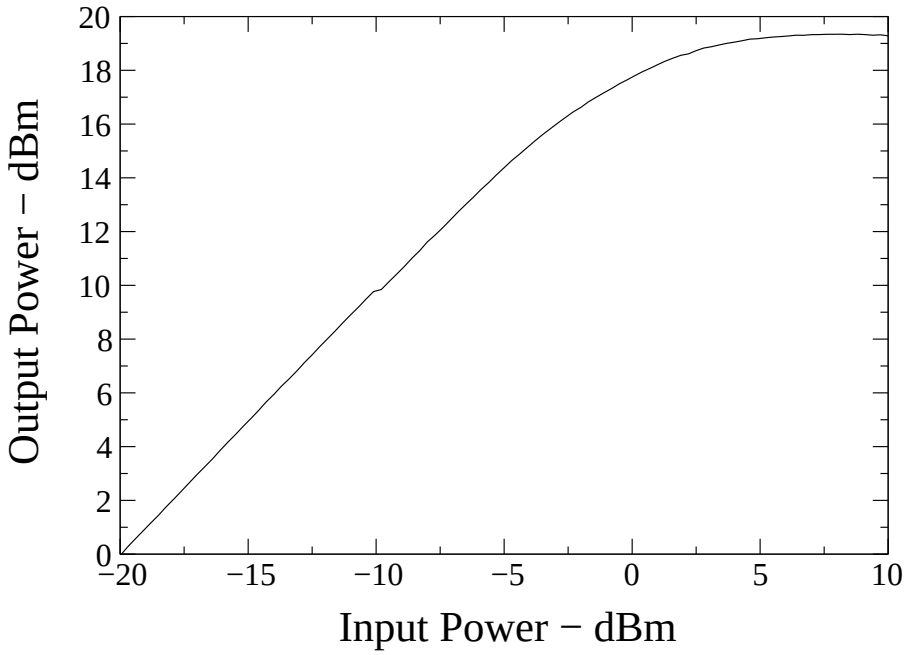

Figure 6.26: The measured output power versus input power of a *Filtronic LMA411*™ MMIC amplifier at 9.6 GHz.

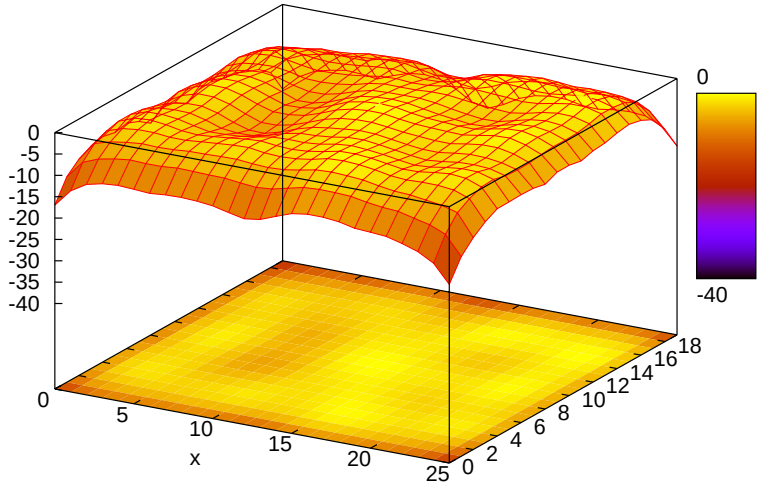

Figure 6.27: The measured near-field amplitude distribution of the hard-horn used with the second 5x5 amplifier array at 9.6 GHz.

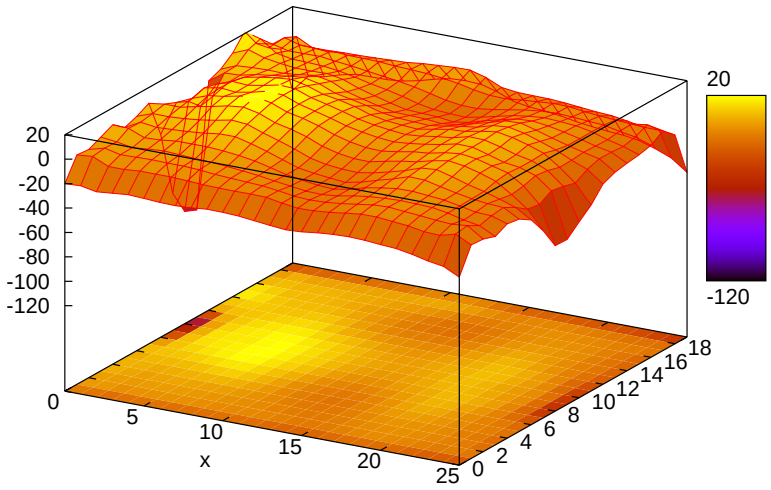

Figure 6.28: The measured near-field phase distribution of the hard-horn used with the second 5x5 amplifier array at 9.6 GHz.

hard-horn are as follows:

$$\begin{aligned} a_1 &= 123.698 \text{ mm} \\ b_1 &= 91.948 \text{ mm} \\ \rho_1 &= 304.4 \text{ mm} \\ \phi_1 &= 11.48^\circ \\ \rho_2 &= 279.0 \text{ mm} \\ \phi_2 &= 9.36^\circ \end{aligned}$$

where the definition of the dimensions were given by Figs. 3.3(a) and 3.3(b). A *Rogers RT5880 Duroid*™ with an $\epsilon_r = 2.2$, dissipation factor of 0.0009, and thickness of 6.35 mm was used for the dielectric side walls. Furthermore, the lens was fabricated from an $\epsilon_r = 1.2$ dielectric foam.

Several measurements were performed on the hard-horn antenna. First, the near-field magnitude and phase was measured and are shown in Figs. 6.27 and 6.28, respectively. These figures give a qualitative view of the field uniformity across the horn aperture. This can be compared with the field distribution of the standard horn before modification (Figs. 6.29 and 6.30). In addition, the insertion loss and return loss of the hard-horn antennas were measured in a back-to-back configuration as illustrated in Fig. 4.3. The resulting insertion loss is less than 2.5 dB from 9.55 GHz to 10.4 GHz, and the return loss is less than 10-dB over most of this same band as shown in Fig. 6.31.

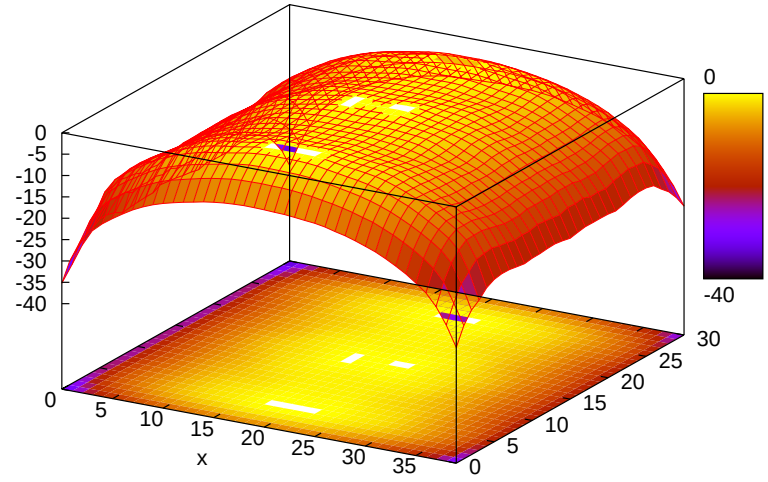

Figure 6.29: The measured near-field amplitude distribution of the horn used with the second 5x5 amplifier array without hardening.

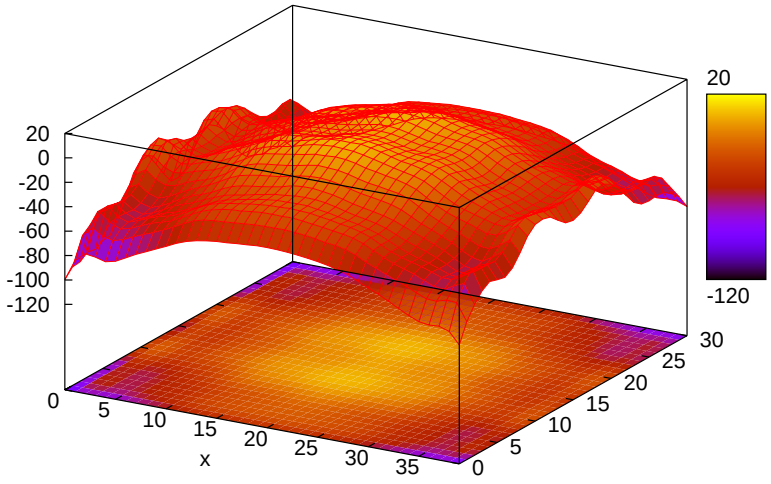

Figure 6.30: The measured near-field amplitude distribution of the horn used with the second 5x5 amplifier array without hardening.

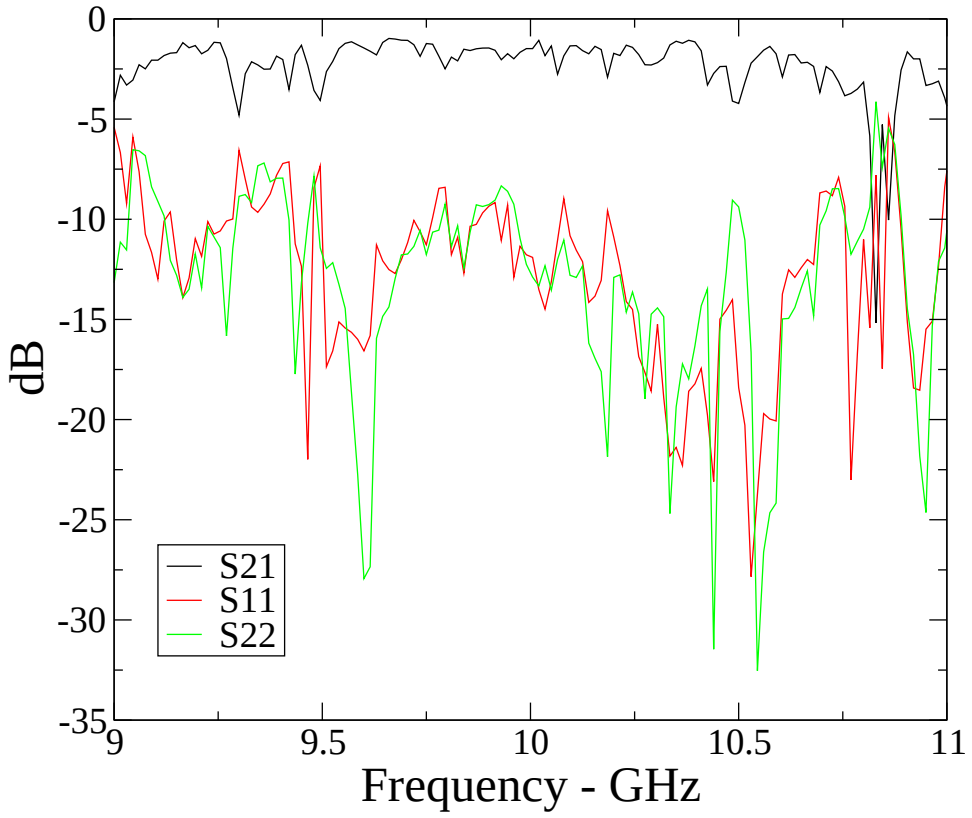

Figure 6.31: The measured insertion loss and return loss of the two hard-horn feeds back-to-back for the second version of the 5x5 array.

6.3.3 Array Measurement Results

Several experiments were performed to test the active and passive versions of the array. This included both near-field and far-field measurements. The near-field measurements were performed with an input and output hard-horn as illustrated by Fig. 4.3. This setup was used to measure the passive array insertion loss and to measure the small signal gain of the active array. The passive array insertion loss and return loss are illustrated in Fig. 6.32, where the insertion loss is 5 dB at 10 GHz with a 3-dB bandwidth of 315 MHz. Fig. 6.33 shows the small signal gain of the active 5x5 perpendicularly-fed array with hard-horn feeds. The amplifier array provided 16 dB of gain with 280 MHz of 3-dB bandwidth.

In addition to the small signal gain, the output power versus input power was measured in both a near-field and far-field configuration. The measurement setups for both experiments are shown in Fig. 6.34. The first experiment, shown in Fig. 6.34(a), is a closed system containing the amplifier array with both feeding and collecting hard-horns. In this experiment, the power compression curve of the amplifier array was measured and is shown in Fig. 6.35 at 9.6 GHz, where 29.1 dBm

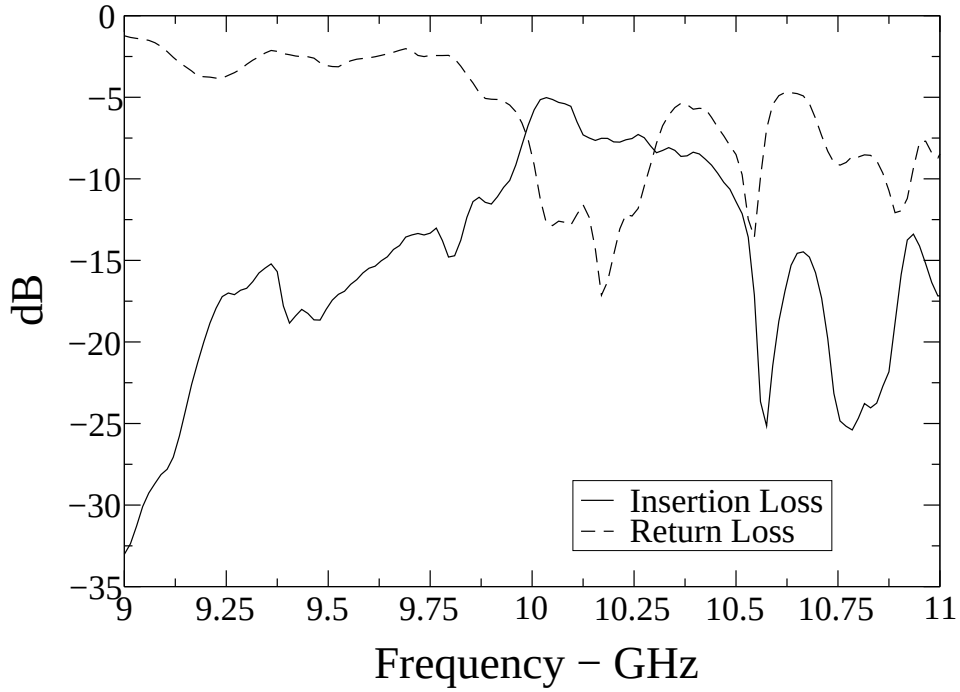

Figure 6.32: The measured insertion loss and return loss of the second version of the passive 5x5 array.

was obtained under 3-dB compression. This results in nearly 50% power combining efficiency, since the unit cell can provide 18.4 dBm under 3-dB compression. In addition, this gives a power added efficiency (PAE) of 4.3% at 9.6 GHz.

For the second experiment, the effective transmitter power was found [111] using the setup shown in Fig. 6.34(b). The array was placed at a distance of 1 m from a standard gain horn having a gain of 16 dB at 9.6 GHz. The directivity of the array was calculated to be 17.8 dB using the following formula based on the physical size of the antenna array [89]:

$$D_t = \frac{4\pi A}{\lambda_0^2} \tag{6.2}$$

where A is the area of the array, and λ_0 is the free space wavelength. The effective transmitter power can then be found as follows:

$$P_e = \frac{P_r}{D_t G_r} \left(\frac{4\pi R}{\lambda_0}\right)^2 \tag{6.3}$$

where D_t is the directivity of the transmitting antenna, G_r is the gain of the receiving antenna, R is the distance between the transmitting and receiving antenna, and P_r is the power received at the receiving antenna. Therefore if the power received at the standard gain horn is known, the effective

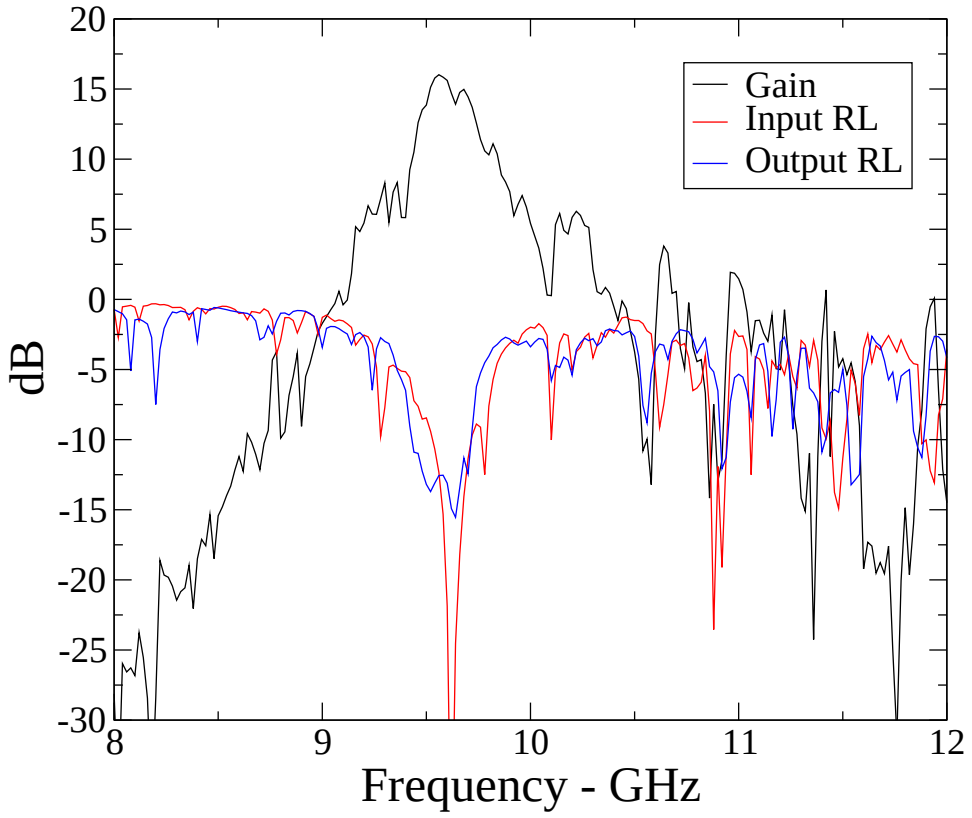

Figure 6.33: The measured small signal gain and return loss of the second version of the active 5x5 array.

transmitter power can be found. The resulting power versus input power to the array is shown in Fig. 6.36. The resulting effective transmitter power under 3-dB compression was 28.4 dBm. This is less than the gain and output power of the closed system, which has the additional combining loss of the hard-horn feed at the output.

6.3.4 Device Failure Analysis

Two experiments were performed to test the fault tolerant behavior of the spatial power combining amplifier array. The first experiment was a closed near-field measurement as shown in Fig. 6.34(a). In this experiment, the power compression curve of the amplifier array was measured for several cases of device failures. In each case, the frequency was set to 9.6 GHz, and the input power was swept from 0 to 25 dBm. The power compression curves for several device failures are shown in Fig. 6.37. In each case (1 cell, 2 cells, etc.), 5 random combinations of cells were chosen (turned off) and measured with the exception of the 1 cell case. For this case, all 25 cells were turned off one at a time. The worst case performance degradation (lowest gain) was plotted for all combina-

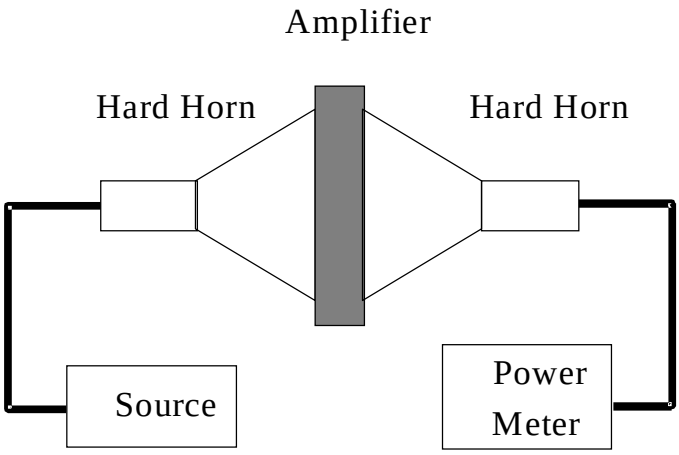

(a)

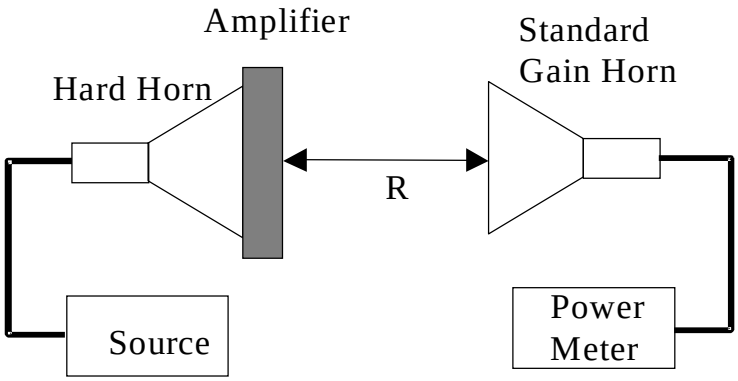

(b)

Figure 6.34: (a)A near-field and (b) far-field power compression measurement setup: $R > 2D^2/\lambda_0$.

tions of the device failure measurements. Simulated results for the same experiment are shown in Fig. 6.38. The amplifiers were modeled using the reported gain and compression characteristics of the MMIC amplifier, due to the lack of a nonlinear model for it. As can be seen when 20% of the active devices fail across the array, the measured array gain drops by approximately 2.7 dB while simulations predict 1.9 dB of drop in gain. These results compare well to the expected loss in power of 36%. This expected loss is true when the power division to each cell in the array is considered uniform. For an array with N unit cells, the coupling or transmission coefficient, T_n, to each unit cell, n, is:

$$T_n = \frac{1}{\sqrt{N}} \tag{6.4}$$

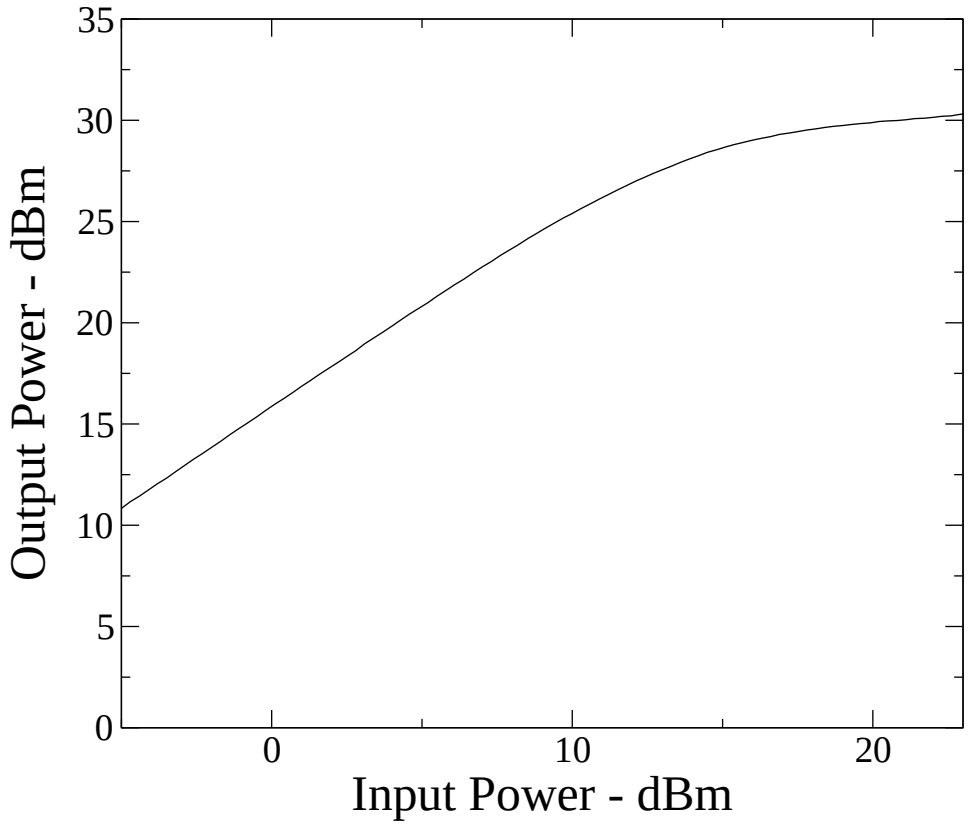

Figure 6.35: The measured output power versus input power of the second 5x5 amplifier array at 9.6 GHz in a near-field measurement setup.

This represents the S_{n1} and S_{1n} S-parameter coefficients. However, this represents only half the problem. To obtain the total transmission, the input and output networks must be cascaded, yielding the following transmission coefficient for an ideal network with perfectly matched ports:

$$T = \sum_{1}^{N} \frac{1}{N} \tag{6.5}$$

The normalized power will be represented by T^2 and should equal unity when all the amplifiers are operational. When only n amplifiers are operational, the total output power is lower and is given the following expression:

$$P_c = P_0 \left(\frac{n}{N}\right)^2 \tag{6.6}$$

where P_c is the total combined power, P_0 is the ideal combined power (power per unit cell times the number of cells), n is the number of active cells, and N is the total number of cells. Therefore the theoretical efficiency of the power combiner with n cells active is given by:

$$\eta_n = \left(\frac{n}{N}\right)^2 \tag{6.7}$$

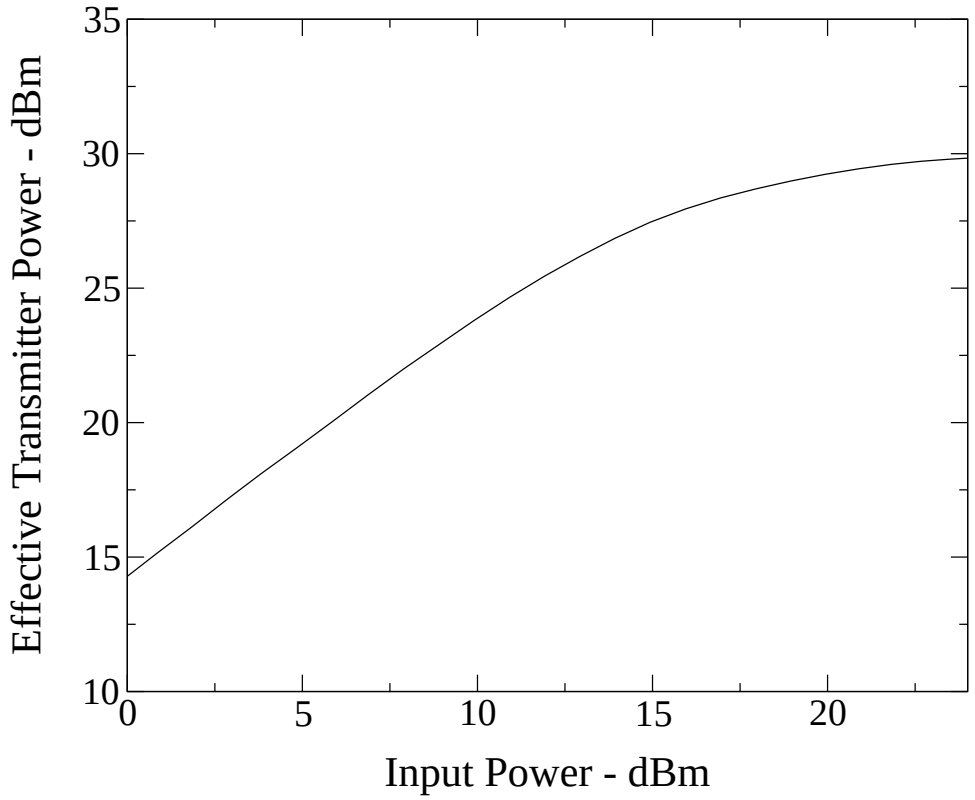

Figure 6.36: The measured output power versus input power of the second 5x5 amplifier array at 9.6 GHz in a far-field measurement setup at a distance of 1 m.

This equation gives an efficiency of 64% when 20% of the devices are failed or a reduction in power of 36%. The 1.9 dB of simulated loss is just slightly less than the theoretical 1.94 dB of power lost when 20% of the devices failed. In fact, the 2.7 dB reduction in power for the experimental case is only 10% below the best expected results.

It should be noted that the worst case cells are typically at the center of the array, indicating errors in the uniformity of the power distribution across the horn aperture. This may explain why the curves converge under compression in the experiment, since under compression the device output power varies less for a given input power.

For the second experiment, the effective transmitter power was found using the measurement setup illustrated in Fig. 6.34(b). The array was again placed at a distance of 1 m from a standard gain horn having a gain of 16 dB at 9.6 GHz. The directivity of the array was calculated to be 17.8 dB as discussed in the previous section. The same cells were then turned off as with the closed system. Fig. 6.39 shows the results for this experiment.

One additional set of simulations were performed for the failure analysis. Furthermore, the far-field radiation pattern was calculated using *PCAAD*™ for the same device failures previously simulated.

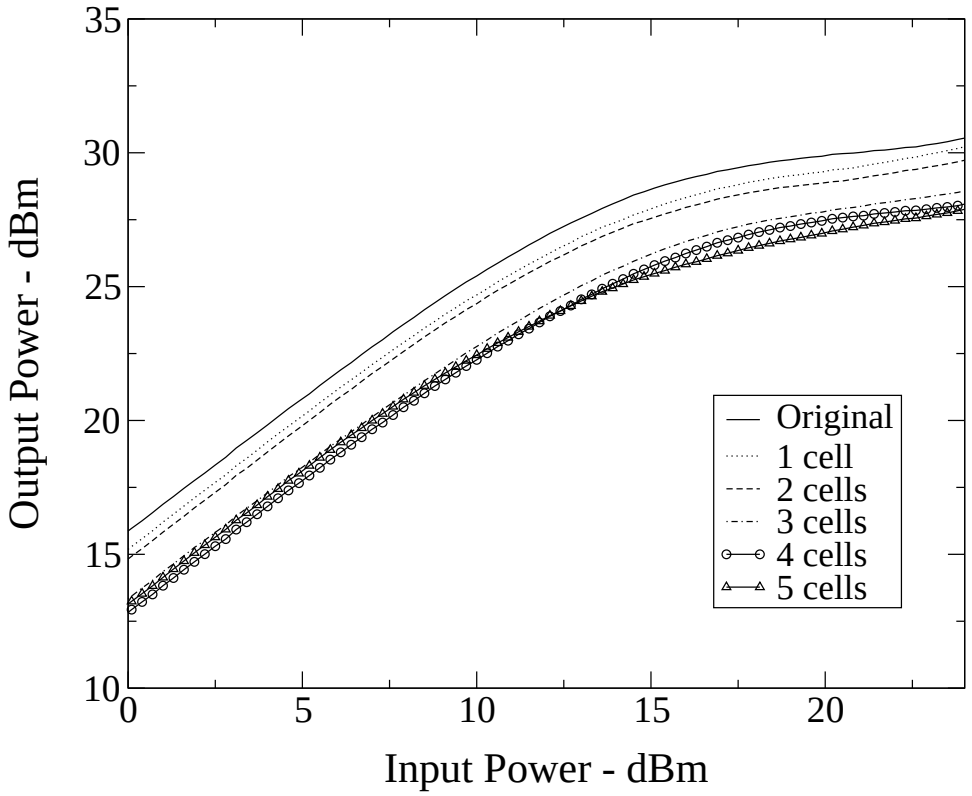

Figure 6.37: The measured output power versus input power of the second 5x5 amplifier array at 9.6 GHz in a near-field measurement setup for several device failures.

The antenna excitation (magnitude and phase) was extracted from the electromagnetic simulation for a case in which no collecting hard-horn feed was present. Furthermore, this simulation included the input horn excitation cascaded with the method of moments model for the array and finally with the amplifiers. Each amplifier was then terminated with a port. The resulting 26-port simulation yielded the input excitation to each microstrip patch antenna used in the *PCAAD*™ simulation. In all cases, the main lobe of the radiation pattern is unaffected and only the sidelobe levels increase by several dB when 20% of the array elements fail, as illustrated by the E- and H-plane radiation patterns shown in Figs. 6.40 and 6.41.

6.4 A 49-Element Array

In the previous two sections, the design, fabrication, and experimental results for two X-band tray-based arrays were presented. These designs were based on the perpendicularly-fed patch antenna and microstrip-to-waveguide transition introduced in Section 6.1. In this section, a Ka-band version of the tray-based array will be discussed, including the design, fabrication, and experimental

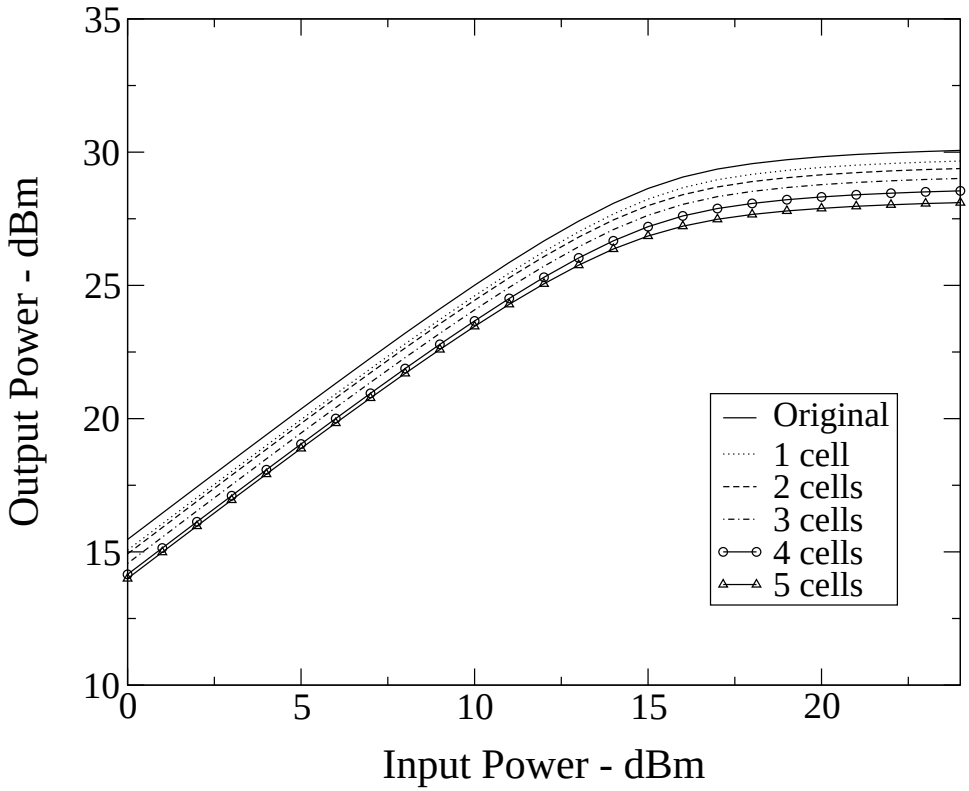

Figure 6.38: The simulated output power versus input power of the second 5x5 amplifier array at 9.6 GHz in a near-field measurement setup for several device failures.

results. A photograph of the new Ka-band array is shown in Fig. 6.42. It is conceptually identical to the previous designs at X-band.

The X-band tray-based array has been extended to the Ka-band frequency range for the verification of the perpendicularly-fed tray-based spatial power combining concept at millimeter-wave frequencies. In addition, the potential for efficient power combining and high output power levels was desired. Such potential for high combining efficiencies are a direct result of previous experiments at X-band. A scaled version at Ka-band is therefore expected to deliver similar combining efficiencies. Furthermore, the system topology provides an amiable framework for the verification of the fault tolerant nature of spatial power combining arrays at millimeter-wave frequencies.

The conceptual view of the perpendicularly-fed patch array was shown in Fig. 6.1. This same configuration will again be used in the design of a 7x7 array at Ka-band. In this figure, the hard-horn feed on the left of the diagram irradiates the array of microstrip patch antennas with a uniform electric-field (both in amplitude and phase). This signal is then coupled through an aperture in the microstrip groundplane to a dielectric filled waveguide (seen on the lower right side of the figure). A microstrip-to-waveguide transition then couples the energy into a microstrip transmission line,

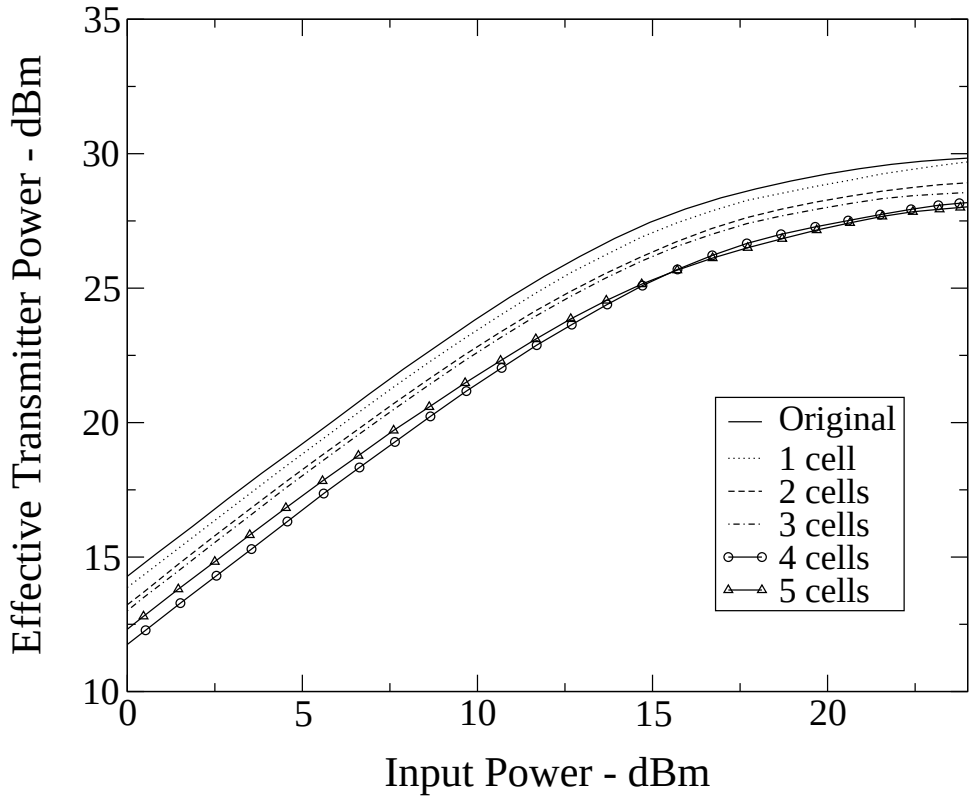

Figure 6.39: The measured output power versus input power of the second 5x5 amplifier array at 9.6 GHz in a far-field measurement setup at a distance of 1 m for several device failures.

where it then passes through an amplifier. After amplification, the signal is radiated into free space in the same manner as it was received on the input side of the array. A more detailed description of the perpendicularly-fed patch antenna and microstrip-to-waveguide transition can be found in Section 6.1.

In the following subsections, the design, fabrication, and experimental results for a 7x7 perpendicularly-fed, tray-based amplifier array will be given. This will include a discussion of the unit cell design (antennas, microstrip-to-waveguide transitions, and amplifier circuitry), the hardware assembly, and the hard-horns. In addition, experiments will be performed on both a passive and active version of the 49-element array. The insertion loss and gain of both the active and passive arrays will be measured. Furthermore, the output power versus input power will be obtained for the active array, including cases in which devices are turned off (fault tolerance analysis). Finally, thermal data will be included as part of the active array analysis.

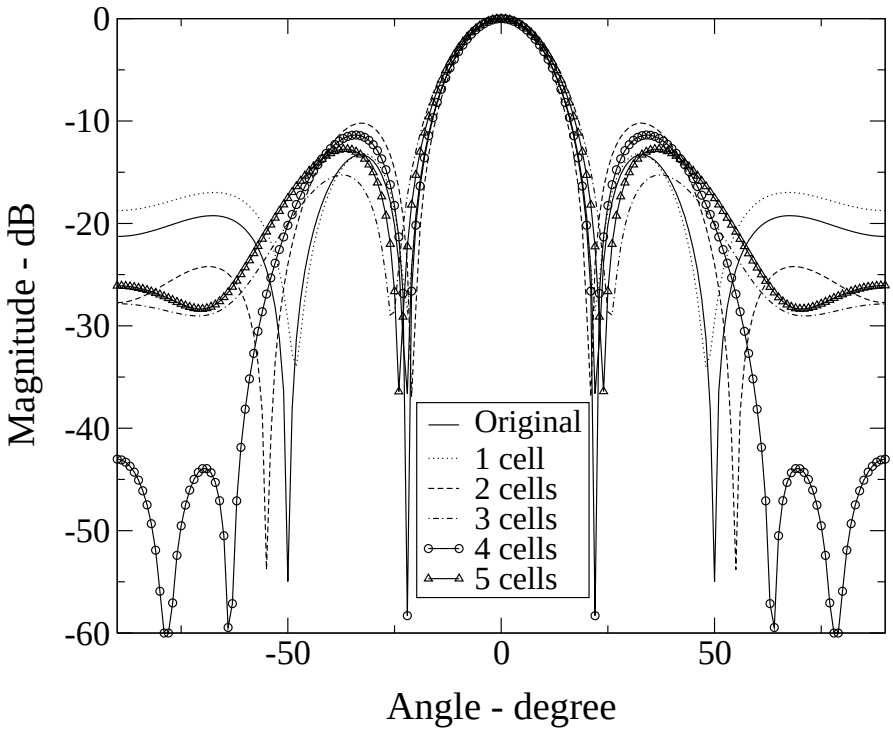

Figure 6.40: The simulated E-plane radiation pattern for the 5x5 amplifier array at 9.6 GHz.

6.4.1 Unit Cell Design

The unit cell design for the 49-element array includes the design of the perpendicularly-fed patch antenna, the microstrip-to-waveguide transition, and the amplifier biasing circuitry. An illustration of the perpendicular-fed patch antenna and microstrip-to-waveguide transition was given in Fig. 6.2, where the dielectric filled waveguide was formed by stacking the individual trays shown in Fig. 6.1. In addition, the perpendicularly-fed patch antenna and microstrip-to-waveguide transition have been discussed thoroughly in Section 6.1 of this chapter. Therefore, only the results of this design process will be given in this section for these components. However, a detailed discussion of the amplifier circuitry will be presented, since this is specific to the 49-element array.

The operating frequency of operation of the Ka-band tray based amplifier was chosen to be 32 GHz For this array, a frequency of 32 GHz was chosen. This choice was due to several factors, including the optimum operating point of two hard-horn feeds, which were previously designed. Again, the perpendicularly-fed patch antenna was simulated using *Agilent - HFSS*™ as was described in Section $6.1.1$. The resulting dimensions for the perpendicularly-fed microstrip patch antenna are as follows:

$$L_p \quad = \quad 2.159 \text{ mm}$$

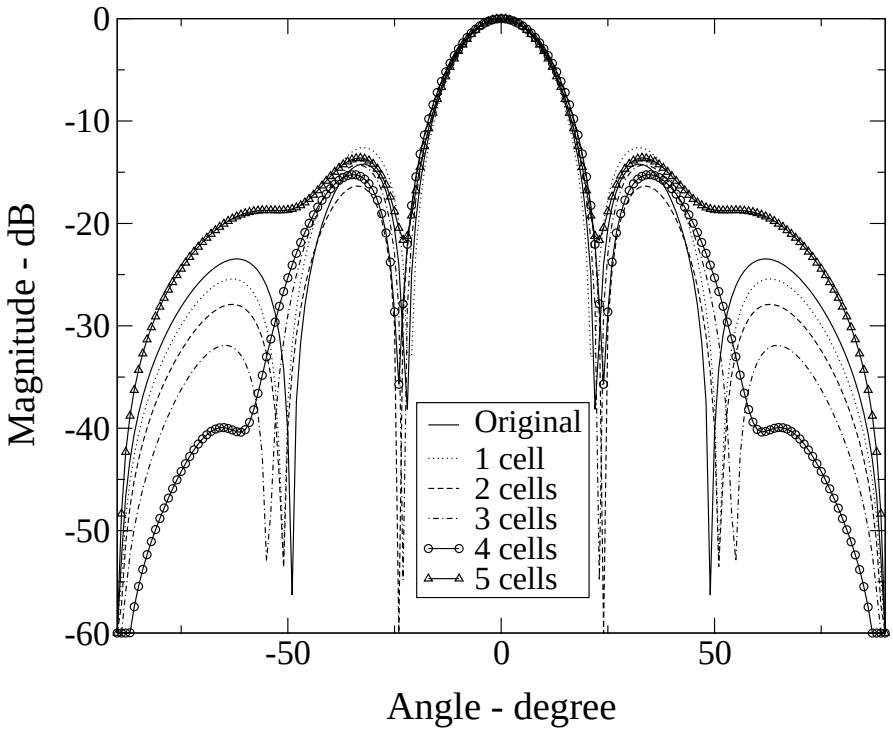

Figure 6.41: The simulated H-plane radiation pattern for the 5x5 amplifier array at 9.6 GHz.

$$
\begin{aligned}
W_p &= 2.9972 \text{ mm} \\
L_s &= 1.6 \text{ mm} \\
H_s &= 0.254 \text{ mm} \\
H_w &= 0.254 \text{ mm} \\
W_w &= 2.286 \text{ mm} \\
L_w &= 2.54 \text{ mm}
\end{aligned}
$$

where L_p and W_p are the resonant length and width of the patch antenna, L_s and H_s are the length and height of the slot aperture, and H_w, W_w, and L_w are the height, width, and length of the dielectric filled waveguide, respectively. In addition, a *Rogers TMM3*™ dielectric material with an $\epsilon_r = 3.27$, dissipation factor of 0.002, and thickness of 0.381 mm was used for the microstrip patch antenna substrate. A *Rogers RT6006*™ dielectric material with an $\epsilon_r = 6.15$, dissipation factor of 0.0027, and thickness of 0.254 mm was chosen for the dielectric filled waveguide. The resulting simulations yielded the return loss shown in Fig. 6.43. This simulation includes the effect of the dielectric filled waveguide, and thus the input port is looking into the microstrip transmission line. A 10-dB return loss bandwidth is achieved from 28.5 to 32 GHz.

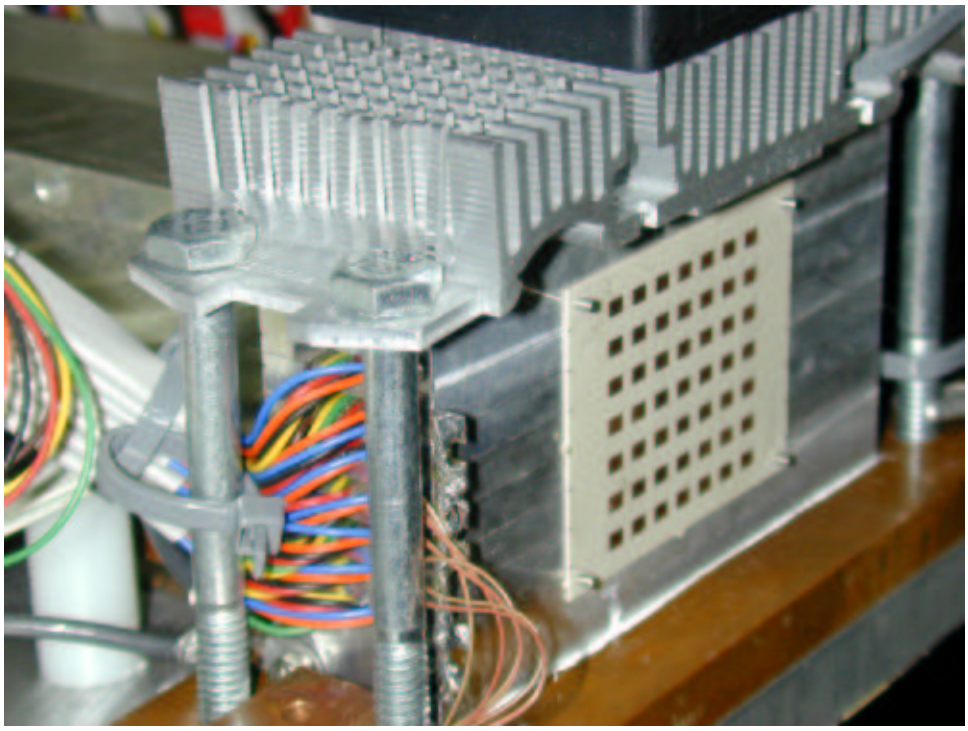

Figure 6.42: A photograph of the 49-element spatial power combiner being fed by a hard-horn.

A microstrip-to-waveguide transition was also designed in the same manner outlined in Section 6.1.2, (6.8). The dimensions of the dielectric filled waveguide were given above. Also, an impedance transformer was used to better match the impedance of the dielectric filled waveguide to the $50\ \Omega$ microstrip line. This was unfortunately necessary, since the design frequency was actually changed after the hardware was built. However, the design frequency of the microstrip-to-waveguide transition can be changed by the simple addition of an impedance transformer. The resulting dimensions of the transformer are as follows:

$$\begin{aligned} W_1 &= 0.7112\ \text{mm} \\ W_2 &= 0.5334\ \text{mm} \\ L_2 &= 1.1176\ \text{mm} \\ W_3 &= 0.381\ \text{mm} \end{aligned}$$

where W_1 is the width of the microstrip line in the waveguide, W_3 is the width of the $50\ \Omega$ microstrip line, and W_2 and L_2 are the width and length of the impedance transformer. The width of the microstrip line within the waveguide is actually the width of the waveguide. This allows a better connection to be formed between the top wall of the waveguide and the microstrip line. A simulation of two such transitions back-to-back was performed, and the resulting return loss and

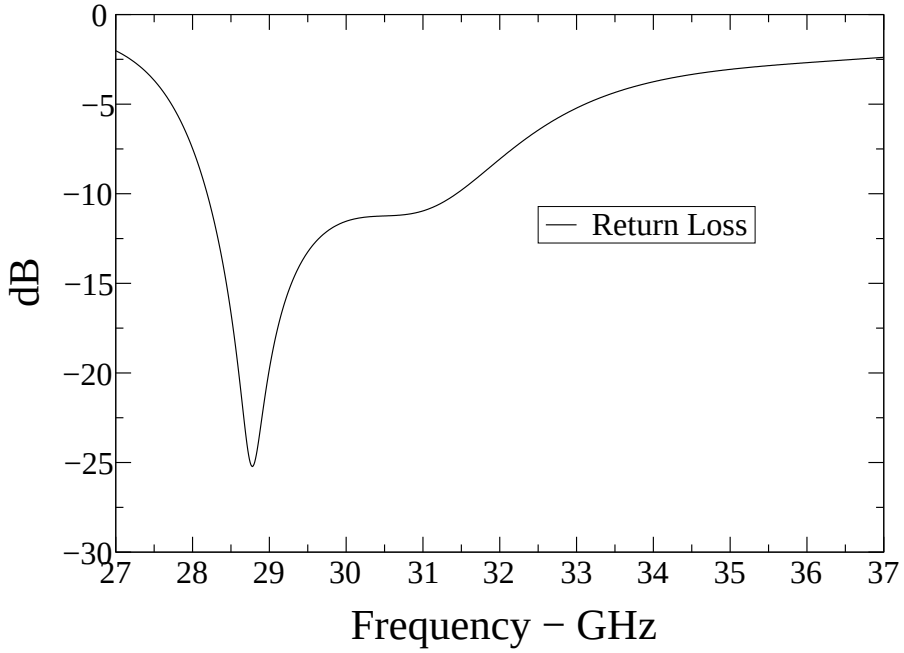

Figure 6.43: The simulated return loss of the perpendicularly-fed patch antenna for the 49-element array.

insertion loss are shown in Fig. 6.44. As can be seen in the figure, a low insertion loss of less than 0.5 dB is obtained from 30 GHz to 37 GHz.

The amplifier layout was the last portion of the unit cell design to be performed. For this layout, *Triquint TGA1073A*™ PHEMT MMIC amplifiers were used to provide gain. They provide a nominal 19 dB of gain with 25 dBm output power under 1-dB compression when biased at $V_{DS} = 6$ V and $I_{DS} = 220$ mA. The unit cell layout is shown in Fig. 6.45. The MMIC amplifier, as well as the microstrip lines, were epoxied to the aluminum tray using a two part silver epoxy (*EPO-TEK H20E*™) at $120°$C for 15 minutes. Three gold bondwires (0.0254 mm diameter) were used to connect the input and output of the amplifier to the microstrip lines. In addition, several capacitors were placed on the gate and drain bias lines for stability. These are illustrated in Fig. 6.45, where the smaller capacitors are single layer types with a capacitance of 100 pF, and the larger capacitors are 0.01μF chip capacitors. Furthermore, 47μF capacitors were placed along both the gate and drain bias lines to suppress low frequency oscillations. The resulting gain for the amplifier in a microstrip test fixture is shown in Fig. 6.46 along with the input and output return loss. Also, the output power versus input power was measured and is given in Fig. 6.47. Both measurements compare well with the data provided by the manufacturer.

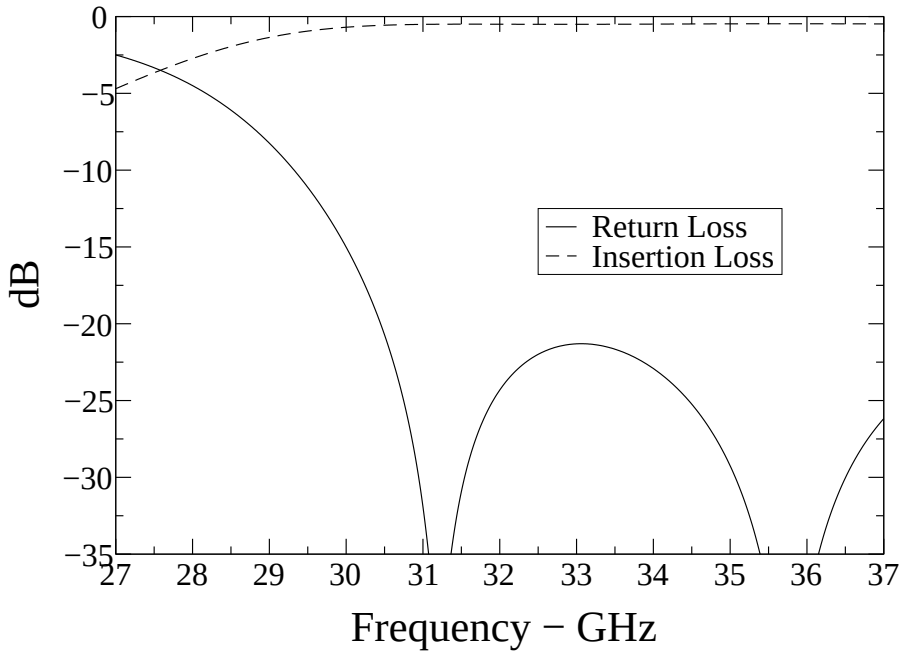

Figure 6.44: The simulated insertion loss and return loss of the microstrip-to-waveguide transition with microstrip-to-waveguide transition for the 49-element array.

6.4.2 Design of Array Hardware

The 7x7 array was constructed using seven trays, each holding seven unit cell circuits, and one cover layer. A photograph of the assembled structure is shown in Fig. 6.48. Two versions of the array were fabricated: one for the passive array and one for the active array. Both versions were basically the same, but with some additional size added to the active array version for improved thermal heat sinking. In addition, both designs followed the dimensions of the dielectric filled waveguide given in the previous section (2.54x2.286x0.254 mm). Furthermore, the total width of the tray is 25.4 mm, leaving 2.032 mm for the microstrip circuitry.

A more detailed illustration of the trays are given by schematics of the top, side, and front views shown in Figs. 6.49, 6.50, and 6.51, respectively. These illustrations are for the active array version of the tray. The passive version is slightly smaller, having a total width of 55.88 mm compared with the active array version width of 101.6 mm. In addition, an isometric view of the tray is shown in Fig. 6.52. This figure illustrates the recessed portion of the aluminum plate in which the dielectric filled waveguides are placed. The cavity can be seen in the bottom view of the tray. This cavity occupies the space above the microstrip lines and the MMIC devices.

After the aluminum trays were machined, the active and passive components were put in place. Each amplifying cell consisted of an input and output microstrip line, a MMIC amplifier, and five biasing capacitors. All components were epoxied to the aluminum tray using a two part silver

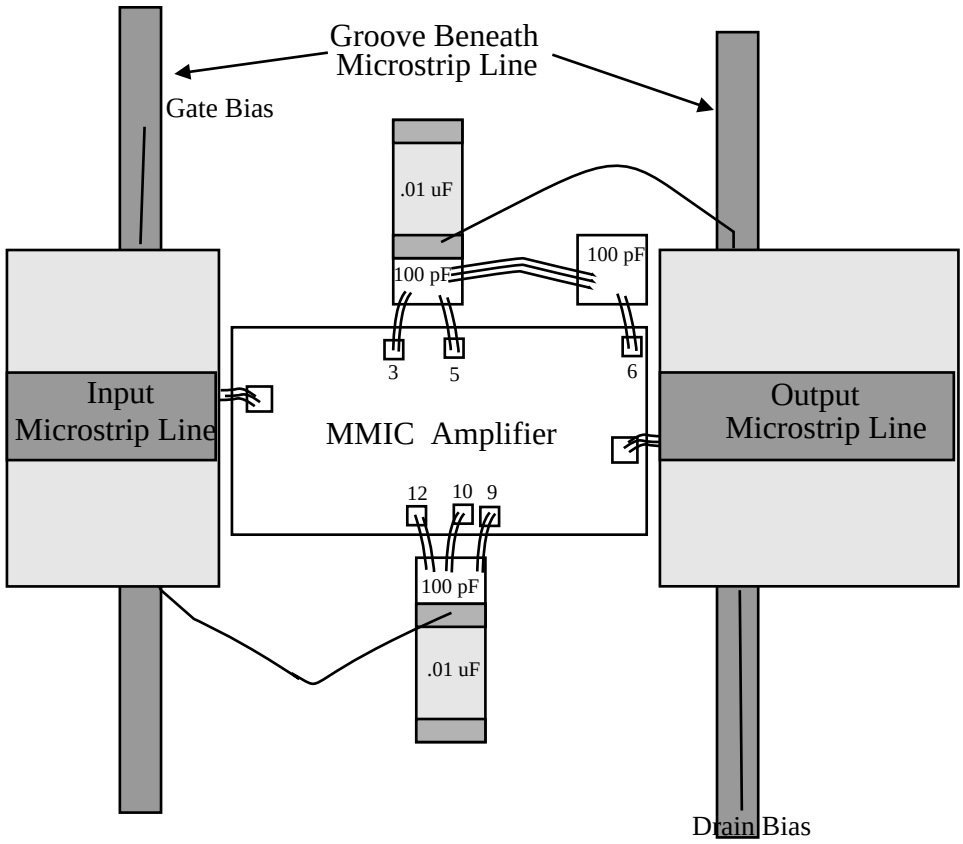

Figure 6.45: The amplifying cell of the 49-element array.

epoxy (*EPO-TEK H20E*™). A coated magnet wire (0.0508 mm diameter) was used to bias the gate and drain of each amplifier. These bias lines were placed in grooves machined into the aluminum plate, beneath the input and output microstrip lines. This allowed separate gate and drain bias lines for each amplifier in the array. This control would be necessary for the array fault tolerance study to follow. The resulting tray is shown in Fig. 6.53. It should also be noted that low frequency bias capacitors were placed along the gate and drain bias lines shown on the left and right sides of the tray.

The seven trays plus the cover tray were then stacked to form the array. After assembly, the input and output microstrip antennas were glued to the amplifier array using a low loss contact adhesive. This completed the amplifier array fabrication and is shown in Fig. 6.48.

Several other details in fabricating the array should be mentioned. For example, a copper gasket was placed between the trays to improve the connection between the microstrip lines and the top wall of the waveguide. This was found necessary during testing of the passive array (i.e. variations in phase resulted from inconsistent contacts). Since a cavity is present above each tray of

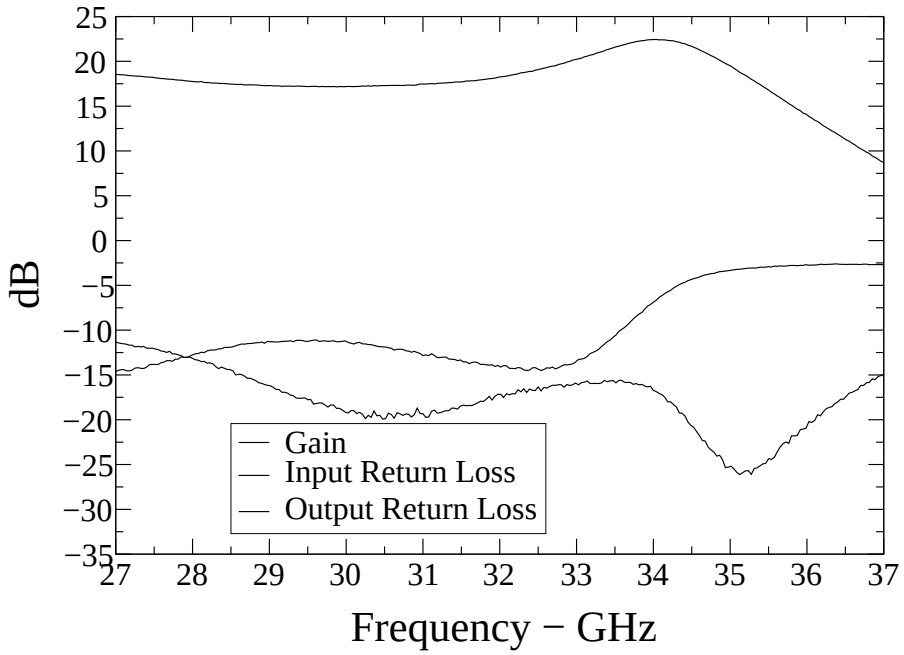

Figure 6.46: The gain and return loss of the *Triquint*™ amplifier in a microstrip test fixture.

amplifiers, the possibility of cavity mode oscillations is also present. To prevent such unwanted oscillations from occurring, an *Eccosorb BSR-1/SS 6M*™ microwave absorbing material with a thickness of 0.254 mm was placed along the top wall of the cavity. With this addition, no oscillations were observed in the active array.

To facilitate the failure analysis of the 49-element array, an external biasing circuit was fabricated. This circuit consisted of potentiometers for each gate bias line and single-pole, double-throw (SPDT) switches for each drain bias line. The potentiometers allowed each amplifier's current to be adjusted for the optimum 220 mA specified by the data sheet at a fixed drain voltage of 6 V. Also, the SPDT switches allowed the individual amplifiers to be turned on or off to simulate the effect of device failures. These components can be seen in a photograph of the complete assembled active array shown in Fig. 6.54. In addition, fans were placed above the array and also at the side of the array for improved air flow. The potentiometers can be seen in the foreground of the figure, while the SPDT switches are visible on the far side of the figure.

6.4.3 Unit Cell Measurement Results

Experiments were performed on both the passive and active versions of the unit cell, using waveguide probes. This was necessary for the characterization of the unit cell amplitude and phase variations within the array. It was also performed on a single unit cell to verify the operating

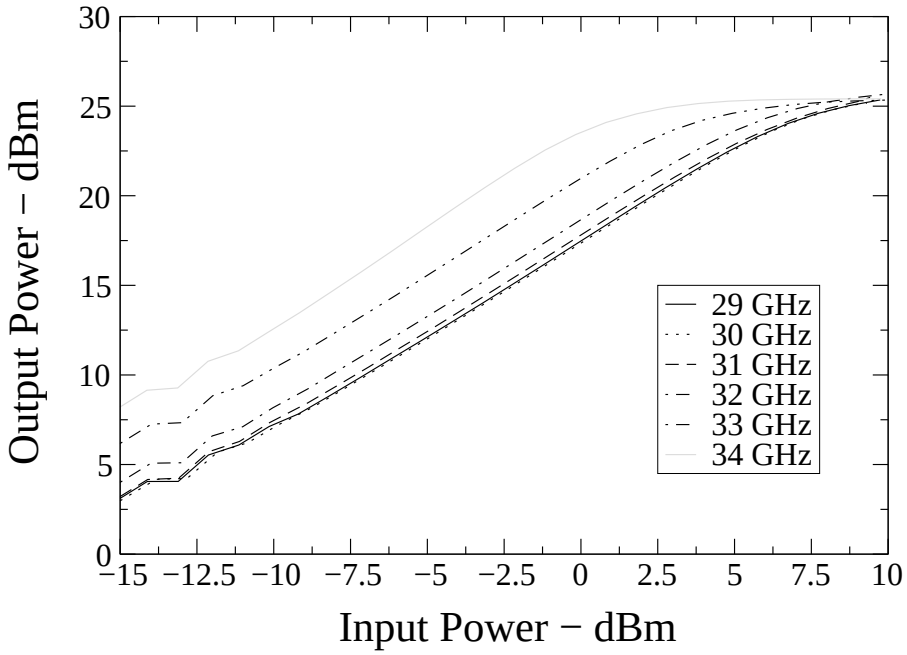

Figure 6.47: The output power versus input power for the *Triquint*™ amplifier at several frequencies.

performance before populating the entire array. These experiments were performed using the procedure outlined in Section $4.2.2$.

The passive array unit cell was measured first with the waveguide probes nearly in contact with the antenna substrate. The results of this measurement are shown in Fig. 6.55. The resulting insertion loss is 4.2 dB at 31.975 GHz with a 3-dB bandwidth of more than 4.35 GHz. Also after fabricating the entire array, a variation of ± 1.1 dB in magnitude and $\pm 30^\circ$ in phase was observed over the 49 unit cells, using the same procedure. The passive array loss from a single unit cell is quite low. In fact, less than 2.1 dB is from a single antenna feed and half the microstrip circuitry. Since the microstrip circuitry only contributes 0.2 dB, the loss of the perpendicularly-fed patch antenna to the microstrip-to-waveguide transition is less than 1.9 dB, yielding an efficiency of 65%. Furthermore, this should be less due to the losses unaccounted for by the waveguide probe.

The active array unit cell was also measured, using the waveguide probe technique. Again, the probes are placed nearly in contact with the antenna substrate. The active array unit cell provided 12 dB of gain at 31.9 GHz. The variation in unit cell performance was also measured across the entire array using waveguide probes. The magnitude varied by ± 1.8 dB and the phase by $\pm 40^\circ$ at 31.9 GHz.

As was mentioned in the hardware design, a copper gasket placed between the trays improved the variation between unit cells. This is perhaps due to an inconsistent contact between the microstrip

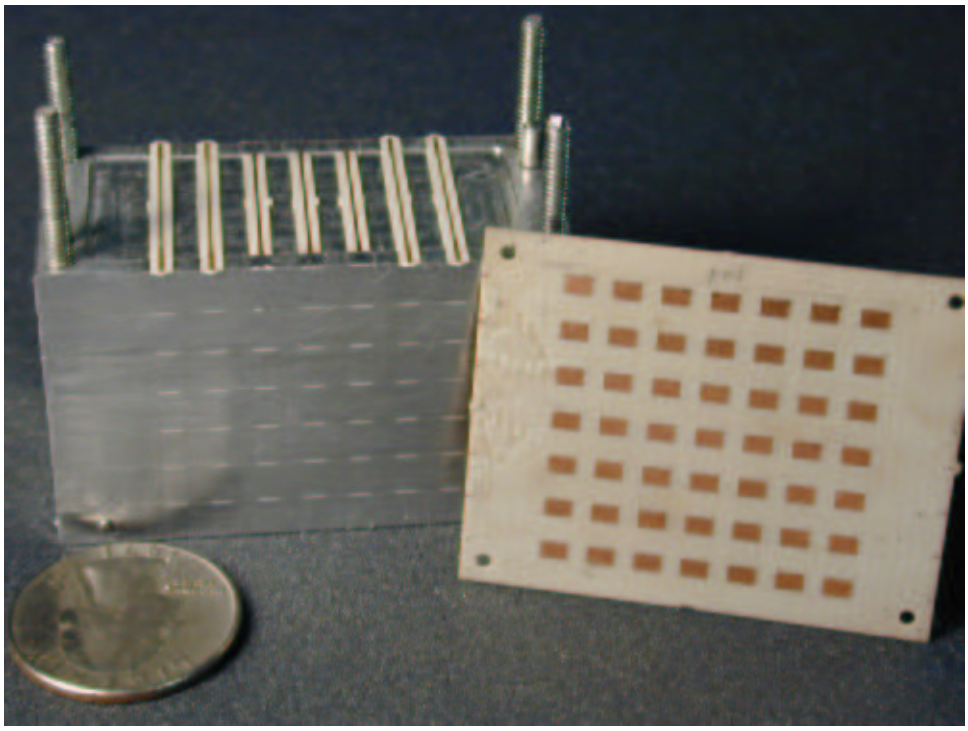

Figure 6.48: A photograph of the partially assembled 49-element array.

line and the top wall of the dielectric filled waveguide. Another possibility is from a poor contact between the top wall of the waveguide and the sidewalls of the waveguide. The latter possibility will actually effect the phase more due to the high current along this edge.

6.4.4 Hard-Horn Feed

Two hard-horn feeds were designed and fabricated using the same method outlined in Chapter 3. Both horns were custom designed and fabricated. The resulting dimensions of the optimized hard-horn are as follows:

$$\begin{aligned} a_1 &= 51 \text{ mm} \\ b_1 &= 42 \text{ mm} \\ \rho_1 &= 161 \text{ mm} \\ \phi_1 &= 9.62^\circ \\ \rho_2 &= 153 \text{ mm} \\ \phi_2 &= 7.82^\circ \end{aligned}$$

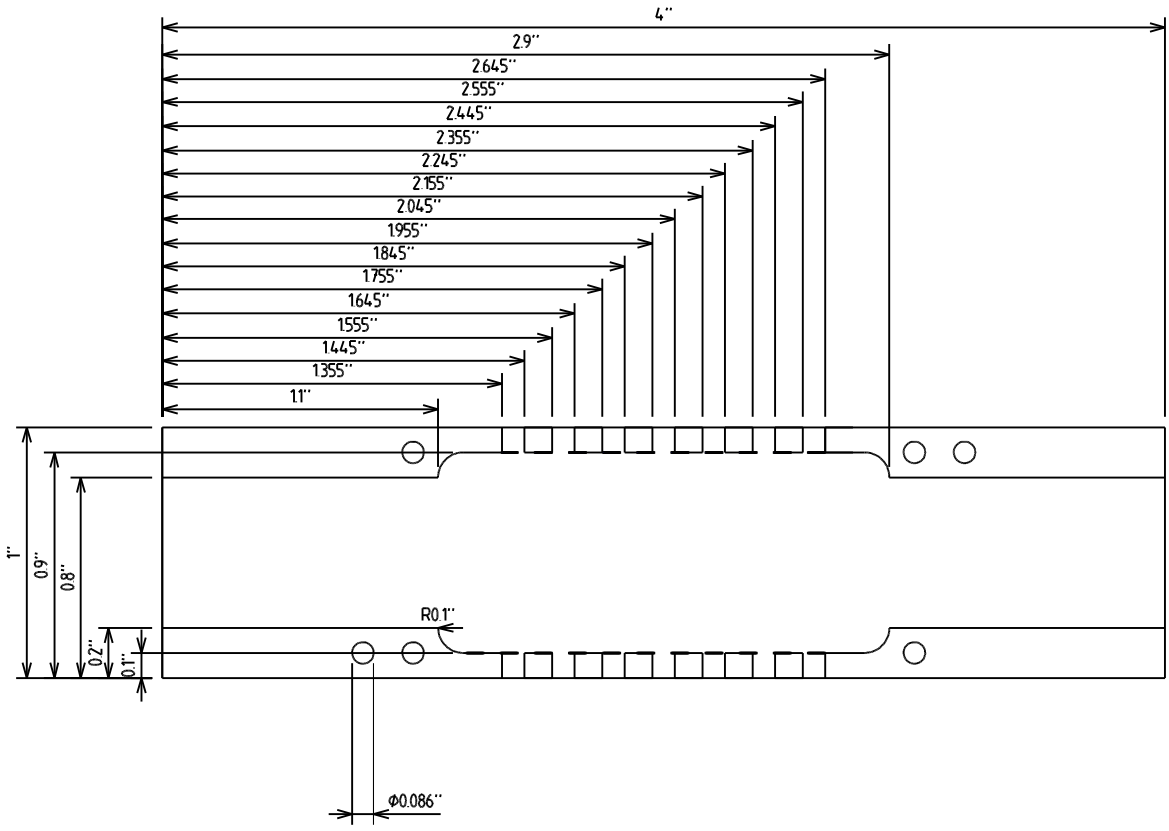

Figure 6.49: A schematic drawing of a tray for the 49-element array (Top View).

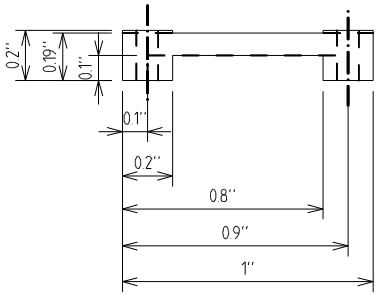

Figure 6.50: A schematic drawing of a tray for the 49-element array (Side View).

where the definition of the dimensions were given by Figs. 3.3(a) and 3.3(b). A substrate with an $\epsilon_r = 1.4$ and thickness of 4.572 mm was used for the dielectric side walls. Furthermore, the lens was fabricated from an $\epsilon_r = 1.14$ dielectric foam.

Several measurements were performed on the hard-horn antenna. First, the near-field magnitude

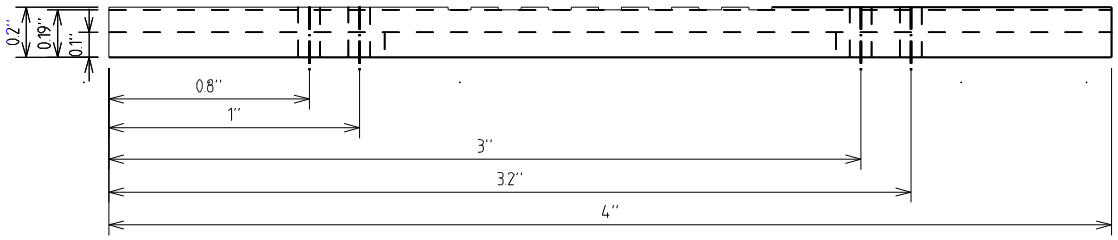

Figure 6.51: A schematic drawing of a tray for the 49-element array (Front View).

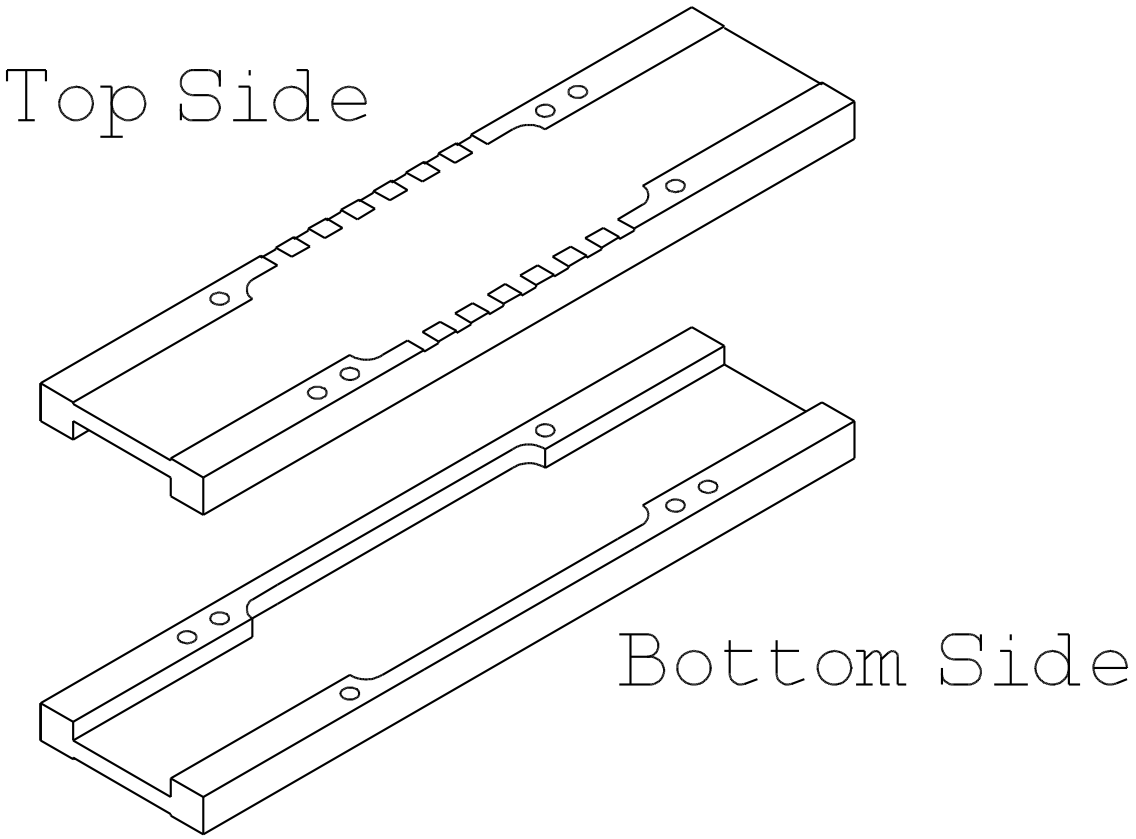

Figure 6.52: A schematic drawing of a tray for the 49-element array (Isometric View).

and phase was measured and are shown in Figs. 6.56 and 6.57, respectively. These figures give a qualitative view of the field uniformity across the horn aperture. In addition, the insertion loss and return loss of the hard-horn antennas were measured in a back-to-back configuration as illustrated in Fig. 4.3. The resulting insertion loss is less than 1.5 dB from 30.5 GHz to 33 GHz, and the return loss is less than 10-dB over this same band as shown in Fig. 6.58.

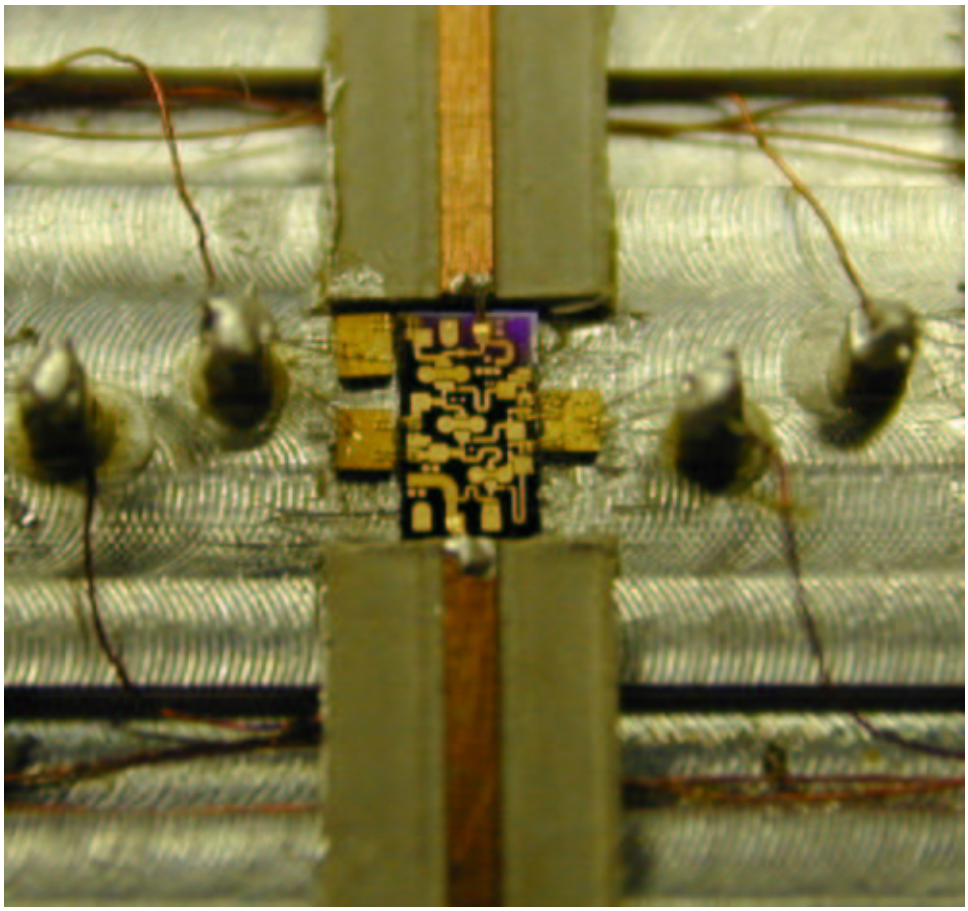

Figure 6.53: A photograph of a unit cell within the 49-element array.

6.4.5 Array Measurement Results

As with the other amplifier arrays, several measurements were performed on both the passive and active versions of the array. These measurements included both near-field and far-field experiments for the evaluation of the passive array insertion loss and for the small and large signal performance of the active array. The near-field measurements were performed with an input and output hard-horn as illustrated by Fig. 4.3. This setup was used to measure the passive array insertion loss and to measure the small signal gain of the active array. The passive array insertion loss and return loss are illustrated in Fig. 6.59, where the insertion loss is 5.3 dB at 32 GHz with a 3-dB bandwidth of 2.7 GHz. Fig. 6.60 shows the small signal gain of the active 7x7 perpendicularly-fed array with hard-horn feeds. The amplifier array provided 11.6 dB of gain with 1 GHz of 3-dB bandwidth.

In addition to the small signal gain, the output power versus input power was measured in both a near-field and far-field configuration. The measurement setups for both experiments are shown in Fig. 6.34. The first experiment, shown in Fig. 6.34(a), is a closed system containing the amplifier

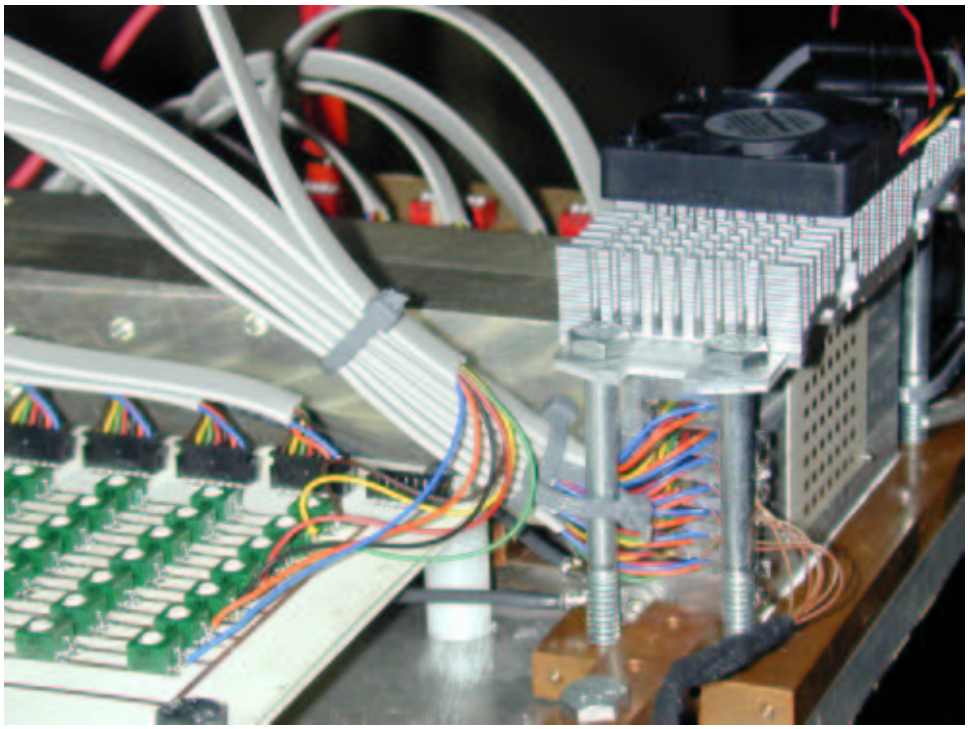

Figure 6.54: A photograph of a the active 49-element array.

array with both feeding and collecting hard-horns. In this experiment, the power compression curve of the amplifier array was measured and is shown in Fig. 6.61 at 31.9 GHz, where 37.1 dBm or 5.12 Watts was obtained under 1-dB compression. This results in nearly 36% power combining efficiency, since the unit cell can provide about 24.5 dBm under 1-dB compression. In addition, this gives a power added efficiency (PAE) of 7.6% at 31.9 GHz. Unfortunately, the amplifier was not compressed into saturation. Therefore, power combining efficiencies under higher compressions are not available.

For the second experiment, the effective transmitter power was found using the setup shown in Fig. 6.34(b). The array was placed at a distance of 40 cm from a standard gain horn having a gain of 24 dB at 32 GHz. The directivity of the array was calculated to be 21.9 dB using Eq. 6.2 based on the physical size of the antenna array. The effective transmitter power was then found using Eq. 6.3. The resulting effective transmitter power versus input power to the array is shown in Fig. 6.62. The resulting effective transmitter power under 1-dB compression was 35 dBm.

6.4.6 Device Failure Analysis

Several experiments were performed to determine the amplifier's output power degradation as a function of multiple device failures in the 49-element tray-based amplifier array. The first experi-

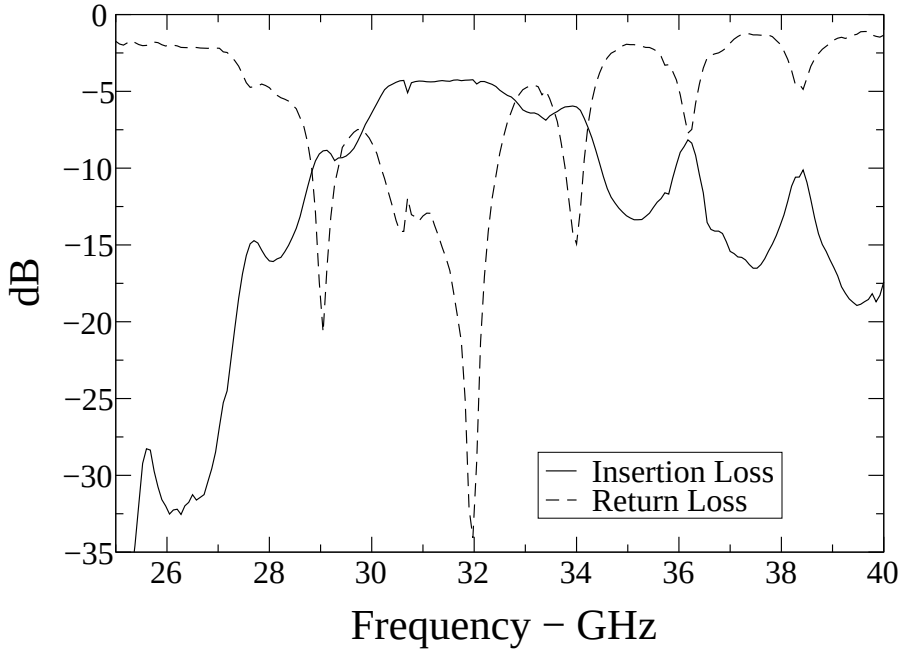

Figure 6.55: The measured insertion loss of a unit cell in the passive 49-element array using waveguide probes.

ment was a closed near-field measurement as shown in Fig. 6.34(a). In this experiment, the output power versus input power of the amplifier array was measured for several cases of device failures. In each case, the frequency was set to 31.9 GHz, and the input power was swept from 6 to 28 dBm. The power compression curves for several device failures are shown in Fig. 6.63. In each case (1 cell, 2 cells, 3 cells, etc.), random combinations of cells were chosen (turned off). The worst case performance degradation (lowest gain) was plotted for all combinations of the device failure measurements. In addition, each row and column of the array were turned off. The resulting measurements are shown in Figs. 6.64 and 6.65 for the rows and columns, respectively. As can be seen when 16% (8 of 49) of the active devices fail across the array, the measured array gain drops by approximately 2.2 dB. This result compares well to the expected loss in power of 30% or 1.55 dB. This is based on the expression for combining efficiency given in Eqs. 6.6 and 6.7.

It should be noted that the worst case cells are typically at the center of the array, indicating errors in the uniformity of the power distribution across the horn aperture. If the field distribution were completely uniform, then the loss would be the same regardless of which cell was turned off, since all of the cells would have the same output power. This may explain why the curves become closer under compression in the experiment, since under compression the device output power varies less for a given input power.

Additionally, thermal measurements were performed for the failure analysis. Furthermore, the temperature of each tray was measured using a thermocouple beneath the center of each tray. The

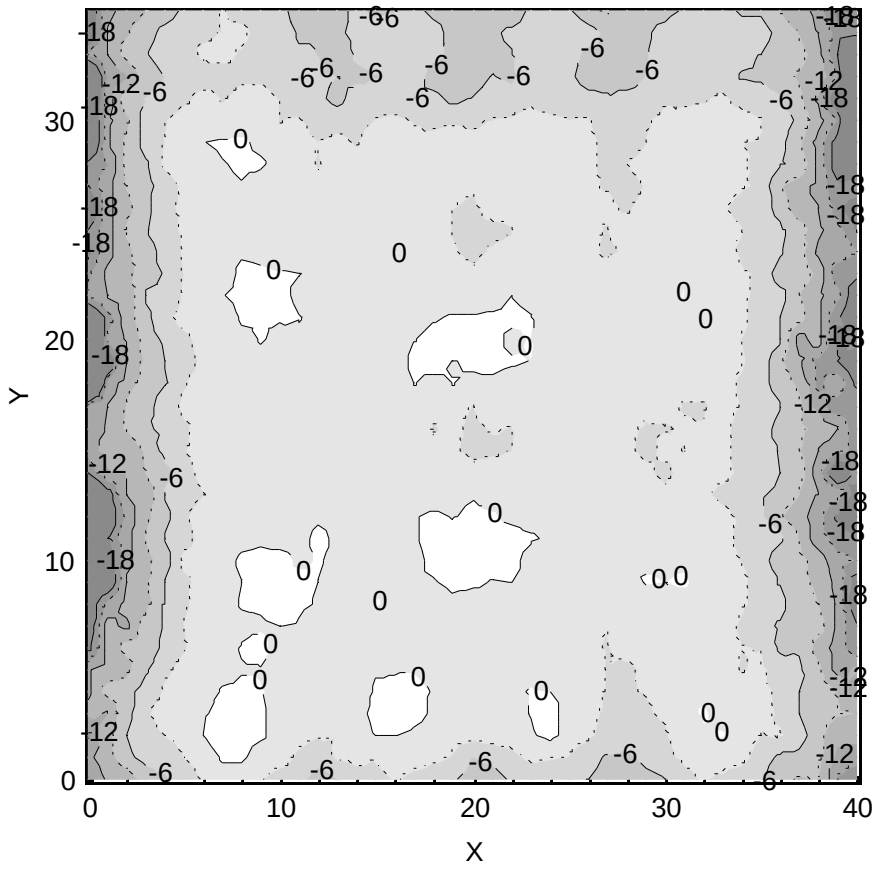

Figure 6.56: The measured near-field amplitude distribution of the hard-horn used in the 7x7 amplifier array at 32 GHz.

temperature was measured versus time for several experiments. The resulting temperature curves versus time are shown in Fig. 6.66, where six trays have been measured. The bottom tray is not given, since the aluminum thickness is significantly larger than that of the other trays. As expected, the center trays heat up more quickly than those at the top or bottom. It should be noted that the amplifier was biased from approximately 30 seconds until 75 seconds. This corresponds to the rapidly increasing temperature. After the array was turned off, the temperature decayed gradually back to the ambient room temperature. A steady state temperature was never observed, since the amplifier array was not biased for any larger lengths of time. Such experimentation should however be precluded by thermal analysis, which were not performed for this array.

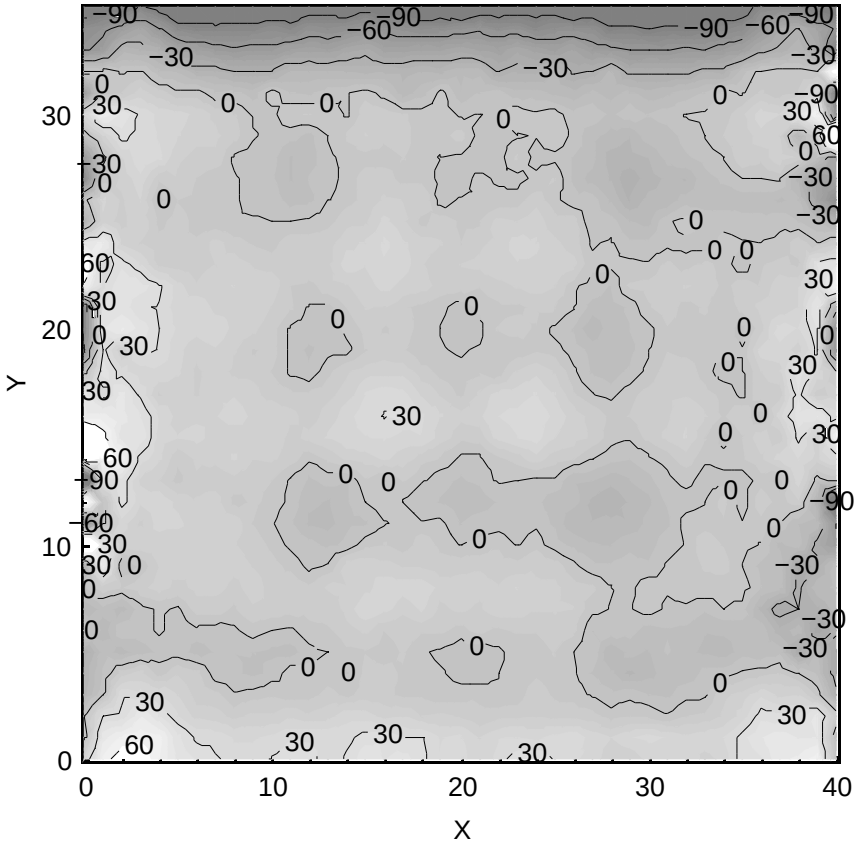

Figure 6.57: The measured near-field phase distribution of the hard-horn used in the 7x7 amplifier array at 32 GHz.

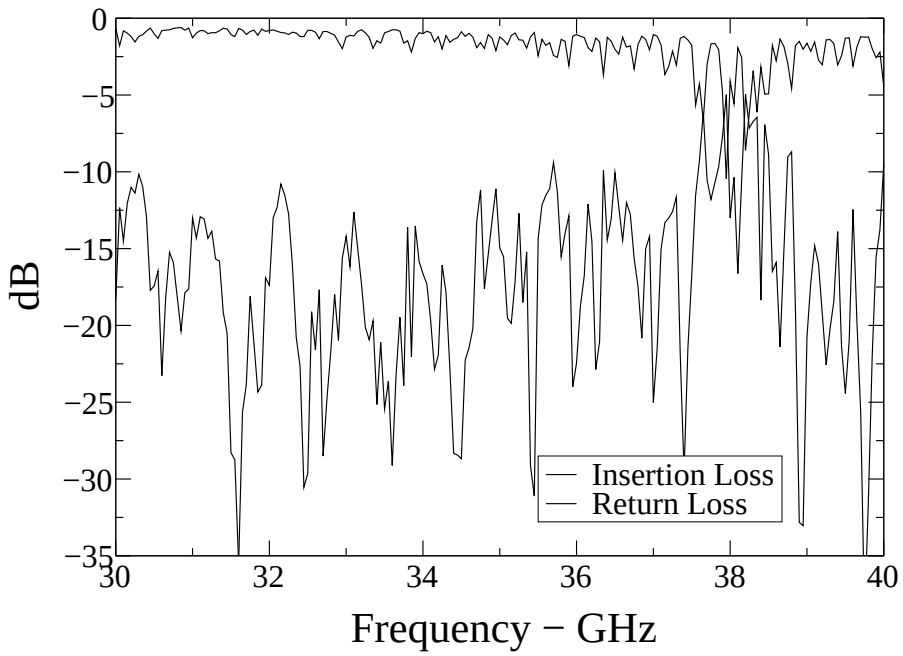

Figure 6.58: The measured insertion loss and return loss of the two hard-horn feeds back-to-back for the second version of the 7x7 array.

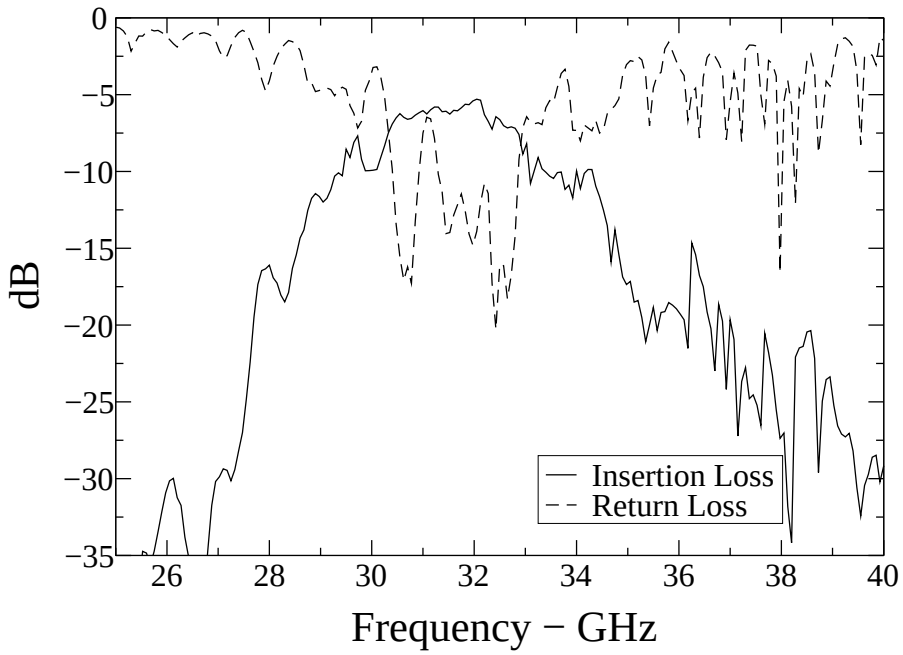

Figure 6.59: The measured insertion loss and return loss of the passive 7x7 array.

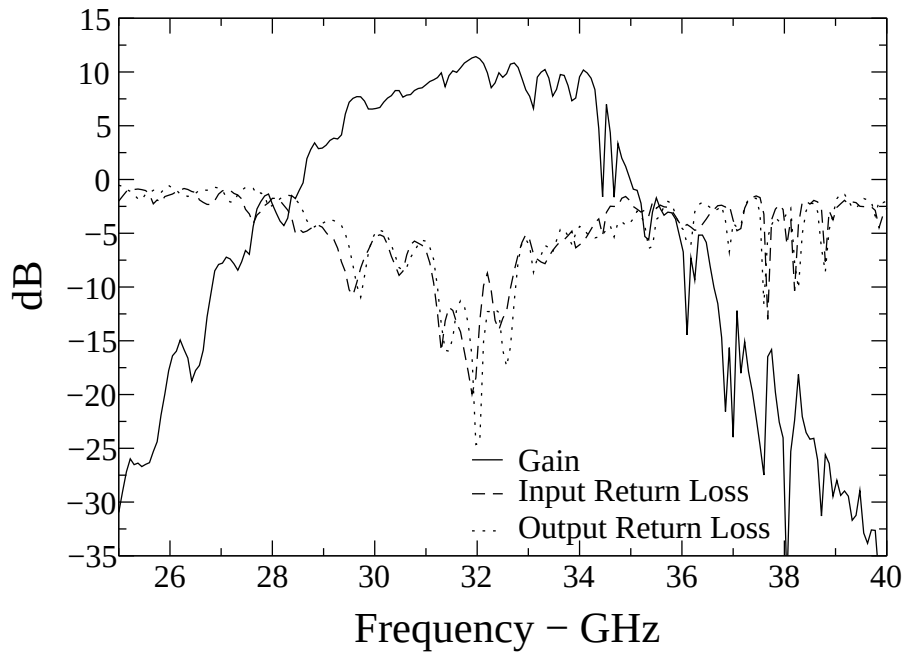

Figure 6.60: The measured small signal gain and return loss of the active 7x7 array.

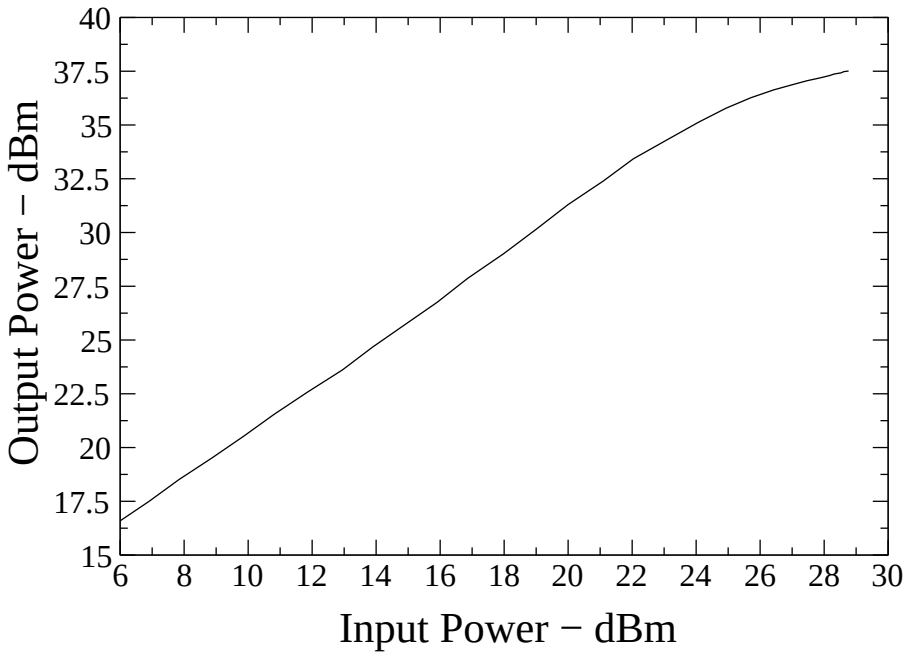

Figure 6.61: The measured output power versus input power of the 7x7 amplifier array at 31.9 GHz in a near-field measurement setup.

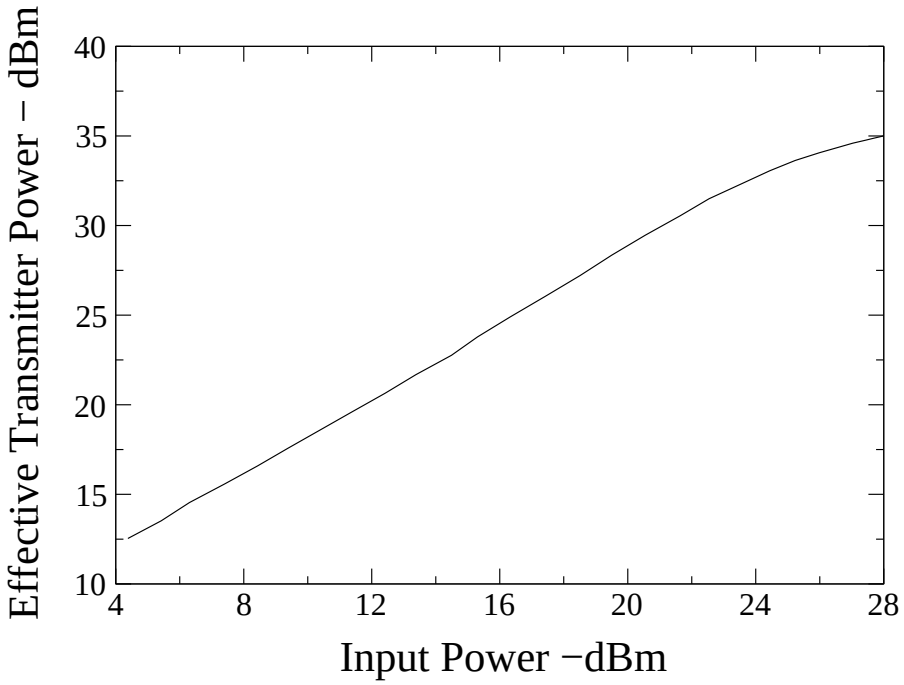

Figure 6.62: The measured output power versus input power of the 7x7 amplifier array at 31.9 GHz in a far-field measurement setup at a distance of 40 cm.

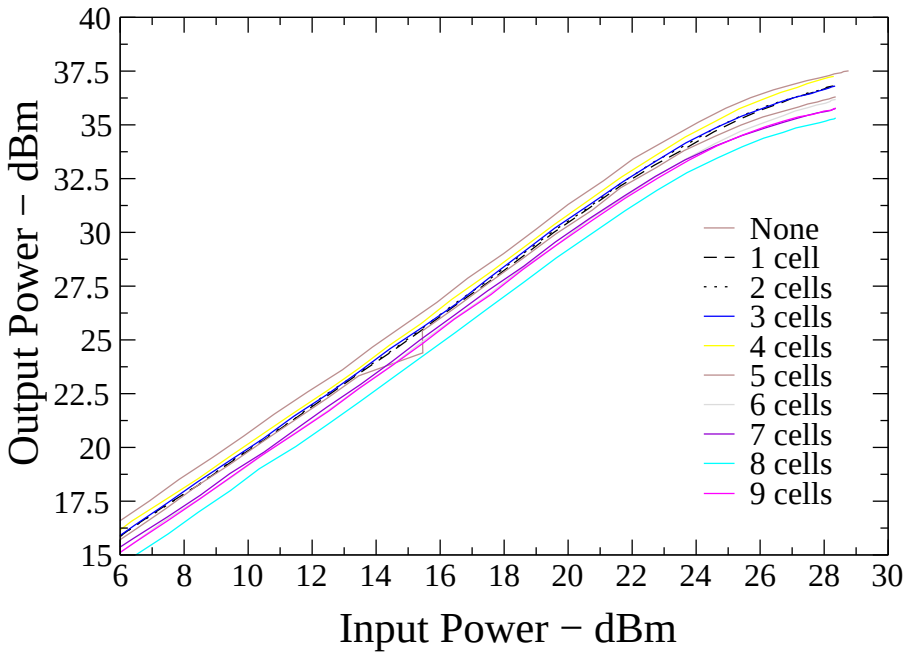

Figure 6.63: The measured output power versus input power of the 7x7 amplifier array at 31.9 GHz in a near-field measurement setup for several device failures.

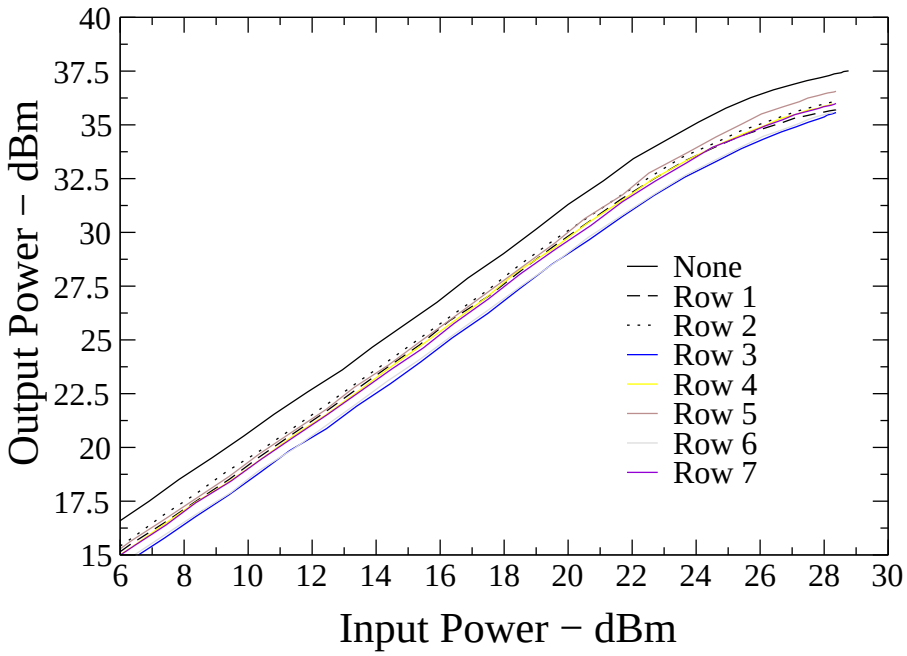

Figure 6.64: The measured output power versus input power of the 7x7 amplifier array at 31.9 GHz in a near-field measurement setup for several row failures.

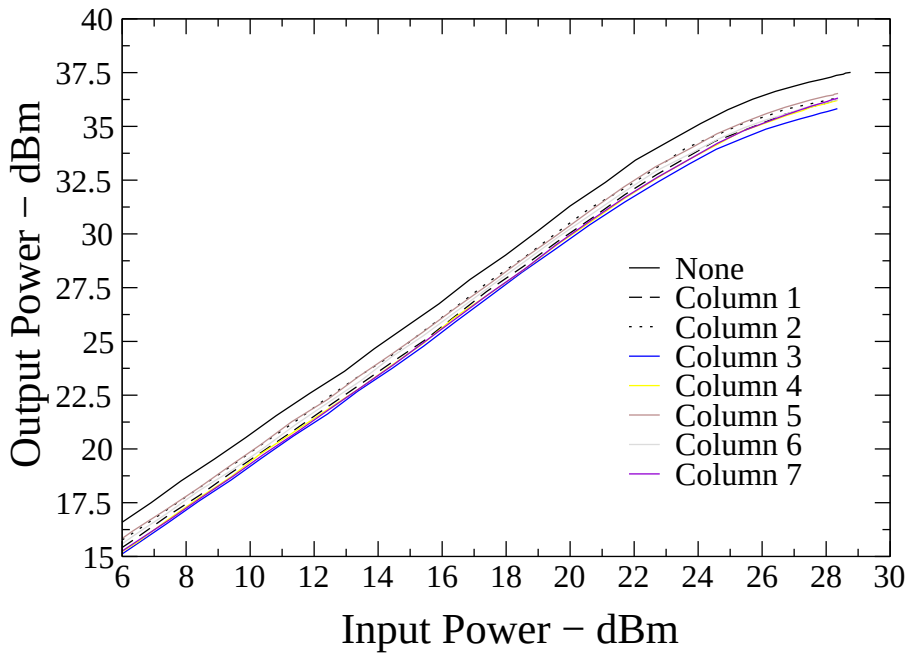

Figure 6.65: The measured output power versus input power of the 7x7 amplifier array at 31.9 GHz in a near-field measurement setup for several column failures.

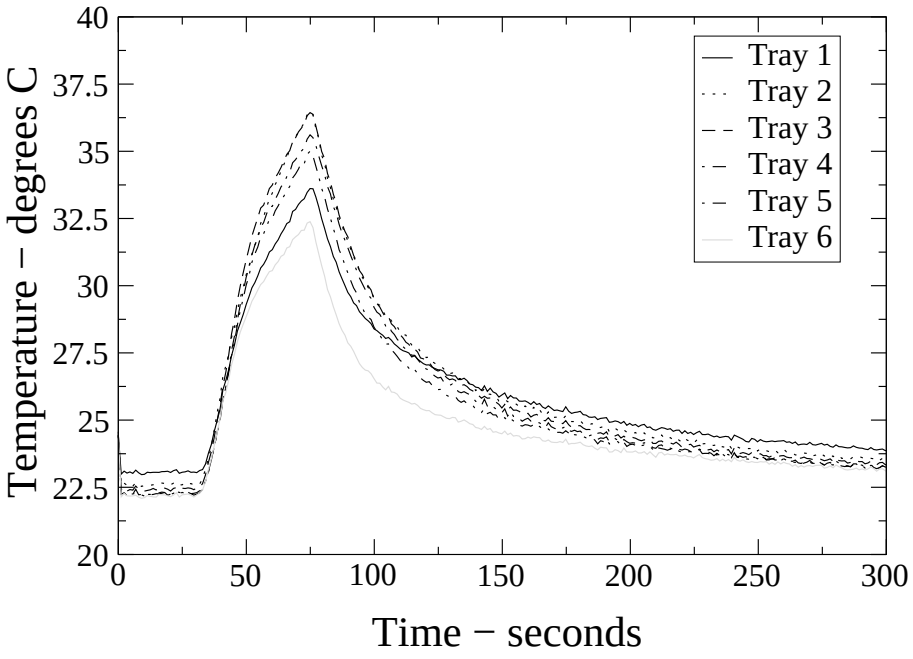

Figure 6.66: The measured temperature versus time for the 7x7 amplifier array.

Chapter 7

Conclusions and Recommendations

7.1 Conclusions of the Research

This work has described the design, fabrication, and experimental results for two methods of spatial power combining: tile- and tray-based. The spatial power combining method has been implemented for its potential to provide high output power levels at millimeter-wave frequencies, while at the same time providing high power combining efficiencies. Such potential is a direct result of the spatial power dividing/combining methodology – to use free space as the power dividing/combining medium. Both tile- and tray-based topologies were investigated thoroughly. In addition, several arrays were produced to verify the utility of the spatial power combining method using tray- and tile-based arrays.

Each tile- and tray-based array had several items in common. Most importantly, a hard-horn antenna was used to distribute power equally among the unit cells of the spatial amplifier array. Furthermore, a dielectric lens within the hard-horn distributed the power with a uniform phase. The combination of a hard-horn and lens provides the unit cells with a signal of equal magnitude and phase. This allowed for both coherent and efficient power combining. A detailed methodology was given for the design and fabrication of both hard-horns and dielectric lenses. In addition, practical experimental results were produced to verify this methodology. Several key points of this design methodology are as follows:

- Small semi-flare angles should be used in hard-horn design.
- Low relative permittivity for both the hard-horn and lens.
- Inaccurate or non-symmetrical fabrication techniques will cause over-moding within the horn.
- Near-field scanning should be used to verify the design.

- A low insertion loss does not guarantee high power combining efficiency.

The last point two points are especially important. A low back-to-back insertion loss does not guarantee a high power combining efficiency. This only means that the phase has been made uniform (coherent power combining). However, the amplitude distribution may still be non-uniform, thereby causing inefficient power combining. Only a plot of the near-field distribution will accurately describe problem.

A second common aspect between the tile- and tray-based arrays is the effect of the unit cell spacing and lattice. The choice in unit cell spacing and lattice depend heavily on the type of spatial amplifier array. In general, the triangular lattice provides the greatest area for the placement of active devices and is thus the best choice for tile-based arrays. However, more unit cells can be placed in an array using the rectangular lattice. This may be advantageous for tray-based arrays, where the unit cells spacing may be small. Finally, a unit cell spacing of approximately $0.5\lambda_0$ was found to provide a minimum insertion loss.

With these items in mind, three tile-based arrays were designed and fabricated at Ka-band under a DARPA MAFET-3 program with Lockheed Martin Corp. as the primary investigator. The resulting arrays contained 13-, 45-, and 98-elements arranged in a triangular lattice, respectively. Hard-horn feeds with lenses were also designed and fabricated for each array. The 13-element array provided 4 Watts of radiated power and 18 dB of small signal gain at 34 GHz. Each unit cell of the array contained an input microstrip patch antenna, two amplifiers, a microstrip-slot-microstrip transition, and an output microstrip patch antenna. These results provided the framework for the design and fabrication of two larger arrays.

The 45- and 98-element tile-based arrays are essentially the same. Each unit cell contains input and output microstrip patch antennas, driver and power amplifiers, and a through-plate coaxial transition. However the 98-element array provides a thicker groundplane, containing liquid cooling tubes. In addition, both arrays provide phase adjusters to compensate for unit cell variations. Each array provided in excess of 25 Watts of radiated power at Ka-band. Furthermore, the 45-element array gave 10 dB of small signal gain at 34 GHz with a 3-dB bandwidth of 800 MHz. The 98-element array provided nearly 5.3 dB of small signal gain at 33.5 GHz with a 3-dB bandwidth of 700 MHz. At the time of this publication, the 25 Watts of radiated power was the highest power level obtained by a spatial amplifier array at Ka-band.

A key aspect to both of the tile-based arrays was the removal of excess heat. Both designs provided an efficient method of heat removal through either a thick groundplane or through liquid cooling tubes. In addition, the liquid cooling tubes provided the best solution in terms of temperature stability. A second aspect of these designs was the circuit stability. No oscillations were observed. This was due to the large array spacing and the biasing scheme employed.

A novel perpendicularly-fed patch antenna and microstrip-to-waveguide transition have been developed in this work. This antenna feed provided the impetus for the design and fabrication of the three tray-based arrays. The study of these arrays was funded under an Army Research Office MURI grant. Furthermore, the fault tolerance analysis of a spatial power combiner was of great

interest to the program. This resulted in the development of two 25-element X-band arrays and a 49-element Ka-band array. All three included the design and fabrication of hard-horn feeds for the efficient distribution of power to and from the arrays.

The first 25-element X-band array was designed to verify the utility of the perpendicular-fed patch antenna with a microstrip-to-waveguide transition in a spatial amplifier array. The resulting array contained 25 unit cells, each containing an input and output perpendicularly-fed patch antenna, microstrip-to-waveguide transition, and two matched monolithic amplifiers. The resulting array provide 12.4 dB of gain at 10 GHz with a 3-dB bandwidth of 310 MHz. It should be noted that a passive version of the same array gave only 3.9 dB of loss at 10 GHz. The total collected power was 20.65 dBm giving a power combining efficiency of 20%.

A second version of the 25-element X-band array was also fabricated. This array was essentially the same as the first. However, the capability to bias each of the 25 MMIC amplifiers was added. The resulting amplifier array provided 16 dB of small signal gain with a 3-dB bandwidth of 280 MHz. A total collected output power of 29.1 dBm was obtained under 3-dB compression at 9.6 GHz, yielding nearly 50% power combining efficiency. Furthermore, a fault tolerance analysis was performed on the array by turning off individual amplifiers. This gave useful insight into the power output degradation versus the number of devices failed. As expected, the spatial power combining array's output power decreased gracefully as the number of failed devices increased. In fact, the observed rate in power degradation followed predicted values closely.

The final tray-based amplifier array to be designed and fabricated contained 49-elements and operated at Ka-band. This array consisted of seven trays, each containing seven amplifiers. Each unit cell also consisted of an input and output perpendicularly-fed patch antenna, microstrip-to-waveguide transition, and a MMIC amplifier. Furthermore, all amplifiers were individually biased to facilitate the fault tolerance analysis. Both a passive and active versions of the array were built. The passive version provided 5.3 dB of insertion loss at 32 GHz with a 3-dB bandwidth of 2.7 GHz, while the active version provided 11.6 dB of small signal gain with a 3-dB bandwidth of 1 GHz. The total collected output power was 37.1 dBm or over 5 Watts under 1-dB compression. This gives a power combining efficiency of 36% and PAE of 7.6% under 1-dB compression at 31.9 GHz. This is a remarkable collected power combining efficiency from a 49-element power combiner at Ka-band. Finally, the fault tolerance analysis of the 49-element array yielded similar results to those of the X-band array. In addition, a graceful degradation in output power versus the number of devices failed was observed. This further verified the fault tolerant nature of spatial power combiners.

The most important aspect of the tray-based arrays is the microstrip-to-waveguide transition. It is critical that each connection is formed in the same manner. If inconsistencies occur, variations in both insertion loss and phase will be created from one unit cell to the next. Therefore, the pressure contact must be made reliable. In particular, the use of hard ceramic substrates is preferable to soft substrates. The soft substrates tend to become deformed as a result of the pressure contact. This causes inconsistent connections from one unit cell to the next. Furthermore, a large microstrip line within the waveguide provides a larger surface area for the formation of a contact between it and

the top wall of the dielectric filled waveguide.

Finally, several spatial power combiners were developed in this work. Noteworthy output power levels and power combining efficiencies were obtained. In addition, a new tray-based array topology was introduced, using a novel perpendicularly-fed patch antenna. In addition, this is the research yielded the highest output power levels at Ka-band from a spatial amplifier array and the introduction of a previously unpublished microstrip-to-waveguide transition.

7.2 Recommendations for Future Research

Although much was accomplished in this work, there is of course much left to be investigated. In particular, a more exhaustive study of array losses versus array spacing and lattice structure should be undertaken. Further work should also study alternative fabrication methods for the microstrip-to-waveguide transition. The investigation of various types of radiating elements in the tray-based array should also be undertaken.

Several key points can be investigated in relation to the unit cell spacing and lattice structure. In addition, particular attention should be given to the distance between the antennas and the hard-horn feed. This will include the effect of changing the number of unit cells and their arrangement within close proximity to the horn. Finally, such work should focus on predicting the insertion loss using simple empirical models derived from either experimental or numerical studies.

The fabrication of the microstrip-to-waveguide transition using pressure contacts was found to be unsatisfactory at millimeter-wave frequencies. This pressure contact between the microstrip line and the top wall of the dielectric filled waveguide produced random variations in phase between unit cells. It would be preferable if the dielectric filled waveguide were produced from a single homogeneous dielectric slab completely coated with a layer of gold, having either end cut off to reveal the open ended dielectric filled waveguide. This would create a continuous metal surface around the dielectric core, rather than having the top, side, and bottom walls connected through pressure contacts. In addition, the new dielectric filled waveguide could be epoxied to the same trays developed in this work. The only difference being the contact between the microstrip line and the top wall of the dielectric filled waveguide. In the new topology, a bondwire or solder connection would be used to connect the two. In addition, the dielectric waveguide would need to extend into the cavity for such a connection to be made.

Finally, different radiating elements should be investigated for the tray-based array topology. Specifically, a dielectric filled horn antenna seems a natural extension to the application of the microstrip-to-waveguide transition. In addition, the dielectric filled waveguide can be flared to produce a dielectric filled horn antenna. Thus an array of dielectric filled horn antennas would be created instead of the array of perpendicularly-fed microstrip patch antennas. This may provide higher bandwidths and increased power combining efficiencies. However, much study is necessary for the implementation of such an antenna feed.

Bibliography

[1] R. A. York and Z. B. Popovic, *Active and quasi-optical arrays for solid-state power combining*. John Wiley and Sons, Inc, 1st ed., 1997.

[2] B. Toland and W. C. Wong, "Design of a spatial power combining array feed for a satellite cross link terminal," in *IEEE Aerospace Conf.*, pp. 431–439, 1998.

[3] K. J. Russel, "Microwave power combining techniques," *IEEE Trans. Microwave Theory and Techs.*, vol. 27, pp. 472–478, 1979.

[4] K. Chang and C. Sun, "Millimeter-wave power-combining techniques," *IEEE Trans. Microwave Theory and Techs.*, vol. 31, pp. 91–107, 1983.

[5] E. J. Wilkinson, "An N-way hybrid power divider," *IRE Trans. Microwave Theory and Techs.*, vol. 8, pp. 116–118, 1960.

[6] P. A. Rizzi, *Microwave Engineering: Passive Circuits*. Prentice Hall, 1st ed., 1988.

[7] D. Antsos, R. Crist, and L. Sukamto, "A novel Wilkinson power divider with predictable performance at K and Ka-band," in *IEEE MTT-S Int. Microwave Symp. Dig.*, pp. 907–910, June 1994.

[8] A. Mortazawi, T. Itoh, and J. Harvey, *Active antennas and quasi-optical arrays*. IEEE Press, 1st ed., 1999.

[9] P. F. Goldsmith, *Quasioptical systems: gaussian beam quasioptical propagation and applications*. IEEE Press, 1st ed., 1998.

[10] M. Kim, J. J. Rosenberg, R. P. Smith, R. M. W. II, J. B. Hacker, M. P. DeLisio, and D. B. Rutledge, "A grid amplifier," *IEEE Microwave Guided Wave Letts.*, vol. 1, pp. 322–324, 1991.

[11] R. J. Trew, "Wide bandgap semiconductor transistors for microwave power amplifiers," *IEEE Microwave Magazine*, vol. 1, pp. 46–54, 2000.

[12] R. J. Trew, J.-B. Yan, and P. M. Mock, "The potential of diamond and SiC electronic devices for microwave and millimeter-wave power applications," *Proceedings of the IEEE*, vol. 79, pp. 598–620, 1991.

[13] W. V. Muench, P. Hoeck, and E. Pettenpaul, "Silicon carbide field-effect and bipolar transistors," in *International Electron Devices Meeting Dig.*, pp. 337–339, 1977.

[14] S. Yoshida, H. Daimon, M. Yamanaka, E. Sakuma, and K. Endo, "Schottky-barrier field-effect transistors of 3C-SiC," *Journal of Applied Physics*, vol. 60, pp. 2989–2991, 1986.

[15] H. Daimon, M. Yamanaka, M. Shinohara, E. Sakuma, S. Misawa, K. Endo, and S. Yoshida, "Operation of Schottky-barrier field-effect transistors of 3C-SiC up to 400 C," *Applied Physics Lett.*, vol. 51, pp. 2106–2108, 1987.

[16] S. T. Allen, J. W. Palmour, and C. H. C. Jr., "Silicon carbide MESFETs with 2W/mm and 50 % pae at 1.8 GHz," in *IEEE MTT-S Int. Microwave Symp. Dig.*, pp. 681–684, June 1996.

[17] A. W. Morse, P. M. Esker, R. C. Clarke, C. D. Brandt, R. R. Siergeij, and A. K. Agarwal, "Application of high power silicon carbide transistors at radar frequencies," in *IEEE MTT-S Int. Microwave Symp. Dig.*, pp. 677–680, June 1996.

[18] R. J. Trew, "Microwave power amplifiers fabricated from wide bandgap semiconductor transistors," in *IEEE MTT-S IMOC Proceedings*, pp. 577–580, 1999.

[19] R. A. Sadler, S. T. Allen, W. L. Pribble, T. S. Alcorn, J. J. Sumakeris, and J. W. Palmour, "SiC MESFET hybrid amplifier with 30-W output power at 10 Ghz," in *Conference Proc. on High Performance Devices*, pp. 173–177, 2000.

[20] U. K. Mishra, R. Vetury, L. McCarthy, Y. Smorchkova, S. Keller, H. Xing, N. Zhang, J. S. Speck, R. York, S. DenBaars, Y.-F. Wu, P. Parikh, and P. Chavarkar, "AlGaN/GaN HEMTs and HBTs for microwave power," in *Device Research Conference Dig.*, pp. 35–36, 2000.

[21] M. A. Khan, A. Bhattarai, J. N. Kuznia, and D. T. Olson, "High electron mobility transistor based on a GaN-AlGaN heterojunction," *Applied Physics Lett.*, vol. 63, pp. 1214–1215, 1993.

[22] Y. F. Wu, B. P. Keller, S. Keller, D. Kapolnek, S. P. Denbaars, and U. K. Mishra, "Measuredd microwave power performance of AlGaN/GaN MODFET," *IEEE Electron Device Lett.*, vol. 17, pp. 455–457, 1996.

[23] J. C. M. Hwang, L. T. Kehias, J. A. Cook, and M. C. Calcatera, "Wide-bandgap-semiconductor wide-bandwidth wide-temperature-range power amplifiers," in *GaAs IC Symposium*, pp. 51–54, 1999.

[24] J. J. Xu, Y.-F. Wu, S. Keller, G. Parish, S. Heikman, B. J. Thibeault, U. K. Mishra, and R. A. York, "1-8 GHz GaN-based power amplifier using flip-chip bonding," *IEEE Microwave Guided Wave Letts.*, vol. 9, pp. 277–279, 1999.

[25] Y.-F. Wu, R. A. York, S. Keller, B. P. Keller, and U. K. Mishra, "3-9-Ghz GaN-based microwave power amplifiers with L-C-R broad-band matching," *IEEE Microwave Guided Wave Letts.*, vol. 9, pp. 314–316, 1999.

[26] Y.-F. Wu, D. Kapolnek, J. Ibbetson, P. Parikh, B. P. Keller, and U. K. Mishra, "14-W GaN-based microwave power amplifiers," in *IEEE MTT-S Int. Microwave Symp. Dig.*, pp. 963–965, June 2000.

[27] B. M. Green, S. Lee, K. Chu, K. J. Webb, and L. F. Eastman, "High efficiency monolithic gallium nitride distributed amplifier," *IEEE Microwave Guided Wave Letts.*, vol. 10, pp. 270–272, 2000.

[28] D. M. Pozar, *Microwave Engineering*. Addison-Wesley Publishing Company, Inc., 1st ed., 1990.

[29] R. S. Symons, "Tubes still vital after all these years," *IEEE Spectrum*, vol. 35, pp. 52–63, 1998.

[30] P. E. Ferguson, G. Valier, and R. S. Symons, "Gyrotron-TWT operating characteristics," *IEEE Trans. Microwave Theory and Techs.*, vol. 29, pp. 794–799, 1981.

[31] D. Shiffler, J. A. Nation, L. Schachter, J. D. Ivers, and G. S. Kerslick, "Review of high power traveling wave tube amplifiers," in *IEEE MTT-S Int. Microwave Symp. Dig.*, pp. 515–517, 1992.

[32] M. I. Lopin, A. S. Pobedonostsev, and B. V. Sazonov, "High-power multiple beam TWTs and the TWT-based amplifying chains," in *IEEE MTT-S Int. Microwave Symp. Dig.*, pp. 145–146, 1992.

[33] M. I. Lopin, B. A. Belyavsky, K. G. Simonov, V. A. Cherepenin, A. D. Zakurdayev, B. S. Grishin, A. A. Negirev, and A. S. Pobedonostsev, "High-power millimeter-wave tubes," in *IEEE MTT-S Int. Microwave Symp. Dig.*, pp. 1119–1122, 1993.

[34] J. J. Choi, C. M. Armstrong, A. K. Ganguly, and M. L. Barsanti, "Design of a 50 kW, wideband Ka-band slow wave cyclotron amplifier," *IEEE Trans. Plasma Science*, vol. 22, pp. 465–475, 1994.

[35] J. R. Sirigiri, K. E. Kreischer, M. A. Shapiro, and R. J. Temkin, "Novel quasioptical W-band gyro-TWT," in *Int. Vacuum Electronics Conf.*, 2000.

[36] K. T. Nguyen, J. P. Calame, D. E. Pershing, B. G. Danly, M. Garven, B. Levush, and J. T. M. Antonsen, "Design of a Ka-band gyro-TWT for radar applications," *IEEE Trans. Electron Devices*, vol. 48, pp. 108–115, 2001.

[37] P. F. Goldsmith, *Reference data for radio engineers*. Federal Telephone and Radio Corporation, 3rd ed., 1949.

[38] M. C. Smith and L. P. Dunleavy, "Comparison of solid state, MPM, and TWT based transmitters for spaceborne applications," in *IEEE Proc. SoutheastCon '98*, pp. 256–259, 1998.

[39] B. R. Chalamala, R. H. Reuss, and B. E. Gnade, "Displaying a bright future," *IEEE Devices and Circuits Mag.*, vol. 16, pp. 19–30, 2000.

[40] K. Shoulders, "Microelectronics using electron beam activated machining techniques," *Advances in Computers*, vol. 2, pp. 135–293, 1961.

[41] C. A. Spindt, "A thin film field emission cathode," *Journal Appl. Phys.*, vol. 39, pp. 3504–3505, 1968.

[42] R. N. Thomas, R. A. Wickstrom, D. K. Schroder, and H. C. Nathanson, "Fabrication and some applications of large-area silicon field emission arrays," *Solid-State Electronics*, vol. 17, pp. 155–163, 1974.

[43] S. W. McKnight, T. Treado, A. Sahin, and N. E. McGruer, "A design of a resonant vacuum microelectronic microstrip amplifier at 10 and 60 GHz," in *Proc. IEEE Vacuum Microelectronics Conf.*, pp. 158–159, 1993.

[44] A. Galdetskiy, "Distributed amplifier based on FEA and low-lossy transmission line," in *International Vacuum Microelectronics Conf.*, pp. 140–141, 1998.

[45] D. R. Whaley, B. M. Gannon, C. R. Smith, C. M. Armstrong, and C. A. Spindt, "Applications of field emitter arrays to microwave power amplifiers," *IEEE Trans. Plasma Science*, vol. 28, pp. 727–747, 2000.

[46] B. Zeng and Z. Yang, "Simulation of wedge field emission microtriode," in *Int. Conf. on Microwave and Millimeter Wave Tech. Proc.*, pp. 730–732, 1998.

[47] D.-I. Park, J.-H. Lee, S.-H. Hahm, J.-H. Lee, and J.-H. Lee, "Fabrication of a novel polysilicon lateral field emission triode with a high current density and high-transconductance," in *International Vacuum Microelectronics Conf.*, pp. 148–149, 1998.

[48] D. Arslan, A. DasGupta, M. Flath, and H. L. Hartnagel, "Fabrication and characterizaion of a gaas field emission triode for low voltage operation at atmospheric pressure," in *International Vacuum Microelectronics Conf.*, pp. 287–288, 1998.

[49] L. P. Sadwick, D. J. Schaffer, Y. J. Zhang, D. G. Petelenz, and R. J. Hwu, "Experimental and theoretical investigation of microminiature thermionic vacuum tube devices," in *International Electron Devices and Materials Symp.*, pp. 6–6–21–6–6–24, 1994.

[50] D. Rutledge, J. B. Hacker, M. Kim, R. M. W. II, R. P. Smith, and E. Sovero, "Oscillator and amplifier grids," in *IEEE Int. Microwave Symp. Dig.*, pp. 815–818, June 1992.

[51] M. Kim, E. A. Sovero, J. B. Hacker, M. P. D. Lisio, J.-C. Chiao, S.-J. Li, D. R. Gagnon, J. J. Rosenberg, and D. B. Rutledge, "A 100-element HBT grid amplifier," *IEEE Trans. Microwave Theory and Techs.*, vol. 41, pp. 1762–1771, 1993.

[52] C.-M. Liu, E. A. Sovero, W. J. Ho, J. A. Higgins, M. P. D. Lisio, and D. B. Rutledge, "Monolithic 40-GHz 670-mW HBT grid amplifier," in *IEEE Int. Microwave Symp. Dig.*, pp. 1123–1126, June 1996.

[53] M. P. D. Lisio, S. W. Duncan, D.-W. Tu, S. Weinreb, C.-M. Liu, and D. B. Rutledge, "A 44-60 GHz monolithic pHEMT grid amplifier," in *IEEE Int. Microwave Symp. Dig.*, pp. 1127–1130, June 1996.

[54] M. P. D. L. S. W. Duncan, D.-W. Tu, C.-M. Liu, A. Moussessian, J. Rosenberg, and D. B. Rutledge, "Modeling and performance of a 100-element pHEMT grid amplifier," *IEEE Trans. Microwave Theory and Techs.*, vol. 44, pp. 2136–2144, 1996.

[55] B. Deckman, D. S. D. Jr., E. Sovero, and D. Rutledge, "A 5-watt, 37 GHz monolithic grid amplifier," in *IEEE Int. Microwave Symp. Dig.*, pp. 805–808, June 2000.

[56] F. Lecuyer, R. Swisher, I.-F. F. Chio, A. Guyette, A. Al-Zayed, W. Ding, M. D. Lisio, K. Sato, A. Oki, A. Gutierrez, R. Kagiwada, and J. Cowles, "A 16-element reflection grid amplifier," in *IEEE Int. Microwave Symp. Dig.*, pp. 809–812, June 2000.

[57] T. Mader, J. Schoenberg, L. Harmon, and Z. B. Popovic, "Planar MESFET transmission wave amplifier," *Elec. Lett.*, vol. 29, pp. 1699–1701, 1993.

[58] C.-Y. Chi and G. M. Rebeiz, "A quasi-optical amplifier," *IEEE Microwave Guided Wave Lett.*, vol. 3, pp. 164–166, 1993.

[59] J. A. Benet, A. R. Perkons, S. H. Wong, and A. Zaman, "Spatial power combining for millimeterwave solid state amplifiers," in *IEEE Int. Microwave Symp. Dig.*, pp. 619–622, June 1993.

[60] N. Sheth, T. Ivanov, A. Balasubramaniyan, and A. Mortazawi, "A nine HEMT spatial amplifier," in *IEEE Int. Microwave Symp. Dig.*, pp. 1239–1242, June 1994.

[61] T. P. Budka, M. W. Trippe, S. Weinreb, and G. M. Rebeiz, "A 75 GHz to 115 GHz quasi-optical amplifier," *IEEE Trans. Microwave Theory and Techs.*, vol. 42, pp. 899–901, 1994.

[62] T. Ivanov and A. Mortazawi, "Quasi-optical microstrip amplifiers based on multilayer coupled structures," in *URSI Int. Symp. Signal, Systems, and Elec. Proc.*, pp. 99–102, 1995.

[63] T. Ivanov, A. Balasubramaniyan, and A. Mortazawi, "One and two stage spatial amplifiers," *IEEE Trans. Microwave Theory and Techs.*, vol. 43, pp. 2138–2134, 1995.

[64] J. F. Hubert, J. Schoenberg, and Z. B. Popovic, "High-power hybrid quasi-optical Ka-band amplifier design," in *IEEE MTT-S Int. Microwave Symp. Dig.*, pp. 585–588, June 1995.

[65] T. Ivanov and A. Mortazawi, "A two-stage spatial amplifier with hard horn feeds," *IEEE Microwave Guided Wave Lett.*, vol. 6, 1996.

[66] E. A. Sovero, Y. Kwon, D. S. Deakin, A. L. Sailer, and J. A. Higgins, "A PHEMT based monolithic plane wave amplifier for 42 GHz," in *IEEE Int. Microwave Symp. Dig.*, pp. 1111–1114, June 1996.

[67] T. Ivanov, S. Ortiz, and A. Mortazawi, "A passive double-layer microstrip array for the construction of millimeter-wave spatial power-combining amplifiers," *IEEE Microwave Guided Wave Lett.*, vol. 7, pp. 365–367, Nov. 1997.

[68] S. Ortiz, T. Ivanov, and A. Mortazawi, "A transmit-receive spatial amplifier array," in *IEEE MTT-S Int. Microwave Symp. Dig.*, pp. 679–682, June 1997.

[69] S. Hollung, A. E. Cox, and Z. B. Popovic, "A bi-directional quasi-optical lens amplifier," *IEEE Trans. Microwave Theory and Techs.*, vol. 45, pp. 2352–2357, 1997.

[70] J. Vian and Z. Popovic, "A transmit/receive active antenna with fast low-power optical switching," in *IEEE Int. Microwave Symp. Dig.*, pp. 847–850, June 2000.

[71] H. S. Tsai and R. A. York, "Quasi-optical amplifier array using direct integration of MMICs and 50 ohm multi-slot antennas," in *IEEE Int. Microwave Symp. Dig.*, pp. 593–596, June 1995.

[72] S. Ortiz, T. Ivanov, and A. Mortazawi, "A CPW-fed microstrip patch quasi-optical amplifier array," *IEEE Microwave Theory and Techs.*, vol. 48, pp. 276–280, 2000.

[73] N. J. Kolias and R. C. Compton, "A monopole-probe-based quasi-optical amplifier array," *IEEE Trans. Microwave Theory and Techs.*, vol. 45, pp. 1204–1207, 1997.

[74] E. A. Sovero, J. B. Hacker, J. A. Higgins, D. S. Deakin, and A. L. Sailer, "A Ka-band monolithic quasi-optic amplifier," in *IEEE Int. Microwave Symp. Dig.*, pp. 1453–1456, June 1998.

[75] J. Hubert, L. Mirth, S. Ortiz, and A. Mortazawi, "A 4 watt Ka-band quasi-optical amplifier," in *IEEE MTT-S Int. Microwave Symp. Dig.*, pp. 551–554, June 1999.

[76] S. Ortiz, J. Hubert, E. Schlecht, L. Mirth, and A. Mortazawi, "A 25 watt and a 50 watt Ka-band quasi-optical amplifier," in *IEEE MTT-S Int. Microwave Symp. Dig.*, June 2000.

[77] A. Alexanian and R. A. York, "Broadband spatially combined amplifier array using tapered slot transitions in waveguide," *IEEE Microwave Guided Wave Lett.*, vol. 7, pp. 42–44, 1997.

[78] N.-S. Cheng, A. Alexanian, M. G. Case, and R. A. York, "20 watt spatial power combiner in waveguide," in *IEEE Int. Microwave Symp. Dig.*, pp. 1457–1460, June 1998.

[79] N. Cheng, T. Dao, M. Case, D. Rensch, and R. York, "A 60-watt X-band spatially combined solid-state amplifier," in *IEEE MTT-S Int. Microwave Symp. Dig.*, pp. 539–542, June 1999.

[80] N.-S. Cheng, P. Jia, D. B. Rensch, and R. A. York, "A 120-W X-band spatially combined solid-state amplifier," *IEEE Trans. Microwave Theory and Techs.*, vol. 47, pp. 2557–2561, 1999.

[81] C. E. Saavedra, W. Wright, K. Y. Hur, and R. C. Compton, "A millimeter-wave quasi-optical amplifier array using inclined-plane horn antennas," *IEEE Microwave Guided Wave Lett.*, vol. 8, pp. 81–83, 1998.

[82] C. E. Saavedra, W. Wright, and R. C. Compton, "A circuit, waveguide, and spatial power combiner for millimeter-wave amplification," *IEEE Trans. Microwave Theory and Techs.*, vol. 47, pp. 605–613, 1999.

[83] S. Ortiz and A. Mortazawi, "A perpendicularly-fed patch array for quasi-optical power combining," in *IEEE MTT-S Int. Microwave Symp. Dig.*, pp. 667–670, June 1999.

[84] S. Ortiz and A. Mortazawi, "A perpendicular aperture-fed patch antenna for quasi-optical amplifier arrays," in *IEEE Antennas and Propag. Soc. Int. Symp.*, pp. 2386–2389, July 1999.

[85] A. B. Yakovlev, S. Ortiz, M. Ozkar, A. Mortazawi, and M. B. Steer, "Electromagnetic modeling and experimental verification of a complete waveguide-based aperture coupled patch amplifier array," in *IEEE MTT-S Int. Microwave Symp. Dig.*, pp. 801–804, June 2000.

[86] A. B. Yakovlev, S. Ortiz, M. Ozkar, A. Mortazawi, and M. B. Steer, "Electromagnetic modeling of an aperture-coupled patch array in the n-port layered waveguide for spatial power combining applications," in *IEEE Antennas and Propag. Soc. Int. Symp.*, pp. 518–521, July 2000.

[87] S. Ortiz, M. Ozkar, A. B. Yakovlev, M. B. Steer, and A. Mortazawi, "Fault tolerance analysis and measurement of a spatial power amplifier," in *to be published in IEEE MTT-S Int. Microwave Symp. Dig.*, June 2001.

[88] J. Sowers, D. Pritchard, A. White, W. Kong, and O. Tang, "A 36 W, V-band, solid state source," in *IEEE MTT-S Int. Microwave Symp. Dig.*, pp. 235–238, June 1999.

[89] C. A. Balanis, *Antenna Theory: Analysis and Design*. John Wiley and Sons, Inc., 2nd ed., 1997.

[90] G. N. Tsandoulas and W. D. Fitzgerald, "Aperture efficiency enhancement in dielectricaly loaded horns," *IEEE Trans. Antennas and Propagation*, vol. 20, pp. 69–74, 1972.

[91] P.-S. Kildal, "Definition of artificially soft and hard surfaces for electromagnetic waves," *Electron Letters*, vol. 24, pp. 168–170, 1988.

[92] P.-S. Kildal, "Bandwidth of a square hard horn," *Proceedings of the IEE: Antennas and Propagation*, vol. 135, pp. 275–278, 1988.

[93] C. A. Balanis, *Advanced Engineering Electromagnetics*. John Wiley and Sons, Inc., 1st ed., 1989.

[94] M. A. Ali, S. Ortiz, T. Ivanov, and A. Mortazawi, "Analysis and measurement of hard horn feeds for the excitation of quasi-optical amplifiers," in *IEEE MTT-S Int. Microwave Symp. Dig.*, pp. 1469–1472, June 1998.

[95] M. A. Ali, S. Ortiz, T. Ivanov, and A. Mortazawi, "Hard horn feeds for the excitation of quasi-optical amplifiers," in *IEEE Antennas and Propag. Soc. Int. Symp.*, pp. 490–493, July 1998.

[96] M. Ali, "Analysis of hard horn feeds for the excitation of quasi-optical amplifiers," Master's thesis, University of Central Florida, Orlando, FL, 1998.

[97] T. Ivanov, *Constrained package millimeter-wave quasi-optical power combining amplifiers*. PhD thesis, University of Central Florida, Orlando, Florida, 1997.

[98] A. D. Olver, P. J. B. Clarricoats, A. A. Kishk, and L. Shafai, *Microwave Horns and Feeds*. IEE Press, 1st ed., 1994.

[99] A. D. Yaghjian, "An overview of near-field antenna measurement," *IEEE Trans. Antennas and Propagation*, vol. 34, pp. 30–45, 1986.

[100] K. T. Selvan, "Simple formulas for the gain and far-field of open-ended rectangular waveguides," *IEE Proc. Microw. Antennas Propag.*, vol. 145, pp. 80–84, 1998.

[101] J. J. Lee, E. M. Ferren, D. P. Woollen, and K. M. Lee, "Near-field probe used as a diagnotic tool to locate defective elements in an array antenna," *IEEE Trans. Antennas and Propagation*, vol. 36, pp. 884–889, 1988.

[102] K. Yang, T. Marshall, M. Forman, J. Hubert, L. Mirth, Z. Popovic, L. P. B. Katehi, and J. F. Whitaker, "Active-amplifier-array diagnostics using high-resolotution electrooptic field mapping," *IEEE Microwave Theory and Techs.*, vol. 49, pp. 849–857, 2001.

[103] J. Bluestone, "Calculation of aperture distribution from nearfield data for low sidelobe aperture antennas," in *International Conf. on Antennas and Propagation*, pp. 356–358, 1989.

[104] D. M. Pozar, "Microstrip antennas," *Proceedings of the IEEE*, vol. 80, pp. 79–91, 1992.

[105] M. A. Ali, S. Ortiz, T. Ivanov, and A. Mortazawi, "Analysis and measurement of hard-horn feeds for the excitation of quasi-optical amplifiers," *IEEE Microwave Theory and Techs.*, vol. 47, pp. 479–487, 1999.

[106] A. C. Buck and D. M. Pozar, "Aperture-coupled microstrip antennas with a perpendicular feed," *IEEE Electron. Letts.*, pp. 125–126, 1986.

[107] P. R. Haddad and D. M. Pozar, "Analysis of an aperture coupled microstrip patch antenna with a thick ground plane," in *IEEE Antennas and Propag. Int. Symp. Dig.*, pp. 932–935, June 1994.

[108] M.-H. Ho, K. A. Michalski, and K. Chang, "Waveguide excited microstrip patch antenna - theory and experiment," *IEEE Trans. Antennas and Propagation*, vol. 42, pp. 1114–1125, 1994.

[109] P. A. Izadian, *Microwave Transitions and Applications*. Artech-House, Inc., 1st ed., 1988.

[110] D. Lancombe and J. Cohen, "Octave-band microstrip DC blocks," *IEEE Microwave Theory and Techs.*, pp. 555–556, 1972.

[111] M. Gouker, "Toward standard figures-of-merit for spatial and quasi-optical power-combined arrays," *IEEE Trans. Microwave Theory and Techs.*, vol. 43, pp. 1614–1617, 1995.